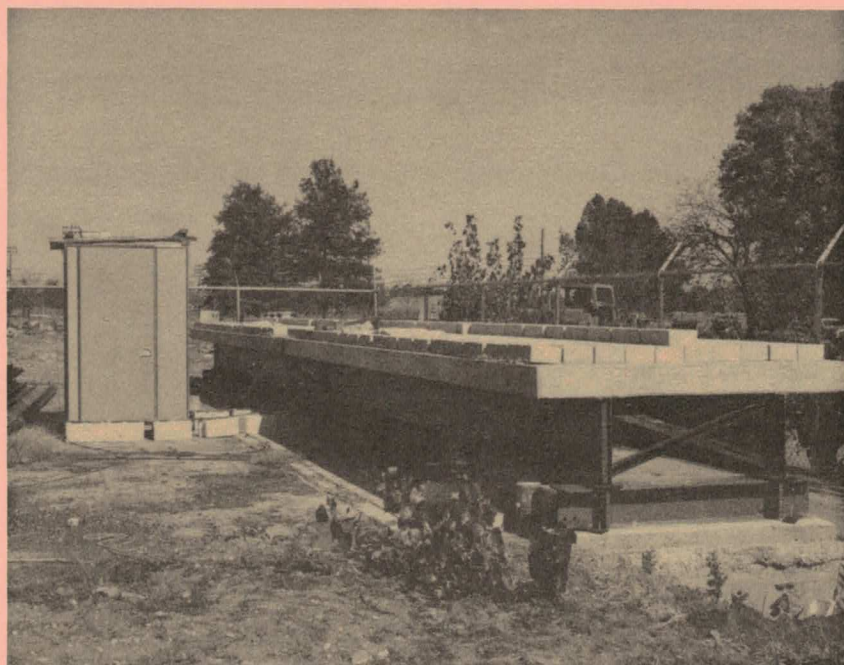# EXPERIMENTAL STUDY OF TWO PRESTRESSED STEEL BEAM-CONCRETE SLAB BRIDGE UNITS

FINAL REPORT

BY   THOMAS A. DENSFORD AND
THOMAS M. MURRAY, PRINCIPAL INVESTIGATOR

AUGUST 1986

sponsored by
OKLAHOMA DEPARTMENT OF TRANSPORTATION
RESEARCH AND DEVELOPMENT DIVISION

conducted at
FEARS STRUCTURAL ENGINEERING LABORATORY
SCHOOL OF CIVIL ENGINEERING AND ENVIRONMENTAL SCIENCE
UNIVERSITY OF OKLAHOMA, NORMAN

Final Report

EXPERIMENTAL STUDY OF TWO PRESTRESSED
STEEL BEAM-CONCRETE SLAB BRIDGE UNITS

by

Thomas A. Densford
and
Thomas M. Murray
Principal Investigator

FEARS STRUCTURAL ENGINEERING LABORATORY
School of Civil Engineering and Environmental Science
University of Oklahoma
Norman, Oklahoma 73019

TECHNICAL REPORT STANDARD TITLE PAGE

1. REPORT NO. FHWA/OK (6)	2. GOVERNMENT ACCESSION NO.	3. RECIPIENT'S CATALOG NO.
4. TITLE AND SUBTITLE Experimental Study of Two Prestressed Steel Beam-Concrete Slab Bridge Units		5. REPORT DATE
		6. PERFORMING ORGANIZATION CODE
7. AUTHOR (S) Thomas A. Densford and Thomas M. Murray		8. PERFORMING ORGANIZATION REPORT
9. PERFORMING ORGANIZATION NAME AND ADDRESS Fears Structural Engineering Laboratory University of Oklahoma 303 E. Chesapeake St. Norman, OK 73019		10. WORK UNIT NO.
		11. CONTRACT OR GRANT NO. Agreement #28, 82-02-2
12. SPONSORING AGENCY NAME AND ADDRESS Research and Development Division Oklahoma Department of Transportation 200 NE 21st Oklahoma City, OK 73105		13. TYPE OF REPORT AND PERIOD COVERED Final
		14. SPONSORING AGENCY CODE

15. SUPPLEMENTARY NOTES in cooperation with

Federal Highway Administration, US Department of Transportation

16. ABSTRACT The behavior of two 55 ft. long prestressed, composite steel beam-concrete slab bridge units was studied. The type of unit tested is currently used in county road bridge construction, where the use of prefabricated units is especially economical.

In primary test phases, the first unit was subjected to 3 years of sustained loading, over 2,000,000 cycles of fatigue loading was statically loaded to failure. The second unit underwent 500,000 cycles of fatigue loading and was statically loaded to its yield level.

In supplementary test phases, pushout-type specimens with channel and stud shear connectors, identical to those in the bridge units, were studied to determine the difference between the two connector types under sustained and ultimate loading conditions. In addition, transverse slab strength tests were performed at six locations on the first unit, and on six similar, simply supported, control slabs. The transverse slab strength tests were performed to verify that arching action occurs in the bridge slab. The presence of arching action in the bridge slab changed the mode of slab failure from a relatively ductile flexural failure, to a sudden punching failure at a much higher concentrated load.

Test results were compared to theoretical predictions and AASHTO Specification limitations. It was found that the behavior of the unit was reasonably predictable, and that with a minor connection detail change, the prestressed, composite steel beam design concept is suitable for county road bridge use.

17. KEY WORDS bridge, pre-stressed, composite, pre-fabricated, creep, shear connector, fatigue	18. DISTRIBUTION STATEMENT no restrictions		
19. SECURITY CLASSIF. (OF THIS REPORT) none	20. SECURITY CLASSIF. (OF THIS PAGE)	21. NO. OF PAGES 286	22. PRICE

METRIC CONVERSION FACTORS

Approximate Conversions to Metric Measures

Symbol	When You Know	Multiply by	To Find	Symbol
		LENGTH		
in	inches	*2.5	centimeters	cm
ft	feet	30	centimeters	cm
yd	yards	0.9	meters	m
mi	miles	1.6	kilometers	km
		AREA		
in^2	square inches	6.5	square centimeters	cm^2
ft^2	square feet	0.09	square meters	m^2
yd^2	square yards	0.8	square meters	m^2
mi^2	square miles	2.6	square kilometers	km^2
	acres	0.4	hectares	ha
		MASS (weight)		
oz	ounces	28	grams	g
lb	pounds	0.45	kilograms	kg
	short tons (2000 lb)	0.9	tonnes	t
		VOLUME		
tsp	teaspoons	5	milliliters	ml
Tbsp	tablespoons	15	milliliters	ml
fl oz	fluid ounces	30	milliliters	ml
c	cups	0.24	liters	l
pt	pints	0.47	liters	l
qt	quarts	0.95	liters	l
gal	gallons	3.8	liters	l
ft^3	cubic feet	0.03	cubic meters	m^3
yd^3	cubic yards	0.76	cubic meters	m^3
		TEMPERATURE (exact)		
°F	Fahrenheit temperature	5/9 (after subtracting 32)	Celsius temperature	°C

*1 in = 2.54 (exactly). For other exact conversions and more detailed tables, see NBS Misc. Publ. 286, Units of Weights and Measures, Price $2.25, SD Catalog No. C13.10 286.
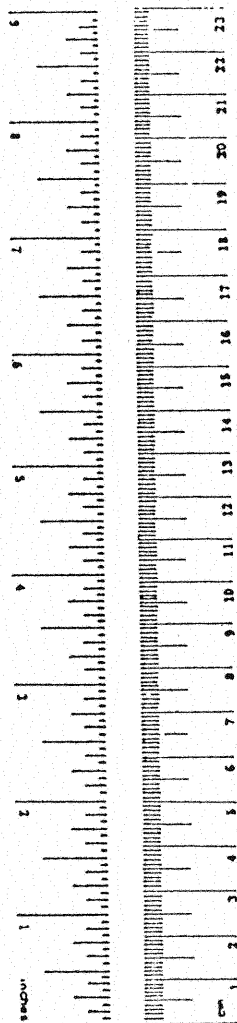
Approximate Conversions from Metric Measures

Symbol	When You Know	Multiply by	To Find	Symbol
		LENGTH		
mm	millimeters	0.04	inches	in
cm	centimeters	0.4	inches	in
m	meters	3.3	feet	ft
m	meters	1.1	yards	yd
km	kilometers	0.6	miles	mi
		AREA		
cm^2	square centimeters	0.16	square inches	in^2
m^2	square meters	1.2	square yards	yd^2
km^2	square kilometers	0.4	square miles	mi^2
ha	hectares (10,000 m^2)	2.5	acres	
		MASS (weight)		
g	grams	0.035	ounces	oz
kg	kilograms	2.2	pounds	lb
t	tonnes (1000 kg)	1.1	short tons	
		VOLUME		
ml	milliliters	0.03	fluid ounces	fl oz
l	liters	2.1	pints	pt
l	liters	1.06	quarts	qt
l	liters	0.26	gallons	gal
m^3	cubic meters	35	cubic feet	ft^3
m^3	cubic meters	1.3	cubic yards	yd^3
		TEMPERATURE (exact)		
°C	Celsius temperature	9/5 (then add 32)	Fahrenheit temperature	°F

ABSTRACT

The behavior of two 55 ft. long prestressed, composite
steel beam-concrete slab bridge units was studied. The type
of unit tested is currently used in county road bridge
construction, where the use of prefabricated units is
especially economical.

In primary test phases, the first unit was subjected to
3 years of sustained loading, over 2,000,000 cycles of
fatigue loading and was statically loaded to failure. The
second unit underwent 500,000 cycles of fatigue loading and
was statically loaded to its yield level.

In supplementary test phases, pushout-type specimens
with channel and stud shear connectors, identical to those
in the bridge units, were studied to determine the
difference between the two connector types under sustained
and ultimate loading conditions. In addition, transverse
slab strength tests were performed at six locations on the
first unit, and on six similar, simply supported, control
slabs. The transverse slab strength tests were performed to
verify that arching action occurs in the bridge slab. The
presence of arching action in the bridge slab changed the
mode of slab failure from a relatively ductile flexural
failure, to a sudden punching failure at a much higher
concentrated load.

Test results were compared to theoretical predictions
and AASHTO Specification limitations. It was found that the
behavior of the unit was reasonably predictable, and that
with a minor connection detail change, the prestressed,
composite steel beam design concept is suitable for county
road bridge use.

TABLE OF CONTENTS

LIST OF FIGURES

LIST OF TABLES

EXPERIMENTAL STUDY OF TWO PRESTRESSED
STEEL BEAM - CONCRETE SLAB BRIDGE UNITS

CHAPTER 1

INTRODUCTION

1.1 General

This report is the culmination of a four year research program involving the experimental study of two prototype precast, prestressed steel beam-concrete slab bridge units. Typically, two to four of these used are used to construct country road bridges. The testing program was implemented to investigate the behavior of prototype units under simulated conditions of typical bridge use. Long term sustained loading was used to study the effects of temperature change and concrete creep, repeated loading was used to determine the adequacy of the bridge unit design under a lifetime of repeated truck loading, and the ultimate strengths of the unit in both longitudinal and transverse directions were determined under static loads. The research program was conducted at the Fears Structural Engineering Laboratory, University of Oklahoma, under the auspices of the Oklahoma Department of Transportation.

The prestressed composite bridge units studied consist of a concrete slab connected by shear connectors to two steel beams as shown in Figure 1.1. These units are usually prefabricated and transported to a site. There, a bridge is constructed by placing two or more units on abutments and individual units connected with angle X-brace steel

Reinforced
Concrete
Slab

A

Steel Beam

A

(a) Elevation of Bridge Unit

Shear
Connectors

Reinforced
Concrete
Slab

Steel
Beam
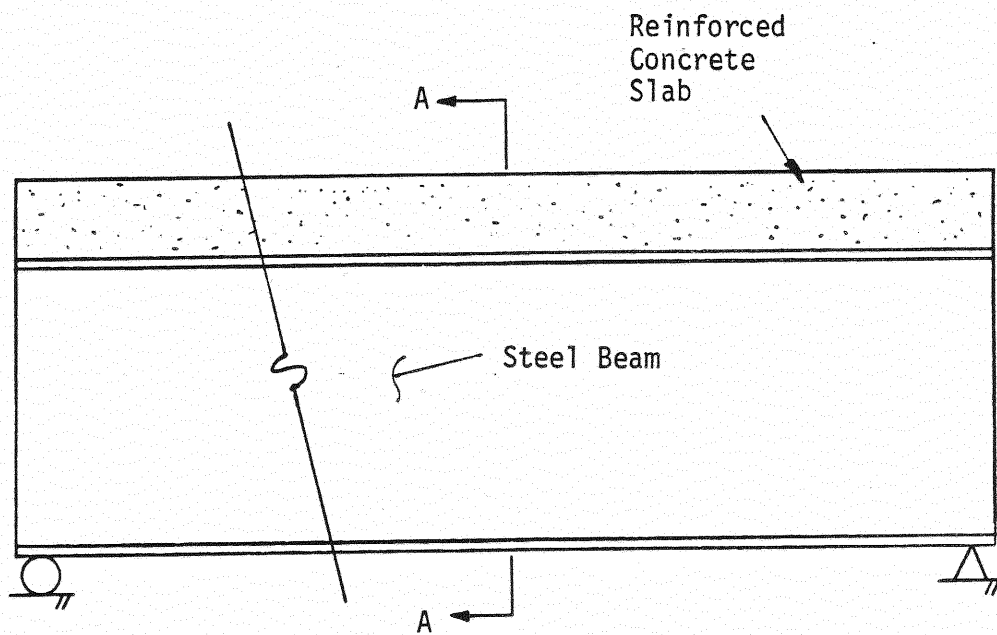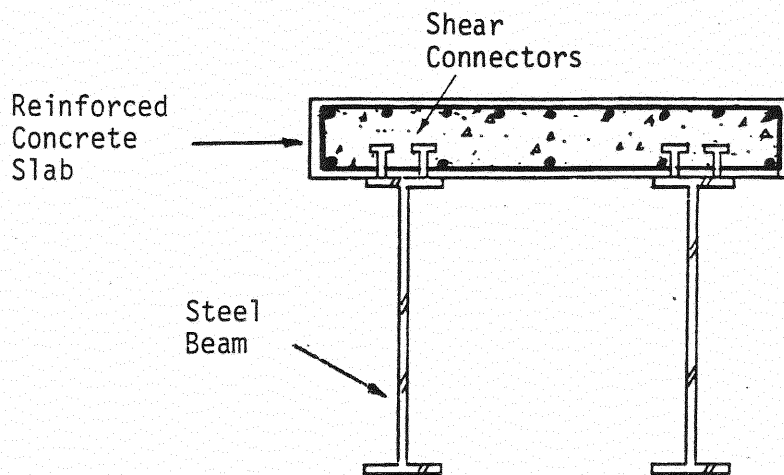
(b) Section A-A

Figure 1.1 Typical Bridge Unit Configuration

diaphragms. These bridge units are now being used primarily for county road bridges, but the possibility of use in state highway bridges exists.

The method of construction used in the production of the bridge unit is unique and patented. Shear connectors are welded to two steel beams which are inverted and simply supported above a form which contains a mat of concrete reinforcing steel. Concrete forms are then hung from the steel beams as shown in Figure 1.2. The bridge deck concrete is then poured into the forms and additional dead load may be applied to the beams to increase the unit deflection to a predetermined level such that the proper prestress level is obtained in the steel beams. When the concrete has cured and the unit is unloaded, forms are stripped, and the unit turned over. The resulting composite beam is similar to a composite beam obtained using shored construction methods, with additional stressing of the steel beam in the direction opposite to in-place gravity stresses.

This prestressing extends the service load range of the units (shored) as illustrated in Figure 1.3, which is a comparison to the behavior of a conventional composite beam constructed without shores. Upon removal of the shoring, the dead loads are resisted by the full capacity of the composite beam. This results in substantially reduced dead load deflection and tension flange stresses when compared with what occurs with unshored composite construction. The net result is an increased service load range for the beam. The service load range for the prestressed units is further increased since the bottom flange in the upright unit is in compression (or at least the tension stresses are significantly reduced) because of the construction method. However, as Figure 1.3 shows, the ultimate moment capacity of the cross-section is not affected by the choice of construction method.
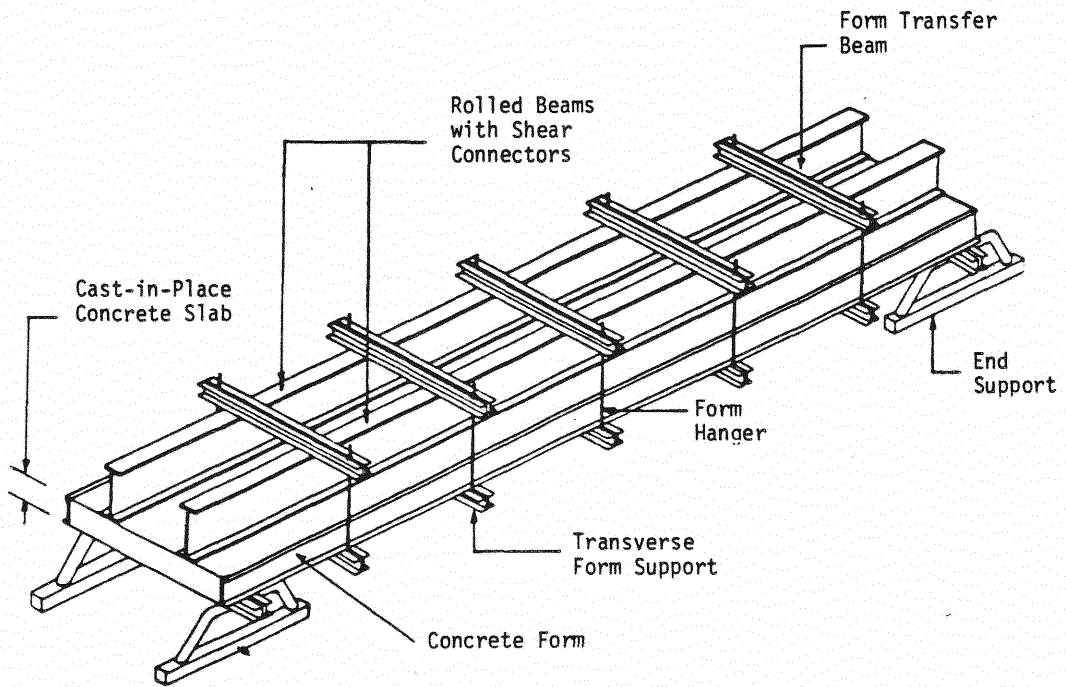
Figure 1.2 Method of Fabrication of Bridge Unit
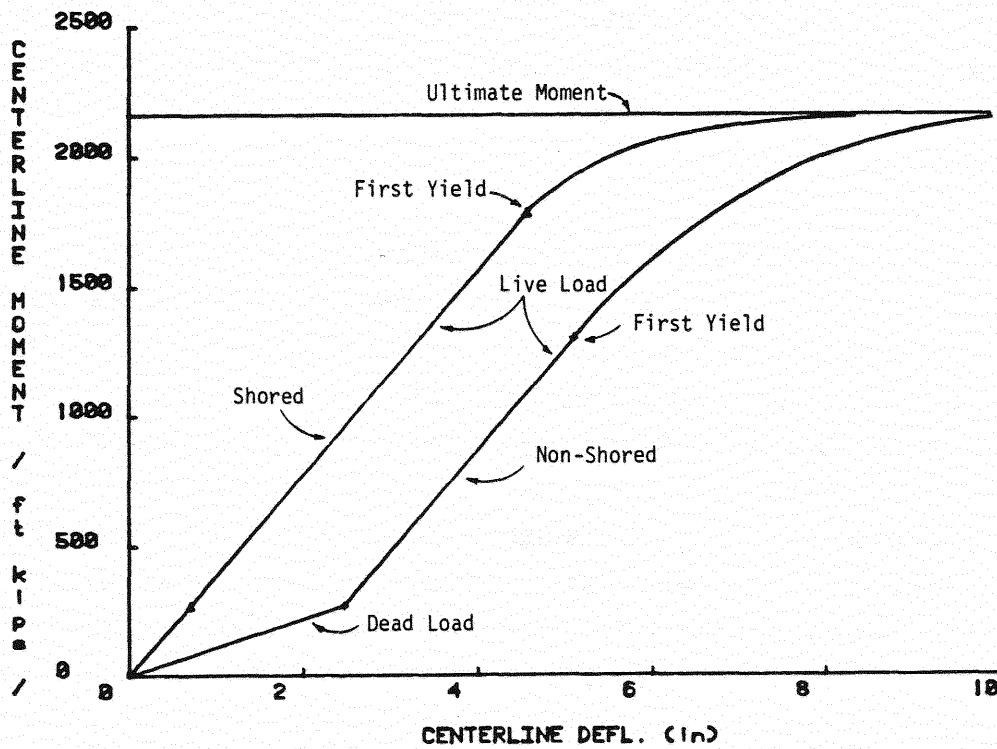
Figure 1.3   Bridge Unit Moment vs. Centerline Deflection

Another advantage of the prestressed composite bridge unit is that the permeability of the deck may be reduced. A reduction in concrete deck permeability may be obtained because the bleedwater capillaries in the curing concrete open toward the bottom of the in-place unit, since the slab was cast in an inverted position. The resulting possible resistance to water penetration may reduce corrosion of the deck reinforcing steel and accompanying maintenance problems.

A disadvantage of this method of construction is that mild steel is used as the prestressing element as opposed to very high strength steels (prestressing strands) that are used in the construction of conventional prestressed concrete beams. Since the service load capacity of the bridge units is dependent on a sustained level of prestressing, the Oklahoma Department of Transportation decided that an extensive study of the behavior of bridge units under sustained, repeated and static failure loadings be conducted. In addition, supplementary test series were conducted to investigate other aspects of the structural behavior of the units.

1.2 Testing Program

1.2.1 General

The testing program was divided into the phases shown in Table 1.1. Two nearly identical bridge units were used to conduct the tests with the research phases separated into primary and supplementary tests. In the primary test phases, one of the units was subjected to alternating periods of sustained loading and repeated loading to simulate typical service life conditions. This unit was also subjected to overloading and to ultimate strength tests

Table 1.1

Research Phases

PHASE	DESCRIPTION

Unit 1

I.   First bridge unit preparation and one year of observation under sustained loading.

II.   Repeated (HS-20) loading of 500,000 cycles.

III.   Operating rating (HS-30) loading test.

IV.   Two years of observation under sustained loading (totaling three years of sustained loading).

V.   An additional 1,500,000 cycles of repeated (HS-20) loading (totaling 2,000,000 cycles).

VI.   Repeated operating rating (HS-30) loading of 2,000 cycles.

VII.   Repeated unbalanced loading of 100,000 cycles.

VIII.   Static flexural test to failure of first unit.

Unit 2

IX.   Second bridge unit preparation and 500,000 cycles of repeated (HS-20) loading.

X.   Static flexural test to first yield of second unit.

XI.   Observation of second bridge unit under sustained loading.

Supplementary Tests

XII.   Transverse slab strength tests on first bridge unit.

XIII.   Shear connector specimen observation and strength tests.

in the primary phases. The first unit was accidentally dropped between Phases IV and V (see Table 1.1) and as a consequence, the results of the static flexural test to failure (Phase VIII) are questionable. A second unit was then constructed and used for Phases IX thru XI.

In the two supplementary test phases, tests were conducted on the first bridge unit to determine the ultimate strength of the concrete deck in the transverse direction, and on separately constructed shear connector specimens to study possible sustained loading effects for two types of shear connectors.

Test setup details for all phases are found in Appendix C at the end of this report. Table 1.2 shows the chronological order of the test phases.

1.2.2 Primary Tests

Phases I through X were considered to be primary test phases. Photographs of the loading configurations are shown in Figure 1.4. Phase I consisted of one year of observation of the first bridge unit under sustained loading. The goal of this phase was to determine the response of the bridge unit to sustained loading, as well as, its response to temperature fluctuation. In Phase II, the bridge unit was subjected to a simulated truck traffic volume in the form of 500,000 cycles of repeated loading. The load magnitude corresponded to AASHTO Specification [1] HS-20 loading, adjusted by axle fraction and impact coefficients. Phase III consisted of subjecting the unit to a static overload which produced a maximum tension flange stress equal to 75% of the material yield stress corresponding to an operating rating load as defined in the AASHTO Specification [1]. This overload is equal to 1.5 times the HS-20 load magnitude

Table 1.2

Chronological Summary of Research

DATES	COMMENTS
1 April 1982	Concrete poured for first bridge unit.
8 April 1982	First bridge unit placed outside Fears Structural Engineering Laboratory (FSEL).
22 April 1982- 11 May 1983	Phase I, observation of first bridge unit under long term (one year) sustained loading.
3 March 1983- 19 July 1985	Phase XIII A, observation of shear connector specimens under long term sustained loading (810 days).
2 June 1983- 15 Sept 1983	Phase II, first unit moved into FSEL and subjected to 500,000 cycles of repeated (HS-20) loading.
23 Sept 1983	Phase III, first unit tested under operating rating (HS-30) loading.
30 Sept 1983- 4 Sept 1985	Phase IV, first unit moved outside FSEL and observed under two years of sustained loading (700 days).
5 Sept 1985	First unit accidentally dropped when transport was attempted.
6 Sept 1985- 2 Oct 1985	Repair and curing of damaged portion concrete slab of first unit.
21 Sept 1985	Phase XIII B, shear connector specimen failure tests.
3 Oct 1985- 20 Nov 1985	Phase V A, first unit brought into FSEL and subjected to 600,000 cycles of repeated (HS-20) loading (1,100,000 total cycles).
21 Nov 1985	Phase VI, first unit subjected to 2,000 cycles of operating rating (HS-30) loading.
25 Nov 1985- 1 Jan 1986	Phase V B, first unit subjected to 900,000 cycles of repeated (HS-20) loading (2,000,000 total cycles).

Table 1.2, Continued

Chronological Summary of Research

DATES	COMMENTS
8 Jan 1986- 20 Jan 1986	Phase VII, first unit subjected to 100,000 cycles of repeated unbalanced loading.
6 Feb 1986	Phase VIII, static flexural test to failure of first unit.
19 Mar 1986	Concrete poured for second bridge unit.
21 Mar 1986- April 1986	Phase XII, transverse slab strength tests using the first unit.
17 April 1986	First bridge unit removed from FSEL.
18 April 1986	Second bridge unit brought into FSEL.
22 April 1986- 22 May 1986	Phase IX, second unit subjected to 500,000 cycles of repeated (HS-20) loading.
28 May 1986	Phase X, test on second unit to determine first yield of cross section.
2 June 1986	Second bridge unit removed from FSEL.
3 June 1986- July 1986	Phase XI, observation of second bridge unit under sustained loading.
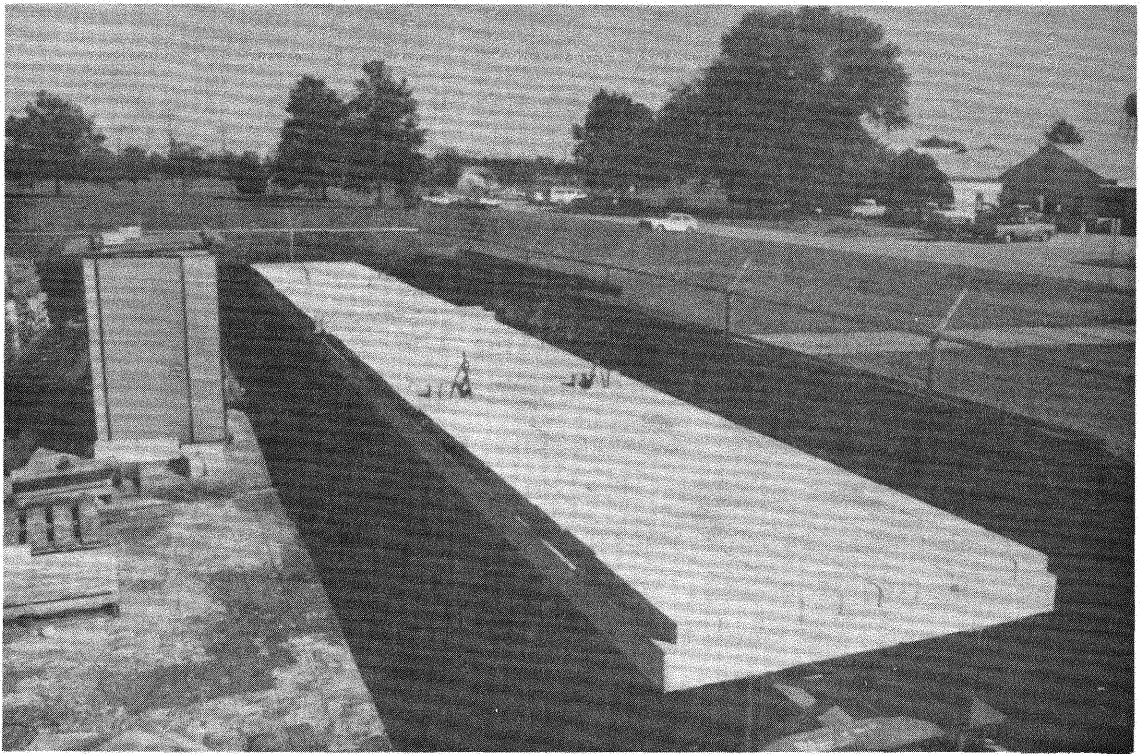
(a) Sustained Loading Configuration
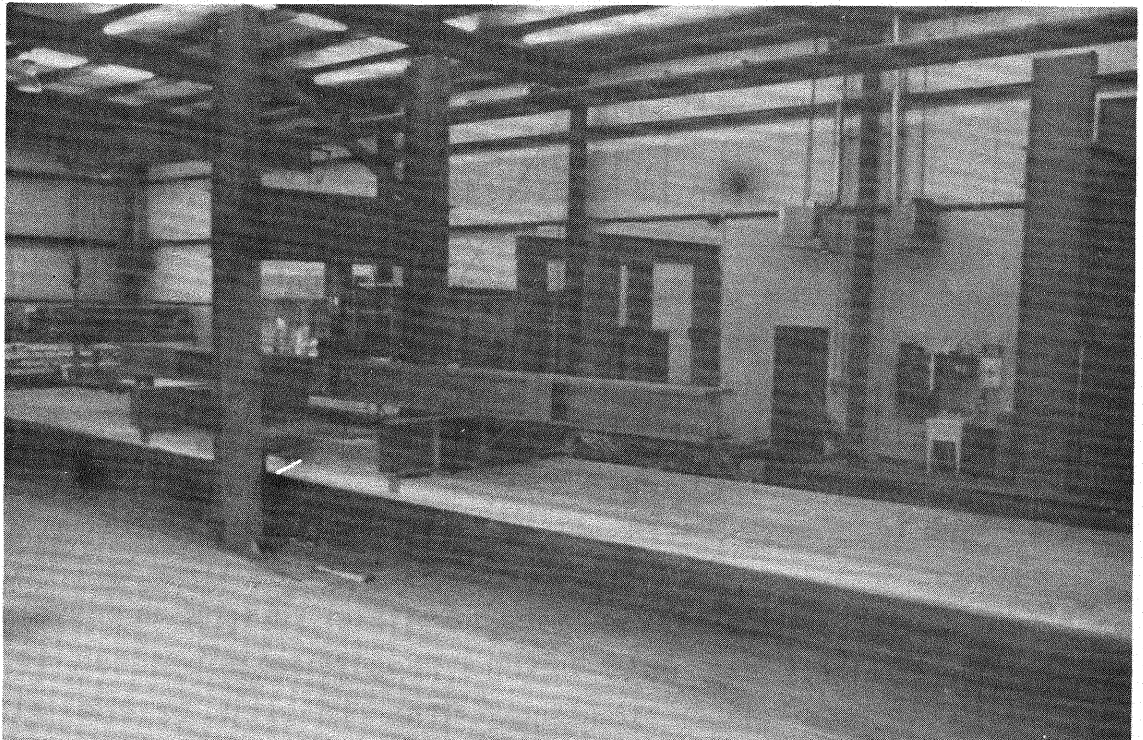
(b) Fatigue and Static Loading Configuration

Figure 1.4 Primary Test Loading Configurations

and is referred to herein as an HS-30 loading. The unit was then observed under sustained loading for two additional years which comprised Phase IV, and which was similar to Phase I.

Phase V consisted of cycling the same bridge unit an additional 1,500,000 times under HS-20 loading (totaling 2,000,000 cycles, the requirement for an interstate highway rating for the bridge design). Phase VI consisted of subjecting the bridge unit to 2000 cycles of operating rating (HS-30) loading, which represented a permit overload ratio of one in one thousand trucks. In Phase VII, the bridge unit was cyclically loaded similarly to the repeated HS-20 loading of Phase V, except that the load was applied eccentrically with respect to the longitudinal centerline of the unit. This test conservatively simulates the unbalanced load condition which results when only one line of wheel loads is on a unit in a multi-unit bridge. Finally, in Phase VIII, the first unit was loaded statically until flexural failure occurred.

Phase IX consisted of subjecting the second bridge unit to 500,000 cycles of repeated (HS-20) loading. In Phase X, the second unit was loaded to first yield so that the amount of remaining prestress in the unit could be quantified after the repeated loading of Phase IX. Phase XI was a short observation period under sustained loading.

1.2.3 Supplementary Tests

Phase XII involved the determination of the transverse strength of the first unit bridge deck when subjected to a simulated single wheel loading. The in-situ bridge slab strength was compared to the strength of simply supported slab sections which were constructed using the same specifications as used for the first test unit deck.

Phase XIII was initiated during Phase I of the primary
tests to determine the role of shear connectors on sustained
loading performance of the bridge units. It was theorized
during Phase I that the smaller contact area of welded
studs, which were used in the first unit, might result in
sufficiently high stress concentrations in the concrete deck
to cause an unacceptable amount of creep and resulting loss
of prestress. One set of pushout-type specimens was
constructed using welded shear connectors identical to those
in the first unit. A second set was constructed using
channel-type shear connectors. The specimens were observed
under long term sustained loading so that creep and slip
effects could be evaluated. On completion of the
observation period, the failure strength of the shear
connector specimens was experimentally determined (Phase XII
B).

1.2.4 Bridge Unit Test Specimens

Two composite girder bridge units of nearly identical
configuration were tested. Each unit consisted of two
upright, parallel, 55 ft. long W21x50 steel beams of A588
Grade 50 steel, connected by 3x3x¼ in. steel angle
cross-frame diaphragms, located at the ends and third points
of the beams. Pairs of 3/4 in. diameter by 4 in. high
welded stud shear connectors, spaced along the beam flanges
in accordance with the AASHTO specification were welded to
the beams prior to casting the concrete deck. For each
unit, a full length, reinforced concrete slab of 6 ft. - 9
1/2 in. width was cast against the top flanges of the
parallel steel beams. Slab thicknesses were 7 1/2 in. and 7
in. for the first and second units, respectively. The slabs
were cast using 5000 psi design strength concrete,
reinforced with longitudinal and transverse, top and bottom,
number 4 bars of Grade 60 yield strength steel. Details,
including reinforcing bar spacings, are found in Appendices

-13-

A and B for the first and second units, respectively. Measured material properties for each unit are found in Appendix L.

Instrumentation was similar for both units. Electrical resistance strain gages were mounted on selected longitudinal reinforcing steel bars and on the top and bottom flanges of the steel beams before the concrete slabs were cast. After the concrete slabs had cured and the units were stripped from formwork and turned upright, additional electrical resistance strain gages were mounted on the top surface of the concrete slabs. All strain gages were located at the midspans of the units. Dial gages were used to measure relative movement of the concrete slabs with respect to the steel beams for the fatigue static loading phases of the research. Displacement transducers were used to measure support and midspan vertical movements. The test setups, instrumentation details and testing procedures are described in Appendix C.

1.3 Organization of Report

The majority of this report is devoted to the discussion of test results. The results are presented in two chapters dealing with primary and supplementary test phases. The primary phases are further divided into three categories: sustained loading tests, fatigue loading tests, and static loading tests. Specimen dimensions, details, and material properties; test setups and instrumentation details; and selected test results are contained in the appendices. Necessary strength calculations are also found in an appendix. Calculations were made using measured yield strengths of 56.0 ksi and 58.0 ksi and concrete crushing strengths of 7.4 ksi and 6.4 ksi for test units 1 and 2, respectively. Measured material properties for the various test specimens are given in Appendix L.

CHAPTER II

SUMMARY OF PRIMARY TEST RESULTS

2.1 General

In the following sections, results of the primary test phases are presented in three series: sustained loading tests, fatigue loading tests, and static loading tests. The tests were considered to be primary in that they were used to determine the adequacy of the bridge unit design through the study of long term bridge unit deflection due to temperature change and sustained loading, fatigue of the shear connectors and connection details, and the stiffness and bending strength of the bridge unit.

The results of Phases I thru III (initial sustained loading, fatigue and overload tests) have been reported by Hendrick [2], in which he included an extensive literature survey of research concerning composite beams, prestressed steel beams, prestressed concrete slabs, and strength and fatigue behavior of shear connectors. Phase IV (two year sustained loading observation) has been presented by Majumdar [3] along with a discussion of research found in the literature concerning creep, shrinkage, and temperature change effects on reinforced concrete beams and composite steel-concrete beams.

Is is evident that much research has been devoted to the study of phenomena related to concrete and steel and

their coexistence in structural members, but, as Hendrick stated, "a full-scale bridge unit constructed such as the one discussed herein has never been tested."

2.2 Sustained Loading Tests

2.2.1 Overview

The effects on the bridge unit of creep and shrinkage of the concrete deck and of temperature change on the composite bridge unit were examined during periods of sustained loading of the unit, since it was unknown if these phenomena would cause undesirably significant changes in camber and prestress level in the bridge unit. Phase I, the initial period of sustained loading began shortly after the concrete deck was poured for the first unit and lasted for one year. To determine whether or not repeated loading had an effect on the sustained loading behavior of the unit, the second period of sustained loading, Phase IV, was begun after the first unit had undergone repeated loading in Phase II.

Study of the bridge unit under sustained loading consisted of monitoring strain and deflection changes over the periods of observation in which the unit was located outdoors and loaded with a layer of concrete blocks to simulate the weight of an asphalt overlay. A description of the test setup and instrumentation is found in Appendix C.

The sustained loading behavior of a composite concrete-steel girder is characterized by an increase in strain energy per unit volume of the member due to strains caused in the concrete primarily as a result of a creep and shrinkage phenomena. Neglecting shear strain energy, the strain energy (U) of a composite beam may be written as

$$U = \int \frac{M^2}{2EI}\, dx \qquad\qquad (2.1)$$

where the "M" term reflects the loading on the member and the "EI" term reflects the cross-sectional properties of the member. Thus, to effect an increase in strain energy due to creep and shrinkage in the concrete, either the cross-sectional properties term ("EI") may be decreased or the loading term (M) may be increased (or both). The first approach is called the effective concrete elastic modulus approach and is used in the AASHTO Specifications [1]. The second approach is suggested by Branson [4]. Both approaches account for the increased strain energy per unit volume caused by concrete shrinkage and creep phenomena.

The effective concrete elastic modulus approach is suggested in the AASHTO Specification when composite girders are used to resist sustained loads. The transformed composite section properties are determined by arbitrarily increasing the ratio of the steel elastic modulus to the concrete elastic modulus (the modular ratio denoted as n) by a factor of 3.0. This results in an effective concrete elastic modulus of one third its original value, which reduces the moment of inertia of the section and changes the neutral axis location. The resulting section properties are then used to calculate the stresses on the cross-section and member deflection due to sustained loading. It is noted that the modular ratio (n) is not increased for non-sustained loading analysis.

In Branson's composite section method, creep and shrinkage strains in the concrete are determined with time as a percentage of empirically determined ultimate creep and shrinkage strains, and then adjusted for factors such as humidity, slump, etc., as described in Reference 4. These

strains are mathematically converted to stress, and then to
a force which is first applied in tension to the slab alone
and then applied as compression to the composite section,
with both forces being applied at the slab centroid.

The method is further explained considering a two part
procedure. In the first part, the concrete slab is removed
from its bonded position and a tensile force (calculated
from the empirical strain value) applied to both ends of the
slab at the slab centroid as shown in Figure 2.1(a). In the
second part, the slab is returned to its original bonded
location in the composite section, and the creep and
shrinkage force applied in the opposite (compressive)
direction, again at the slab centroid as shown in Figure
2.1(b). Equilibrium is satisfied since the applied forces
in the two parts were colinear and equal, but since the
forces were applied to two different areas and the second
force was applied eccentrically to the composite section, a
non-uniform stress distribution results as shown in Figure
2.1(c). The resulting stress distribution also causes a
downward deflection, D, given by the expression

$$D = \frac{QeL^2}{8EI} \tag{2.2}$$

where Q = the applied creep and shrinkage force, e = the
distance between the slab centroid and the composite section
centroid, L = the length of the composite beam, E = the
elastic modulus of the transformed section, and I = the
moment of inertia of the transformed The resultant stress in
the concrete region of the transformed section is divided by
the modular ratio n to obtain the actual concrete stress.

From the above discussion, it is seen that Branson's
composite section method is based on the assumptions that

-18-
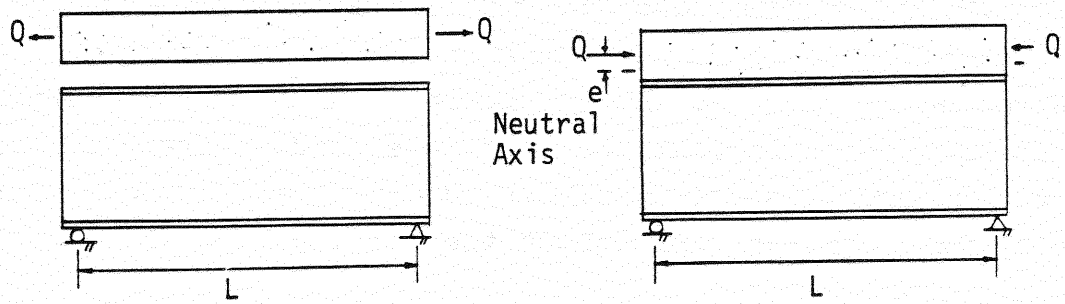
(a) Part 1, Creep and Shrinkage
Force Applied to Separated
Concrete Slab at Slab Centroid

(b) Part 2, Creep and Shrinkage
Force Applied to Composite
Section at Slab Centroid
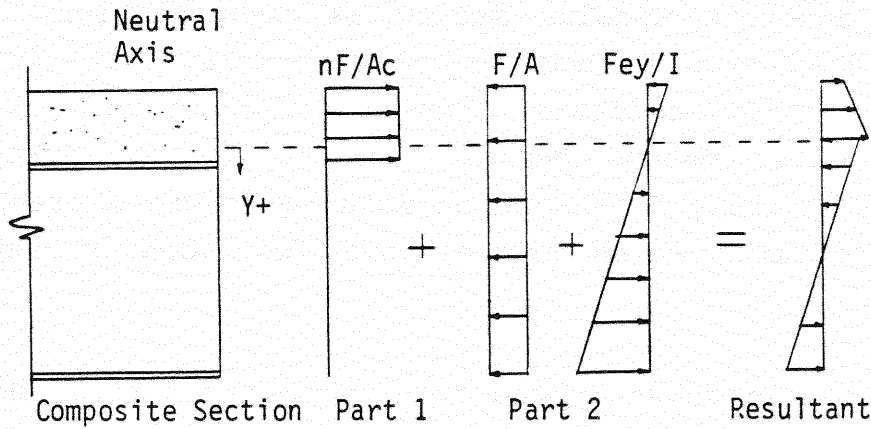
(c) Superposition of Stress Distributions Due to Creep and
Shrinkage Force

Figure 2.1   Analysis of Creep and Shrinkage Effects by Branson's
Composite Section Approach

superposition and statics are applicable to creep and shrinkage effect analysis and that once the concrete has cured and the slab and steel beam are locked together, creep and shrinkage strains in the slab may be converted to internal slab forces which are resisted by the total composite section. Also, it is assumed that the modulus of elasticity of the concrete is not affected by creep or shrinkage. As will be discussed later, static tests performed on the two bridge units in this project support this assumption in that the stiffness (and, correspondingly, the concrete elastic modulus) of the two units remained relatively constant throughout the testing program.

Branson's method provides a better qualitative understanding of the effects of creep and shrinkage (and may be used in analyzing temperature effects) than does the effective concrete elastic modulus method, although the effective concrete modulus method is much simpler. And, although Branson's method is more precise, it is not necessarily more accurate than the effective concrete elastic modulus method because the results of Branson's method are entirely dependent on assumed concrete creep and shrinkage strains which are elusive functions of several parameters.

It will be shown in the results of tests from Phase I that the prescribed strains used in predicting creep and shrinkage behavior by Branson's method resulted in an overestimation of deflection of the bridge unit due to creep and shrinkage effects. However, both methods account for increases in strain energy (as related by Equation 2.1) in the composite beams due to creep and shrinkage with the result being that both methods give qualitatively appropriate, although not necessarily similar, increases in cross-sectional stress and downward deflection.

Branson's method was used in the research described in this report, and although the method can only be approximate since concrete behavior is dependent on a wide range of conditions and material properties, the use of this simple approach has resulted in qualitatively accurate predictions. Details of the method and example calculations are found in Section D.1 of Appendix D.

2.2.2 Discussion of Phase I Results

Phase I, observation of the first bridge unit under one year of sustained loading, began 21 days after the concrete deck was poured and ended 384 days later (22 April 1982 to 11 May 1983). Test results consist of change in centerline deflection, change in strain on the concrete slab top surface at midspan, and change in reinforcing steel and steel beam strains all with respect to time and temperature changes. In addition, the bridge unit apparent neutral axis was determined from strain readings and plotted against time and temperature change. Plots and tables of selected results are found in Section D.2 of Appendix D.

As was previously mentioned, Branson's composite section method was used to predict the shrinkage, creep, and temperature deflection behavior of the bridge unit during sustained loading test phases. The calculations are explained in Appendix D. Table D.1 provides a comparison between predicted deflection behavior of the unit and measured change in deflection, with shrinkage and creep effects combined. This data is also shown graphically in Figure D.1.

Figure D.1 shows the midspan change in deflection of the bridge unit compared to the change in air temperature over the time period comprising Phase I. The graph shows

that after an initial period of what appears to be high sustained loading effects, the change in deflection of the bridge unit is directly related to fluctuation in air temperature, that is, as the air temperature increases, the bridge unit deflects downward and when the air temperature decreases the bridge unit deflects upward. (The thermal expansion of steel is about 15% greater than for concrete; therefore, as the air temperature increases, the bottom of the unit (steel) expands more than the top (concrete) causing the unit to deflect downward.)

In Figure D.2, measured midspan deflection and predicted (using Branson's method) temperature and combined creep and shrinkage deflections are plotted for the nearly 400 days of observation. The graph shows that the measured midspan deflections increased at a rapid rate for the first approximately 160 days of observation and then decreased for the next 80 days and then remained essentially constant for the remaining days of the 384 day observation period. Predicted changes in midspan deflections due to creep effects also increase at a rapid rate for the first 100-150 days but then became asymptotic at approximately 0.75 in. Predicted temperature effects are, of course, a direct function of temperature strain.

The shape of the total predicted creep, shrinkage, and temperature curve in Figure D.1, is in good agreement with the shape of the measured deflection curve, however, the predicted deflections are somewhat higher. Also, the measured deflections closely follow the predicted temperature effects curve. Thus, it is concluded that the predicted creep and shrinkage effects are higher than the actual effects.

Cross-sectional stresses and strains were also found to be sensitive to creep, shrinkage, and change in air temperature. Figure D.3 shows the change in strain of the top surface of the concrete; Figure D.4 shows the change in stress of the beam flanges; and Figure D.5 shows the change in stress of the longitudinal reinforcing bars in the concrete slab. (Stress was calculated from measured strains assuming a modulus of elasticity of steel of 29,000 ksi.) All are plotted with change in air temperature over the time period of Phase I. Again, after an initial period of sustained loading effects, the change in strains and stresses are directly affected by changes in air temperature.

Table D.2 shows the change in strain values in the beam flanges and the resulting shift of apparent neutral axis location of the cross-section. Each beam strain shown in Table D.2 is the change in strain from the strain level at which the data acquistion systems were initialized. For this unit, the data acquistion systems were initialized when the unit was in the inverted position and just before it was turned upright and loaded with the simulated asphalt overlay (concrete blocks). From this reference point, the changes in strains of the bottom and top flanges were used to determine an apparent neutral axis location, e.g. location of point of zero strain assuming a linear variation of strain over the instrumental cross section. The resulting apparent location of the neutral axis location is plotted versus time in Figure D.6.

The movement shown in Figure D.6 should not be interpreted as loss of stiffness due to creep or shrinkage effects. Examination of the change in top or bottom flange strain values (Table D.2) between successive observation days shows that these changes are relatively constant.

Thus, the location of the neutral axis calculated from these strains remains at approximately the same location, indicating that a loss of stiffness is not occuring.

The difference between the two neutral axis locations is illustrated in Figure 2.2. The combined effect of axial compression and bending of the composite section (due to creep, shrinkage, and temperature change in the concrete slab) as measured in the steel beam results in a daily strain change as shown in Figure 2.2(a), and a strain change from the initial strain as shown in Figure 2.2(b). As Figure 2.2(b) shows, the change in neutral axis location determined from the reference strains depends greatly on the reference position (hence the initial strains) chosen.

Even though the apparent neutral axis location as determined with respect to the inverted reference position is not a true neutral axis location, its location is a good measure for determining the time dependent nature of creep and shrinkage behavior. Figure D.6 shows that after an initial period of about 100 days, the position of the apparent neutral axis had become relatively stable. This is even more evident in Table D.2 where it may be seen that the "average flange stress" (strain times E) changed rapidly during the first 100 days of observation, at which time the flange strains reached a relatively stable range with fluctuations most due to temperature variation.

2.2.3 Discussion of Phase IV Results

At the end of Phase I, one year of observation under sustained loading, the unit was moved inside Fears Laboratory. After the repeated loading of Phase V and the overload test of Phase III, the unit was returned to the sustained loading location outside Fears Laboratory for the

-24-

Elevation of
Bridge Unit
Section

Beam Strain Distributions

Tension ←——→ Compression

Tension ←——→ Compression
Initial Strain
Daily Strain Change

Apparent Neutral
Axis Location

Daily Strain Change

Initial Strain

Daily Strain Change

(a) Daily Strain Change
Due to the Combined
Axial and Bending
Effects of Creep and
Shrinkage Forces

(b) Location of Apparent Neutral Axis
as Affected by the Initial Strain
Reference Chosen

Figure 2.2 Beam Strains Measured in Determining Apparent Neutral Axis Location

second period of observation under sustained loading, which tested for two years. The test setup, instrumentation, and simulated asphalt overlay loading were the same as for Phase I (see Appendix C.1 for details).

The purpose of this test was to observe any changes in behavior of the bridge unit under sustained loading which might have been caused by either the half million repeated loading cycles of Phase II or the overload test of Phase III.

The test results for Phase IV are found in Section D.3 of Appendix D. Branson's method was again used to predict the deflection response of the bridge unit. The predicted and measured midspan deflections are given in Table D.3. Figure D.7 shows variation of measured vertical deflection and temperature versus time in days for the observation period. It is obvious from this figure that there is a close, but inverse, correlation between midspan vertical deflection changes and temperature changes. To further investigate this relationship, predictions using Branson's method were determined and Figures D.8 thru D.11 were plotted.

Figure D.8 shows the measured and predicted total deflection of the bridge unit for the 700 days of Phase IV. The predicted curve is generally accurate, with a maximum deviation of approximately 0.1 inches with plus or minus five days of the time of the measurement.

In Figure D.9, the measured midspan deflection and the predicted temperature deflection are plotted along with air temperature. The plot shows that the deflection of the bridge unit is sensitive to temperature change and that the predicted temperature deflection swung to somewhat extreme

values, although the predicted and measured deflections followed a similar path. Predicted creep and shrinkage deflection along with measured midspan deflection are shown in Figure D.10. This plot shows that predicted creep deflection behavior fluctuates about the point of zero change. This may be explained since, in the creep and shrinkage prediction, the change in deflection due to the time dependent response had attenuated, leaving humidity change as the governing parameter. Accordingly, the predicted creep and shrinkage effects curve shows little resemblance to the measured deflection curve, since the effect of humidity change (and therefore creep and shrinkage) is masked by the more substantial effect of temperature change on deflection. The governing effect of temperature change alone on predicted total deflection is shown in Figure D.11, from which it is concluded that the effect of humidity and age are minimal on the change in vertical midspan deflections.

Figure D.12 shows the average change in stress on the beam flanges with temperature change over Phase IV. The beam top flange stress change does not fluctuate as much as the beam bottom flange stress. The change in both flanges roughly follows the change in temperature, but is not nearly as sensitive to temperature change as is midspan deflection. Reinforcing bar surface stresses fluctuated with temperature change more than the surface flange stresses did, as may be seen in Figure D.13.

2.2.4 Discussion of Phase XI Results

During the fatigue loading test of the second unit (Phase IX), it was observed that the camber of the unit was decreasing and the beam flange strains were increasing. This behavior was similar to that of the first unit, which

was observed during the first sustained loading period (Phase I). Hence, even though no attempt was made to induce sustained loading behavior in the second unit, the characteristic phenomena (which, for this discussion, includes all time-dependent behavior) did occur and is discussed in this section.

The unit was initially brought to Fears Laboratory, subjected to 500,000 cycles of repeated HS-20 loading, and statically loaded to first yield. It was then decided to move the unit outside Fears Laboratory for a period of observation (Phase XI) under sustained loading, to determine whether or not sustained loading behavior had attenuated during fatigue loading.

After the unit was moved outside, it was observed for 10 days, then loaded with concrete blocks to 40 psf and observed for 19 days. During the 29 days of sustained loading observation, a surveyor's level was used to determine the camber of the unit on a nearly daily basis.

Table D.4 is a tabular description of the major events which occurred during the test period, with the marks corresponding to the marks on the data plots. Figure D.14 shows the change in midspan deflection of the unit plotted over the entire testing period of the second unit. As the figure shows, the rate of change in midspan deflection decreased as the number of repeated loading cycles increased. Hence, it was seen that the time dependent effects of sustained loading were accelerated by the application of repeated loading when compared to the response of the first unit under sustained loading in Phase I. The figure also shows that the first yield test caused slightly less than 1 in. of permanent deflection. When the unit was moved outside after the first yield test the

change in midspan deflection was seen to follow the change
in temperature and was relatively constant even after the
application of concrete blocks.

Table D.5 lists the strains measured on the beam top
and bottom flanges during the repeated loading test.
Reading of the strains was terminated after the first yield
test was completed (the high strains recorded in the first
yield test are not included in this analysis of sustained
load behavior). The strain reference position was the same
as for the first unit; that is, the strain readings reflect
the change in flange strain with respect to the flange
strains existing just before the unit was set upright. The
strain readings have been adjusted for the instantaneous
strains resulting from the placement of the spreader beams
(see Appendix C) on the fifth day, in order to maintain the
sustained loading reference.

As shown in the midspan deflection versus time plot,
the temperature inside the laboratory was relatively
constant during the period of fatigue loading observation.
Therefore, the changes in strains shown in Table D.5 were
attributed to sustained loading effects, which are
characterized by creep and shrinkage in the concrete slab.
The table also shows the apparent neutral axis location from
the bottom of the beam, which was calculated from the
average top and bottom flange strains.

The beam strains in Table D.5 were converted to
stresses and plotted in Figure D.15. The lettered marks on
the plot are noted in Table D.4. The stresses are plotted
up to the time of the first yield test, and to the same
ordinate scale as the midspan deflection versus time plot.
The stresses in both flanges increased at about the same
rate over the repeated loading test and by the last day, the

top flange stress had increased by 4.1 ksi (compression) and the bottom flange stress by 3.8 ksi (tension).

Figure D.16 shows the location of the apparent neutral axis change due to sustained loading effects over the repeated loading test period. It is shown that the apparent neutral axis moved toward the bottom of the beam, in a manner similar to that seen during the sustained loading of the first unit (Phase I) but over a shorter time period. Table D.6 shows the measured and predicted changes in bottom flange stress and midspan deflection of the second unit during construction and fatigue loading testing. The stress was measured as strain; with a negative value denoting compression and a positive value tension. The midspan deflection was obtained with a surveyor's level, with the positive direction being upward displacement of the unit in its upright state. The loading steps are briefly noted in the table, and a more detailed description of loading steps and theoretical calculations is found in Appendix K.

Since the strain gage readings were initialized when the unit was in an unstressed state (see Appendix C), the measured stress is the actual stress at the bottom flange extreme fiber. The change in stress at each loading step is shown and and total stress and stepwise stress change is compared with the theoretical prediction of stress. It is seen that the change in measured and predicted stresses at each loading step were approximately the same, but the differences totaled 3.2 ksi.

Loading steps 1 thru 4 concerned the steel beams before the concrete slab had hardened and the stresses and deflections were calculated using the section properties of the steel beams. Stresses and deflections for loading steps 5 thru 8 were calculated using the section properties of the

-30-

full transformed section. The same calculations for steps 5 thru 8 were performed using the composite section properties obtained with the modular ratio increased by a factor of 3.0. This was done to account for sustained loading effects as prescribed by AASHTO.

The identical calculations using the two different transformed sections resulted in a difference in stress of 3.0 ksi, which is the predicted stress change listed for loading step 9, in which no real increase in load occurred. Between the time the unit was set in Fears Laboratory and the first yield test was begun, the increase in stress in the bottom flange was 3.8 ksi. When the spreader beams were set in place in step 7, the instantaneous stress change was measured to be 2.4 ksi, but the change in stress measured between the time the unit was set in the laboratory and after the spreader beams were set in place was 3.4 ksi, indicating that 1.0 ksi of flange stress increase had occurred without an increase in bridge unit applied load, before the spreader beams had been set in place. The additional 2.8 ksi increase in stress due to sustained loading effects listed in step 9 occurred due to the repeated loading prior to the first yield test. The predicted stress change due to sustained loading effects was not too different from the measured change of 3.8 ksi.

The same behavior was observed in the change in midspan deflection of the unit, although the measured and predicted changes in deflection were not as close as were the changes in bottom flange stress. Some of the error is attributable to surveying error, but most of the difference between measured and predicted deflection was due to differences in actual and assumed construction loads. The exception to this is the deflection measurement shown in loading step 1. Since the weight and section properties of the steel beam

alone are known with a certain degree of accuracy, the measurement shows that the beams had an average precamber of 0.2 in. As is shown in Table D.6, the deflections for loading step 6 were not measured, because the unit was turned 1/4 revolution.

The difference in measured and predicted deflection changes between loading steps 7 and 8 again shows that sustained loading behavior had begun immediately after the unit was turned upright and set in Fears Laboratory. When the spreader beams were placed on the unit, the instantaneous midspan deflection was 0.16 in. But the total displacement between steps 7 and 8 was 0.38 in., indicating that 0.22 in. of deflection had occurred due to sustained loading effects. The theoretical total deflection was 0.58 in. and is shown in step 9. The measured sustained loading deflection of 0.22 in. before the spreader beams were set inplace, and the 0.55 in. deflection measured after the repeated loading was completed add up to 0.77 in. of sustained loading deflection.

Hence, for this unit, it was seen that calculations based on the assumed loadings and increased modular ratio resulted in an underestimation of the effects of sustained loading phenomena. However, with the analysis used, deflection of the unit was more sensitive to sustained loading effects than was the more critical stress change in the beam bottom. This is predicted and discussed in Appendix K.

2.2.5 Findings

Study of the bridge unit under a total of three years of sustained loading leads to the conclusion that available theory on composite beam behavior under sustained loading

and in a service environment may be applied to the bridge units under investigation with reasonably accurate results. It was observed that, as predicted, creep and shrinkage effects were pronounced for approximately the first 100 days of loading, at which point these time dependent effects reached an asymptotic level. Once the creep and shrinkage influence on behavior stabilized, midspan vertical deflection of the bridge unit closely mirrored, but in an inverse manner, temperature change.

Branson's method for predicting composite beam behavior was found to be qualitatively accurate, although his method for determining creep and shrinkage effects resulted in an overestimation of related deflections; predicted temperature deflections were more accurate. It is noted that even though predictions using Branson's method did not consider the effects of fatigue loading and an overload test, which were conducted between the two sustained loading phases, the theoretical predictions were generally conservative (due to the overestimation of creep and shrinkage strains) and thus effects of fatigue and overload do not need to be considered in sustained loading calculations. Concrete under sustained load is known to respond with an increase in strain under constant stress. The phenomenon is labeled as "creep", and the ratio between creep strain and the initial strain reaches a maximum value after a period of time. Branson's method for determining stresses and deflections in composite beams is extended here, resulting in a method of analyzing for creep separately from the analysis for shrinkage.

Long term concrete creep strain is proportional to initial concrete strain due to sustained loads. Neglecting shear strain effects, time dependent creep strain in the

concrete is proportional to the initial bending strain over the depth of the concrete slab and follows the same bending moment diagram along the length of the member. Therefore, a time dependent "creep factor" consisting of material and geometric properties of the composite section may be applied to the bending moment diagram of any sustained loading configuration, from which the deflection and an imaginary moment due to creep at any point along the member may be found. And from the imaginary creep moment, a creep force may be determined and the resulting change in cross-sectional stresses may be found at any section by the same method as used to determine concrete shrinkage-caused stresses.

The results of the following derivation of the "creep factor" is applicable only to composite sections where the neutral axis lies above the steel beam. Also the derivation is simplified by considering only the concrete above the composite section neutral axis as contributing to creep behavior, whereas, concrete in tension exhibits similar creep behavior as concrete in compression. As shown in Figure 2.3, this simplification is justified since the neutral axis lies very close to the beam flange for the units in this testing program. However, the derivation could be extended to include the concrete in tension, and rederived for the case in which the neutral axis lies within the steel beam.

The nomenclature for the following derivation is similar to that used by Branson as follows:

M_c = imaginary moment due to creep

Y_{cT} = distance from composite section neutral axis to concrete top fiber

Q_c = imaginary virtual creep resultant force

-34-

E_{cT} = creep strain at Y_{cT}

E_i = instantaneous strain at Y_{cT} due to sustained loads

C_t = creep coefficient at time, t, days

t = time, in days, after application of sustained load

C_u = ratio of ultimate creep strain to initial elastic creep strain

M_i = midspan moment at application of sustained loading

I_c = transformed section moment of inertia

E_2 = steel elastic modulus

E_1 = concrete elastic modulus

W = width of concrete slab

n = modulus ratio concrete to steel elastic

C = creep factor

D_c = deflection due to creep

D_i = instantaneous deflection at application of sustained loading due to creep

y = distance from neutral axis to stressed fiber, downward positive

F_2 = stress in steel beam at distance y from the neutral axis

F_1 = stress due to creep in concrete slab at distance y from the neutral axis

The moment, M_c, due to creep at any point along the member is equal to the resultant creep force, Q_c, times its moment arms, see Equation 1 of Table 2.1. The creep force is determined in Equation 2 by finding the average creep strain, multiplying by the concrete elastic modulus and by the slab area in compression. The creep strain is a time
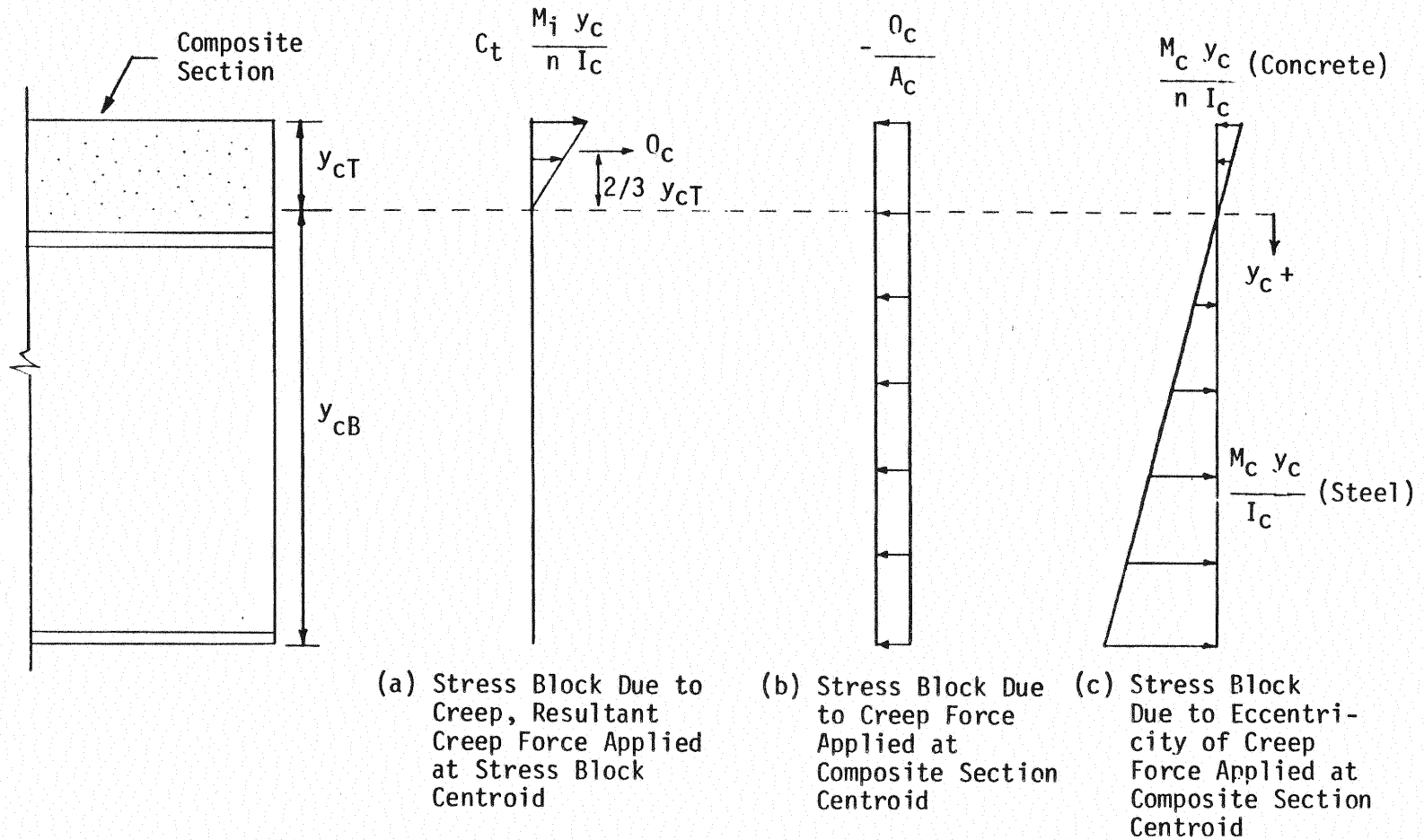
Figure 2.3   Stress Distributions Due to Concrete Creep

Table 2.1

Extension of Branson's Method for Creep -- Equations

$$M_c = \frac{2}{3} Y_{cT} Q_c \qquad (1)$$

$$Q_c = \frac{E_{cT}}{2} E_1 Y_{cT} W \qquad (2)$$

$$E_{cT} = C_t E_i \qquad (3)$$

$$C_t = \frac{t^{0.6}}{10 + t^{0.6}} C_u \qquad (4)$$

$$E_i = \frac{M_i Y_{cT}}{I_c E_2} \qquad (5)$$

$$M_c = \frac{C_t}{3} \frac{E_1}{E_2} \frac{Y_{cT}^3}{I_c} W \quad M_i \qquad (6)$$

$$\frac{E_1}{E_2} = \frac{1}{n} \qquad (7)$$

$$M_c = \frac{C_t W Y_{cT}^3}{3 n I_c} M_i \qquad (8)$$

$$C = \frac{C_t W Y_{cT}^3}{3 n I_c} \qquad (9)$$

$$D_c = C D_i \qquad (10)$$

$$Q_c = \frac{3 M_c}{2 Y_{cT}} = \frac{3 C M_i}{2 Y_{cT}} \qquad (11)$$

$$F_2 = \frac{M_c Y}{I_c} - \frac{Q_c}{A_c} = \frac{C M_i Y}{I_c} - \frac{Q_c}{A_c} \qquad (12)$$

$$F_1 = \frac{C M_i Y}{n I_c} - \frac{C_t M_i Y}{n I_c} - \frac{Q_c}{A_c} = (C - C_t) \frac{M_i Y}{n I_c} - \frac{Q_c}{A_c} \qquad (13)$$

-37-

dependent multiple of the initial strain due to sustained loads, Equation 3, in which the multiple is found at any time, t, in days, after initial loading, from emperical Equation 4. The average value of the ultimate creep strain, C_u, in Equation 4 is given as 2.35 in Reference 5. The initial top fiber strain due to sustained loads is determined from simple flexure theory, Equation 5. The substitution of Equations 2, 3, and 5 into Equation 1 results in Equation 6, which shows that the imaginary moment at any section along the composite beam length due to creep is a time dependent factor involving only material and geometric properties of the transformed section. Equation 6 is further simplified into Equation 8 with the substitution of Equation 7.

The imaginary creep moment at any section at a given time is related by Equation 8, with the result being that the creep moment diagram is merely a scaled version of the moment diagram due to sustained load. The scaling factor, or creep factor, is given in Equation 9. Since the deflection of a beam is directly related to its moment diagram (and therefore its curvature), the product of the creep factor and initial deflection due to sustained loads gives the deflection due to creep, Equation 10.

However, the determination of the cross-sectional stress changes in the composite section due to creep is not as simple, since the imaginary creep force is applied eccentrically to the composite section. The creep force may be found directly from Equation 1, which is transformed as Equation 11. The stress at any depth on the cross-section is found by the superposition of the three stress blocks shown in Figure 2.3. The stress due to creep in the steel beams is given by Equation 12, and the creep stress in the concrete is given by Equation 13.

Analyses for creep effects were performed on both units. The creep factor (Equation 9) for the first unit was found to be 0.39 and 0.47 for the second unit. For the first unit, the analysis was carried out for the period of initial sustained loading (Phase I, day 363), since the data was continuous. The analysis for the second unit was performed for the period of fatigue loading (Phase IX), with the assumption that fatigue loading had accelerated the creep effects to the ultimate creep strain. Separate analyses by Branson's method for concrete shrinkage effects were also performed for both units, for the period of Phase I for the first unit, and for the period of Phase IX (day 40) for the second unit. The procedure used was the same as described in Appendix D, except that the shrinkage force, Q, was not reduced by a factor of two to account for creep relaxation, since creep was treated separately.

Table 2.2 gives the change in measured top and bottom flange stress and midspan deflections (camber) of both units, along with the predicted values from the extension of Branson's method for creep discussed above and Branson's method for shrinkage. In addition, the predicted values calculated by the effective concrete elastic modulus method are included in the table.

The stress changes are negative for compression and positive for tension. The absolute value of the ratio between the top and bottom flange stress changes is included as the "stress ratio".

The table shows that for both units the stress ratio obtained from the extension of Branson's method for concrete creep was very close to that of the measured stresses. The stress ratio from Branson's method for concrete shrinkage was the furthest from the measured stress ratio. The stress

-39-

Table 2.2

Measured and Predicted Changes in Beam Flange Stress
and Camber of Both Units, Sustained Loading Effects

(a) First Unit						(b) Second Unit					
Method	Description	Change in Beam Flange Stress (ksi)		Stress Ratio	Downward Change in Camber (in)	Method	Description	Change in Beam Flange Stress (ksi)		Stress Ratio	Downward Change in Camber (in)
		Top	Bottom					Top	Bottom		
Measured	Phase I	- 7.1	5.4	1.31	0.40	Measured	Phase IX	- 4.1	3.8	1.08	0.94
Branson	Creep @ 363 Days	- 6.2	5.0	1.24	0.80	Branson	Creep @ ultimate	- 7.0	6.2	1.13	0.92
	Shrinkage @ 363 Days	-13.7	4.9	2.80	1.61		Shrinkage @ 40 Days	- 7.9	3.1	2.55	0.96
	Total	-19.9	9.9	2.01	2.41		Total	-14.9	9.3	1.60	1.88
Effective Concrete Elastic Modulus	Total	- 5.84	3.8	1.54	0.61	Effective Concrete Elastic Modulus	Total	- 3.85	3.0	1.28	0.58

ratio obtained from the effective concrete elastic modulus method resulted in a relatively close prediction of the stress ratio for both units, although this method was deduced to be only a simple design tool, as discussed in Section 2.2.1, rather than the statically correct approach developed by Branson. Accurate predictions from Branson's method, however, are very sensitive to the assumed values of ultimate creep and shrinkage strains. The results, therefore, are not necessarily more correct than those obtained by the effective concrete modulus method. Also, the combined total of creep and shrinkage predictions overestimated the measured changes in stresses and deflection.

A great deal of variability is seen in the change in camber predictions for both units. The prediction by the concrete modulus method gave the best results for the first unit, and Branson's method for creep and shrinkage both gave the same accuracy for the second unit.

Generally, the results from each method gave reasonably close predictions for the change in deflection and for the more critical change in bottom flange stress.

2.3 Fatigue Loading Tests

2.3.1 Overview

A simulated lifetime of repeated loading was used to study the fatigue characteristics of the bridge units in order to verify the adequacy of fatigue design procedures used. Of particular interest were the effects of fatigue on bridge unit stiffness, prestress retention, and shear connector behavior. Also, change in camber and connection detail response to fatigue loading were studied.

-41-

The first bridge unit was subjected to the repeated loading of a simulated HS-20 truck as defined in the AASHTO Specification [1] for a total of 2,000,000 cycles. The unit was also subjected to 2,000 cycles of AASHTO HS-30 truck loading, which is a fifty percent increase in load magnitude over the HS-20 truck loading. The second unit was subjected to 500,000 cycles of repeated HS-20 truck loading in Phase IX.

The two million HS-20 load cycles were applied to the first unit in three series. In the first series, Phase II, 500,000 cycles were applied between the sustained loading periods of Phases I and IV, and just before the overload test of Phase III. After sustained loading Phase IV, the unit was subjected to an additional 600,000 cycles of HS-20 loading (Phase VA), which was followed by the 2,000 HS-30 overload cycles of Phase VI. The last 900,000 HS-20 load cycles (Phase VB) were then applied to this unit. In addition to the HS-20 and HS-30 repeated loadings which were applied along the centerline of the bridge unit, the unit was loaded off center (over one steel beam instead of between beams) for 100,000 cycles to simulate one line of wheel loads of unsymmetrical HS-20 truck traffic (Phase VII).

Since the sustained loading observations were conducted with the bridge units outside the Laboratory, it was necessary to move the units a number of times. During transfer of the first unit from its Phase IV outside sustained loading observation location to the Laboratory for Phase V, the failure of a lifting device allowed the unit to drop approximately 8 ft. to the ground. The unit landed upside down, partially supported by the orginial support beams as shown in Figure 2.4. Both ends of the unit were damaged; the more severely damaged end is shown in Figure

Figure 2.4   Photograph of Damaged Bridge Unit

2.4. In addition to suffering extensive damage at the ends, the slab was twisted in the fall, causing random cracking across the slab over its entire length. The slab was repaired at the ends by jacking up the bridge unit and supporting it on timbers in a level position. All loose concrete was then removed and replaced with new concrete of similar strength. The unit was then transported, without incident, into the laboratory area for the remaining tests.

A description of the test setups and instrumentation for the fatigue loading test phases may be found in Appendix E.2.

Results of the fatigue loading tests consist of changes in midspan deflection, stiffness, and cross-sectional strains and stresses which were measured at certain intervals during the fatigue loading test phases. These results are found in Appendix E. Unless otherwise noted, these results were obtained during periodic static load applications and do not include dead load effects. Elastic flexural theory (with n = 6.64 for the first unit and n = 5.44 for the second unit) and transformed sections were used to determine theoretical deflections and stresses as described in Appendix K. Section properties used for the theoretical predictions are found in Appendix A for the first bridge unit and in Appendix B for the second bridge unit. Material properties were obtained from the supplementary tests discussed in Chapter IV of this report.

2.3.2 Discussion of Phase II Results

Phase II consisted of subjecting the first bridge unit to 500,000 cycles of HS-20 truck loading. During this testing phase, the simulated HS-20 truck load was applied as shown in Figure C.5 and C.6, as described in Appendix C, Section C.2.

Results of this phase consist of the deflection, stress and strain, and neutral axis location plots found in Appendix E, Section E.1. The plotted data was obtained during periodic static load applications (generally at the completion of each 50,000 cycles of repeated loading) on the bridge unit throughout the testing phase.

Figure E.1 shows load vs. midspan deflection curves for the first and last cycles of the test phase. The curves for the first and last cycles are approximately parallel past the 10 kips applied load level, which shows that the stiffness of the unit had not been appreciably degraded because of the 500,000 cycles of repeated loading and that the stiffness of the unit was slightly greater than predicted. Figure E.2 shows midspan deflection versus number of load cycles over the duration of the test phase. These results again show that the stiffness of the unit remained approximately constant throughout the test phase, although slightly greater than predicted.

Figure E.3 is a comparison of the strain level at the top of the concrete slab at two applied load levels as a function of the number of applied cycles. The plot shows that the measured strains fluctuated about the theoretical strain values. These fluctuations were not observed in later repeated loading phases, and the discrepancy may be due to instrumentation problems with measuring the very small strain changes.

Figure E.4 shows the variation of the steel beam flange and upper layer rebar surface stresses over the duration of the test phase. The stresses were relatively constant at the 55 kip applied load level, although somewhat less than predicted. Finally, Figure E.5 shows that the neutral axis of the bridge unit remained at a relatively constant and

predictable level above the beam bottom flange. The neutral axis location was determined from the change in upper and lower steel beam flange strains measured during the static test load applications.

The maximum measured slip at the slab/beam interface was less than 0.001 inches. The initial and final camber measurements were both 0.36 inches positive camber.

2.3.3 Discussion of Phase V Results

Phase V consisted of cycling the first bridge unit an additional 1,500,000 cycles of simulated HS-20 truck loading. The first part of the test phase consisted of 600,000 cycles of HS-20 loading, and the second of 900,000 cycles. Phase VI, 2,000 overload cycles of HS-30 truck loading, occurred between the two parts of Phase V.

Results of this phase consist of deflection, stress and strain, and neutral axis location plots, and are found in Appendix E, Section E.2. Test setup and instrumentation details are discussed in Appendix C, Section C.2.

Figure E.6 shows plots of load vs. midspan deflection, measured at both steel beam midspans, for the first and last cycles of this test phase. The curves for the first and last cycles closely agree with the theoretical curve. The broader area enclosed by the "0 cycles" curve shows that some energy was dissipated in the first cycle. This was probably due to the slab being forced in compression, which would tend to align and close the crack surfaces created when the unit was dropped. The curve for the last cycle indicates an increased stiffness of the unit which may also have been due to the aligning of the cracked concrete slab. Figure E.7 shows that the variation of stiffness of the unit

as a function of applied cycles. The deflection plotted in Figure E.7 is for full HS-20 simulated loading.

Figure E.8 shows the downward change in camber of the unit over the testing period. A loss of camber of about 0.1 in. occurred after the first load cycle. The camber then remained relatively constant up to 600,000 cycles, at which point the 2,000 overload (HS-30) cycles were applied, causing a direct camber loss of an additional 0.1 in. The west side of the unit then steadily lost camber until stabilizing at about 0.4 in. loss at 1,400,000 load cycles. Camber of the east beam was also lost but may have been due to micro-cracking at an interior cross frame connection point on the west beam, thus causing a redistribution of dead load forces which would have caused camber loss in the east beam. Formation of cracks in the steel beam at interior cross frame connections points was observed in Phase VII, repeated unbalanced loading, and will be discussed in the Section 2.3.5.

Figure E.9 shows the concrete strain measured during the static load applications conducted during the test phase. The strain was consistent but less than predicted. The steel stresses (strains) measured throughout the test phase (Figure E.10) were also very consistent, although slightly less than predicted. Figure E.11 shows that the neutral axis location determined from the steel beam strains measured during static test checkups was nearly the same as predicted. This indicates that the material properties of the cross section remained constant and were not affected by the repeated loading.

Dial gages, installed to measure relative slip, at various points along the unit, between the concrete slab and the steel beams, were monitored throughout the test phase. Measured slip never exceeded 0.001 in.

2.3.4 Discussion of Phase VI Results

Phase VI consisted of 2,000 cycles of a simulated HS-30 truck operating rating loading (a load which causes a bottom flange stress equal to 75% of the material yield stress) as defined in the AASHTO Specification [1]. Test setup and instrumentation details are discussed in Appendix C, Section C.2. Results consist of deflection, stress and strain, and neutral axis location plots and are found in Appendix E, Section E.3.

Figure E.12 is a plot of the average midspan deflections for the first and last cycles of the test phase. As in the first cycle of the previous test phase, some energy dissipation occurred during the first loading with a small amount of permanent set resulting. The last cycle load versus deflection curve shows that the unit behaved elastically, but was somewhat stiffer than predicted.

Figure E.13 is a plot of the midspan deflection from full static HS-30 simulated truck loadings versus number of cycles. The plot shows that the maximum measured deflections did not vary significantly and are in good agreement with the predicted values.

Figure E.14 shows that the strain at the top of the concrete slab was nearly constant throughout the test phase, although less than predicted. The steel stresses shown in Figure E.15 were obtained from strain gages mounted on the upper layer of slab reinforcing steel and from the bottom side of the steel beam flanges. Both are close to theoretical values. Figure E.16 shows the neutral axis location referenced from the beam bottom flange. The neutral axis location was calculated from measured strains in the beam upper and lower flanges and coincides with the theoretical location.

As in the previous repeated loading tests, slip at the concrete slab-steel beam interface was monitored during the static load checkups and did not exceed 0.001 in.

2.3.5 Discussion of Phase VII Results

This phase subjected the bridge unit to a loading condition which would occur when only one line of wheel loads of an HS-20 truck are on a unit, resulting in an unbalanced load condition. For this phase, the test load was reduced by one-half and centered over the west steel beam. The unit was subjected to 100,000 cycles of this loading. The setup and instrumentation for this test phase are discussed at greater length in Appendix C, Section C.2.

After the 100,000 cycles had been applied, it was observed that the steel beams had cracked at three of the four points where the interior cross frame steel angles were welded to the beam webs near the bottom flanges, at Sections B-B and C-C in Figure A.2 of Appendix A. A photograph of the most severely cracked location is shown in Figure 2.5. The spacing of these interior cross frames was 18 ft. and the applied load points were spaced at 14 ft. symmetrically about the centerline. Thus, the cross frames were located 2 ft. from the maximum repeated live load moment. The fillet weld connecting the cross frame steel angles to the beam webs was continuous around the perimeter of the angle with the horizontal leg of the angle closer to the composite section neutral axis. According to the AASHTO Specification [1], the base metal adjacent to the edge of this three inch weld of the horizontal angle leg falls into stress category E and the base metal adjacent to the three inch weld of the vertical angle leg falls into category C. The allowable stress ranges for over 2,000,000 cycles are 5 ksi and 12 ksi for stress categories E and C, respectively. The calculated stress range due to the simulated HS-20 loading for the base

-49-
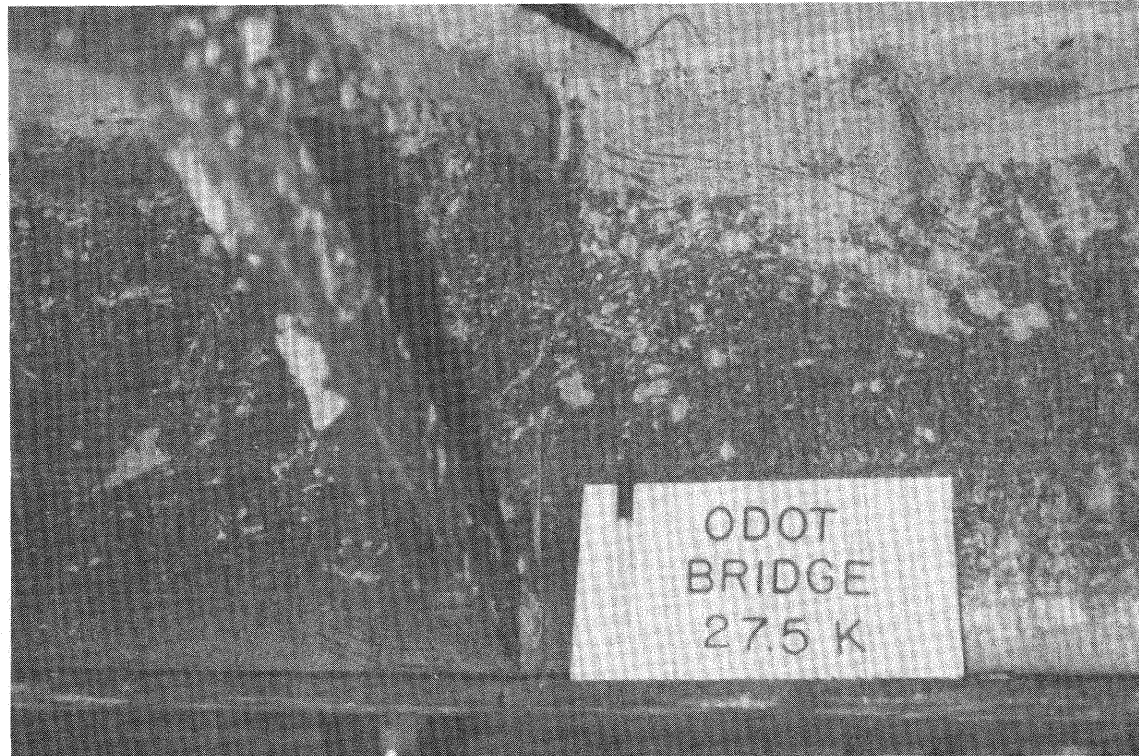
Figure 2.5   Photograph of Steel Beam Crack
at Interior Crossframe

metal edge near the horizontal weld was 14.9 ksi (versus 5 ksi allowable) and for the vertical weld base metal was 17.6 ksi (versus 12 ksi allowable). These points of critical stress had undergone 2,000,000 cycles of HS-20 loading, 2,000 cycles of HS-30 loading, and 100,000 cycles of unbalanced HS-20 loading before any signs of cracking were observed. The cracks appeared to have been initiated in the web base metal along the vertical fillet weld, then propagated down to the bottom of the beam flange, and then across the beam bottom flange. The cracks at the two interior cross frames connected at the web bottom of the east beam did not completely separate the bottom flange; whereas the one crack in west beam had extended up into the web before it was seen.

The test results of this phase show that the cracking in the beam webs probably did not propagate through the beam flanges until well into this final phase of repeated loading. Figure E.17 shows the load versus midspan deflection curves for both of the first unit beams at the first and last cycles of the test phase. The same theoretical curve as was used in the symmetrical loading cases is also plotted for reference to the previous load cases. The curves for the first cycle show that the west beam (the loaded beam) deflected more than the east beam, with the two curves straddling the symmetrical loading theoretical curve. The second plot shows that after 100,000 loading cycles, the west beam had lost a large degree of stiffness, allowing the applied load to be transmitted to the east beam causing increased deflection of that beam.

Figure E.18 shows the measured strain on the top surface of the concrete slab at the first and last load cycles. The theoretical line was determined for symmetric loading and its length is equal to the slab width. The

reference location for edge distance is the west edge of the concrete slab. The curves show that the concrete strain was higher on the west (loaded) side and decreased almost linearly across the slab for the first load cycle. After 100,000 cycles of loading, the strains were greater on the east or unloaded side. In Figure E.19, similar results are shown for an upper layer reinforcing bar.

Figure E.20 shows that the west steel beam did not completely crack until repeated loading of this phase was underway. The theoretical curve is the same as was used for symmetrical loading. The "0 cycles" plot shows that the west (loaded) beam flange stress was greater than the east flange stress. The "100,000 cycles" plot shows that the stress levels in the east and west beams had reversed magnitudes with respect to the first cycle plot. However, even though the west beam was cracked over most of its depth prior to the last load cycle, the applied load was adequately resisted because of redistribution.

The cracks in the beams were subsequently repaired, and a test was performed to determine how much force was transmitted through the cross frames when the bridge unit was subjected to unbalanced loading. The interior cross frame angle connected to the west beam web at the uncracked south location was instrumented with strain gages and an unbalanced load was applied. The measured strain in the cross frame angle remained virtually unchanged under the maximum applied unbalanced load of 27.5 kips. Thus it was concluded that cracking of the beam webs was caused by bending stress concentrations at the cross frame welds.

2.3.6 Discussion of Phase IX Results

The concrete deck for the second bridge unit was cast on 19 March 1986 and turned upright and placed in Fears Lab on 18 April 1986. Phase IX, 500,000 cycles of HS-20 repeated loading, was begun on 22 April 1986 (34 days after pouring) and ended on 22 May 1986. The purpose of this test of the second bridge unit was the same as for the first unit. (The test was repeated because the first unit was dropped as previously explained.) Details of the test setup and instrumentation are identical to those for the first unit and are discussed in Appendix C, Section C.2. Specimen details and section properties are found in Appendix B.

Results for this phase consist of deflection, stress and strain, and neutral axis location plots from data obtained during periodic static load applications (generally every 100,000 cycles). Theoretical predictions were determined using the section properties in Appendix B.

Figure E.21 shows load vs. midspan deflection plots for both beams for the first and last load cycles of the test phase. The stiffness of the unit was the same for the first and last cycles, but the unit was stiffer than predicted (as was the first unit during its initial period of fatigue loading). Figure E.22 shows the variation of midspan deflection of the unit when subjected to the simulated HS-20 loading versus number of loading cycles.

Figure E.23 shows the change in camber as a function of loading cycles. A loss of camber of approximately 0.4 in. (of the initial 2.0 in.) occurred during the test phase, and is attributed to the repeated loading having caused accelerated creep and shrinkage type effects on the unit.

-53-

Figure E.24 shows that the measured strain on the concrete slab surface was consistent throughout the test phase but was somewhat less than predicted. Figure E.25 shows that the stresses on the steel beam bottom flange and on the surface of the top layer of reinforcing bar were also consistent but somewhat less than predicted.

Neutral axis locations were calculated from steel beam ·strain changes during the static load applications. These locations, as shown in Figure E.26, coincided with the predicted value throughout the test phase.

Dial gages mounted at the concrete slab-beam flange interface showed that slip did not exceed 0.001 in. (as in the first unit) and was not significant.

2.3.7 Findings

From the fatigue loading tests of the first bridge unit, it was found that 500,000 cycles of repeated HS-20 loading, and one operating rating (HS-30) loading cycle had no noticeable effect on the stiffness of the bridge unit. (The unit had been designed for 100,000 HS-20 loading cycles.) An additional 1,500,000 cycles of HS-20 loading and 2,000 cycles of HS-30 loading was withstood by the unit without a significant change in stiffness, strength, or slip at the concrete slab-steel beam flange interface, which indicated that the integrity of the cross-section (including shear connectors) was maintained until near the last phase of fatigue loading even though that unit had been accidently dropped. In the final phase of fatigue loading 100,000 cycles of unbalanced repeated HS-20 loading was applied. During this phase the steel beams developed fatigue cracks at beam web cross-frame connection welds. The cracking occurred due to a relatively high bending stress range at the connection detail.

-54-

The second bridge unit showed no noticeable signs of loss of stiffness when subjected to 500,000 cycles of HS-20 loading, although creep and shrinkage type effects appeared to have been accelerated by the fatigue loading. These effects were characterized by a loss in camber, which decreased at a decreasing rate as the testing progressed. Stiffness, strength, and other properties of the unit were not affected by the fatigue loading; and, as was the case for the first unit, the response of the unit to static load was consistent and predictable within acceptable accuracy by classical, elastic flexural theory.

2.4 Static Loading Tests

2.4.1 Overview

Phase III, operating rating loading test of the first bridge unit, occurred on 23 September 1983, after the first sustained load test and the first 500,000 cycles of repeated HS-20 loading. The operating rating loading test consisted of loading the unit so as to produce a tension flange stress equal to 75% of the yield stress of the material. This overload is equal to 1.5 times the HS-20 design loading and is referred to herein as an HS-30 loading. Phase III was first reported by Hendrick in Reference 2.

Phase VIII, ultimate strength test of the first bridge unit, occurred on 6 February 1986, after all sustained loading and fatigue loading tests were completed, and consisted of loading the unit to failure.

Phase X, first yield strength test of the second bridge unit, occurred on 28 May 1986, after the unit had undergone 500,000 cycles of repeated HS-20 loading cycles. The test consisted of applying an incremental load to the bridge unit until signs of yielding in the beam tension flanges were detected.

The test setup used in the static test phase is described in Appendix C, Section C.2. During the tests, the instrumentation described in Section E.3 was monitored. The results of the static tests consist of displacement and strain data obtained and are composed to theoretical values obtained from elastic flexural analyses. Strength considerations and the theoretical calculations (using material strengths from Appendix L) are described in Appendix K. . The resulting plots, with two exceptions, are for the applied loads and do not include the weight of the unit or of the loading spreader beams. The theoretical strengths plotted with the results for the ultimate and first yield strength tests have been adjusted for prestress and bridge unit and spreader beam weights.

2.4.2 Discussion of Phase III Results

Phase III consisted of applying one overload cycle to the bridge unit to simulate the loading of an HS-30 truck. The loading applied after the first period of sustained loading and the first 500,000 cycles of repeated loading. Test results consist of deflection and strain data obtained during the test and are found in the form of plots in Appendix F, Section F.1. Strains measured on the steel beams were converted to stress by multiplying by the elastic modulus of the steel (29,000 ksi).

The main objective of this test was to establish that the behavior of the unit would remain elastic up to 1.5 times the service load level of (85 kips applied load). Figure F.1 shows that the deflection of the unit remained elastic throughout this load range and that the unit exhibited slightly greater stiffness than predicted. Figure F.2 shows that the strain at the top of the concrete slab was also linear, although somewhat higher than predicted.

The measured strain did not exceed 10% of the commonly accepted ultimate, concrete design strain, 3,000 micro strain. Steel stresses versus applied load are shown in Figure F.3 and were elastic throughout the test. The flange stress was less than predicted, although relatively close to the theoretical stress. The measured stress on the top layer monitored longitundinal reinforcing bar was considerably less than the theoretical prediction.

From the change in beam strains, it was determined that the neutral axis location remained at a constant 21.1 inches from the bottom of the steel beams which is very close to theoretical distance of 20.8 inches. Slip was also measured during the test, and was found to be insignificant.

The results indicate that the unit remained elastic throughout the test and performed adequately.

2.4.3 Discussion of Phase VIII Results

Phase VIII is the flexural test to failure of the first bridge unit. Prior to this test, the unit had been subjected to 2,000,000 cycles of repeated HS-20 loading, 2000 cycles of repeated HS-30 loading, and had 100,000 cycles of unbalanced HS-20 loading and had been dropped from about eight feet, causing extensive cracking of the concrete slab. As described in Section 2.3, the unit was repaired, but test results must be considered with the understanding that the effects of the damage may have reduced the integrity of the unit.

The test phase was conducted in two parts, denoted in the test results as the "first" and "second" tests. The first attempt to fail the test unit was stopped because of possible instability of the test setup. The problem was

-57-

corrected and the test phase completed on the second attempt. Yielding of the beam tension flanges was detected near the end of the first test. In the second test, the unit continued to yield once the previous maximum load level was reached.

Test results consist of deflection, slip, and strain data recorded during the testing phase; plots of which are in Appendix F, Section F.2. Three horizontal lines on the first four plots indicate theoretical strength limits. The first two mark the calculated load at which first yield would occur. The average measured yield stress of the beam material (58 ksi) was used in the calculations. To determine the lower value (130 kips), the concrete elastic modulus was decreased by a factor of 3.0 (as prescribed in the AASHTO Specification to account for sustained loading effects) and the applied load required to produce first yield in the beam tension flanges determined considering both the existing prestress and dead load stresses. The middle value is the applied load (141.0 kips) at which the predicted first yield occurs when the actual concrete modulus is used. The upper line is the applied load (195.0 kips) at which the sum of the dead and live load moments reach the theoretical ultimate strength of the cross-section. These and other strength considerations are discussed at greater length in Appendix K.

Figure F.4 shows the load versus midspan deflection curves obtained during the first and second tests. The applied load reached in the first test was 125 kips. The onset of yielding occurred at approximately 120 kips, or about 10 kips less than the prediction based on the effective concrete modulus; 94% of the predicted total moment. Figure F.2(b) is for the second test and shows that the unit had actually stiffened somewhat, but remained close

-58-

to the theoretical stiffness. Yielding began after the
previous load of 125 kips was exceeded. At 160 kips, the
east beam fractured at the south repair location. This load
resulted in a total moment of 1918 ft. kips which is 84% of
the calculated ultimate moment of 2273 ft. kips.

Dial gages mounted on the unit to measure the relative
displacement (slip) at the beam flange-slab interface showed
that slip was relatively insignificant in the previous test
phases. The slip was greater at the higher load levels
reached during this phase and is plotted in Figure F.5. Of
the seven dial gages located on each side of the unit (see
Figure C.5), the end and midspan dial gages showed
negligible movement, while the other four dial gages showed
that movememt did occur between the ends and midspan. It is
noted that some elastic deformation was unavoidably included
in these slip measurements.

The average movement determined from the four center
gages on both sides of the unit is shown in Figure F.5. The
slip curve for the first test is similar to typical
load-slip curves obtained from pushoff tests, as discussed
in the shear connector test results in Chapter III.
Reference 6 provides an empirical equation which gives the
ratio of load on one or more shear connectors to the
ultimate load on the connectors as a function of measured
slip. The equation is

$$S/S_u = \frac{80\ D}{1 + 80\ D} \tag{2.3}$$

where S/S_u is the strength ratio discussed and D is the
measured slip. For the maximum slip recorded in the first
test, 0.0085 inches, and that in the second test, 0.021
inches, Equation 2.3 implies that the load on the shear

-59-

connectors in the maximum slip region had reached 40% of their ultimate resistance in the first test, and 63% of their ultimate resistance in the second test.

The curve for the second test shows that slip was relatively linear up to the load magnitude reached during the first test, after which the slip became non-linear, indicating that some combination of shear connector yielding and concrete crushing was occurring. After the steel beam fracture, which occurred at 160 kips applied load, the slip increased markedly, indicating that a redistribution of forces had occurred.

Figure F.6 shows that the strain in the concrete slab was less than predicted in the elastic region, and did not soften in the first test until the 120 kips load level was applied. Softening did not occur in the second test until the previously reached maximum load of 125 kips was exceeded. Since the strain levels were small compared to the accepted 0.003 ultimate strain level, it appears that the increased strain rate was caused by force redistribution due to yielding in the beam bottom flanges.

Load versus stress (measured strain was converted to stress) for the bottom flanges of the beams is shown in Figure F.7. Initially, the measured strain followed the theoretical strain. At the 120 kips load level in the first test, the measured strains remained constant with increasing load. As quoted from Reference 7, in low carbon steels, "This behavior stems from the nonhomogeneous deformation which...propagates through the specimen in the form of observable bands (Luder's bands)." Thus, yielding may have occurred in localized areas which did not include in this case the exact locations where the strain gages were mounted.

However, in the second test, the localized area where the strain gages were mounted on the east beam bottom flange did yield, as is shown in Figure D.7(b). It was observed, after the test, that the mill scale on the bottom flanges showed signs of yielding at various locations in the maximum moment region, but the yielding did not extend through several gage areas. Had the steel beam not cracked, it is reasonable conjecture that yielding would have spread throughout the bottom flange in the maximum moment region.

Yielding occurred in the steel beam at about 120 kips applied load. Without a reduction in the concrete elastic modulus and considering construction and dead load stresses in the steel beam flange, the theoretical yield load was 141 kips. The difference in resulting flange stress from the two different loads is 8 ksi, which means that the effects of sustained loading, fatigue loading, dropping the unit, and repairing the cracked steel beams resulted in a loss of 8 ksi in live load yield strength, or 14% of the steel tensile strength of 56 ksi obtained from coupon tests.

The theoretical yield load obtained for a reduction in the concrete elastic modulus of 3.0 is 130 kips. Correspondingly, the effects of sustained loads will cause an increase in stress in the bottom flanges of about 4 ksi over the stress calculated with no reduction in the concrete elastic modulus. However, even though this approach seems inadequate (since the actual loss in stress was about 8 ksi), no judgement may be made since the effects of damaging the unit may not be separated from sustained loading effects. For this reason a second unit was constructed and tested.

Figure F.8 shows the average measured stress distribution over the unit cross-section. The plot reflects

only applied load stresses on the transformed cross-section; therefore, the concrete stress must be divided by the modular ratio (n = 6.64) to obtain the true applied load stress. Figure F.8a shows that the stress distribution was relatively linear and quite close to the theoretical prediction at 80 kips applied load, one-half of the 160 kips maximum applied load. Figure F.8(b) shows that the measured strains (converted to stresses) were rather scattered at the maximum applied load. The variance in strain distribution may again be attributed to the non-uniform, localized nature of yielding, characterized by Luder's bands. Strains in the upper, less strained region of the cross-section are close to predicted values.

Even though the unit had been fatigued and damaged considerably, the unit developed a total moment resistance of 1918 ft. kips, which was 84% of the 2273 ft. kips theoretical ultimate moment strength, before failure by fracture of the steel beam flanges. (For reference, in early composite beam tests (Reference 8), of fifteen composite beams tested, the average bending strength was 91% of the predicted ultimate strength.)

2.4.4 Discussion of Phase X Results

Construction and testing of a second bridge unit was undertaken because the effects of damaging the first unit were thought to have reduced the strength of that unit. The concrete deck was poured on 19 March 1986, and the unit was turned upright and transported to Fears Laboratory on 18 April 1986. An attempt was made to duplicate the construction of the first unit, except that the slab was slightly thinner and the concrete used contained a super-plasticizing agent. Dimensions and section properties are located in Appendix B.

In order to preserve the unit for possible future use, Phase X consisted of loading the unit only to first yield, instead of to its ultimate strength.

Theoretical considerations and calculations used in the analysis of test results are discussed in Appendix K. Plots of test results are found in Appendix F, Section F.3

The three horizontal lines on the first five test results plots are three theoretical live load limits. The 199 kips load limit denotes the applied load at which point the sum of applied and dead load moments reaches the theoretical ultimate moment of the cross-section. The 156 kips limit is the applied load calculated to cause first yield in the beam bottom flange with no reduction for sustained loading effects. The 148 kips load limit was calculated using a concrete elastic modulus reduced by a factor of 3.0, as suggested in the AASHTO Specification to account for sustained loading effects.

In this test phase, the load was first applied to the 140 kips level (in increments), then reduced to 50 kips, then raised to the 140 kips, and finally increased to highest load level of 146 kips. It was observed from loading the unit in this manner, that the load had in fact exceeded the elastic resistance of the unit.

Figure F.9 shows the applied load-deflection curves for both beams. The unit was slightly stiffer than predicted in the elastic load range, and, although a definite yield point is not apparent from the deflection behavior, the test was stopped at 146 kips applied load due to definite yielding in the beam bottom flanges, as determined from beam flange strains. The loading resulted in slightly less than 1 inch permanent vertical deformation at midspan.

Dial gages mounted at the beam flange-slab interface were monitored and slip at the interface was recorded during the test at the seven dial gage locations on both sides of the unit located as shown in Appendix C, Figure C.5. As in the ultimate strength test of the previous unit, slip at the ends and midspan of the unit was negligible. However, between these points, slip was detected from the dial gage readings. The slip was relatively consistent at these locations and only the averages were plotted as shown in Figure F.10. Initially, the slip was relatively small, but increased at an increasing rate when the applied load exceeded 120 kips. The curve shows that when the unit was unloaded to 50 kips and reloaded, some energy dissipation had occurred. Once the applied load was returned to the 140 kips level, the curve continued on its initial path. Upon unloading, an average residual slip of 0.0044 inches remained. According to Equation 2.3 discussed in the previous section of this chapter, at the maximum recorded slip of 0.0084 inches, 60% of the ultimate strength of the shear connectors had been reached; 41% of the shear connector ultimate strength had been reached at the apparent (from beam flange strains) yield load of 130 kips.

Figure F.11 shows that the average strain on the top surface of the concrete slab was somewhat less than predicted and behaved similarly to the load-midspan deflection behavior. The maximum strain reached was 604 microstrain which was about 20% of the accepted 3,000 ultimate microstrain for concrete. A residual concrete strain of 117 microstrain was measured upon unloading.

Measured steel strains in the beam bottom flanges were multiplied by the steel elastic modulus to obtain stresses. The results for both beams are plotted in Figure F.12. As described in Appendix C, strain gages were applied to the

steel beams when the beams were in an unstressed state, and the strain instrumentation controls were set and left undisturbed throughout the testing of the second unit. Because of this, the actual strain at the gage locations on the beam bottom flanges could be observed at any time. The strains in the beam bottom flanges were found to reach the yield strain of 2,000 microstrain at 130 kips applied load. As Figure F.12(a) shows, the measured strain in the east beam bottom flange remained constant above this applied load level. As described in the results of the ultimate strength test of the first unit, this was probably due to observed yielding in localized regions not having propagated through the strain gage locations. Nonetheless, this phenomenon is as much an indication that yielding had occurred in the beam flange in the constant moment region as is the usual softening of the load-stress curve.

The dead load moment on the unit was 323 ft. kips, and the maximum applied load moment was 1300 ft. kips, which resulted in a total applied moment at yield of 1623 ft. kips. Taking prestressing into account, with no adjustment for sustained loading effects, the applied load yield moment was calculated to be 1,560 ft. kips, and the total moment to be 1,883 ft. kips. Using an effective concrete modulus reduced by a factor of three resulted in an applied load yield prediction of 1480 ft. kips, and a total moment of 1803 ft. kips. Thus, the unit reached 86% of the higher predicted total moment, and 90% of the total moment predicted using a reduced concrete elastic modulus.

Figure F.13 shows the strain (converted to stress) distribution measured over the cross-section at two load levels. The theoretical stress distributions for the transformed section are also plotted. The stresses shown in the concrete (negative stress points) is the stress on the

transformed area, and are to be divided by the modular ratio of 5.4 to obtain the actual stress. Figure F.13(a) shows that at about half (70 kips) of the maximum load reached (146 kips), the stress distribution was linear and very close to the predicted distribution. Figure F.13(b) shows the converted strain distribution over the cross-section at the maximum load level of 146 kips. Except for the strains in the lower part of the plot (in the bottom flange area), the measured strains exceeded the theoretical strains by 10% to 15%, which may have been caused by the slip at the concrete slab-beam flange interface.

As discussed in Section 2.2.4, sustained loading effects on the second bridge unit were predicted to cause approximately a 3 ksi increase in bottom flange stress. Between the day the unit was set in the Fears Laboratory, and the day it was yielded, approximately 3 ksi of stress increase in the bottom flange was measured. On the day the unit was yielded, the total stress in the beam bottom flange was measured to be 6.2 ksi; whereas the predicted total stress was 3.0 ksi--the difference of 3.2 ksi occurring due to differences in assumed and actual construction loads (see Section 2.2.4).

During the yield test, the yield load was 130 kips, but was predicted to be 148 kips, the bottom flange stress difference is 6.7 ksi. Since 3.2 ksi of this 6.7 ksi has been accounted for, the remaining 3.5 ksi discrepancy is attributed to a possible variance in flange yield strength within the 14 ft. of beam length located within the maximum applied load bending moment region. This seems justifiable in that the strain gage data showed that the flange yielded at locations other than at the exact midspan, where the total plus applied load moments are maximum.

2.4.5 Findings

In all of the static tests, it was found that the elastic stiffness and strength of the unit were predictable with reasonable accuracy if the full concrete modulus was used to compute the transformed moment of inertia. The first unit performed as expected during the overload test, and reached 94% of the predicted yield moment obtained by considering that sustained loads (including prestress loads) were resisted by a transformed section calculated with a reduction in the concrete elastic modulus by a factor of 3.0. The ultimate strength of the unit was 84% of that predicted.

For the second unit, reasonable agreement between experimental results and theoretical predictions were also found. Yielding occurred at 90% of the predicted yield moment calculated using the reduced sustained loading resistance as suggested by the AASHTO Specification.

CHAPTER III

SUMMARY OF SUPPLEMENTARY TEST RESULTS

3.1 General

Two series of supplementary tests were conducted as part of the research; transverse slab strength tests and shear connector specimen tests.

The transverse slab strength tests were performed to determine the resistance of the bridge unit deck to concentrated load. And the shear connector specimen tests were performed to study the differences in sustained loading and strength characteristics of channel and stud type shear connector.

3.2 Transverse Slab Strength Tests

3.2.1 Overview

Necessary considerations in the design of a composite bridge unit are the concrete slab thickness and amount of reinforcement required to safely transmit slab loads to the girders. The design of the slabs for the two bridge units tested was obtained by the working stress design method using a bending moment distribution per transverse unit width of slab. The method is based on elastic theory [10], and, according to the bridge unit designer, is the more commonly used method of the two allowed by the AASHTO Specification [13].

However, this method does not give an assessment of the ultimate resistance of the concrete deck to concentrated loads. To experimentally determine the strength of the bridge deck under concentrated load, a series of six tests was conducted on the first bridge unit. A concentrated load was applied until failure occurred at the center of the concrete deck at six points--two in each region of the three different transverse bar spacings. Details of the bar spacings and load locations are in Appendix G, and overall dimensions of the unit are in Appendix A. A description of the test setup instrumentation, and procedure, is in Appendix C, Section C.4. Material properties are given in Appendix L.

For design, the bridge unit deck is considered to be simply supported in the transverse direction, which in reality, is not the case for a concentrated load. A considerable degree of slab restraint occurs at the slab-girder connection, and due to the longitudinal continuity of the deck. The restraint causes two way flexural action in the slab and resistance to translation and rotation of the slab.

To verify this, six square control slabs, similar to the bridge deck, were constructed. The slabs were tested in the same way as the bridge deck, but were simply supported on steel pipes placed at the same span as the bridge deck. Specimen details are found in Appendix G, and a description of the test setup, instrumentation, and procedure is in Appendix C, Section C.4. An overview of the slab test details is in Section 3.2.2, and test results and strength predictions are discussed in Section 3.2.3.

3.2.2 Test Details

The first bridge unit was constructed with three different transverse reinforcement spacings, with two regions of each spacing, as shown in Appendix A. Reinforcement ratios were determined by dividing the area of bottom transverse reinforcement by the longitudinal slab cross section area. The reinforcement ratios were 0.19% (Regions B1 and B2), 0.29% (Regions B5 and B6), and 0.57% (Regions B3 and B4) for transverse reinforcement. Figure G.1 shows the slab regions and points of concentrated load application. Testing of the slab regions consisted of applying and increasing a concentrated load on the concrete deck, until deck failure occurred.

To verify that the bridge deck resists concentrated load by two-way flexural action, six simply supported small control slabs were constructed of similar materials as the bridge deck, and tested in an identical manner. The transverse reinforcement ratios were again 0.19% (slabs S1 and S2), 0.29% (slabs S5 and S6), and 0.59% (slabs S3 and S4) for these control slabs. The slabs were approximately square with side dimensions of 6 ft. 9 1/2 in., which was the same width as the bridge unit deck width. Test specimen details are found in Appendix G and the test setup, instrumentation, and procedures are discussed in greater detail in Appendix C, Section C.4.

In all bridge slab reinforcement regions, little bending was seen and failure occurred when the loaded area was suddenly pushed thru the slab. The failure surface extended from the rectangular load pattern on the top of the slab to the beam flange boundary and a resulting frustrum which was approximately square was observed from the underside of the slabs. Notably, transverse reinforcement ratios did not affect the slab failure mode, although the failure load increased with increase in reinforcement ratio.

Reinforcement ratio governed both the failure load and failure mode in the small control slabs. Ductile flexural failure occurred at relatively low loads for the slabs with the least reinforcement, and a more sudden punching failure occurred at higher loads for slabs with the largest reinforcement. The slabs with medium reinforcement failed in a ductile, combined mode of flexure and punching failure.

Test results are given in more detail in the following section.

3.2.3 Discussion of Phase XII Results

The transverse slab strength tests consisted of applying a concentrated load to the first unit until failure occurred. Similar tests were performed on six small control slabs, constructed similar to the bridge deck, but tested as simply supported, one-way slabs--as opposed to rigidly supported, two-way slabs of the bridge deck. Overall specimen details of the first unit are located in Appendix A, and the load application points and pertinent reinforcing bar details are contained in Appendix G. Specimen details for the small control slabs are also shown in Appendix G. A discussion of the test setup, instrumentation and test procedure is found in Appendix C, Section C.4.

As shown in Figure C.12, instrumentation consisted of extensometers which were used to obtain the effective transverse strain on the concrete surface (measured displacement over 10 in. gage length), and the transverse displacement of the concrete surface measured over the supports. The latter measurement showed that the bridge deck was much more restrained against translation than the simply supported control slabs.

Appendix I contains the slab test results. Test results for the small control slabs are denoted with an "S", and results for the bridge slabs are denoted with a "B", as shown in Appendix G. Strain and displacement versus applied load results for the bridge unit slabs and the control slabs are plotted together by reinforcement ratio. The failure mode in all bridge unit slab tests was a punching failure mode. Longitudinal and transverse cracks and smaller random cracks were observed on the slab underside prior to sudden punching failure. The small slabs failed in flexure and punching, depending on the reinforcement ratio. Longitudinal flexure cracks were seen prior to flexural failure of the slabs with the least reinforcement, and transverse and random cracks became more developed as the slab reinforcement ratio increased.

Figure I.1 shows that the bridge unit slabs with 0.19% reinforcement ratio had much less strain at the concrete surface than did the small slabs. The crookedness of the bridge unit slabs curves was due to the nature of punching failure.

Figure I.2 shows the axial displacement of the concrete slabs, measured in the transverse direction between supports. The figure shows that the bridge unit slabs were restrained from axial movement, whereas once cracking had occurred in the control slabs, the displacement of the small slabs was very large. Displacement results for slab S1 were not obtained, and are therefore not shown.

Figure I.3 shows similar concrete strain behavior for the slabs with 0.29% reinforcement ratio was similar to that of the slabs with 0.19% reinforcement ratio. The larger strain for bridge unit slab B6 over that of B5 was probably due to that bridge unit slab area having been damaged more

severely in the fall as discussed in Chapter II, Section 2.3.5. Figure I.4 again shows that the axial restraint in the bridge unit slabs was much greater than in the simply supported control slabs.

Figures I.1 through I.4 show that the bridge slabs had relatively constant strain and axial displacements up to the attainment of the punching failure loads. Whereas the control slabs had much more strain and axial displacement, which is indicative of the relatively ductile flexural failure observed for these slabs, although slabs S5 and S6 showed the typical punching failure crushed area under the load point.

The control slabs with the larger (0.57%) reinforcement ratio, however, did not fail in a ductile manner as the other small slabs had done. These two control slabs failed in the sudden punching mode, although two-way bending cracks were observed prior to failure. This more sudden failure mode is indicated in Figures I.5 and I.6.

Figure I.5 shows that the concrete strain in the small slabs remained relatively linear, as in the case of the bridge unit concrete strain, until failure occurred. Figure I.6 shows that axial restraint in the small slabs was probably responsible for the stiffer surface strain curve. But the restraint was not enough to stiffen the small slabs to the same level as the bridge unit slabs. The restraint in the small slabs was due to the increase in the amount of reinforcement, which allowed the slab to act as a tied arch.

Similar arching action is known to occur in reinforced concrete slabs restrained against translation and rotation at the supports. An explanation and historical review of arching action (or membrane compression) is given in Reference 11. The following is quoted from Reference 11:

-73-

A simple explanation of this behavior is that in pure bending of reinforced concrete with small steel proportions, the neutral axes at failure are close to the surface. Thus pure bending is accompanied by extensions of the middle surface. If such deformations are incompatible with the support conditions, collapse with pure bending cannot occur.

Thus, the flexural strength of the bridge unit slabs was increased above that of the smaller control slabs, due to edge restraint, in addition to two-way action. While arching action is easily understood qualitatively, closed form mathematical solutions are not readily available due to the actual complexity of the phenomenon.

For ultimate strength design, the ACI (Reference 12) punching shear equation was adopted by AASHTO (Reference 13). The equation (AASHTO Equation 8-58) is reproduced here as Equation 3.1

$$V_c = (2 + 4/\beta_c) \sqrt{f'_c} \, b_o d \leq 4\sqrt{f'_c} \, b_o d \qquad (3.1)$$

where V_c is the punching failure load, β_c is the ratio of load pattern long to short side dimensions, f'_c is the concrete compressive strength, b_o is the length of the load pattern perimeter plus 2d, where d is the depth from the slab surface to reinforcement. This equation is a lower limit to several empirical test results equations, as discussed in Reference 14.

Two schools of thought on the subject of slab shear strength exist (Reference 14). One maintains that the strength depends primarily on concrete strength, and the other that the reinforcement ratio governs the slab strength. However, it was noted that flexure and shear strengths of slabs are related. Equation 3.1 is a lower limit to the empirical equations of both schools of thought, and is a simple, conservative estimate of punching shear

strength for two-way flexure action. Equation 3.1 was used in this study to predict the punching strength of the slabs, and it will be shown that the equation gave conservative results for the slabs which failed by punching.

The flexural strengths of the slabs were determined using yield line theory. An excellent explanation of yield line theory and analysis is given in Reference 15. The yield line method consists of assuming a kinematically acceptable yield line pattern in the concrete slab, and equating the work done by externally applied forces with the internal work done by ultimate moments acting along the assumed yield lines. The theory relies on energy theorems, therefore solutions obtained are upper bound. But, if several solutions are obtained from different yield line patterns for a given loading case, a practical least upper bound solution is usually obtained. The governing yield line pattern obtained for the bridge unit slabs is shown in Figure 3.1. The pattern was found by assuming that positive (positive ultimate moment) yield lines formed around the load pattern, and extended as shown in Figure 3.1. Negative yield lines were assumed to form along the beams and in the transverse direction as shown in the figure. The yield line pattern governed for the interior bridge unit slabs, as well as the exterior bridge unit slabs, since the distance L_1 was always less than the distance to the free slab edges at the ends of the unit.

Equating the internal and external work done for the symmetrical loading pattern shown in Figure 3.1, resulted in the following yield line equation

$$P = \frac{2(2L_2+Y)}{L_1}(M_{LP}+M_{LN}) + \frac{2(2L_1+X)}{L_2}(M_{TP}+M_{TN}) \qquad (3.2)$$
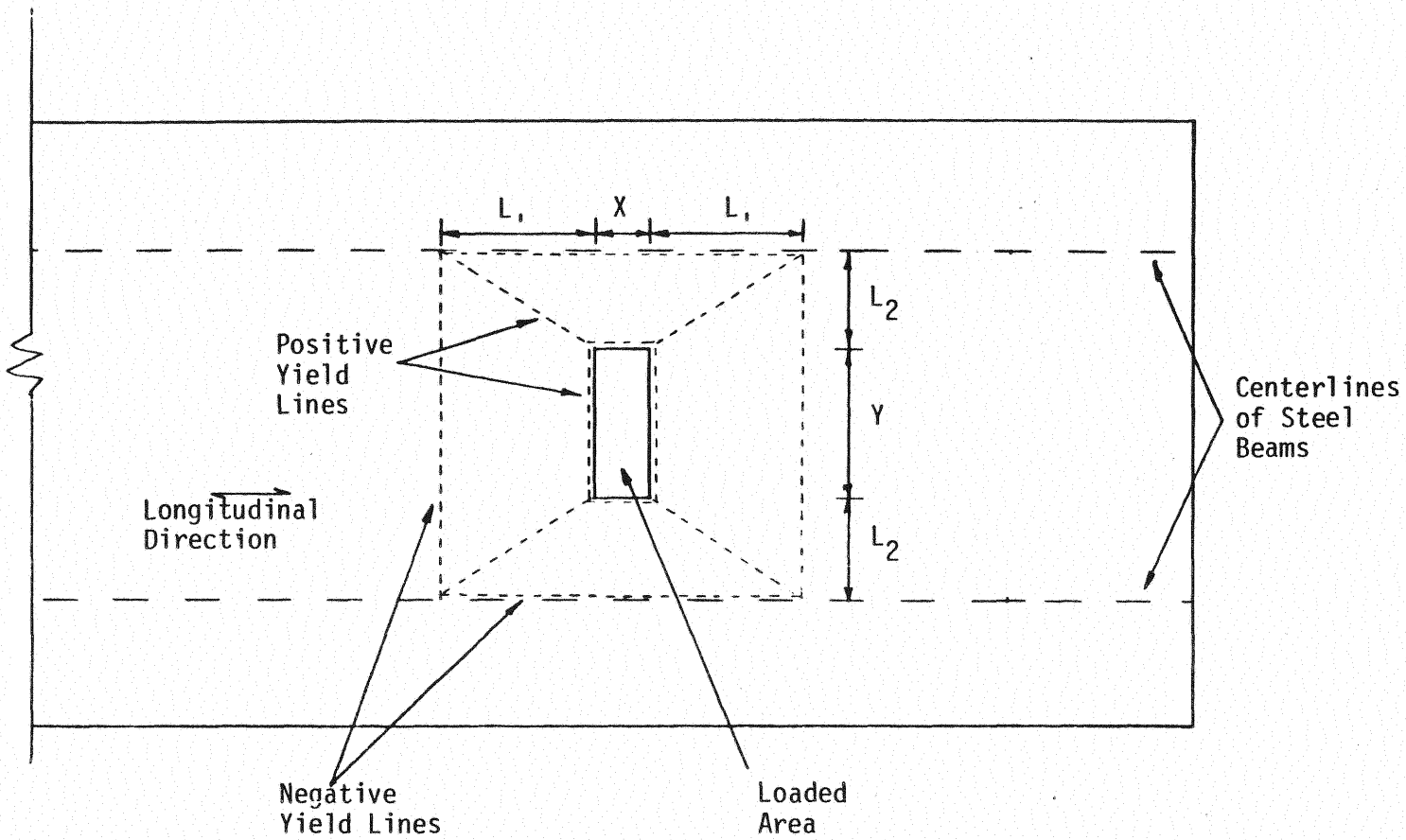
Figure 3.1 Yield Line Pattern for Bridge Unit Slabs

in which P is the failure load; M_{LP} and M_{LN} are the positive and negative ultimate slab moment capacities per unit length considering longitudinal top and bottom reinforcement; M_{TP} and M_{TN} are the positive and negative ultimate slab moment capacities per unit length considering transverse top and bottom reinforcement; L_1 is an unknown dimension; L_2 is the transverse distance from the edge of the load pattern to the centerline of the slab support; and X and Y are the dimensions of the load pattern in the transverse and longitudinal directions, respectively. To find L_1 such that P is a minimum, the derivative with respect to L_1 of Equation 3.2 was set equal to zero, and the resulting expression

$$L_1 = \sqrt{L_2(L_2+Y/2)\ (M_{LP}+M_{LN})/(M_{TP}+M_{TN})} \qquad (3.3)$$

was obtained for L_1.

Equation 3.2 implies that either positive or negative moment reinforcement could be excluded from the slab, and a valid ultimate load solution would still be obtained. However, since yield line theory is based on the assumption that ultimate moment distribution occurs along the yield lines, the existence of both positive and negative moment reinforcement is essential for a valid solution to be obtained. However, it is not known whether or not a minimum necessary amount of reinforcement exists.

For the geometry of the slabs tested here, Equation 3.2 reduces to

$$P = \frac{91.0}{L_1}\ (M_{LP}+M_{LN}) + \frac{(L_1+4)}{3.19}\ (M_{TP}+M_{TN}) \qquad (3.4)$$

and Equation 3.3 reduces to

$$L_1 = 17.03 \sqrt{(M_{LP}+M_{LN})/M_{TP}+M_{TN})} \qquad (3.5)$$

in which the units are kips and inches.

Yield line theory was also used in the failure load prediction of the control slabs. Figure 3.2 shows the pattern which resulted in the following failure load prediction

$$P = 2 \; \frac{L_1}{L_2} \; M_{TP} \qquad (3.6)$$

in which P is the predicted failure load; M_{TP} is the positive ultimate slab moment capacity per unit length, considering transverse top and bottom reinforcement; L_1 is the length of the slab; and L_2 is the distance between a positive yield line and the nearest support. For the geometry of the small slabs tested, Equation 3.6 reduces to

$$P = \frac{L_1}{6.38} \; M_{TP} \qquad (3.7)$$

in which the same variables and units of kips and inches were used. This pattern was used instead of an alternate pattern where one yield line would pass through the center of the loaded area because it was observed during the tests on the small slabs with less reinforcement, that as the center of the slab deflected under one-way action, the elastomeric pad was compressed more at the load pattern edges closer to the supports. This indicated that the applied load had shifted from being evenly distributed over the loaded area to being more concentrated at the loaded area edges closer to the supports. In reality, the load distribution was somewhere in between the two cases discussed.

Positive
Yield Line

Loaded
Area

L_2

Centerlines
of Supports

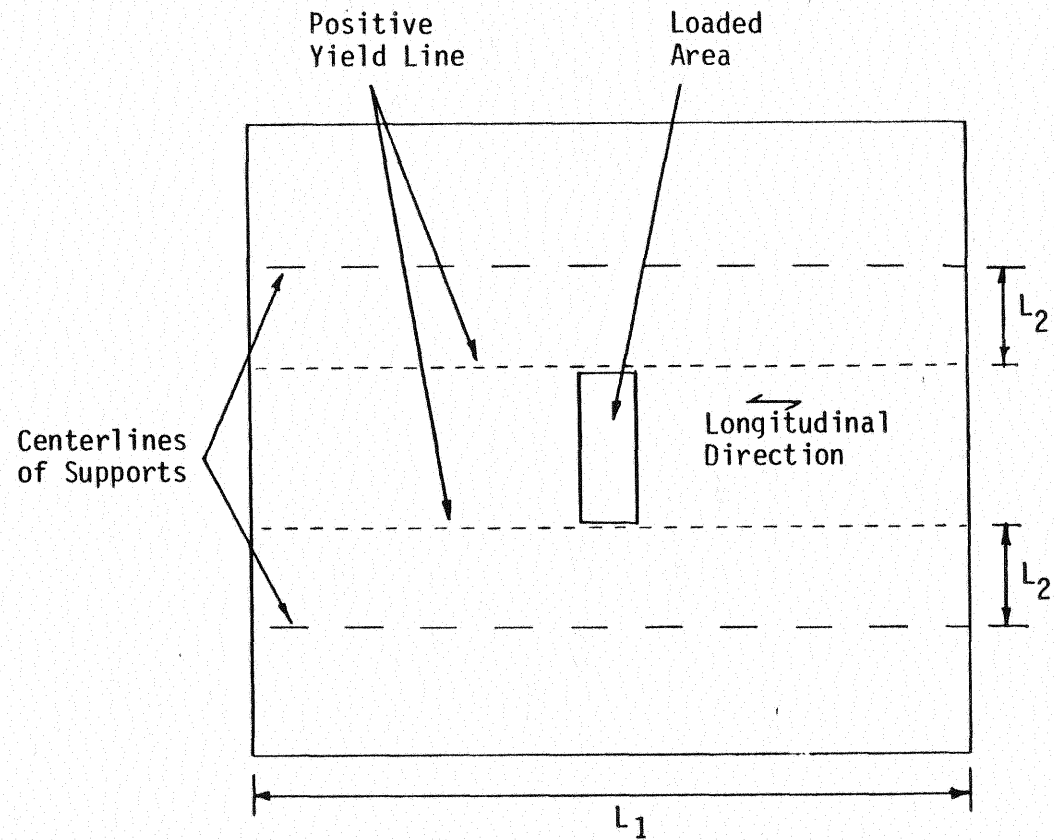Longitudinal
Direction

L_2

L_1

Figure 3.2 Yield Line Pattern for Control Slabs

A similar justification was used in the yield line pattern chosen for the bridge unit slabs, which failed by punching, rather than by flexure. The observed punching failure pattern, which ran along the perimeter of the loaded area, further justified this choice.

The longitudinal and transverse ultimate bending moment capacities were determined using typical strength design methods. The effective depth of reinforcement in both directions was assumed to be the average distance from the extreme compression fiber to the perpendicular reinforcement. In both the positive and negative moment calculations, both layers of reinforcement were calculated to reach yield strains in tension, which indicated that only a small depth of concrete would actively resist the ultimate moment. The slab flexure strengths are shown in Table 3.1.

In addition to the punching and flexure failure predictions obtained for the small slabs, simple transverse shear capacity was also checked for the small slabs. The failure surface was assumed to extend the full length (L_1 in Figure 3.2) of the slab and thru the effective depth of the slab. The concrete shear strength was taken as twice the square root of concrete compressive strength, as stipulated in Reference 13, (AASHTO Equation 8-49).

The experimentally determined failure loads, along with the predicted failure loads, are shown in Table 3.2. In addition, the transverse bar spacings and corresponding reinforcement ratios, failure modes, and ratios between predicted and experimental failure loads are shown for each slab.

These strength results are plotted in Figure I.7, as failure load vs. reinforcement ratio. The triangular points

Table 3.1

Slab Flexure Strengths

Slab	Transverse Reinforcement Ratio (%)	Moment Resistance per Unit Length (in-kips/in)			
		Due to Transverse Reinforcement		Due to Longitudinal Reinforcement	
		Positive, M_{TP}	Negative, M_{TN}	Positive, M_{LP}	Negative M_{LN}
B1,B2	0.19	5.34	4.65	6.54	7.51
B5,B6	0.29	8.22	7.15	6.54	7.51
B3,B4	0.57	15.43	13.33	6.54	7.51
S1,S2	0.19	6.42	---	---	---
S5,S6	0.29	9.44	---	---	---
S3,S4	0.57	17.77	---	---	---

Table 3.2

Test Results for Phase XII, Transverse Slab Strength Tests

	Test Results				Predicted Failure Loads					
Slab	Transverse Bar Spacing (in)	Transverse Reinforcement Ratio (%)	Failure Mode	Failure Load (kips)	Punching (kips)	Pred. Exp.	Flexure (kips)	Pred. Exp.	Shear (kips)	Pred. Exp.
B1	16.5	0.19	punching	155	133	0.86	139	0.90	---	---
B2	16.5	0.19	punching	151	133	0.88	139	0.92	---	---
B5	11.0	0.29	punching	190	133	0.70	176	0.93	---	---
B6	11.0	0.29	punching	160	133	0.83	176	1.10	---	---
B3	5.5	0.57	punching	205	133	0.65	251	1.22	---	---
B4	5.5	0.57	punching	203	133	0.66	251	1.24	---	---
S1	16.5	0.19	flexure	75	125	1.67	83	1.11	147	1.96
S2	16.5	0.19	flexure	75	125	1.67	83	1.11	147	1.96
S5	11.0	0.29	combined	87	125	1.44	114	1.31	137	1.57
S6	11.0	0.29	combined	93	125	1.34	114	1.23	137	1.47
S3	5.5	0.57	punching	145	125	0.86	230	1.59	147	1.01
S4	5.5	0.57	punching	148	125	0.84	230	1.55	147	0.99

on the plots are the respective experimental failure loads of the slabs. A line was drawn between the average of the failure loads for each reinforcement ratio, and plotted with the predictions.

The plot for the first bridge unit slabs shows that the failure load of the slabs (which failed in punching) increased with an increase in reinforcement ratio. This is contrary to the punching failure mode prediction used, which is not a function of the reinforcement ratio. However, the punching failure prediction did provide a lower limit to the test data. The predicted flexure failure curve shows that the yield line prediction was close to the experimental loads for lower reinforcement ratios, but overpredicted the experimental load for the larger reinforcement ratio. This was because the lower punching resistance governed the failure of the more heavily reinforced slabs, and is similar to the results obtained in Reference 16.

A reduced yield line capacity was obtained by assuming that the oblique yield lines in Figure 3.1 intersected at midpoint of the loaded area. By assuming that the yield lines intersect at the center of the load pattern, the resulting yield line prediction is the same as in Equation 3.2, with X and Y equal to zero. Hence, for this case, Equation 3.2 reduces to

$$P = \frac{51.0}{L_1} (M_{LP}+M_{LN}) + \frac{L_1}{3.19} (M_{TP}+M_{TN}) \qquad (3.8)$$

and Equation 3.3 reduces

$$L_1 = 12.75 \sqrt{(M_{LP}+M_{LN})/(M_{TP}+M_{TN})} \qquad (3.9)$$

in which the variables are the same as defined previously. The experimental curve may have been closer to this

alternate yield line capacity curve had the presence of arching action not been apparent.

The experimental and predicted strengths are plotted for the control slabs in a similar manner. The predicted flexure curve provided an upper limit to the experimental curve. An alternate yield line capacity, obtained by assuming that one yield line passed through the center of the load pattern in the longitudinal direction, provided a lower limit to the test data, and showed that the actual yield lines occur somewhere between the cases checked. For the yield line passing through the center of the load pattern, Equation 3.6 is again used, with the substitution half of the distance between supports for L_2. The resulting ultimate load is

$$ P = \frac{L_1}{11.38} M_{TP} \tag{3.10} $$

where the same units and variables are used as in Equation 3.6.

A comparison of Equations 3.4 and 3.8 for the bridge unit slabs, and Equations 3.7 and 3.10 for the control slabs, shows that a change in assume yield line geometry greatly influences the flexure failure predictions.

The punching equation was used to compare the predicted strength with the failure loads obtained for the two control slabs (with more transverse reinforcement) which failed by punching. Again, the predicted punching equation provided a lower limit for these slabs which failed in punching. Flexure shear predicted strength did not govern in any of the small slab tests.

3.2.4 Findings

It was seen in the transverse slab strength tests that the failure of the bridge unit slabs occurred in a punching failure mode. The only variable which was changed in the tests was the slab transverse reinforcement ratio. The experimental failure loads obtained from the tests showed that the punching resistance of the slabs was directly related to the reinforcement ratio. The ultimate predicted punching strength, calculated without consideration of flexure reinforcement, provided a lower limit to the test results for all slabs which failed in punching, including two simply supported control slabs.

Yield line theory provided upper and lower limit predictions to the test results, and the presence of arching action was believed to have pushed the experimental results toward the upper limit solution.

Yield line theory provided similar predictions for six control slabs tested. The presence of arching action was observed in the slabs with the greatest (0.57%) transverse reinforcement ratio, which failed by punching. The predicted punching load again provided a lower limit prediction.

3.3 Shear Connector Specimen Tests

3.3.1 Overview

Phase XIII was devoted to the testing of four pushout-type shear connector specimens constructed of materials similar to those found in the first bridge unit. Specimen details are found in Appendix H and material properties are found in Appendix L. The test phase was divided into two parts: Phase XIII A consisted of 810 days

-85-

of observation of the shear connector specimens under sustained loading; and Phase XIII B consisted of loading the specimens to failure.

Phase XIII A was reported by Hendrick [1] and Majumdar [3], and most of the sustained loading test results discussion which follows, was reproduced from these references. During Phase I, (sustained loading of the first unit), it was theorized that the small aspect ratio of the stud connectors in the bridge unit was causing localized creep in the concrete. Accordingly, two pushout specimens were constructed with welded stud shear connectors and two were constructed with channel shear connectors. It was surmised that the much larger bearing area of the channel connector would reduce any localized creep. It was found that no distinct differences in displacement occurred between the two types of shear connectors.

Phase XIII B consisted of loading the shear connector specimens to failure. The failure loads were reasonably predictable using the strength predictions from References 6 and 9, within limitations discussed in Section 3.3.4.

3.3.2 Test Details

These tests were a sub-project initiated to investigate the creep and slip effects associated with both stud and channel type shear connectors, and to determine the strength of the shear connectors. A description of the test specimens is found in Appendix H, and a descriptions of the test setups, instrumentation, and procedures are located in Appendix C, Sections C.5 and C.6.

In Phase XIII A, each of the four specimens was loaded to 48 kips with large springs. Slip and creep displacements

measured with dial gages "at" the shear connectors and "away" from the shear connectors, were monitored over an 810 day period. The measured behavior of the stud and channel connectors was plotted over the period of observation so that conclusions could be made.

In Phase XIII B, the shear connector specimens were concentrically loaded to failure. As discussed in Appendix C, Section C.6, a static load was applied to the beam section and incrementally increased until the shear connection between the beam and slabs failed.

3.3.3 Discussion of Phase XIII A Results

Shear connector specimen details are described in Appendix H, and the test setup, instrumentation, and procedure are discussed in Appendix C, Section C.5. Plots of test results are found in Appendix J, Section J.1.

Creep and creep plus slip data were recorded for the specimens over an 810 day period. These data include the creep deformations "at" shear connectors as well as "away" (approximately 5 in. away) from shear connectors. The results obtained from the tests are presented graphically in Figures J.1 to J.11. Each of these graphs depicts the time-displacement effect for approximately 810 days of sustained loading. The curves shown are average values for all similar data, e.g., four creep displacement measurements (two sets from two specimens) and four slip plus creep displacement measurements. The time-displacement nature of slip alone is also presented.

Because of the locations (on the surface of the concrete slab) of the support angles for the dial gages used in measuring the relative slip, the values obtained included

the creep effects in the concrete slab about 5 in. away from the shear connectors. As such, the actual slip displacements were determined by subtracting the creep displacements 5 in. away from the combined relative slip plus creep measurements taken with the dial gages.

The average creep displacements at the shear connectors ("creep at") and the creep displacement at approximately 5 in. away from the shear connectors ("creep away") for the stud connector specimen are shown in Figure J.1. In Figure J.2 the average slip plus creep and in Figure J.3 average slip values are shown for the same specimens.

For the channel-connector specimens, the average creep displacements at the shear connectors and at approximately 5 in. away from the shear connectors are plotted in Figure J.4. Figure J.5 shows the average slip plus creep displacements while Figure J.6 shows the average slip value for the channel-connector specimens. Each of the plots also includes the variation of air temperature with time.

Creep, average slip plus creep, and average slip displacements between the stud and channel specimens are compared in Figures J.7 through J.11. Creep displacements "at" and "away" from the shear connectors are compared in Figure J.8 and J.9. Figure J.10 compares slip displacements. Figure J.11 compares the creep "at" and "away" from the shear connectors for each of the two types of specimens.

It is evident from the figures that all the displacement values (creep, slip plus creep, slip) are sensitive to the changes in temperature. Therefore, temperature effect must be taken into consideration in the interpretation of results.

Creep displacements at and away (about 5 in.) from shear connectors are shown in Figure J.1 for the stud connector specimens. It is obvious from the plot that creep displacement at the stud shear connector was considerably larger than the creep displacement approximately 5 in. away from the stud shear connector during the first 170 days of observation. However, these displacements closely followed the change in temperature during this period. For the next 30 days, the measured temperature dropped from approximately 90°F to approximately 70°F. During this period a reduction of creep occurred, both "at" and "away" from the shear connectors. From about day 200, the creep displacements "at" the shear connectors began to increase steadily but at a low rate; the displacements "away" from the stud connectors remained at relatively the same value 0.0015±0.0013 in. However, after day 790, a sharp drop of creep value occurred "at" the shear connector as can be seen from Figure J.1.

The largest value of creep displacement recorded "at" the stud shear connector was 0.0041 in. and that "away" from the stud shear connector was 0.0018 in. which represent strain of 4100 microstrain and 1800 microstrain, respectively.

The average slip plus creep displacement for stud type connector specimens is shown in Figure J.2. The initial value recorded was the relative slip movement which occurred when the specimen was first loaded. Test specimens were moved on the fourth day of loading which caused a loss in slip as shown in the plot. After that the measured displacements steadily increased to approximately day 300. It can be seen from Figure J.2 that slip displacement is sensitive to change in temperature. After day 300, the rate of increase of displacement became negligible and the

displacement remained fairly constant at approximately 0.0035 in. until the last readings were taken. This value represents a strain of 3500 microstrain.

Figure J.3 shows the actual slip displacement measured for the stud connector specimens. These values were obtained by subtracting the creep measurements at 5 in. away from the shear connectors from the measured slip plus creep values. Initial slip displacement of about 0.0011 in. was recorded at the time of loading of the specimens. The slip slightly decreased when the specimens were moved, then increased steadily through approximately the first 50 days. The rate of increase then dropped, but slow, steady increase continued to approximately day 300. The rate of increase became negligible after day 300 with the slip displacement remaining fairly constant at about 0.0020 in. until about day 690. The slip then increased slightly, remained almost constant at 0.0021 in. until the last set of data was taken.

Figure J.4 presents the average creep displacements "at" the shear connectors and at approximately 5 in. "away" from the shear connectors for the channel connector specimens. As with the case of the stud specimens, the creep displacements at the shear connectors were substantially larger than those away from the shear connectors. The temperature versus time curve follows closely these creep displacement curves. As shown in Figure J.4, creep displacements increased steadily with the increase in temperature for approximately the first 170 days of observation, then they decreased with the decrease in temperature until about day 280. Thereafter, creep displacements began to increase again as the temperature increased, but at a slower rate. The largest creep displacement recorded at the shear connector was 0.0039 in. For creep away from the shear connectors, the creep

displacements remained near 0.0014 in. from day 200 until
the last readings were taken. The largest creep
displacement recorded away from the shear connectors was
0.0016 in. The largest displacements represent strains of
3900 microstrain and 1400 microstrain.

The average slip plus creep displacements for the
specimens with the channel shear connectors are shown
graphically in Figure J.5. A displacement value of 0.0016
in. was recorded at the day of loading of the specimens.
This value decreased slightly when the specimens were moved
on day 4, but then increased steadily as creep effects began
to take place. The displacement increased with temperature
until approximately day 170, then it began decreasing, as
did the temperature for the next 30 days. Finally,
displacements began to increase again but at a slower rate.
After about day 450, they became almost constant at a
maximum value of 0.0043 in. The maximum displacement value
recorded was 0.0047 in. until the last readings were taken.
This value is a strain of 4700 microstrain.

The slip displacement curve for specimens with channel
shear connectors is presented in Figure J.6. An initial
displacement of 0.0016 in. occurred when the specimens were
loaded. Displacement values did not significantly increase
during the first 170 days. Then they increased steadily to
day 300 and remained almost constant at about 0.0028 in. to
day 600. A small increase then occurred and the
displacements remained constant at 0.0031 in. until the last
set of readings were taken.

A comparison of average creep displacements "at" the
shear connectors for both stud and channel specimens is
presented in Figure J.7. An examination of the figure shows
that initially, nearly identical creep displacements were

found for the two types of specimens. But the channel connector specimens showed more displacement than the stud connector specimens after day 450.

Figure J.8 compares averages creep displacements away from the shear connectors for each type of specimens. Figure J.8 clearly shows that the average creep displacements were very close for both types of specimens, thought the stud connector specimens produced a little more displacement during the later stages of testing.

A comparison of average slip plus creep values for two types of shear connectors is presented in Figure J.9. Although similar plots were obtained for the two specimens types, the channel connector specimen consistently experienced more slip plus creep values than the stud connector specimens throughout the test. Figure J.10 compares the actual slip displacement comparison of measured deflection with Branson's predicted values. This figure indicates that the measured deflections and predicted temperature deflections are in very good agreement.

3.3.4 Discussion of Phase XIII B Results

The test setup, instrumentation, and testing procedure for Phase XIII B, failure of the shear connector specimens, is located in Appendix C, Section C.6. Specimen details are found in Appendix H.

Phase XIII B consisted of incrementally loading the steel wide-flange section in each shear connector specimen until the specimen failed in shear. The relative displacement between the steel flanges and the concrete slabs was measured at four places on the specimen, and a displacement value was recorded for each load increment.

Test Results consist of load vs. average slip plots and ultimate strength per shear connector data, and are located in Appendix J, Section J.2.

Figure J.12 is a plot of applied load vs. average slip between the steel flange and concrete slab, which was measured at four places on each specimen. As the figure shows, the stud and channel specimens exhibited about the same stiffness up to a slip of approximately 0.01 in. The curves for the stud specimens then lean over at a faster rate, indicating that the stud connectors failed at a lower load level than did the channel connectors. Prior to failure, the probes were removed from the specimens, which accounts for the variance in maximum plotted displacements for the tests.

Table J.1 gives the experimental and predicted values for ultimate load per shear connector for the shear connectors studied. The predicted strengths were calculated from the AASHTO Specification [13]. The equations used for determining the ultimate strength per shear connector for channels and welded studs are as follows:

Channels:

$$S_u = 550 \ (h + t/2) \ W\sqrt{f'_c} \qquad (3.11)$$

Welded studs (for H/d > 4):

$$S_u = 0.4d^2 \ \sqrt{f'_c E_c} \qquad (3.12)$$

where

E_c = modulus of elasticity of the concrete in pounds per square inch;

$$E_c = w^{3/2} \ 33\sqrt{f'_c} \qquad (3.13)$$

S_u = ultimate strength of an individual shear connector in pounds;

h = average flange thickness of the channel flange in inches;

t = thickness of the web of a channel inches;

W = length of a channel shear connector in inches;

f'_c = compressive strength of the concrete in 28 days in pounds per square inch;

d = diameter of stud in inches;

w = unit weight of concrete in pounds per cubic foot;

H = height of stud in inches.

Equation 3.11 was originally determined from empirical studies as discussed in Reference 8. Equation 3.12 was determined from stud shear connector tests (Reference 6) similar to the tests conducted during this phase. While no limit is placed on the strength of channel connectors, the authors of Reference 6 strongly suggest that a limiting concrete compressive strength of 4000 psi be used. From their results, they chose to impose this limit (which is not mentioned in the AASHTO Specification) because when higher strength concrete is used, the shear connection failure mode changes from concrete strength dependent to shear connector steel strength dependent. That is, when the concrete compressive strength was below 4000 psi, specimen failure consisted of the connectors being pulled, out along with a cone of surrounding concrete. For concrete strengths above 4000 psi, failure consisted of the shearing off of the steel studs, with little damage to the surrounding concrete. The authors thus limited the value of the square root term in Equation 3.12 to less than 130,000 psi to limit the shear stress in the steel stud.

For the predicted connector strengths shown in Table J.1, the 28 day concrete compressive strength used was 5735 psi (and a separate calculation for 4000 psi concrete

strengths was performed for the stud connectors). For both
connector types, the predicted strengths were in relatively
good agreement with the experimental strengths, with the
limiting value of 4000 psi concrete compressive strength
giving much better results for the stud connectors than the
actual 28 day strength. This limit was seen to be necessary
because as in previous research [6] the stud shear
connectors failed in shear, with little damage to the
surrounding concrete. A similar but higher limiting.
concrete strength may be justified in the design of channel
connectors as well, since they also failed in shear, but
with more concrete cracking observed at the time of failure.
These limiting values are believed to be very necessary,
since in all probability, the strength of the concrete at
the time of testing (2.5 years after the concrete was cast)
was much greater than the 28 day compressive strength of
5735 psi.

In Reference 6, the authors obtained (by regression
analysis) a load-slip relationship for stud shear connector
specimens which relates the ratio of load per connector (S)
to the ultimate strength of the connector (S_u) at a give
slip displacement (D). The equation has the form of

$$\frac{S}{S_u} = \frac{80\ D}{1\ +\ 80\ D} \tag{3.14}$$

and is plotted in Figure J.13. Each load-slip curve in
Figure J.13 was normalized with respect to the maximum load
reached in the corresponding test, and is also plotted in
Figure J.13. Even though Equation 3.14 was determined for
shear stud specimens, both the channel and stud specimen
cures have similar shapes. Both connector types showed
greater stiffness than predicted, with the channel
connectors showing greater stiffness over the stud

connectors, although both types had good ductility. The difference in stiffnesses at higher normalized load levels was probably due to the failure mode being the shearing of the steel connectors rather than a concrete related failure.

3.3.5 Findings

After 810 days of shear connector specimen observation under sustained loading, test results show that measured displacements "at" the shear connectors are considerably more than those "away" from the shear connectors for both types of specimen. Measurements "at" the shear connectors include both creep and slip effects, while those "away" include only creep effects. However, no distinct differences in the amount of displacement "at" the shear connectors and "away" from the shear connectors were found between the stud connector specimens and the channel connector specimens. Slip at the channel shear connectors was consistently higher in comparison to slip at the stud shear connectors. Both creep and slip displacements were found to be sensitive to temperature. And, as described in Appendix C, Section C.5 and Appendix H, the effects of the beam flanges partially bearing on the concrete slabs is unknown.

Comparison of ultimate shear connector strengths with AASHTO Specification predictions showed that the strength of shear connectors, in the specimens tested, were relatively predictable. However, the equation used in the prediction of stud connector strengths should be used with a limiting 28 day concrete strength of 4000 psi, since, in stronger concrete, typical shear connector failure occurs as the shearing of the steel connector. A similar limiting concrete strength for use in predicted channel connector strengths is also warranted, although this value cannot be

determined from the limited test data available. The AASHTO
Specification does not provide a limiting concrete strength,
thus probably making the calculated ultimate shear connector
strengths unconservative for higher strength concrete,
especially in stud connector design. However, the
relatively stringent (as concluded from fatigue loading
tests, Chapter II) shear connector fatigue requirement may
compensate for this oversight.

CHAPTER IV

SUMMARY AND OBSERVATIONS

4.1 Primary Tests

4.1.1 Test Specimens

The behavior of two 55 ft. long prestressed, composite steel beam-concrete slab bridge units was investigated in this study. The type of unit tested is currently used in county road bridge construction where the use of prefabricated units may be especially economical. Specimen details for the two units are found in Appendices A and B.

In primary test phases, the first unit was subjected to three years of sustained loading, over 200,000 cycles of fatigue loading, and was statically loaded to failure. The second unit underwent 500,000 cycles of fatigue loading and was statically loaded to its yield point. Secondary test phases included shear connector sustained loading and failure tests and transverse slab strength tests.

Test results were compared to theoretical predictions and AASHTO Specification limitations. The following subsections are summaries of each of the test phases.

4.1.2 Sustained Loading Tests

In the sustained loading test phases, discussed in Section 2.2, the first bridge unit was observed for a

total of four years of sustained loading of 40 psf plus its own weight. The observation period for the second unit was less than 100 days, including 500,000 cycles of repeated loading. The following observations were made concerning sustained loading behavior of the two bridge units:

1. Sustained loading phenomena is typified by increases in bottom flange stress and loss in camber of the bridge unit.

2. The effects of sustained loading phenomena on the first unit, characterized by creep and shrinkage of the concrete slab, reached a relatively asymptotic level after approximately 100 days of sustained loading. After that time, the strain and camber change of the unit varied inversely with the temperature change of the testing environment without a long term trend.

3. The effects of sustained loading in the second unit were accelerated by the application of fatigue loading, but reached an asymptotic level upon completion of fatigue loading.

4. The sustained loading induced increase in bottom flange stress, although relatively minor, reduced the yield capacity of the bridge units.

5. The effective concrete elastic modulus method for determining increased flange stresses and camber losses due to sustained loading was reasonably accurate. This method resulted in a predicted increase in bottom flange stress of 3.8 ksi for the first unit, and 3.0 ksi for the second unit, as compared to measured values of 5.4 ksi and 3.8 ksi for the respective units (see Table 2.2). The predicted camber losses were 0.61 in.

for the first unit and 0.58 in. for the second unit, versus measured values of 0.4 in. and 0.94 in. for the respective units.

6. Branson's method for estimating combined shrinkage and creep effects, as described in Section 2.2.1 resulted in accurate predictions of bottom flange stress change in both units and in camber loss in the second unit. Camber loss in the first unit was overpredicted. The predicted flange stress changes were 4.9 ksi for the first unit and 3.1 ksi for the second, versus 5.4 ksi and 3.8 ksi measured stress changes in the respective units (see Table 2.2). The predicted camber losses were 1.61 in. for the first unit and 0.96 in. for the second unit, and the measured sustained loading camber losses were 0.4 in. for the first unit and 0.94 in. for the second unit.

7. Branson's method for estimating sustained loading effects was extended in Section 2.2.5 for prediction of creep effects alone (without shrinkage). The extension gave qualitatively correct predictions of flange stress changes and camber loss (see Table 2.2). The predicted changes in bottom flange stress were 4.9 ksi for the first unit and 6.2 ksi for the second unit, and the measured changes were 5.4 ksi and 3.8 ksi for the respective units. The predicted losses of camber were 0.8 in. for the first unit and 0.92 in. for the second unit, versus 0.4 in. and 0.94 in. measured for the respective units.

4.1.3 Fatigue Loading Tests

In the fatigue loading test phases, discussed in Section 2.3, the first unit was subjected to 2,100,000

cycles of simulated AASHTO HS-20 truck loading and 2000 cycles of HS-30 truck loading. Of the HS-20 cycles, 2,000,000 cycles were applied symmetrically with respect to the longitudinal centerline of the unit, and 100,000 cycles were unsymmetrical with respect to this centerline. The second unit was subjected to 500,000 cycles of HS-20 loading. The following observations were made concerning the fatigue characteristics of the bridge units tested:

1. After 2,000,000 cycles of repeated loading and before the 100,000 cycles of unbalanced fatigue loading were applied, the first unit did not exhibit significant changes in stiffness, and slip at the shear connectors was insignificant.

2. The first unit developed cracks along three interior cross-frame welds during the unbalanced fatigue loading tests. However, the unit was designed for 100,000 cycles of loading and the stress range at the welds was higher than allowed by AASHTO for 2,000,000 cycle design life.

3. The second unit was subjected to 500,000 cycles of repeated loading with no observed changes in stiffness, strength, or slip at the shear connectors.

4.1.4 Static Loading Tests

In the static test phases, discussed in Section 2.4, the first unit was subjected to one HS-30 overload cycle after the first 500,000 HS-20 fatigue loading cycles and was loaded to failure after completion of all the fatigue loading phases. The second unit was loaded to determine its yield point, after the 500,000 fatigue loading cycles were applied. In addition, a static cycle test was conducted

after each 50,000 cycles of fatigue loading. The following observations are drawn from the static loading test results:

1. Unit stiffnesses and stresses in the units are predictable by classical elastic flexure theory if experimentally obtained material properties are used.

2. The concrete modulus of elasticity experimentally obtained using four year old cylinders was very close to the AASHTO prediction of concrete elastic modulus based on the 28 day concrete strength. This indicates that the modulus of elasticity of concrete does not increase over time as does compressive strength. As a result, the stiffness of first bridge unit remained constant during the four year testing program.

3. Prestress losses reduce the yield capacity of the units. The losses in bottom flange prestress due to sustained loading effects were 5.4 ksi for the first unit and 3.8 ksi for the second unit. Due to accumulated error in estimating construction load magnitudes which directly affects prestress levels, the bottom flange of the second unit had an additional 2.4 ksi less prestress than predicted.

4. The first unit reached 94% of its predicted yield moment, which was computed considering the theoretical loss in prestress noted above. The unit reached 84% of its ultimate moment before fracture occurred at a welded flange repair.

5. The second unit reached 90% of the calculated yield moment. Part of this apparent undercapacity is due to differences in estimated and actual construction loads, and the rest resulted from the under-prediction of

sustained loading effects, differences between actual and measured flange yield strengths, and observed slip at shear connectors.

6. The yield strength of the unit is dependent upon the level of prestress in the bottom flange at the time loading, which is a function of the magnitude of construction loads and prestress losses due to sustained loading effects. For optimum design, construction which results in the highest AASHTO allowable flange prestresses should be used, and these loads should be estimated accurately. Prestress loss due to sustained loading effects is predicted reasonably well by the effective concrete elastic modulus method. Branson's method is qualitatively correct, but is dependent upon assumed ultimate concrete creep and shrinkage strains which are not always predictable.

7. To account for construction inaccuracies in developing the calculated prestress only 85% to 90% of the calculated yield load should be considered for design.

4.2 Supplementary Tests

4.2.1 Transverse Slab Strength Tests

In the transverse slab strength tests, discussed in Section 3.2, the first bridge unit concrete slab was failed at six locations by the application of a concentrated load. All bridge unit deck failures were by sudden punching of the concentrated load through the deck. Six simply supported square test control slabs of the same transverse dimension and reinforcement ratios as the bridge deck were tested under similar loading conditions. The failure modes of the

slabs ranged from ductile flexural failure to sudden punching failure, depending on the reinforcement ratio.

Observations from the transverse slab strength tests are as follows:

1.   Due to the degree of axial boundary restraint provided by the slab/beam connection, the bridge unit slabs behaved as if fixed boundary conditions existed, rather than simply supported conditions, and all failed in punching.

2.   The strength of both slab types increased almost linearly with increase in slab transverse reinforcement ratio for the range of reinforcement ratios tested (see Figure I.7).   Thus, the flexural and punching shear capacity are believed to be interdependent.

3.   The control slabs with the smallest reinforcement ratio (0.19%) failed in flexure, while the slabs with medium reinforcement ratio (0.29%) failed in combined flexure and punching.   Even though the control slabs were simply supported, the slabs with the largest reinforcement ratio (0.57%) failed by punching.   Thus, increased reinforcement caused the failure mode to change from purely flexural to punching, with the possibility that arching action is caused by internal, as well as external, lateral restraint.

4.   Punching capacity predicted using AASHTO rules (Equation 3.1) is a conservative lower limit strength for the bridge unit slabs.

5.   Predicted slab strengths in flexure were determined using yield line theory.   The yield patterns assumed provided failure loads (Equations 3.2 through 3.10) which bracketed the experimental failure loads.

6. In the design of bridge unit slabs, conservative strengths in punching and flexure are obtained from the punching equation given in the AASHTO Specification, and from yield line analysis. However, several yield line solutions must be developed so that a least upper bound solution is obtained.

4.2.2 Shear Connector Specimen Tests

During the initial sustained loading period of the first unit, it was surmised that creep at welded stud shear connectors would be greater than at channel shear connectors because of the difference in aspect ratio. To study this hypothesis, four pushout-type specimens were constructed of similar materials as the bridge unit. Two specimens had channel connectors and two had welded stud connectors like those found in the bridge units.

Shear connector tests are discussed in Section 3.3. Each specimen was loaded for 810 days under 48 kips sustained loading, so that creep and slip could be observed. After this sustained loading period, the specimens were loaded to failure to quantify the strength of the shear connectors. Observations from the shear connector tests are as follows:

1. During sustained loading, slip was slightly higher at the channel connectors than at the stud connectors, but no distinct differences were found between the stud connector specimens and the channel connector specimens. However, the beam flanges were slightly embedded in the concrete, and the resulting effects are unknown.

2. In ultimate strength tests, the channel and stud shear connectors failed by shear in the steel, with little damage to the surrounding concrete. Thus, as was noted in Refer-

ence 6, the strength of stud shear connector tests in con-
crete of strengths greater than 4000 psi may not be limited
by the concrete strength, but by connector strength. How-
ever, the AASHTO Specification does not consider failure of
a shear connector without adjacent concrete crushing a limit
state. This design may result in unconservative shear
connector design, when high strength concrete is used in
composite girders.

3. The strength of the channel shear connectors was
accurately predicted by Equation 3.11. However, the 28 day
concrete compressive strength was used, instead of the
actual 810 day strength. The 810 day strength was unknown,
but was certainly greater than the 28 day strength. If the
actual strength would have been used, an unconservative
prediction would probably have resulted.

4. The strengths of the stud shear connectors were
predictable by Equation 3.12, but only with a limiting
concrete compressive strength of 4000 psi.

5. The 28 day compressive strength used in the shear
connector capacity equation provided by AASHTO should be
limited to 4000 psi. Based on the limited test data of this
study, this limitation will result in an accurate estimate
of stud type connector strength and a conservative result
for channel type connectors.

REFERENCES

1. Standard Specification for Highway Bridges. 12th Edition, American Association of State Highway Officials, 1977.

2. Hendrick, T., "Experimental Investigation of a Prestressed Steel-Concrete Slab Bridge Unit". Masters Thesis, University of Oklahoma, 1983.

3. Majumdar, A., "Behavior of a Prestressed Steel Beam-Concrete Slab Composite Bridge Unit Under Sustained Loading". Masters Thesis, University of Oklahoma, 1985.

4. Branson, D.E., Deformation of Concrete Structures. New York: McGraw Hill, 1977.

5. Wang C., and C. Salmon, Reinforced Concrete Design, Third Edition. New York: Harper and Row, 1979, p. 498.

6. Ollgaard, J., Slutter, R., and J. Fisher, "Shear Strength of Stud Connectors in Lightweight and Norman-Weight Concrete", AISC Engineering Journal, Vol. 8, No. 2, April, 1971, pp. 55-64.

7. H. Hayden, et.al., Structures and Properties of Materials, Volume III. New York: Wiley & Sons, 1965, p. 5.

8. Slutter, R., and G. Driscoll, "Flexural Strength of Steel-Concrete Composite Beams", Journal of the Structural Division, ASCE, Vol. 91, No. ST2, April 1965, pp. 71-99.

9. Salmon, C., and J. Johnson, Steel Structures, Second Edition. New York: Harper and Row, 1980, p. 933.

10. Westergaard, H., "Computation of Stresses in Bridge Slabs Due to Wheel Loads", Public Roads, March, 1932.

11. Braestrup, M., "Dome Effect in RC Slabs: Rigid Analysis", Journal of the Structural Division, ASCE, Vol. 106, No. ST6, June 1980, pp. 1237-1262.

12. Building Code Requirements for Reinforced Concrete (ACI 318-83), American Concrete Institute, 1983.

13. Standard Specification for Highway Bridges, 13th Edition, American Association of State Highway and Transportation Officials, 1983.

14. ASCE-ACI Committee 426, "The Shear Strength of Reinforced Concrete Members-Slabs", Journal of the Structural Division, ASCE, Vol. 100, No. ST8, August 1974, pp. 1543-1591.

15. Mills, G., "The Yield Line Theory: A Programmed Text". London: Concrete Publications Ltd., 1970.

16. Yitzaki, D., "Punching Strength of Reinforced Concrete Slabs", Journal of the American Concrete Institute, Vol. 63, May, 1966, pp. 527-542.

APPENDIX A

SPECIMEN DETAILS FOR FIRST BRIDGE UNIT

Concrete
Slab Deck

Longitudinal and Transverse
Reinforcement (#4 Bars-Grade 60)

7 1/2"

W21x50
A588-Grade 50
Steel Beams

A.1

Shear
Connectors

Steel
Beams

54'-0"

1'-6"   3'-9 1/2"   1'-6"

6'-9 1/2"

(a) Elevation

(b) Section A-A
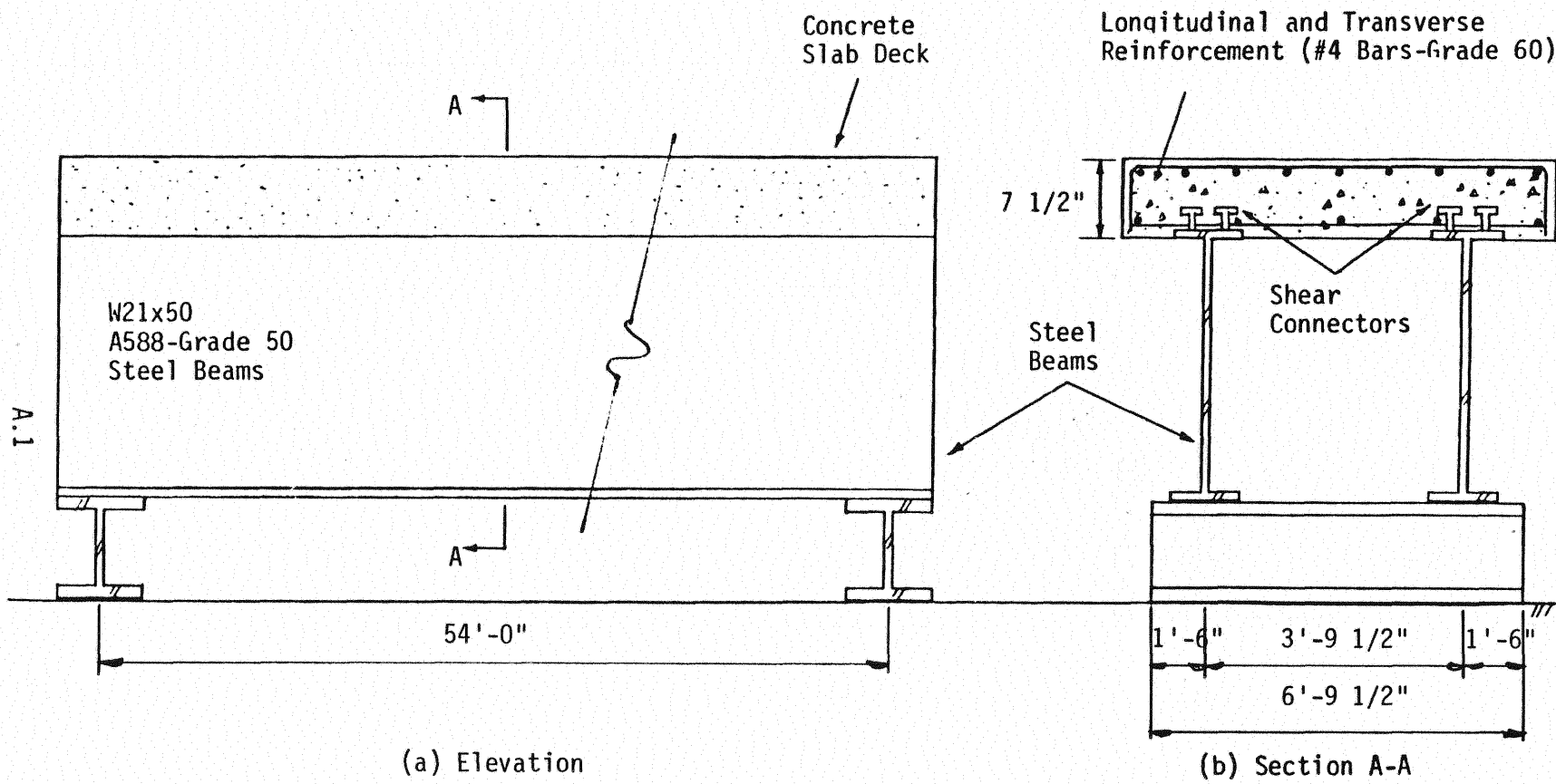
Figure A.1   Overall Dimensions of First Bridge Unit

A.2

2-3"x3"x1/4"
Steel Angles

@ All Four
Ends and
Center Overlap

6"   18"-0"   18'-0"   18'-0"   6"

55'-0"

(a) Steel Angle Diaphragm Locations

(b) Section A-A
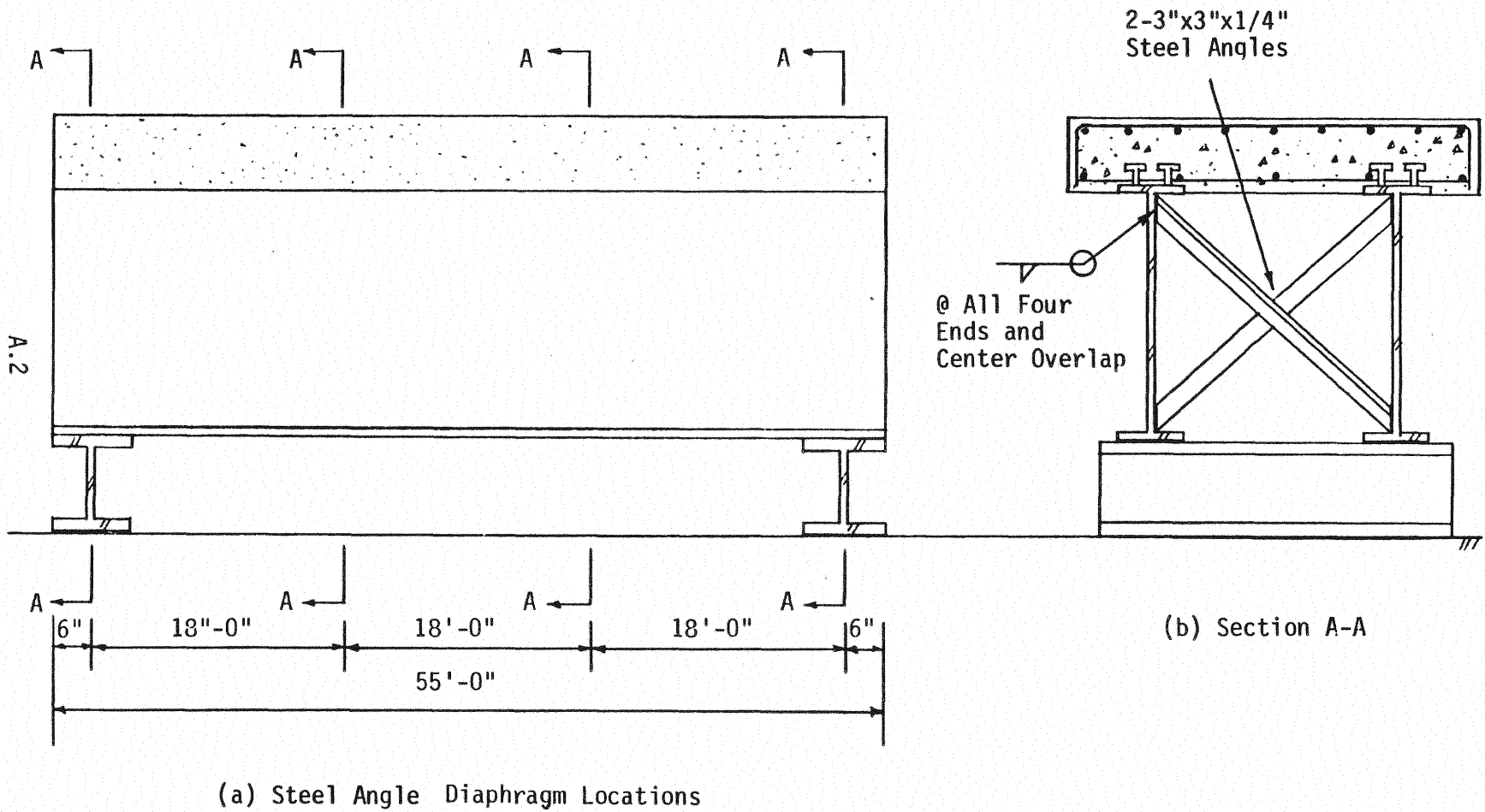
Figure A.2   Cross-Frame Diaphragm Locations on Bridge Unit
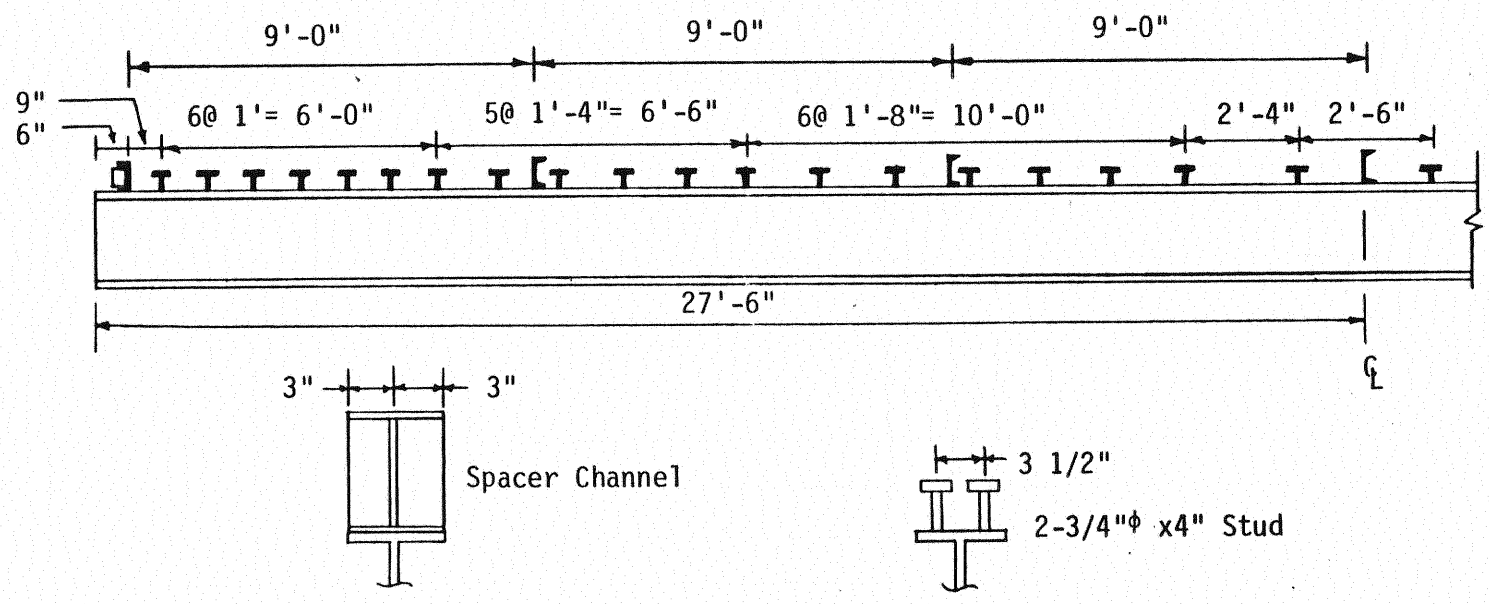
Figure A.3   Shear Connector Details Used for First Bridge Unit

Transverse Reinforcement

Longitudinal Reinforcement

A

A

2"

6@1'-4 1/2"=8'-3"

9@11"=8'-3"

19@5 1/2"=8'-8 1/2"

2 1/4"

3@5 1/2"=1'-4"

27-6"

6 1/4"
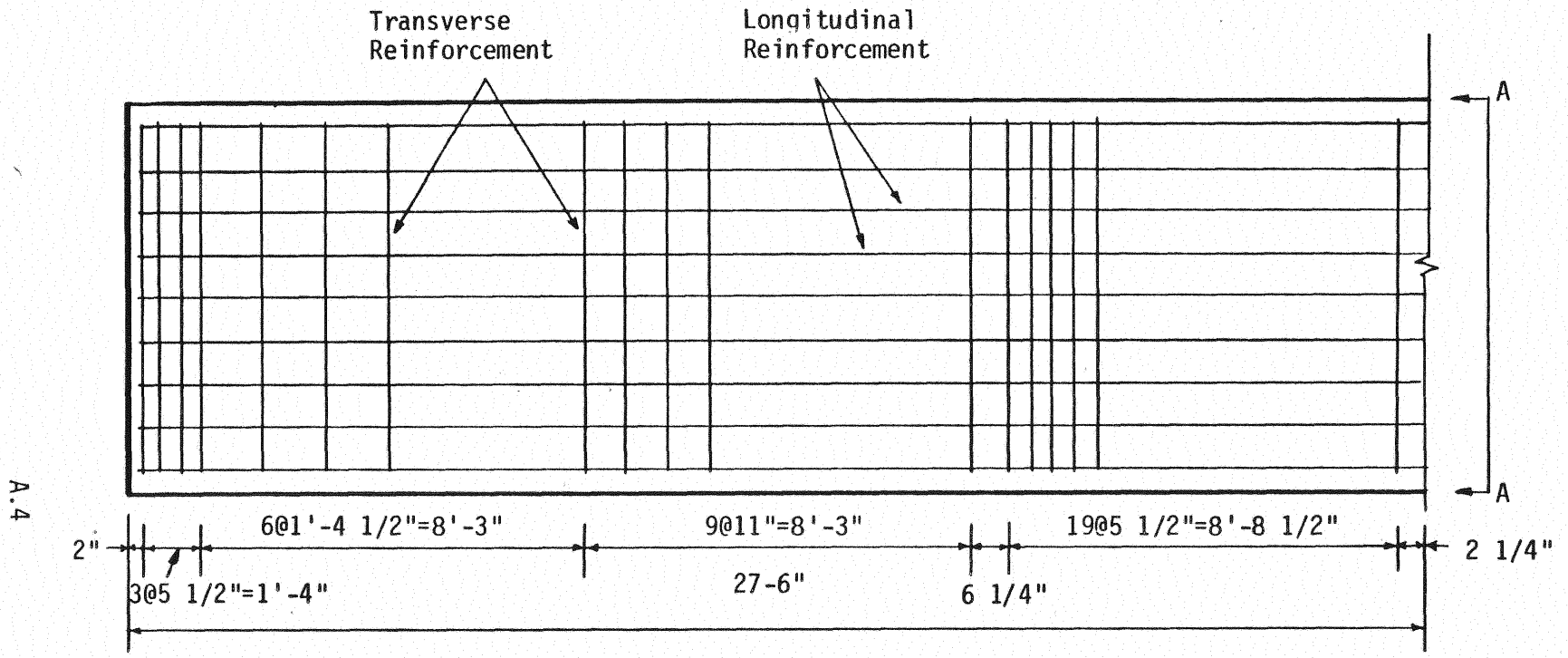
(a) Plan View Bar Spacings

Figure A.4 Reinforcing Bar Details

All Reinforcement
#4 Bar - Grade 60

(b) Section A-A

Figure A.4   Reinforcing Bar Details, Continued

Rebar Areas

Concrete Slab Width $= \dfrac{81.5"}{2n}$

$(1-1/n)0.9"^2$

$(1-1/n)0.5"^2$

4.75"

7"

7.5"

0.5"

1.25"

W21x50 Steel Beam

Concrete Strip Width $= \dfrac{68.4"}{2n}$

y
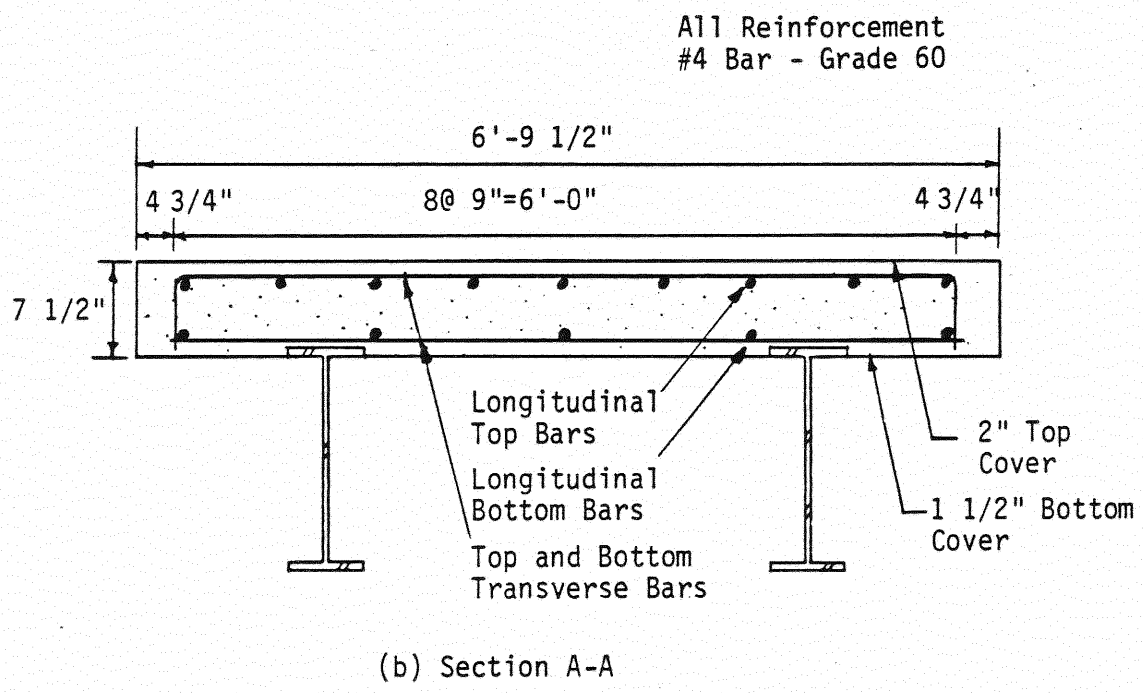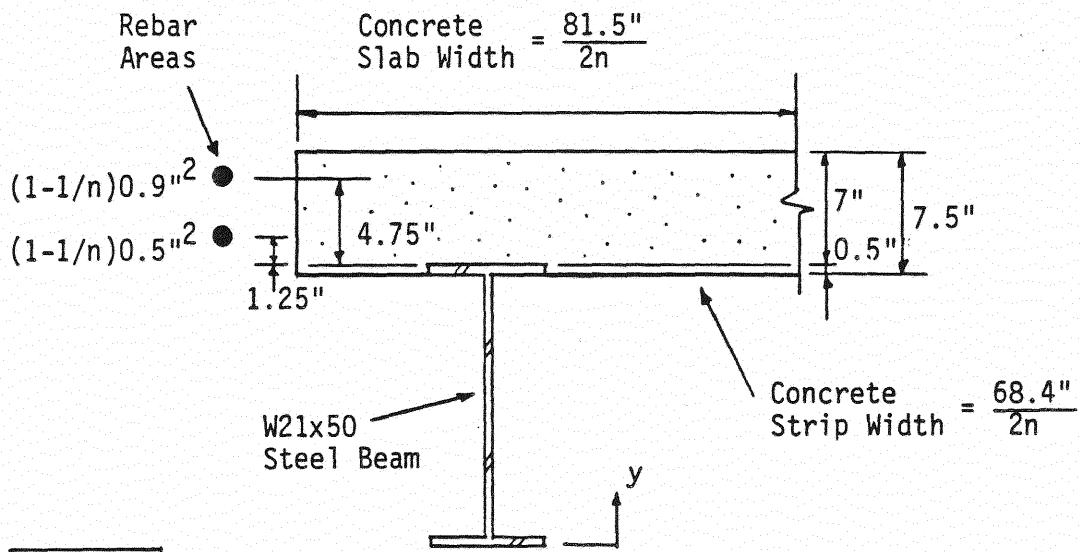
$n = 6.64$

	$A(in^2)$	$y(in)$	$Ay(in^3)$	$Ay^2(in^4)$	$I_o(in^4)$
Concrete	42.90	24.33	1043.8	25394.6	175.42
Concrete Strip	2.60	20.58	53.5	1101.2	-
Top Bars	0.77	25.58	19.7	503.8	-
Bottom Bars	0.43	22.08	9.5	209.6	-
Steel Beam	14.70	10.42	153.2	1596.1	984.0
Totals	61.40		1279.7	28805.3	1159.42

$$I_x = I_o + \Sigma Ay^2 = 29964.7 in^4$$

$$\bar{y} = \frac{\Sigma Ay}{\Sigma A} = 20.83 in$$

$$I/2 = I_x - A\bar{y}^2 = 3293.2 in^4$$
$$I = 6586.0 in^4$$

Figure A.5 Transformed Section Properties for First Bridge Unit

A.6

APPENDIX B

SPECIMEN DETAILS FOR SECOND BRIDGE UNIT
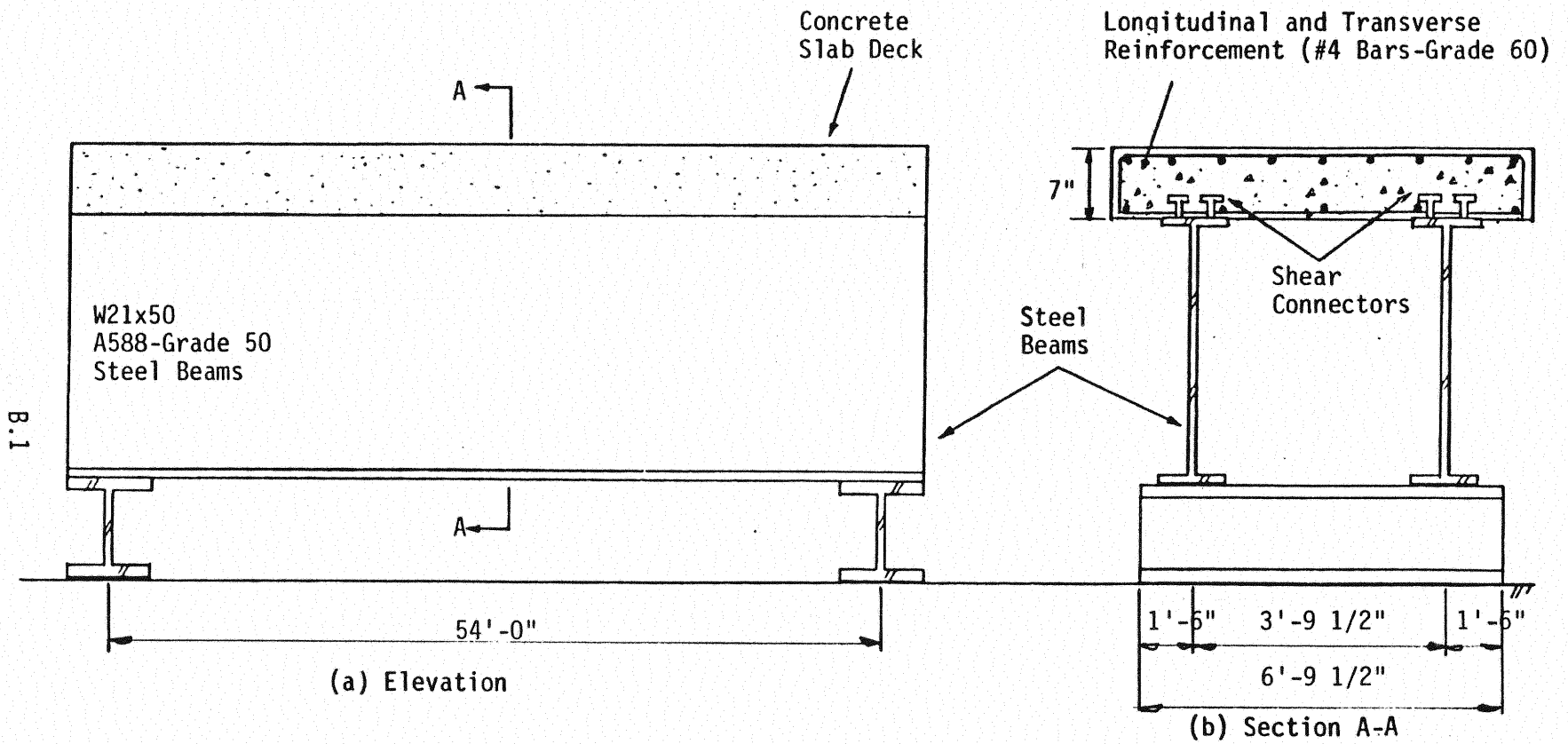
Figure B.1 Overall Dimensions of Second Bridge Unit

2-3"x3"x1/4"
Steel Angles

@All Four
Ends and
Center Overlap

A   A   A   A

A   A   A   A

|6"| 18'-0" | 18'-0" | 18'-0" |6"|

55'-0"

(b)   Section A-A

(a) Steel Angle Diaphragm Locations
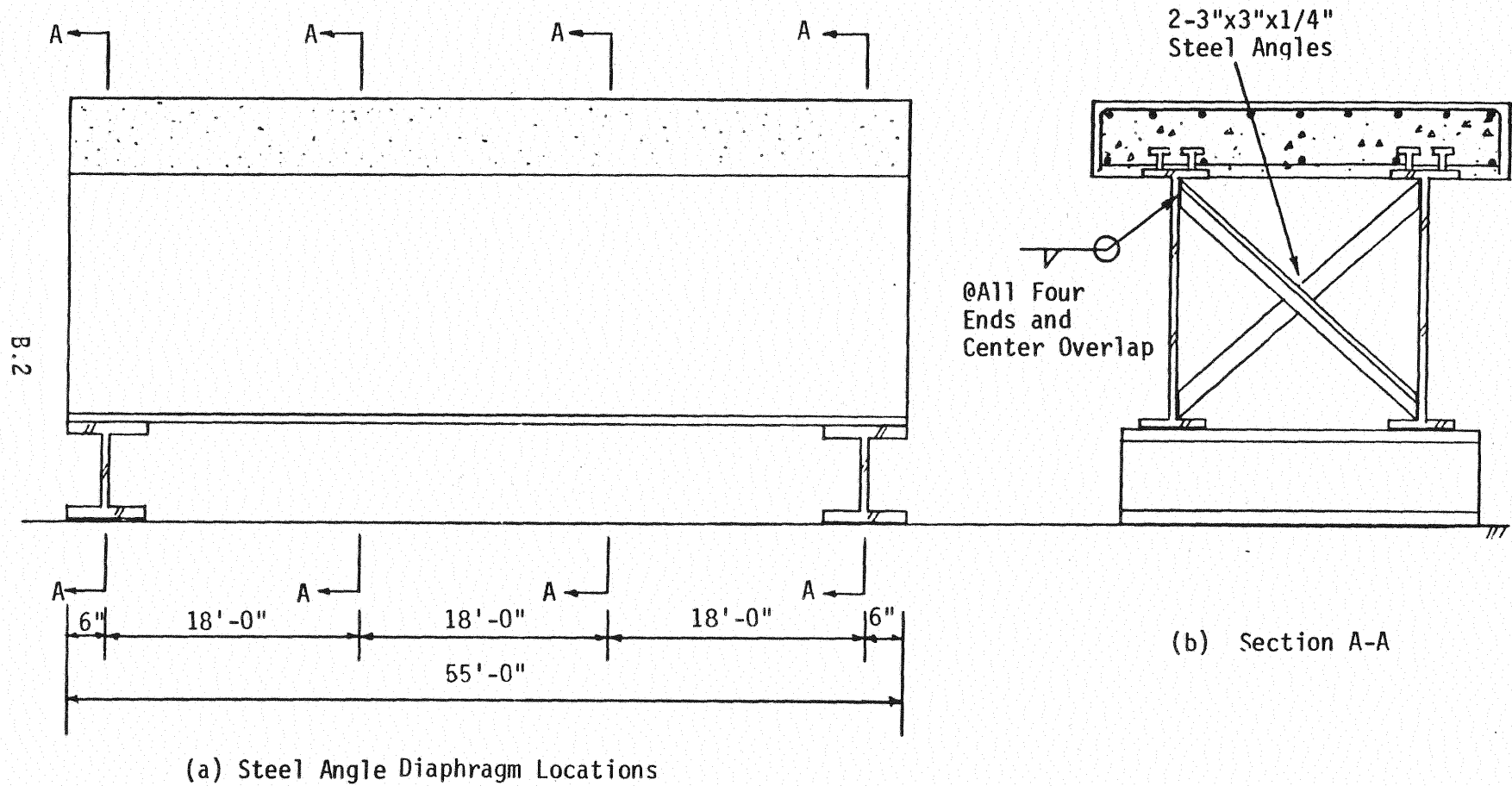
Figure B.2   Cross-Frame Diaphragm Locations on Bridge Units

9'-0"   9'-0"   9'-0"

9"
6"

6@ 1'=6'-0"   5@ 1'-4"=6'-6"   6@ 1'-8"=10'-0"   2'-4"   2'-6"

27'-6"

℄

7"   3"x3"x1/4"
End Angle

3 1/2"
2-3/4" φx4" Stud
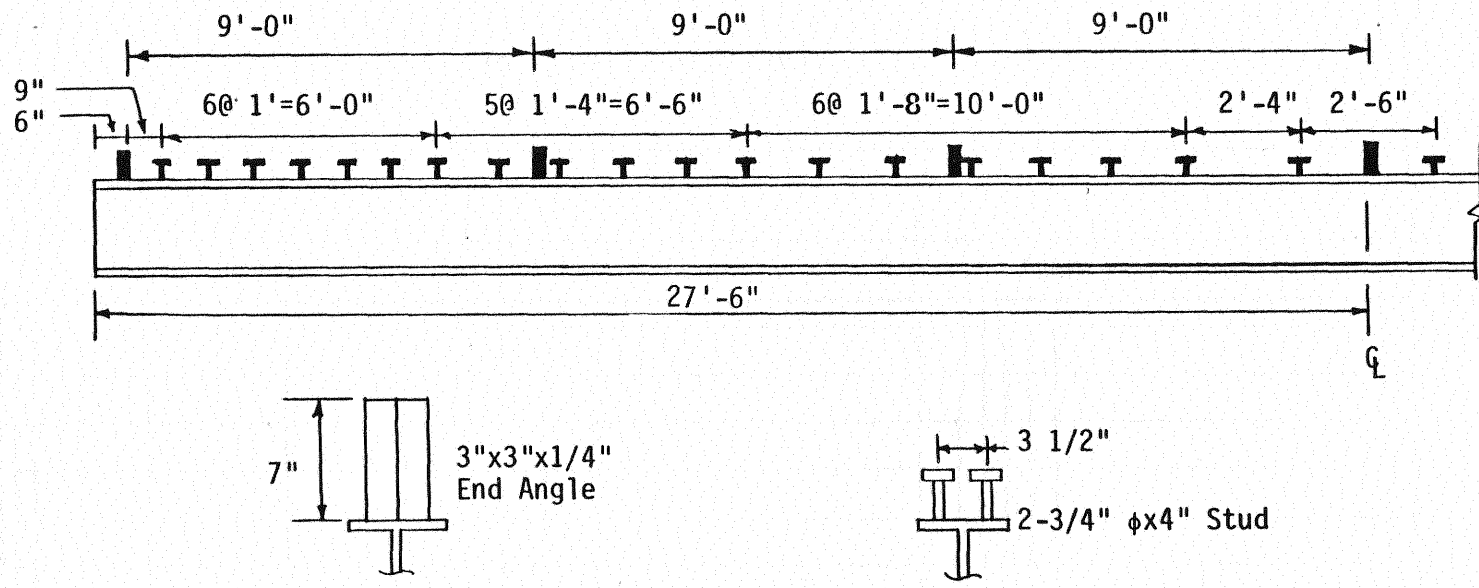
Figure B.3   Shear Connector Details Used for Second Bridge Unit

Transverse Reinforcement

Longitudinal Reinforcement

A

A

B.4

2"

3@5 1/2"=1'4"

6@1'-4 1/2'=8'-3"

9@11"=8'-3"

6 1/4"

19@5 1/2"=8'-8 1/2"

2 1/4"

27'-6"
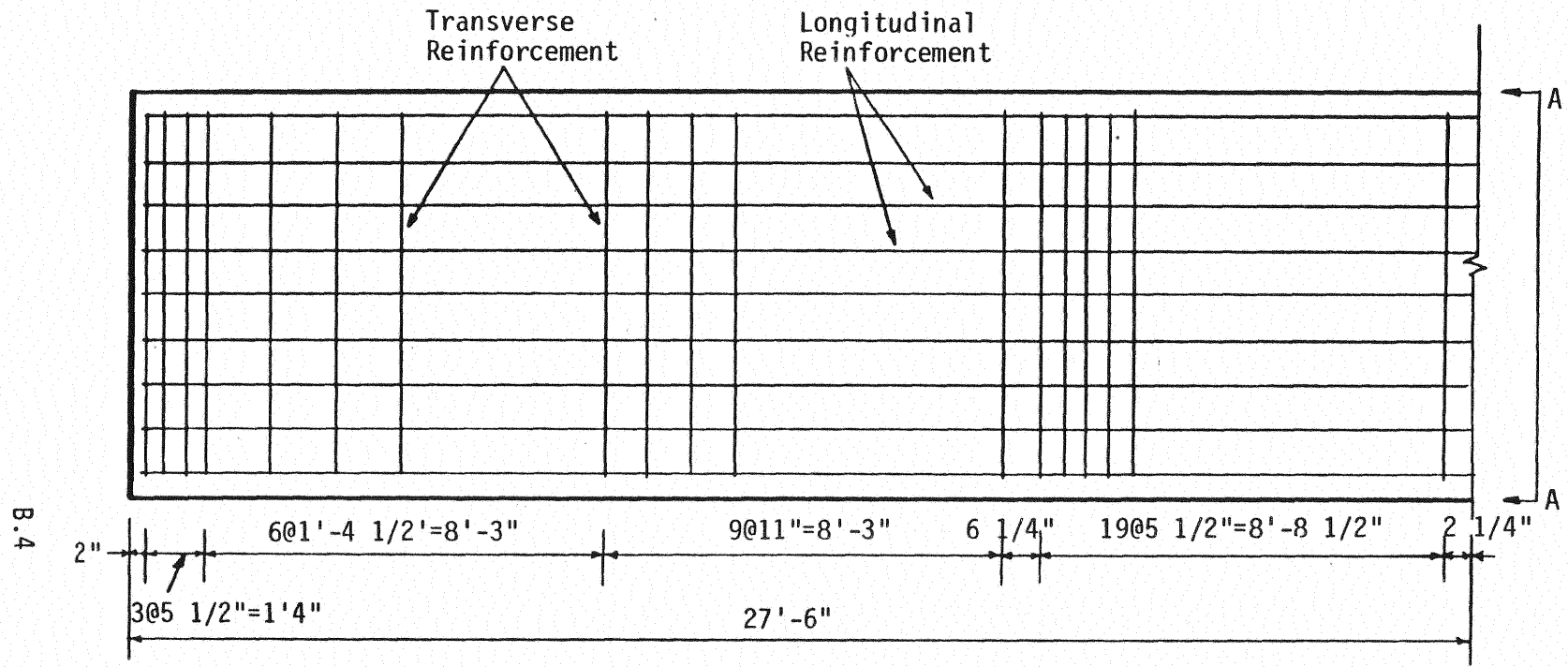
(a) Plan View Spacings

Figure B.4 Reinforcing Bar Details

All Reinforcement
#4 Bar - Grade 60

6'-9 1/2"

4 3/4"   8@9"=6'-0"   4 3/4"

7"

2" Top
Cover
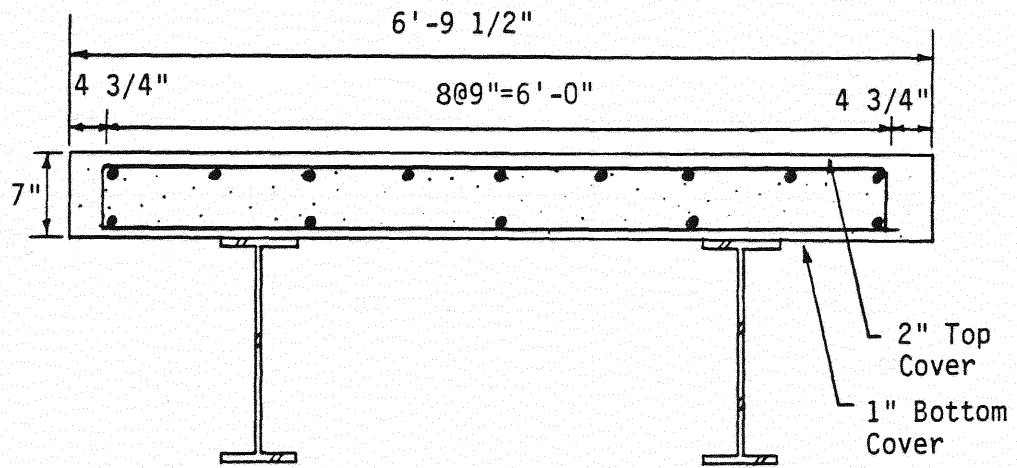
1" Bottom
Cover

(b) Section A-A

Figure B.4   Reinforcing Bar Details, Continued

B.5

Rebar Areas

Concrete Slab Width $= \dfrac{81.5"}{2n}$

$(1-1/n)0.9"^2$

$(1-1/n)0.5"^2$

4 3/4"

1.25"

7"

W21x50 Steel Beam

y
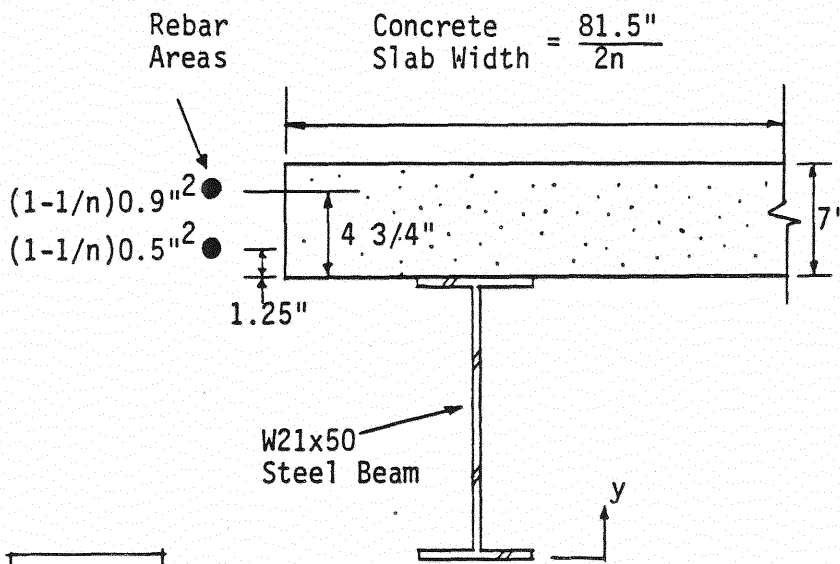
n = 5.44

	$A(in^2)$	$y(in)$	$Ay(in^3)$	$Ay^2(in^4)$	$I_o(in^4)$
Concrete	52.44	24.33	1275.9	31041.8	214.12
Top Bars	0.73	25.58	18.8	480.9	-
Bottom Bars	0.41	22.08	9.0	198.9	-
Steel Beam	14.70	10.42	153.2	1596.1	984
Totals	68.3		1456.9	33317.7	1198.12

$I_x = I_o + \Sigma Ay^2 = 34516.0 in^4$

$\bar{y} = \dfrac{\Sigma Ay}{\Sigma A} = 21.33 in$

$I/2 = I_x - A\bar{y}^2 = 3439.0 in^4$

$I = 6878.0 in^4$

Figure B.5 Transformed Section Properties for Second Bridge Unit

APPENDIX C

TEST SETUPS

APPENDIX C

C.1 Sustained Loading Test Setup

During the sustained loading periods of Phases I and IV, the bridge unit was located outdoors and was simply supported with ends resting on elastomeric pads. To simulate an asphalt overlay of 40 psf, the concrete deck was loaded with 33 lb. concrete blocks as shown in Figure C.1.1.

Strain gages were attached to the steel beams and to both longitudinal and transverse reinforcing bars during fabrication of the unit as shown in Figure C.1.2. After the initial curing period, but before the unit was turned over, two 10 inch gage length extensometers were attached to the concrete slab to measure strain (see Figure C.1.3). The extensometers were later replaced with concrete strain gages as shown in the same figure. After the unit had been placed outside Fears Laboratory, two displacement transducers were mounted at the midspan of the unit as shown in Figure C.1.4. Thermometers were also placed on the steel bottom flanges and a thermometer was embedded in the concrete so that temperature data could be recorded.

During the periods of sustained loading, strain, displacement, and temperature data, along with weather conditions, were periodically recorded. Also periodic camber measurements were made with a surveyor's level.

331b Concrete Blocks
(40psf)

A

Bridge
Unit

C.2

A

Elastomeric Bearing Pad

Support Beam
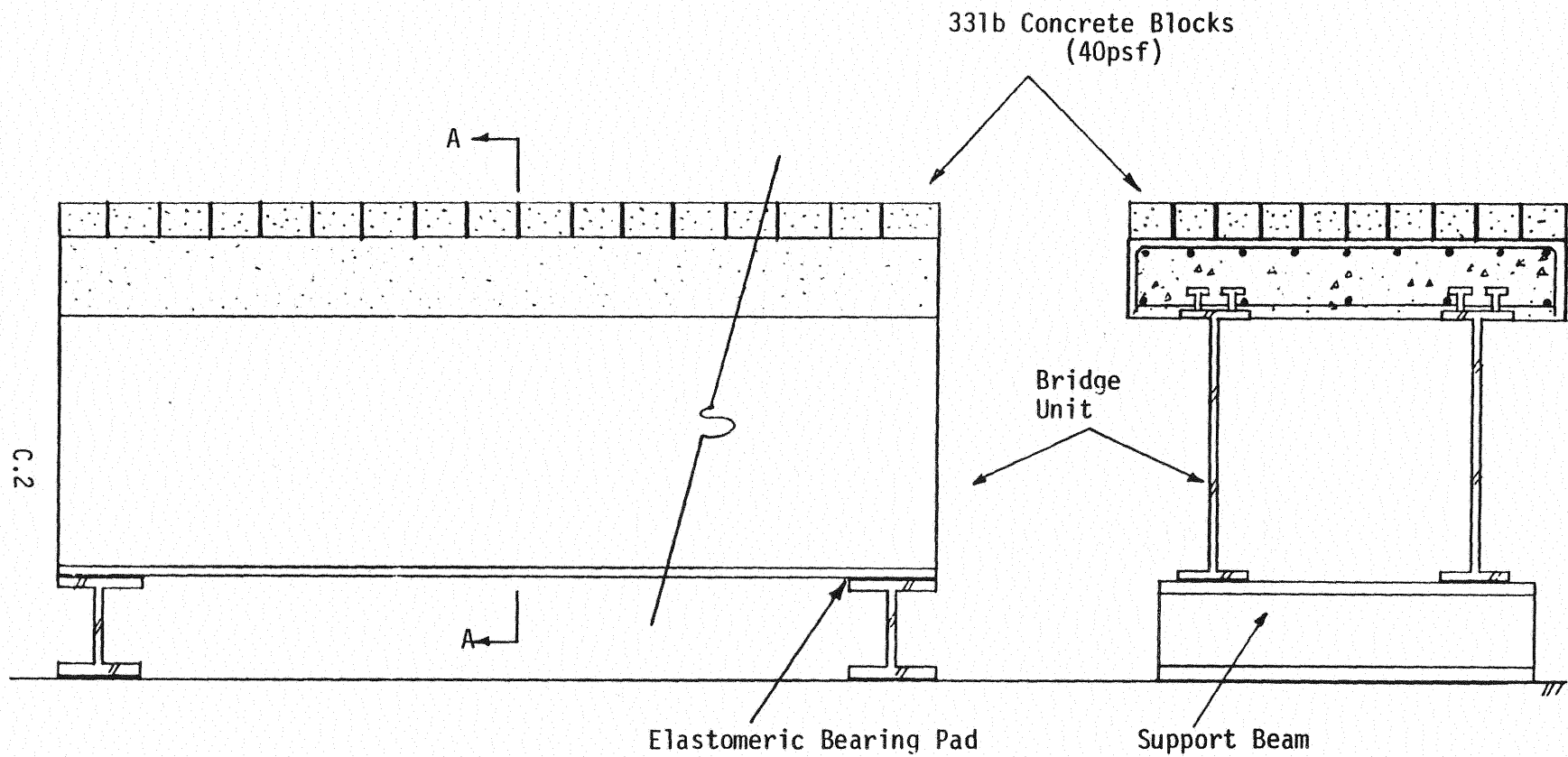
(a) Elevation of Loaded Bridge Unit

(b) Section A-A

Figure C.1 Sustained Loading Test Setup
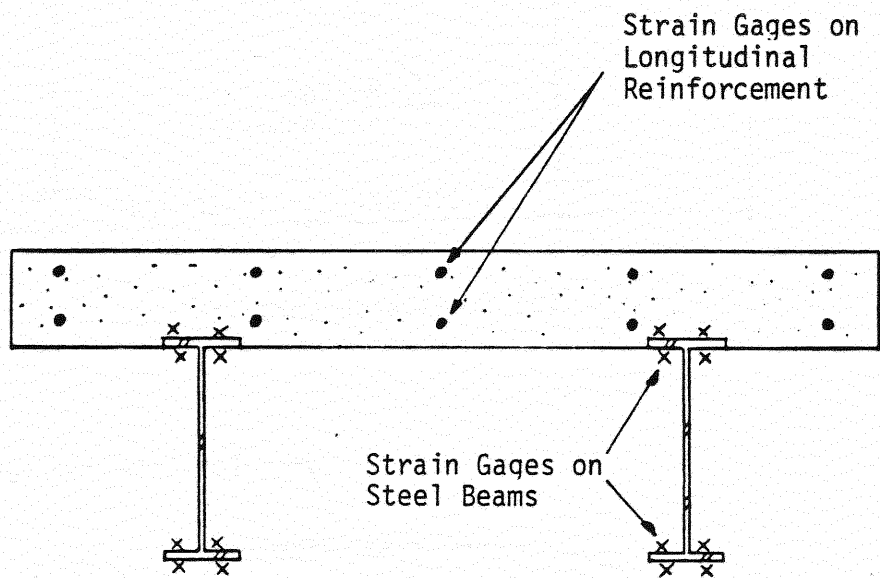
Figure C.2 Location of Steel Strain Gages on Bridge Unit
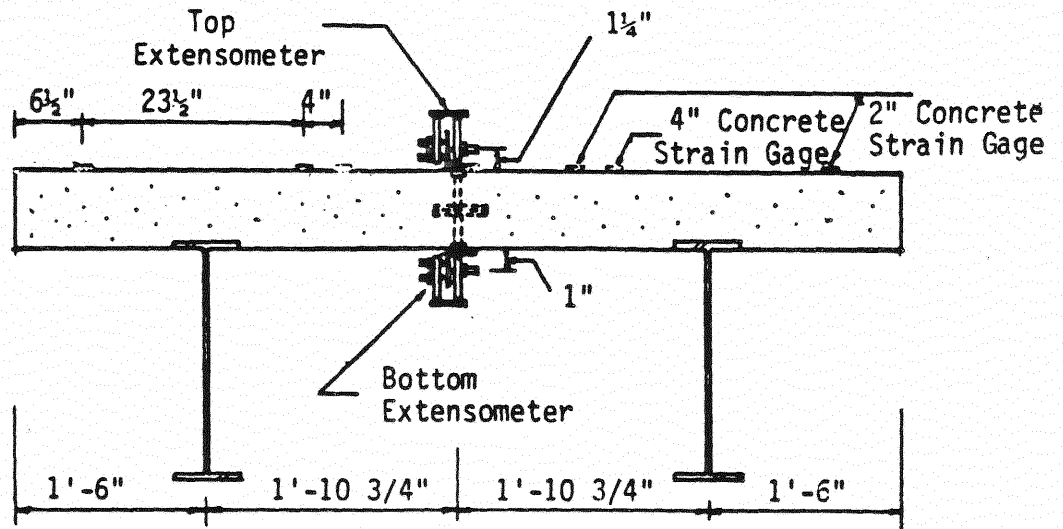
(a) Transverse Location
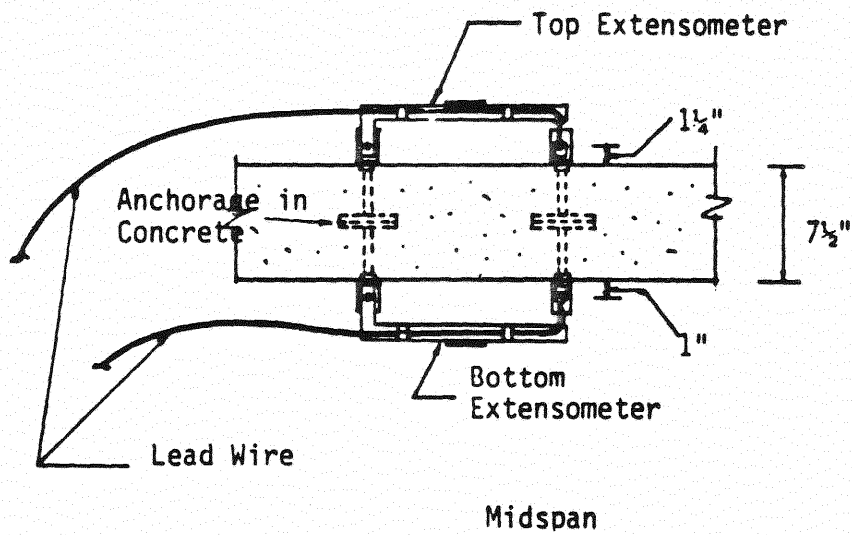
Midspan

(b) Longitudinal Location (at Midspan)

Figure C.3   Details of Extensometer and Location of Concrete
             Strain Gages
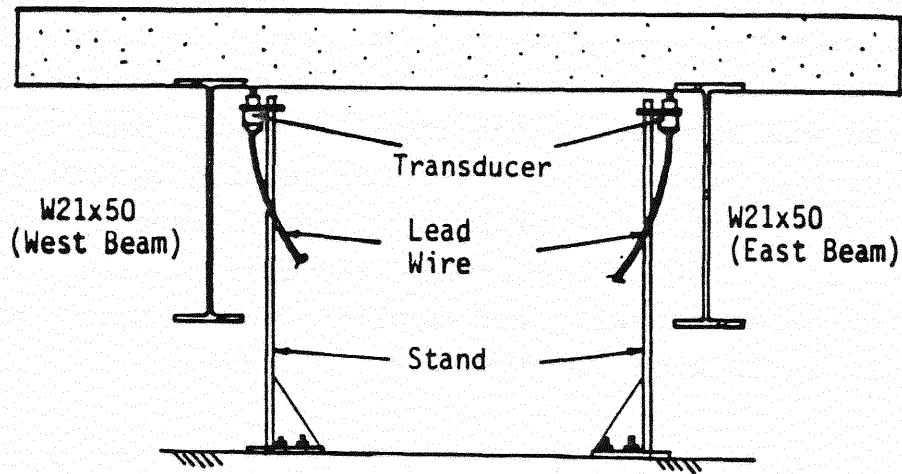
Figure C.4 Location of Deflection Transducers
on Bridge Unit (at Midspan)

C.2 Fatigue Loading Test Setups

The description of the fatigue loading test setups is applicable to both bridge units, except that the second bridge unit was subjected to only 500,000 cycles of HS-20 loading; whereas the first bridge unit was subjected to 2,000,000 cycles of HS-20 loading, 2,000 cycles of HS-30 loading, and 100,000 cycles of unbalanced loading.

In the fatigue loading test phases, the bridge unit was tested inside Fears Laboratory. The unit was simply supported on neoprene pads bearing on support beams, which transferred the load to the reaction floor, as shown in Figure C.5(a). During HS-20 magnitude repeated loading, the load was applied to the upper spreader beam with a 55 kips capacity closed-loop hydraulic testing system actuator. The frequency of repeated loading cycles ranged from 0.5 to 0.7 Hertz. For HS-30 magnitude repeated loading, the load was controlled manually and applied to the upper spreader beam with a 300 kips capacity hydraulic ram.

As shown in Figure C.5(a), the load from the upper spreader beam was transmitted to two symmetrically placed lower spreader beams, which rested on wood blocks placed directly over the steel beams of the bridge unit. The lower spreader beam spacing was 14 feet, the minimum allowable wheel base of a standard HS truck as defined in the AASHTO Specification [1]. As shown in Figure C.6, the upper spreader beam was located between the steel bridge unit beams for both HS-20 (Phases II and V) and HS-30 (Phase VI) magnitude repeated loadings. The applied loads were 55 kips and 85 kips, respectively. The upper spreader beam was located directly over one bridge unit beam to simulate one line of wheel loads during the unbalanced repeated loading test, Phase VII, Figure C.7. The applied load was 27.5 kips

Hydraulic Actuator/Ram Load

Upper Spreader
Beam

Wood Block
Over Steel
Beam

Lower Spreader
Beam

A

Dial Gages
Spaced @ 9'

Displacement
Transducer

Reaction
Floor

Neoprene
Pad

Support
Beam

A

Displacement
Transducer

20'-0"   14'-0"   20'-0"

54'-0"
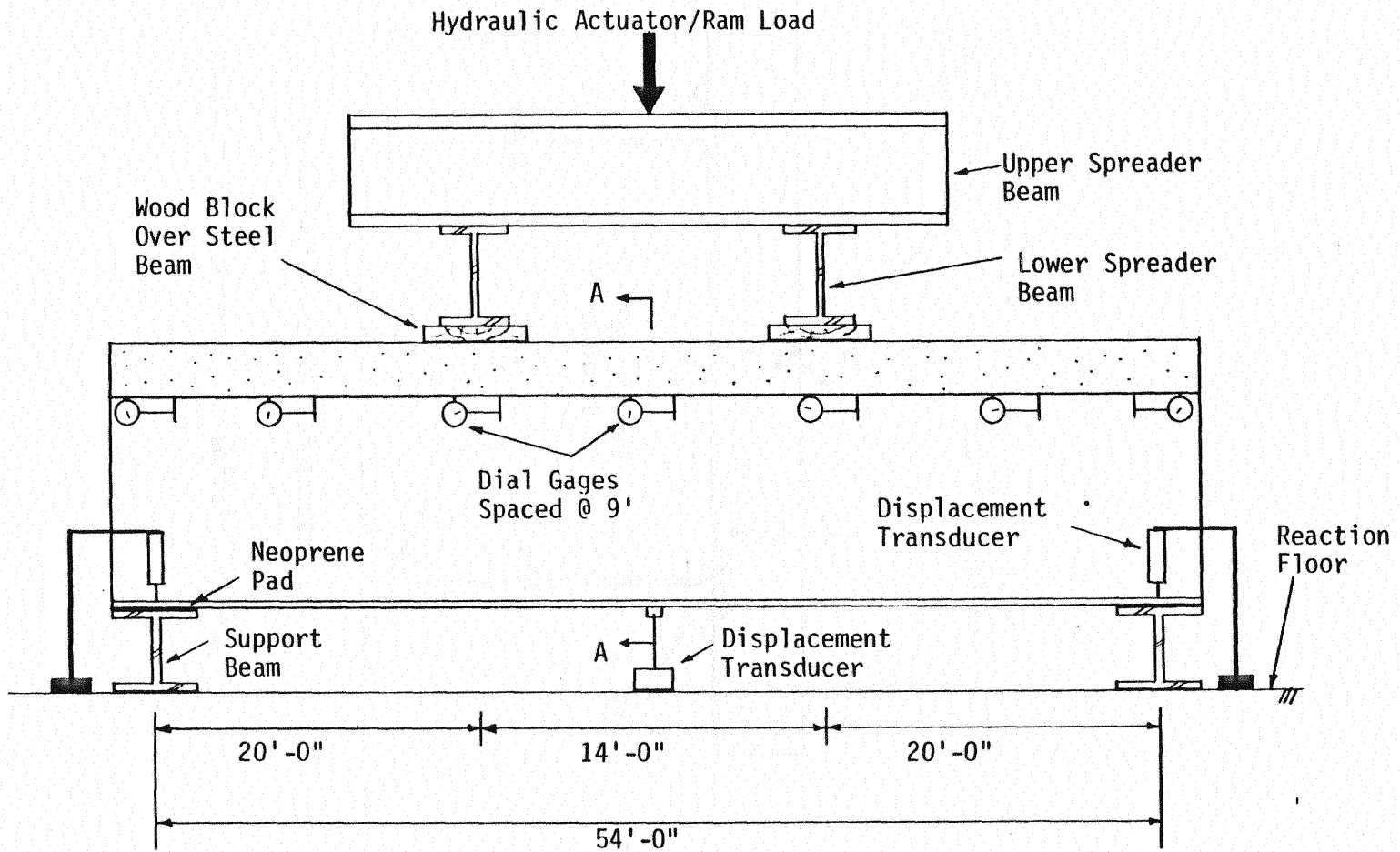
(a) Longitudinal Elevation

Figure C.5 Fatigue Loading Test Setup
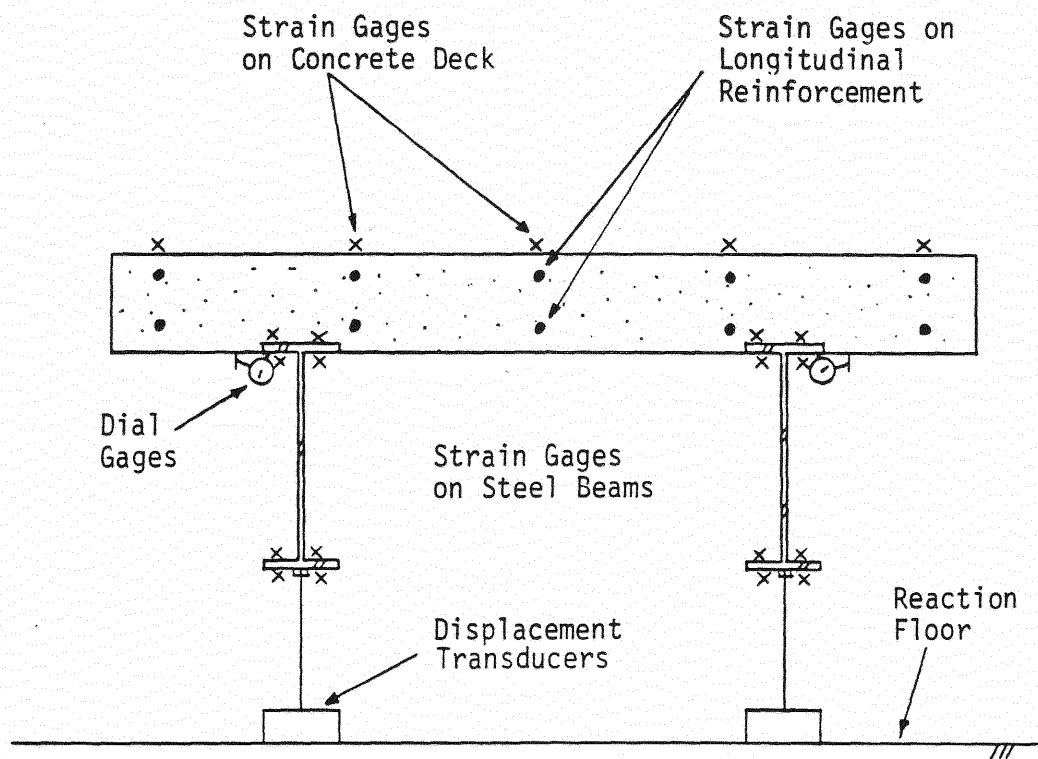
(b) Instrumentation at Section A-A

Figure C.5 Fatigue Loading Test Setup, Continued
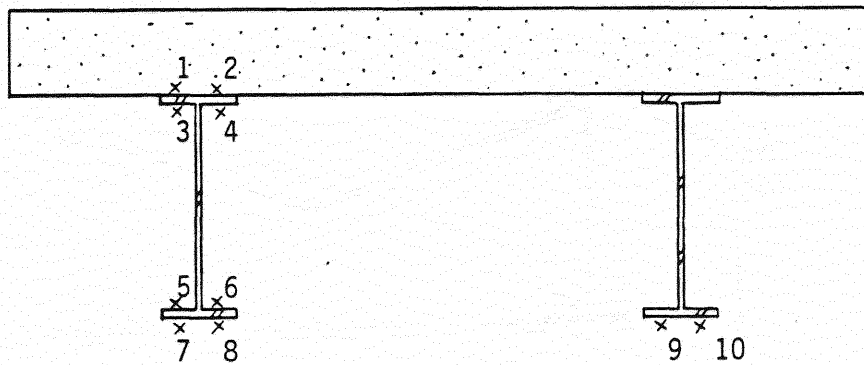
(c) Manually Monitored Instrumentation in Second Unit at Section A-A

Figure C.5 Fatigue Loading Test Setup, Continued
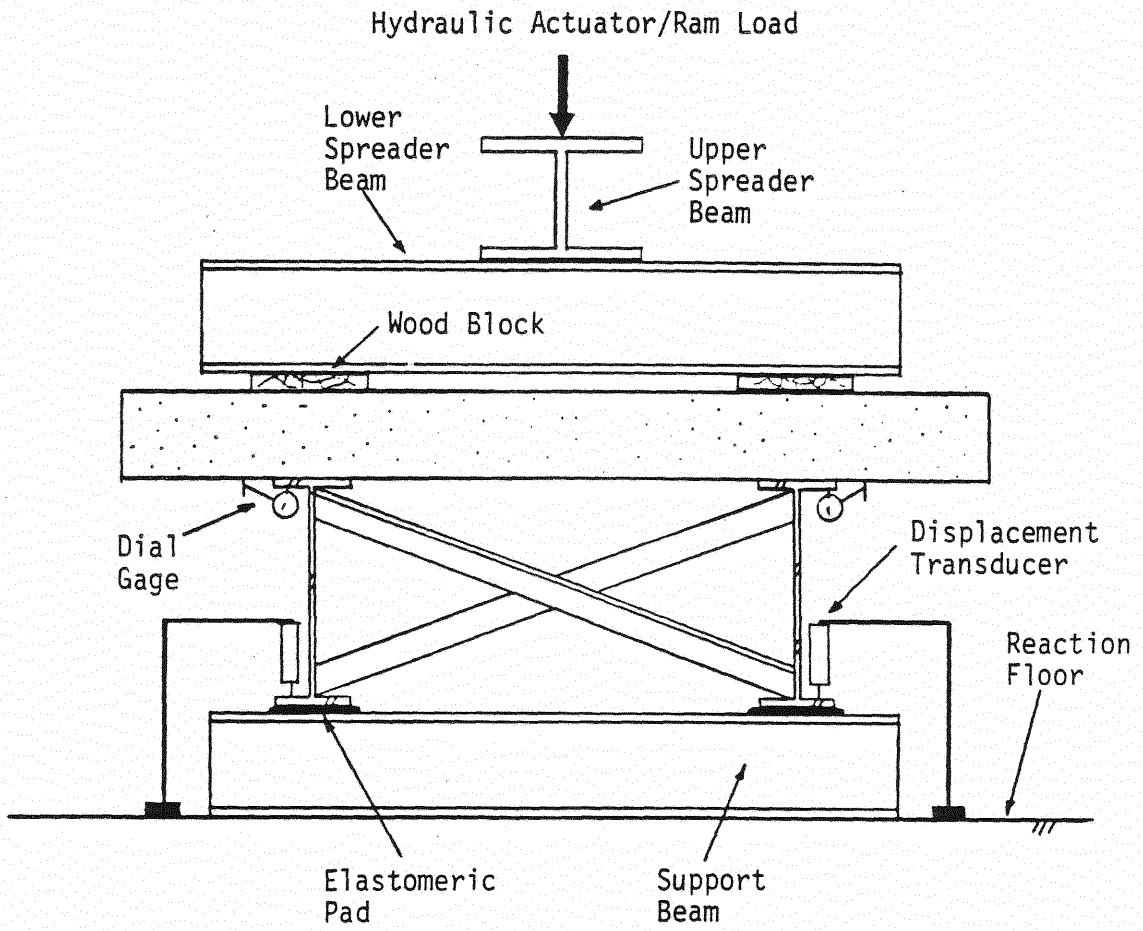
Figure C.6 End View of Test Setup for Repeated Loading Test
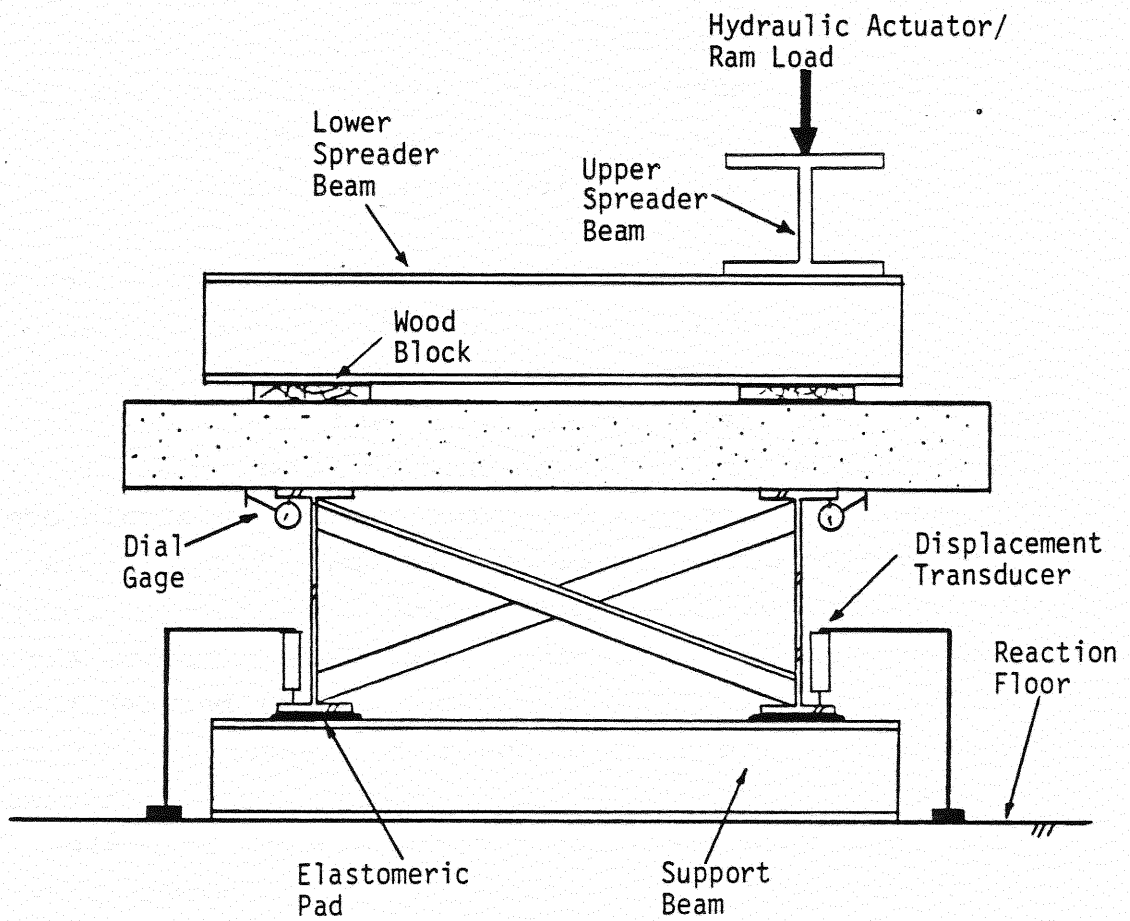
Figure C.7 End View of Test Setup for Unbalanced Repeated Loading Tests

(half of the HS-20 load) and was applied for 100,000 cycles with the hydraulic actuator.

Static cycles with all instrumentation activated, were made during each repeated loading test phase to observe the behavior of the unit at period intervals. During each static cycle, the actuator or ram load was incrementally increased to the maximum applied load level of the current test phase. Instrumentation was monitored and recorded during the tests so that any change in bridge unit behavior over the test phase duration could be detected.

Instrumentation consisted of electrical resistance strain gages, dial gages, and displacement transducers. Electrical resistance strain gages were applied to the concrete deck, reinforcing steel, and steel beam flanges at the centerline of the bridge unit as shown in Figure C.5(b). The gages were used to determine changes in strain over the cross-section during periodic checkups. Figure C.5(a) shows the location of dial gages which were placed along both sides of the unit. The dial gages were attached along the unit so that the relative movement (slip) between the steel beams and concrete slab could be measured. To measure vertical deflection of the bridge unit, displacement transducers were placed at midspan beneath both steel beams and at the ends of the beams over the neoprene pads. The arrangement is shown in Figure C.5. Displacement transducers were placed at the ends of the beams so that the midspan deflection due to compression of the neoprene pads could be measured and subtracted from the measured midspan deflection to obtain the true midspan deflection.

In addition to strain and displacement measurements discussed, the change in camber of the bridge unit was determined with a surveyors level before each static cycle.

All strain gages and displacement transducers for the first bridge unit were monitored with a computer controlled data acquisition system. The strain and displacement measurements for the second bridge unit were monitored and recorded in the same way as for the first unit, with the exception of the ten flange strain gages shown in Figure C.5(c). These ten flange gages were monitored manually with a strain indicator.

These ten gages were connected to the strain indicator with the steel beams resting in an unstressed state as shown in Figure C.8. The strain indicator was adjusted (balanced) initially and no further adjustment was made. With the change in strain referenced to the unstressed state of the beams, the measured changes in strain during both construction and testing could be compared to theoretical values, and any loss in prestress could be quantified.

C.3 Static Loading Test Setup

The static tests for both units were conducted inside Fears Lab, with the same test setup as used for the fatigue loading tests, Figure C.5. A 300 kips capacity ram was used to apply the load to the bridge unit during the overload and ultimate strength tests of the first bridge (Phases III and VIII) and the first yield test of the second bridge unit (Phase X). The instrumentation monitored during the static load tests was identical to that used in the static cycles of the fatigue loading tests (see Figures C.5 and C.6) with the addition of strain gages applied to the steel beam webs (see Figure C.9) for the ultimate strength and first yield tests of the first and second bridge units, respectively.

During the tests, the hydraulic ram load was incrementally increased and strain gages, displacement

C.14

(a) Elevation of Steel Beams

(b) Section A-A
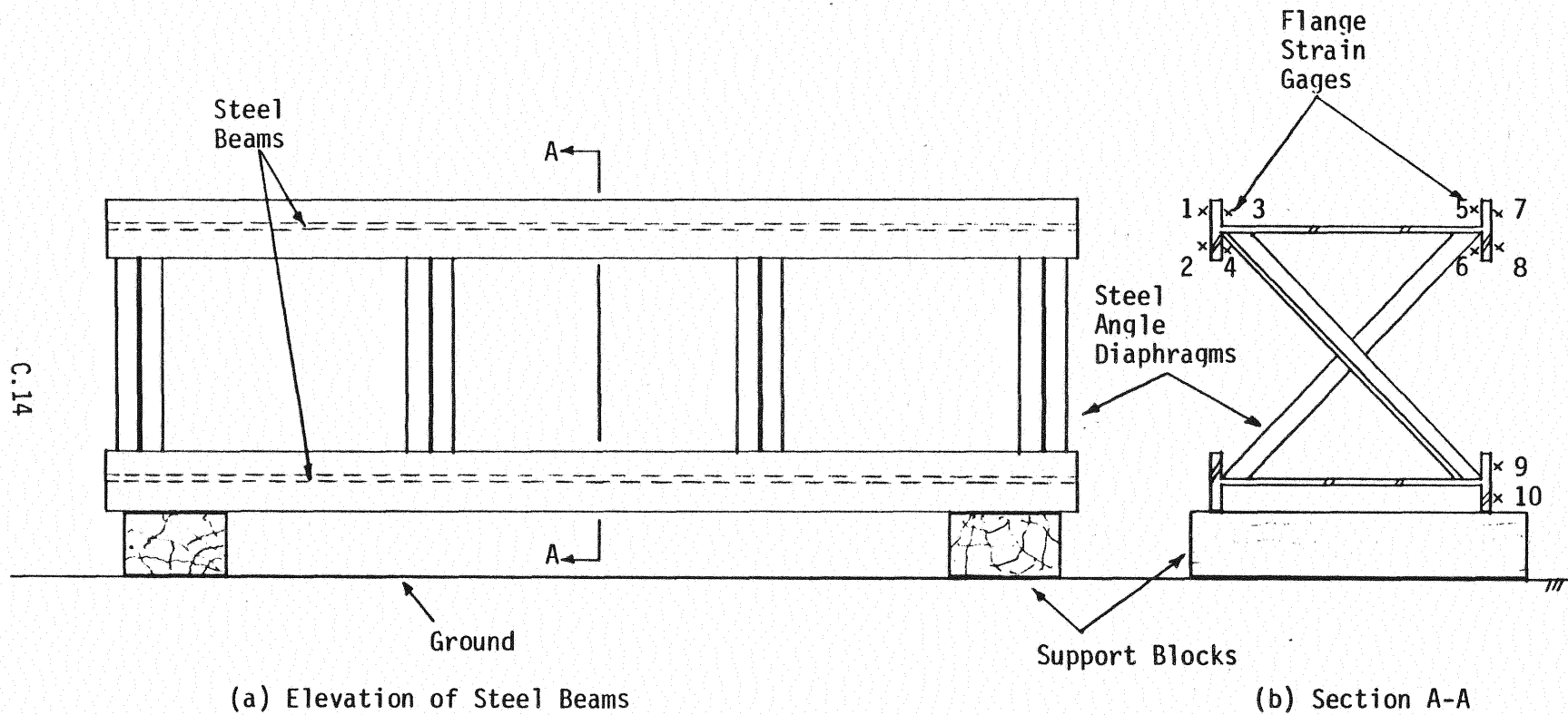
Figure C.8   Position of Second Bridge Unit Beams when
Flange Strain Gages were Initialized
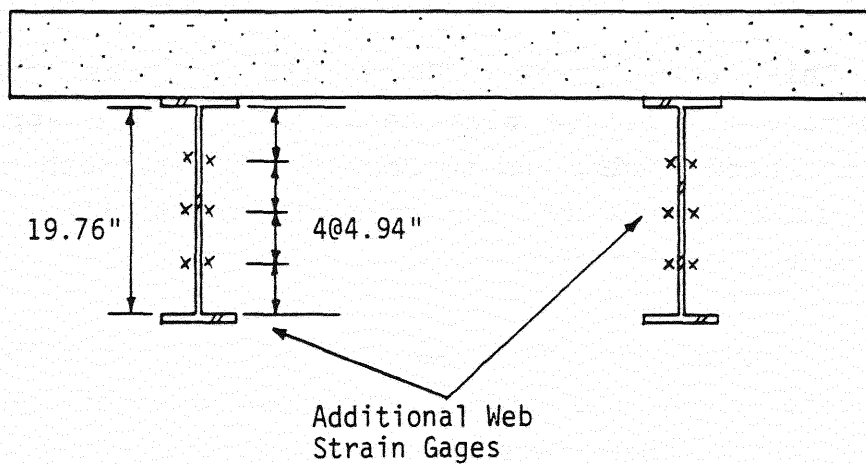
Figure C.9 Additional Web Strain Gages Used
in the Strength Tests of Both Units

transducers, and dial gages were read at each load increment. The midspan deflection and measured strain at the top of the slab and bottom beam flange were plotted at each load increment so that the behavior of the unit could be monitored throughout the test. The bridge units were visually inspected for signs of failure during the tests.

The ultimate strength test of the first unit was considered complete when a repaired flange fractured and the applied load was partially lost. The first yield strength test of the second unit was considered complete when the load-deflection and load-strain curves became nonlinear, indicating the onset of yielding of the beam bottom flanges.

C.4 Transverse Slab Strength Test Setup

This test phase (Phase XII B) was conducted to determine the bridge slab resistance to the application of concentrated loads, and to compare the strength of the first unit bridge deck to the strength of similar, but simply supported, bridge deck.

Although designed as a one-way, simply supported concrete slab, the bridge slab has greater resistance to point loads than does a simply support slab due to the considerable degree of restraint from in-plane movement and rotation at the lines of connection to the steel beams, and to the longitudinal continuity of the slab. The restraint at the slab supports is provided by shear studs, which transmit forces to the steel beams which are held in place by cross frames, as shown in Figure C.10.

In order to verify this edge and slab continuity restraint, six control slab specimens were cast from the same specified concrete mix as the first bridge unit. The
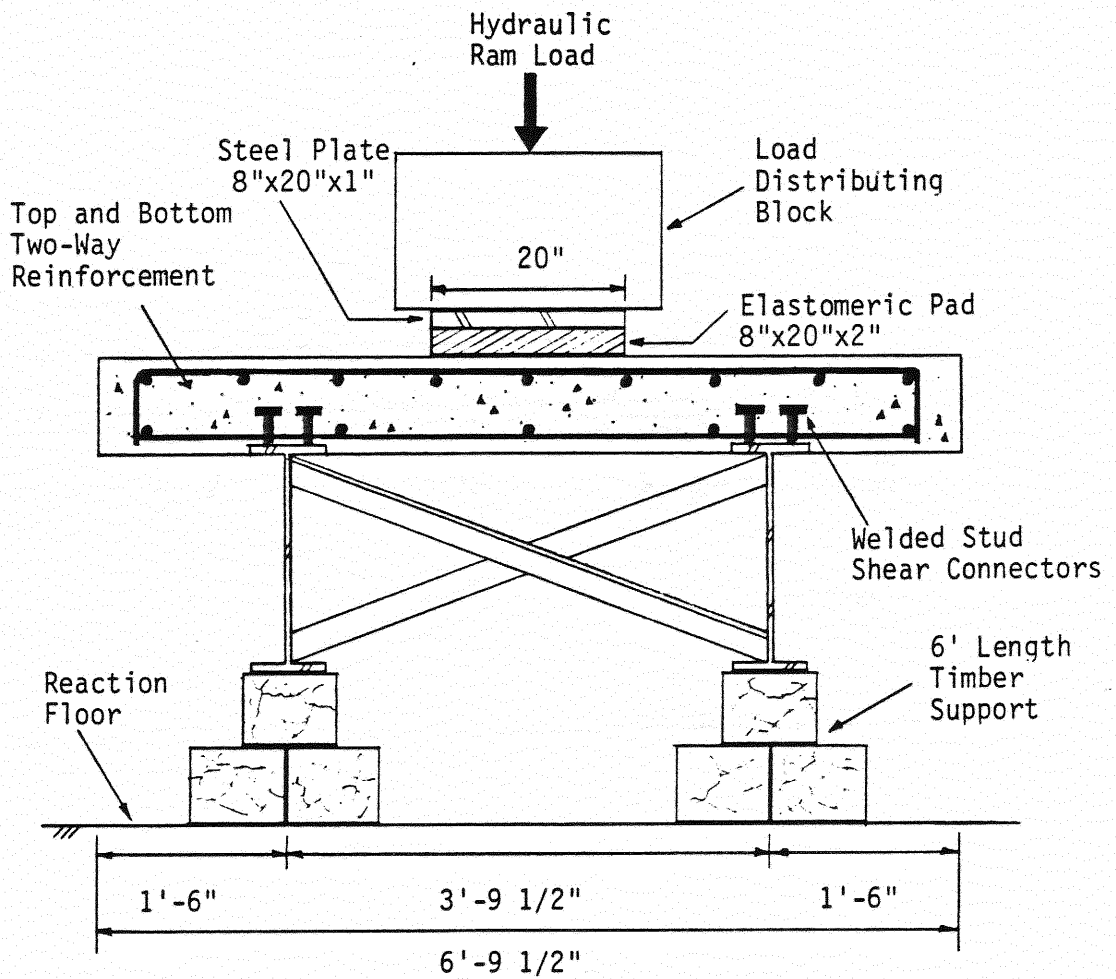
Figure C.10 First Unit Transverse Slab
Strength Test Setup
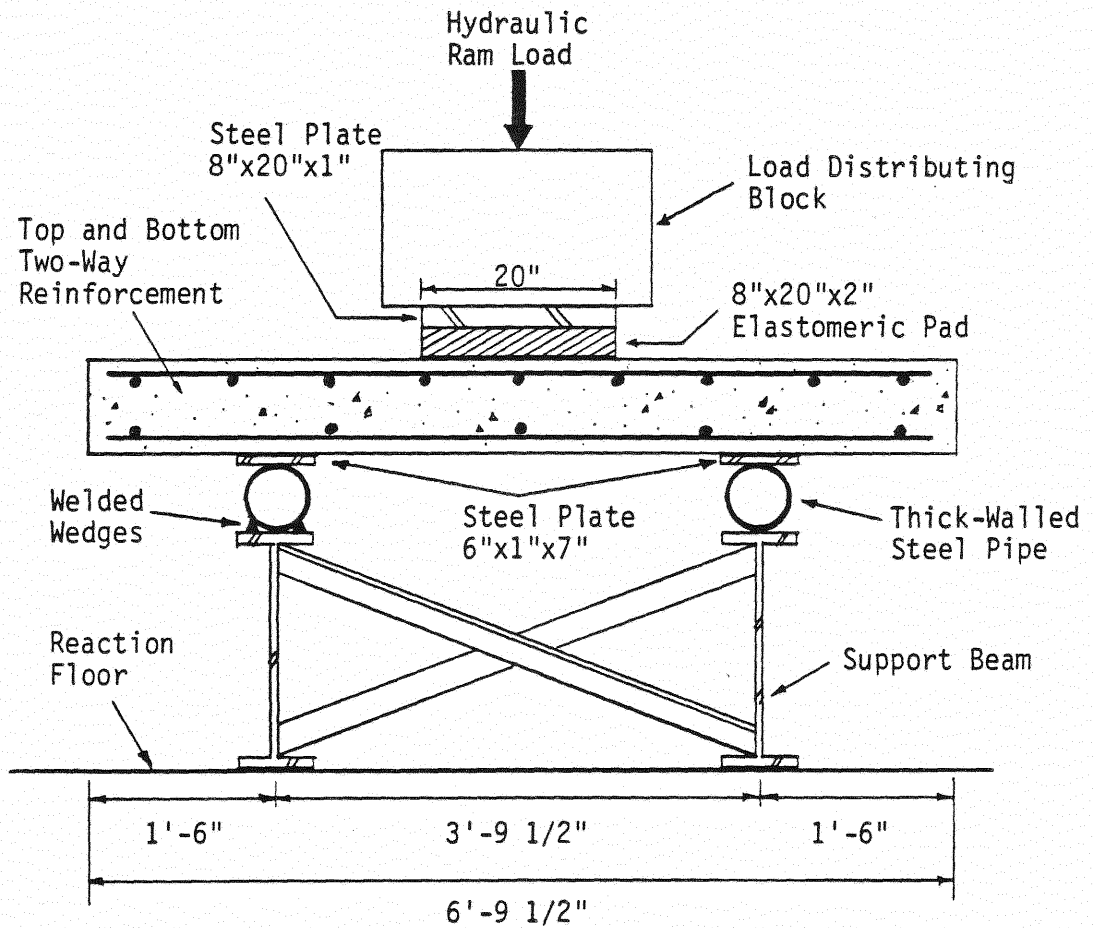
Figure C.11   Control Slab Transverse Slab
Strength Test Setup

C.18

control slabs were square, relieving longitudinal continuity, and were simply supported so the one support could translate and both supports could rotate, as shown in Figure C.11. Details of the control slabs are located in Appendix G, along with pertinent details of the slab tests on the first unit. For the bridge unit tests, the tranverse and longitudinal bar spacings, as well as the locations of the six load points, are shown in Figure G.1.

Figure C.10 shows the test setup for the bridge unit transverse slab strength tests. In order to prevent bending failure of the unit before failure of the slab, both steel beams were longitudinally supported, 3 ft. on either side of the load point by wooden timbers. The load was applied by a 300 kips capacity hydraulic ram, thru a load distributing block, and to the slab by a steel plate bearing on an elastomeric pad. The size of the load pattern was determined from the method given in Article 3.30 of the AASHTO Specification [1], for a 16 kips wheel load.

The test setup used for the control slab tests is shown in Figure C.11. The slabs were loaded in the same way as the bridge unit slabs. But the control slabs were supported in a much different way. The control slabs were approximately square, which resulted in no support from longitudinal continuity (as in the bridge unit slab), and the control slabs were supported on pipe sections, which provided no support resistance to translation or rotation.

The instrumentation for both the bridge unit and the control slabs was identical, and consisted of two extensometers, mounted to the concrete surface at the load point, as shown in Figure C.12. The shorter extensometer was used to record the effective strain at the concrete surface due to applied load. The longer extensometer was
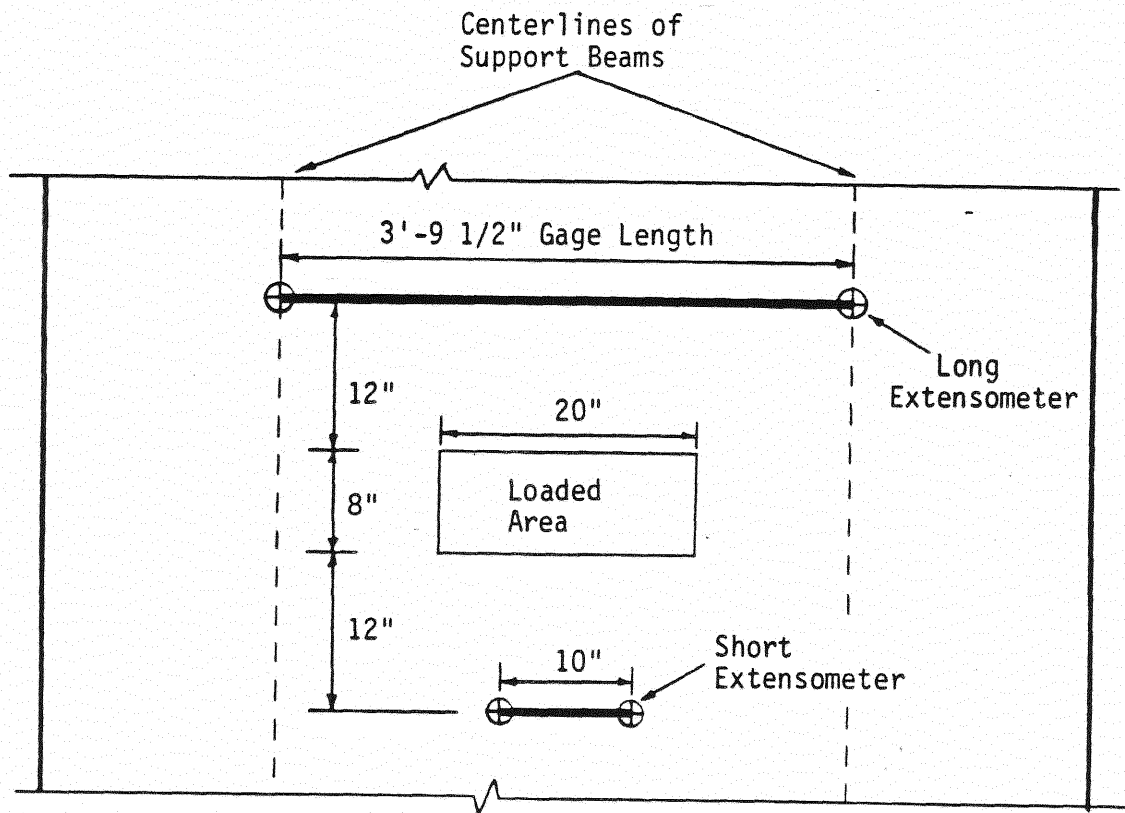
(a) Plan View of Instrumentation on Slab Surface
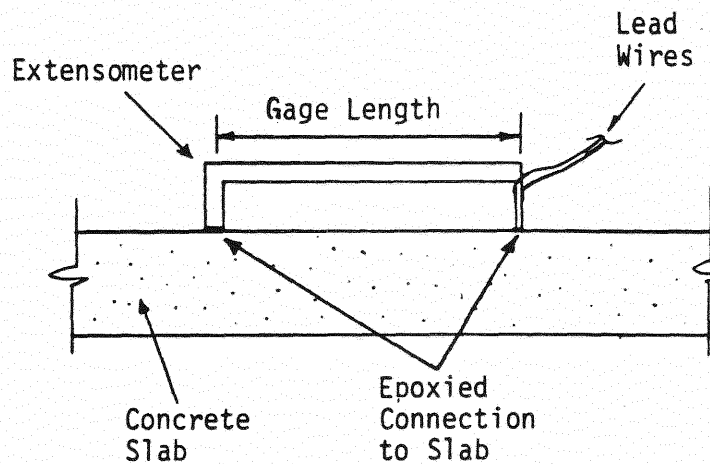
(b) Elevation of Extensometer

Figure C.12 Instrumentation for All Transverse Slab Strength Tests

mounted directly over the centerline of the support beams, and was used to measure the movement of the slab at the supports due to applied load. From these measurements, the relative degree of concrete strain and edge and restraint between the unit slab and the control slabs was determined.

During a given test, the ram load was incrementally increased, and extensometer displacements were recorded at each load increment. Failure was achieved when the ram load could not be increased (flexure failure mode) or when the slab suddenly failed in punching. Test results are discussed in greater detail in Chapter III, Section 3.2.2.

C.5 Shear Connector Specimen Sustained Loading Test Setup

The sustained loading test setup for Phase XIII A is shown in Figures C.13 and C.14. In the figures, stud shear connectors are shown, but the setup was the same for the channel connectors. Each specimen was loaded using a combination of hydraulic ram and springs. Springs were compressed and brought to a desired position (deflection) by using the rams. Upon compression of springs, nuts were tightened on the threaded rods to maintain the compression and the hydraulic rams were removed.

The springs were preloaded several times in a universal testing machine and average deflection was calculated. Thereafter, average stiffness was determined for each set of springs using the following expression,

$$K = P/D \qquad\qquad (C.1)$$

where K = average stiffness value (lbs./in.), P = load on springs (lbs.), and D = average deflection (in.). Loading on each test specimen was determined from measurements of
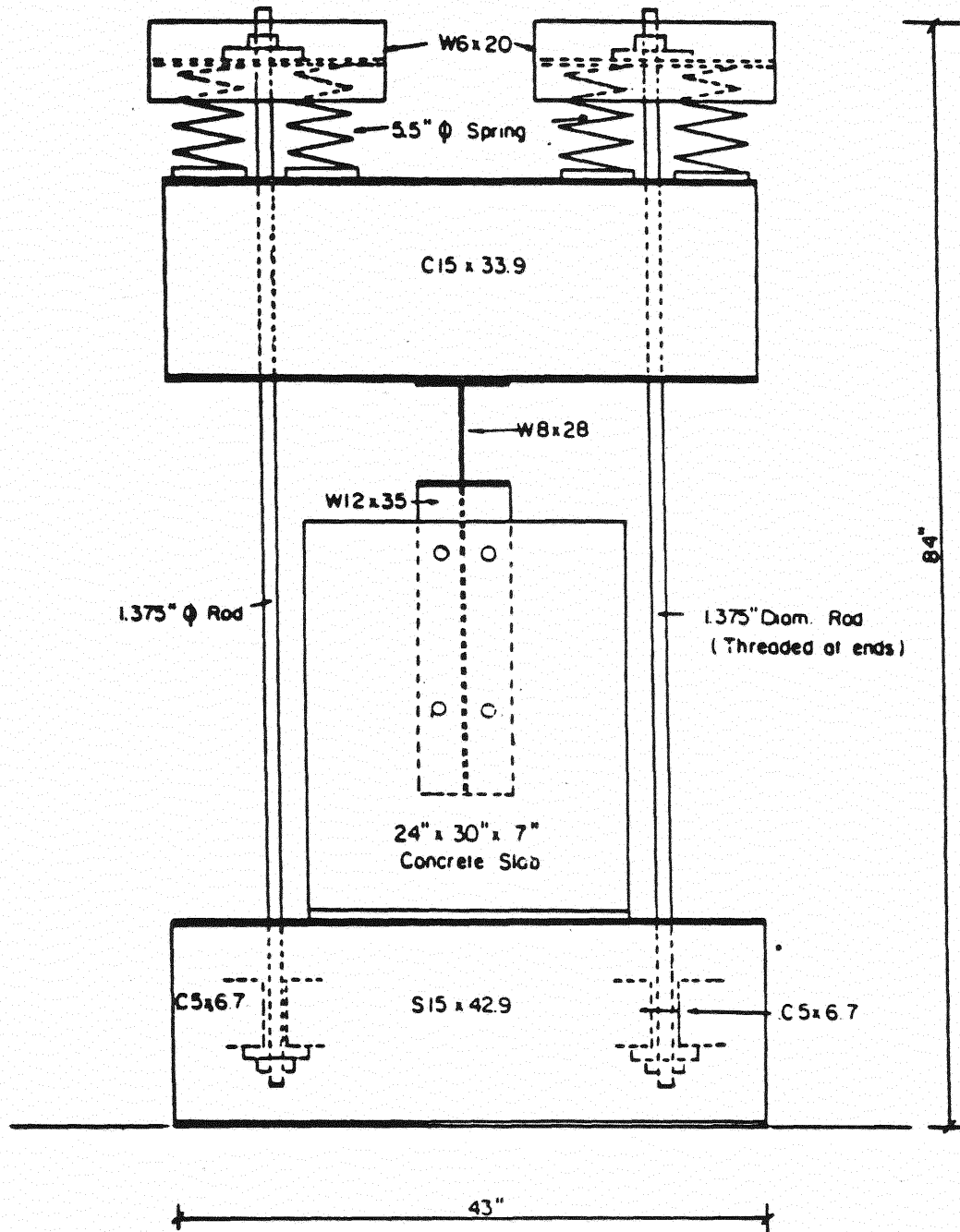
Figure C.13   Front View of Shear Connector Specimen Sustained
              Loading Test Setup
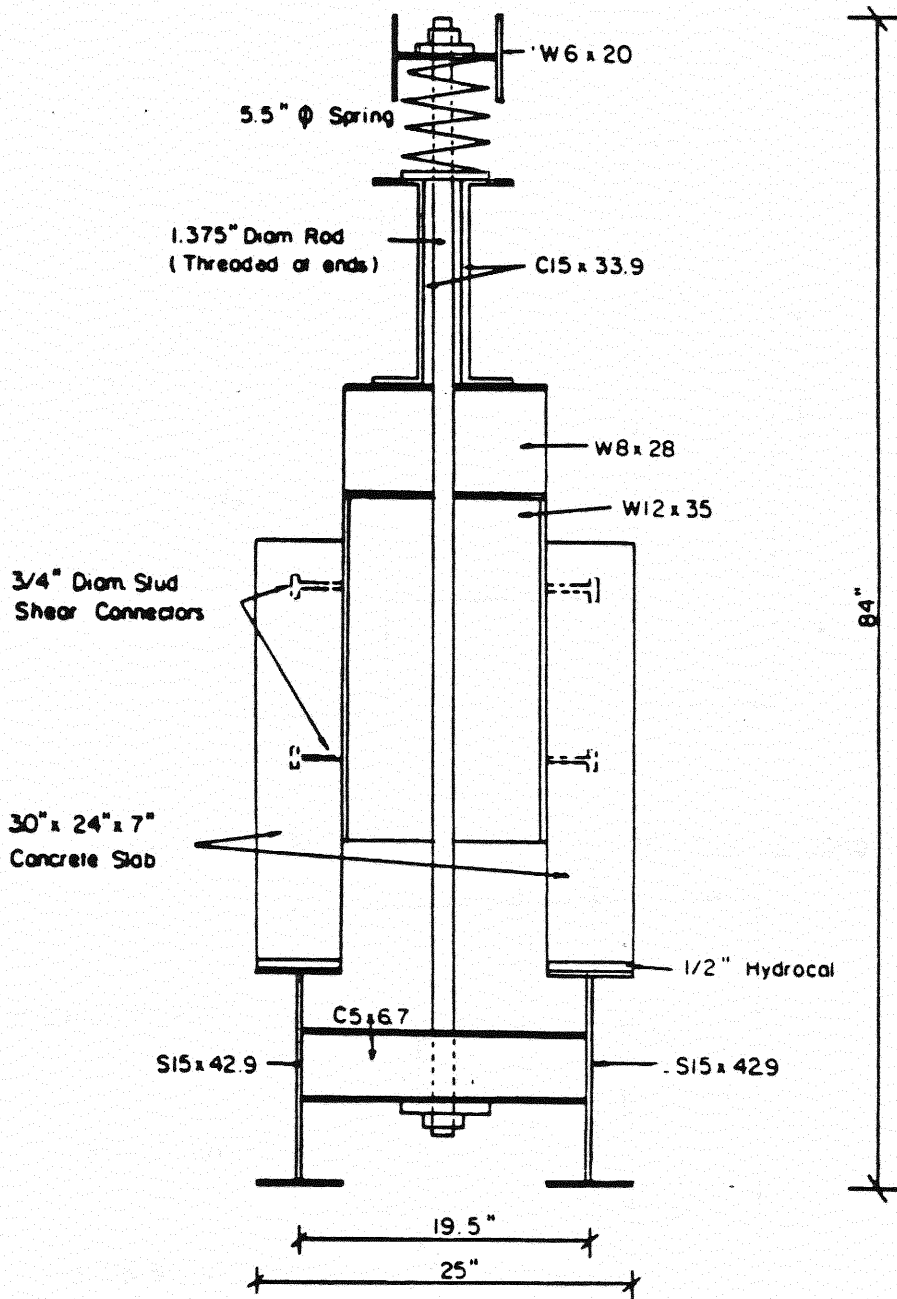
Figure C.14 Side View of Shear Connector Specimen
Sustained Loading Test Setup
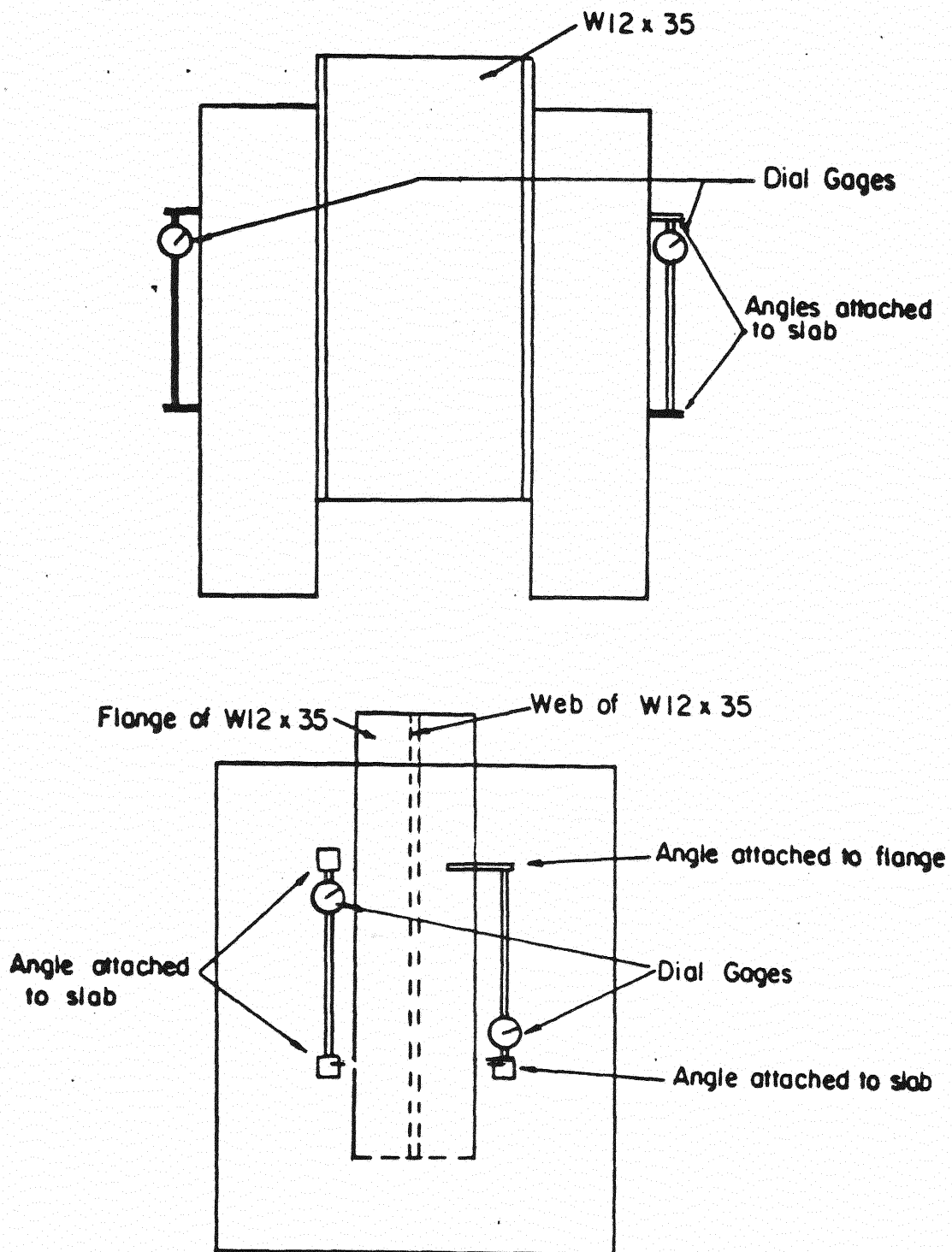
Figure C.15 Instrumentation for Shear Connector Specimen
Sustained Loading Test

the spring height and using the calculated stiffness values. Each specimen was loaded to 48,000 lbs. to simulate the effect of the sustained loading at supports of the bridge unit. Spring height measurements were made periodically to ensure that the compression was maintained.

Instrumentation consisted of individual dial gages with one end attached to the concrete slab and the other end to the steel beam. Figure C.15 shows the location of the dial gages on the test specimens. As shown in the figure, each dial gage was attached to a small angle and had a 10 in. rod extension that extended to another angle mounted 12 in. below (or above) the top (or bottom) angle. The dial gages which measure the relative slip plus creep between the slab and the beams were mounted in the same manner, except one of the angles was welded to the flange of the beam.

Six 0.0001 in. dial gages were used per specimen to record the creep deformation in the concrete slab and the relative slip plus creep displacement between the slab and steel wide flange section. One gage was placed just below the shear connector on the front side of each slab to measure the creep "at" the shear connector. The second one was placed on the back side of each slab, 5 in. from the vertical centerline of the slab but at the same height as the dial gage on the front. This dial gage measures the creep "away" from the shear connectors. The location of the third dial gage on each slab was the same as the second one but on the opposite of the web. This gage was used to measure the initial slip between the slab and the beam and the relative slip resulting from subsequent creep.

Each specimen was loaded to 48,000 lbs. to simulate the effect of sustained loading on shear connectors at the supports of the bridge unit. For the first 60 days, dial

C.25

gage readings were taken on a daily basis. Between 30 and 60 days, recordings were taken every second or third day. Weekly readings were taken after that period. Humidity and temperature were recorded each time dial gage readings were taken. The results of the observation are discussed in Chapter III, Section 3.3.2. But, the results of the tests must be considered in light of the fact that, as described in Appendix H, the beam flanges were partially supported by the concrete slabs in bearing as well as by the shear connectors.

C.6   Shear Connector Specimen Failure Test Setup

Figure C.16 shows the test setup for the shear connector specimen failure tests, Phase XIII B. The setup consisted of grouting the slabs for a uniform bearing surface, and placing a load distributing block and hydraulic ram in place. Bearing of the partially buried flange ends was prevented by chipping away the concrete next to the flanges.

Instrumentation for the test consisted of four probe-type displacement transducers, two each side, as shown in Figure C.17. The probes measured the relative displacement between the concrete slabs and steel beam.

During the test, the ram load was incrementally increased until a shearing failure occurred in the shear connectors. Test results are discussed in Chapter III, Section 3.3.3.

Hydraulic Ram
Load

Load
Distributing
Block

Steel
Wide-flange
Section

Plane of
Shear
Connection

Concrete
Slabs

Gypsum
Cement
Grout

Reaction
Floor
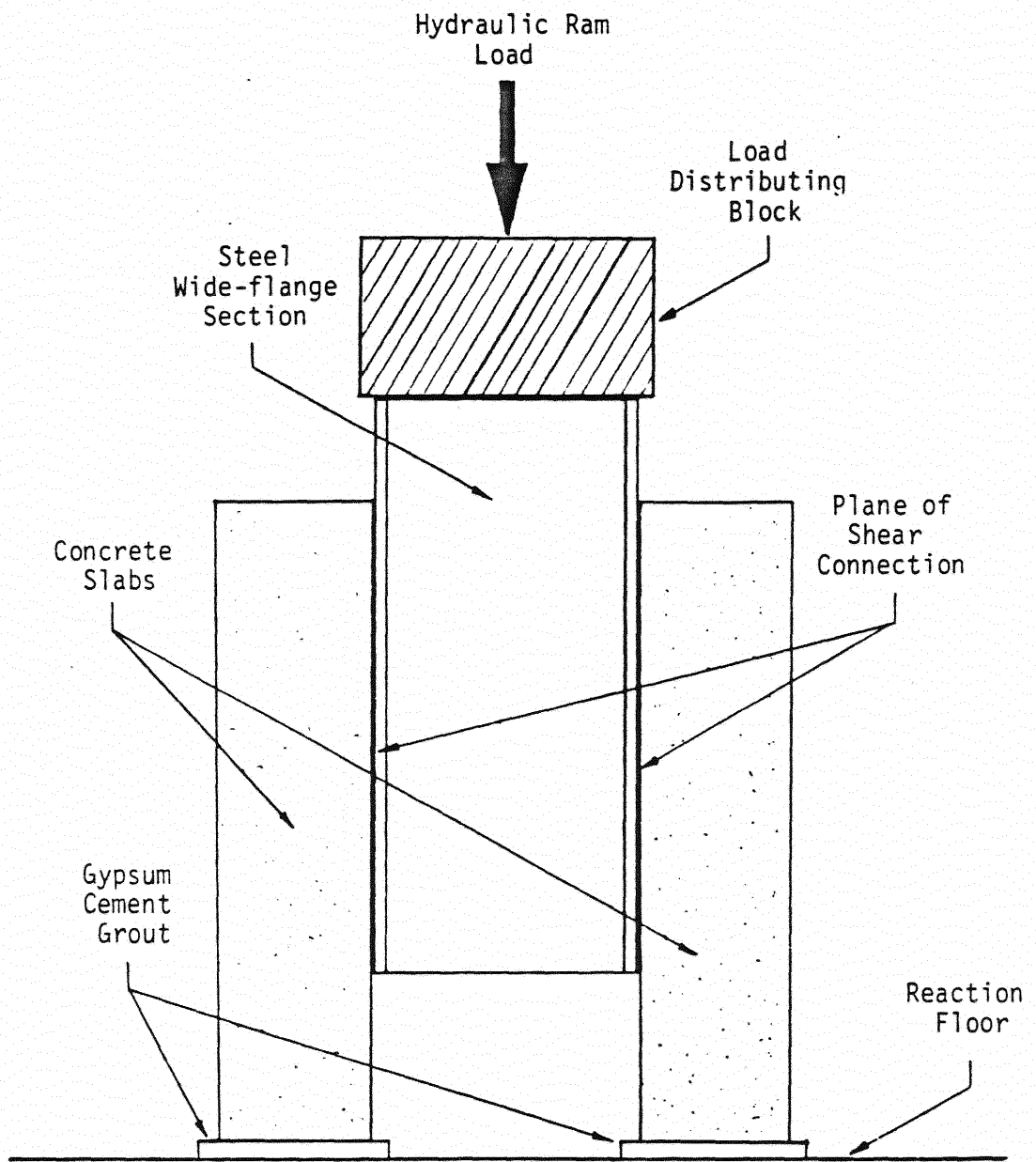
Figure C.16 Shear Connector Specimen Failure Test Setup

Probe-Type Displacement Transducers (2 each side)

Connection to Slab

Connection to Wide Flange Section
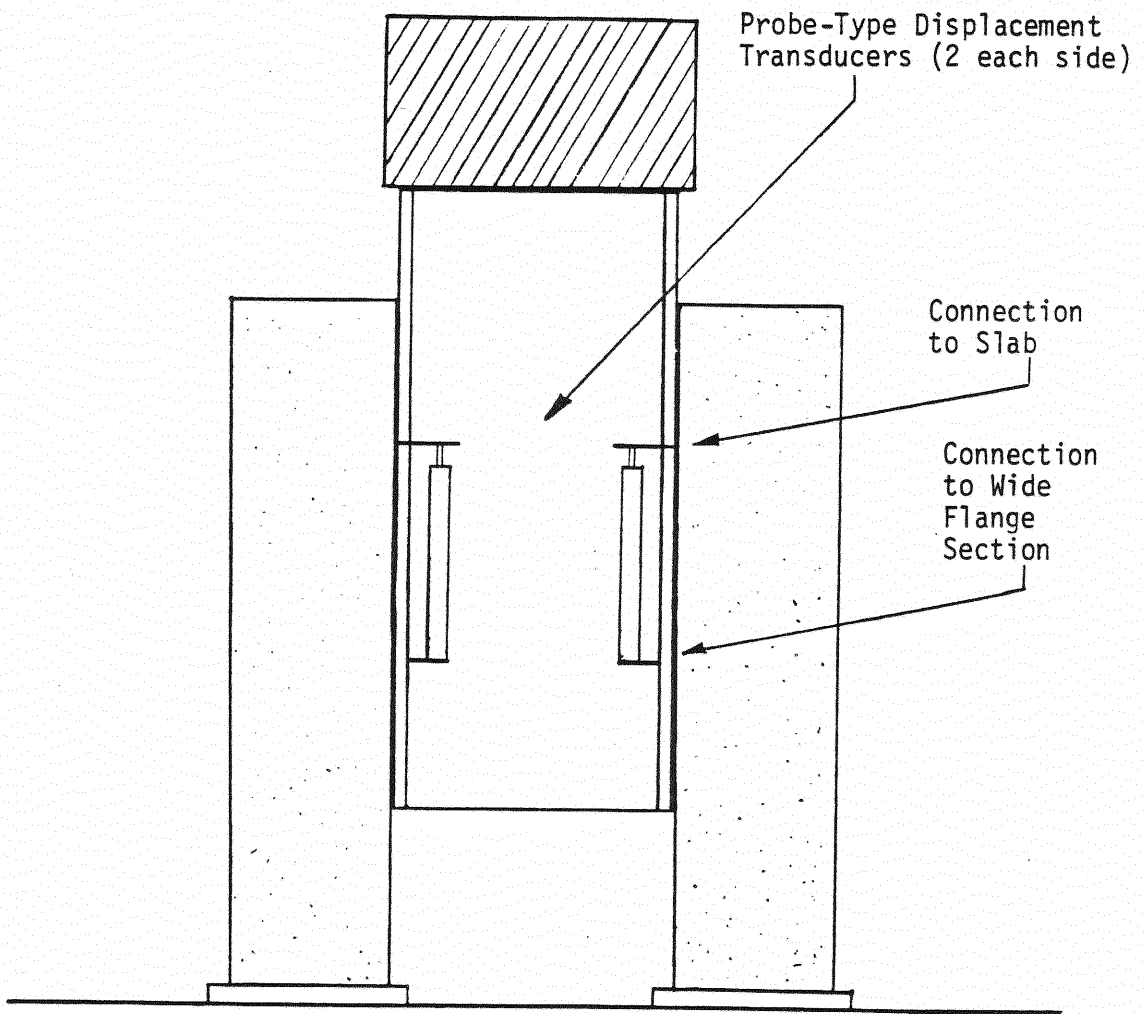
Figure C.17   Instrumentation for Shear Connector Specimen
             Failure Test

APPENDIX D

SUSTAINED LOADING TEST RESULTS

D.1 Prediction of Sustained Loading Effects
(From Reference 2)

Creep and shrinkage effects are complicated to predict because of their dependence on a combination of factors - the constituents of the concrete mix, the water content and water cement ratio, the curing temperature and humidity, the size of the concrete member, the age and duration of loading, the magnitude of stress, and others [4]. Thermal behavior of composite members is also difficult to predict due to nonuniformity in temperatures and material properties and different values of thermal expansion for concrete and steel. Thus, because of the many complexities involved in predicting stresses and deformations due to creep and temperature, many design recommendations for creep and thermal effects are simply gross approximations or even guesses. However, the simplified approach for computing stresses and deflections due to creep, shrinkage, and temperature on a composite steel-concrete beam developed by Branson [4] appears to agree well with the measured results of the sustained loading test.

Branson's method analyzes differential shrinkage and creep stresses and deflections in composite beams based on a simple elastic-theory approach. The differential shrinkage and creep of the slab after it is bonded to the steel beam is assumed to be restrained by the composite section. A slab differential shrinkage and creep force is applied as a concentric tensile force to the slab and then as an equal eccentric compressive force to the composite beam--both applied at the slab centroid. This slab differential shrinkage and creep force (Q) is computed as

$$Q = DA_1E_1 \qquad\qquad\qquad (D.1)$$

where D is the differential shrinkage and creep strain, A_1 is the area of the cast in place slab, and E_1 is the modulus of elasticity of the concrete slab. Generally in the Branson procedure, differential shrinkage and creep strain, D, is analyzed in two parts. First, the effects due to shrinkage are determined using

$$\epsilon_{st} = \{t/(35 + t)\}(\epsilon_{su}) \tag{D.2}$$

where ϵ_{st} = the shrinkage strain at time t, t = time in days after loading, and ϵ_{su} = the ultimate shrinkage strain. Branson suggests that for standard conditions, the average ultimate shrinkage strain for moist-cured concrete is 780 x 10^{-6} in/in. Standard conditions are defined as 40% ambient relative humidity, 7 in. or less slump, minimum thickness of member 6 in. or less, and loading age of 7 days for moist-cured concrete. For other conditions, the standard condition value is to be multiplied by the following corrections factors (CF):

a) Age at loading. For moist-cured concrete,
$$(CF)_a = 1.25t_a^{-0.118} \tag{D.3}$$

where t_a is the age at loading, in days after the initial period of curing.

b) Humidity. For H ≥ 40%,
$$(CF)_h = 1.27 - 0.0067 H \tag{D.4}$$

where H is the ambient relative humidity in percent. Additional correction factors for minimum thickness of member, variations in slump, cement content, percent of fine aggregate, and air content are available but generally may be neglected. For the bridge unit, the correction factors are $(CF)_a = 0.92$ (age at loading = 14 days) and $(CF)_n = 0.80$ (assumed average relative humidity of 70%).

D.2

After the effects due to shrinkage are determined, the combined effects of shrinkage plus creep-under-gravity loads are then estimated. However, for the case of composite slab/steel beams, Branson suggests that creep effects can be ignored because the neutral axis of the composite section lies in the concrete or is very close to the steel-concrete interface and thus the concrete compressive stresses are very low. For the bridge unit being studied here, the initial slab compressive stress due to prestressing is approximately 700 psi (see Appendix B). Branson does not consider this case and no attempt was made to develop coefficients because the measured deflections are less than the predicted deflections when prestressing is ignored as will be shown in the following paragraphs.

The value of the modulus of elasticity of concrete, E_1, was measured in the laboratory by loading three 6 in. diameter by 12 in. long concrete control cylinders, which were cast at the same time the unit was cast, in a universal testing machine. The change in height of the cylinders was measured using 0.0001 in. dial gages from which strains were calculated. The average modulus of elasticity was 4,600,000 psi which corresponds to a modular ratio of 6.3.

Once the shrinkage and creep force, Q, is determined, it is applied to the slab and then to the composite section. The eccentric force, Q, produces a moment, $Q(Y_{cs})$ where Y_{cs} is the distance from the composite section centroid to the cast-in-place slab centroid. For constant moment along a simple span, the midspan deflection is given by

$$M_c = ML^2/8EI = Q\ Y_{cs}\ L^2/8E_2I_c \tag{D.5}$$

where L = length of the beam, E_2 = modulus of elasticity of steel beam and I_c = moment of inertia of the composite section with a transformed slab.

D.3

The composite beam deflection due to differential temperature is calculated in the same manner except that a strain due to temperature, D_T, is substituted for the differential shrinkage and creep strain. The temperature strain is calculated as

$$D_T = \alpha_c \, T \tag{D.6}$$

where α_c = thermal coefficient of the slab concrete, 5.5×10^{-6} in/in $1°F$, and T is the change in temperature in degrees Fahrenheit between measurements.

Example calculations (from Reference 2) follow.

EXAMPLE CALCULATIONS - BRANSON METHOD
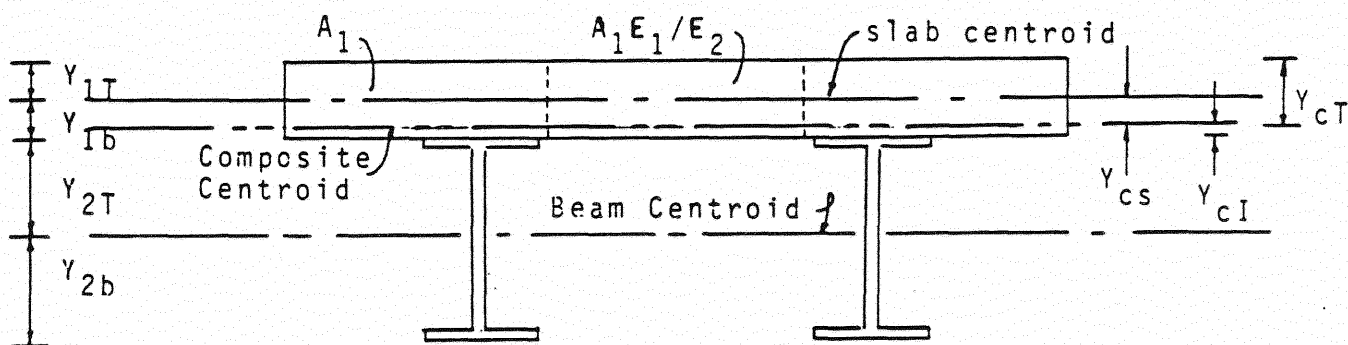
$$A_c = A_1 E_1 / E_2 + A_2$$

$$I_c = I_1 E_1 / E_2 + I_2 + A_1 (E_1 / E_2) Y_{cs}^2 + A_2 (Y_{cb} - Y_{2b})^2$$

Subscript Notation :

1	cast-in-place slab
2	steel beam
b	bottom fiber of section
c	composite section with transformed slab
I	the slab-beam interface
s	slab centroid
T	top fiber of section

Figure C.1 Geometry and nomenclature for bridge unit

Shrinkage and Creep Calculations :

(1) Compute Section Properties

Design Data:

Slab	Beams
t=7.5"	d=20.83"
w=81.5"	A=14.7 sq. in.
f'$_c$ =5000 psi	I=984 in.^{4}
E$_c$=4.6x10^6 psi	

D.5

$E_1 = E_c = 4.6 \times 10^6$ psi

$E_2 = E_s = 29 \times 10^6$ psi

$n = E_s/E_c = 29/4.6 = 6.3$

$A_1 = (81.5)(7.5) = 611.25$ in^2

$A_2 = (2)(14.7) = 29.4$ in^2

$A_c = 611.25(4.6/29) + 29.4 = 126.36$ in^2

$d_1 = 7.5$ in

$d_2 = 20.83$ in

$Y_{2b} = 20.83/2 = 10.415$ in

$Y_{cb} = \dfrac{[29.4(10.415) + 81.5(7.5)(3.75 + 20.83)/6.3]}{[29.4 + 81.5(7.5)/6.3]} = 21.17$ in

$Y_{ci} = 21.17 - 20.83 = 0.34$ in

$Y_{cs} = 3.75 - 0.34 = 3.41$ in

$Y_{cT} = 7.5 - 0.34 = 7.16$

$I_1 = (7.5)^3(81.5)/12$

$I_2 = 2(984) = 1968$ in^4

$I_c = 2865.23(4.6/29) + 1968 + 611.25(4.6/29)(3.36)^2 + 29.4(10.76)^2$
$= 6921$ in^4

(2) Compute Shrinkage and Creep Coefficient, D_u

$\varepsilon_{su} = 780 \times 10^{-6}$ in/in (average shrinkage strain)

$\varepsilon_{st} = [t/(35+t)](\varepsilon_{su})(CF)_h(CF)_a$

At t=150 days, $(CF)_h = 0.80$, $(CF)_a = 0.92$

$(\varepsilon_{st})_{150} = 780 \times 10^{-6}(150/185)(0.80)(0.92) = 465 \times 10^{-6}$ in/in

$D_u = 1.2(\varepsilon_{st}) = 1.2(465 \times 10^{-6}) = 558 \times 10^{-6}$ in/in

D.6

(3) Compute Shrinkage and Creep Force, Q

$$Q = D_U A_1 E_1 / 2 = 558(611.15)(4.6)/2 = 784,478 \text{ lb.}$$

(4) Compute Shrinkage and Creep Stresses

Top of Slab: $F_{1T} = Q/A_1 + (-Q/A_c - QY_{cs}Y_{cI}/I_c)E_1/E_2$

$$F_{1T} = \frac{784,478}{611.25} + \left[\frac{-784,478}{122.35} - \frac{784,478(3.36)(7.11)}{6921}\right]4.6/29$$

$$F_{1T} = -163.2 \text{ psi}$$

Bottom of Slab: $F_{1b} = Q/A_1 + (-Q/A_c + QY_{cs}Y_{ci}/I_c)E_1/E_2$

$$F_{1b} = \frac{784478}{611.25} + \left[\frac{-784478}{122.35} + \frac{784478(3.36)(0.39)}{6921}\right]\frac{4.6}{29}$$

$$F_{1b} = 289.9 \text{ psi}$$

Top of Beam: $F_{2T} = -Q/A_c + QY_{cs}Y_{ci}/I_c$

$$F_{2T} = \frac{-784478}{122.35} + \frac{784478(3.36)(0.39)}{6921}$$

$$F_{2T} = -6263 \text{ psi}$$

Bottom of Beam: $F_{2b} = -Q/A_c + QY_{cs}Y_{cb}/I_c$

$$F_{2b} = \frac{-784478}{122.35} + \frac{784478(3.36)(21.17)}{6921}$$

$$F_{2b} = 1650 \text{ psi}$$

(5) Compute Midspan Deflection,

$$\Delta = QY_{cs}L^2/8E_2I_c$$

$$\Delta = \frac{784478(3.36)(54)^2 144}{8(29\times10^6)6921}$$

$$\Delta = 0.689 \text{ in}$$

D.7

Temperature Calculations

(1) Compute Section Properties - same as previous

(2) Compute Temperature Strain, D_T

$$\alpha = 5.7 \times 10^{-6} \text{ in/in (coefficient of thermal expansion for concrete)}$$

$$\Delta T = 35°F \text{ (assumed)}$$

$$D_T = \quad T = 5.7 \times 10^{-6}(35) = 200 \times 10^{-6}$$

(3) Compute Temperature Force, Q

$$Q = D_T A_1 E_1 / 2 = 200(611.25)(4.6)/2 = 270,000 \text{ lb.}$$

(4) Compute Thermal Stresses (equations same as previous)

$$F_{1T} = -36.91 \text{ psi}$$

$$F_{1b} = 114 \text{ psi}$$

$$F_{2T} = -2155 \text{ psi}$$

$$F_{2b} = 595 \text{ psi}$$

(5) Compute Thermal Deflection

$$\Delta = QY_{cs}L^2/8E_2 I_c = \frac{270,000(3.36)(54)^2 144}{8(29 \times 10^6)6921}$$

$$\Delta = 0.24 \text{ in.}$$

Table D.1
Comparison of Actual Midspan Deflection Due to Shrinkage, Creep, and Temperature
Effects with Predictions By Branson Method, Phase I Sustained Loading

Day No.	Predicted Change In Deflection Due To Temperature Change (in.)	Predicted Change In Deflection Due To Shrinkage and Creep Effect (in.)	Total Predicted Change in Deflection Due To Temperature Plus Shrinkage and Creep (in.)	Actual Measured Change In Deflection (in.)
21	0.029	0.319	0.348	0.156
28	-0.028	0.378	0.350	0.036
35	0.065	0.426	0.491	0.187
42	0.158	0.464	0.622	0.280
49	0.158	0.497	0.655	0.272
56	0.029	0.524	0.553	0.205
63	0.151	0.547	0.698	0.307
73	0.216	0.575	0.791	0.336
95	0.202	0.622	0.824	0.414
121	0.288	0.660	0.948	0.589
154	0.281	0.694	0.975	0.735
179	0.224	0.712	0.936	0.691
207	0.009	0.728	0.737	0.554
238	-0.083	0.742	0.659	0.422
270	-0.094	0.754	0.660	0.392
304	-0.022	0.763	0.741	0.451
335	0.078	0.771	0.849	0.441
363	0.049	0.776	0.825	0.401
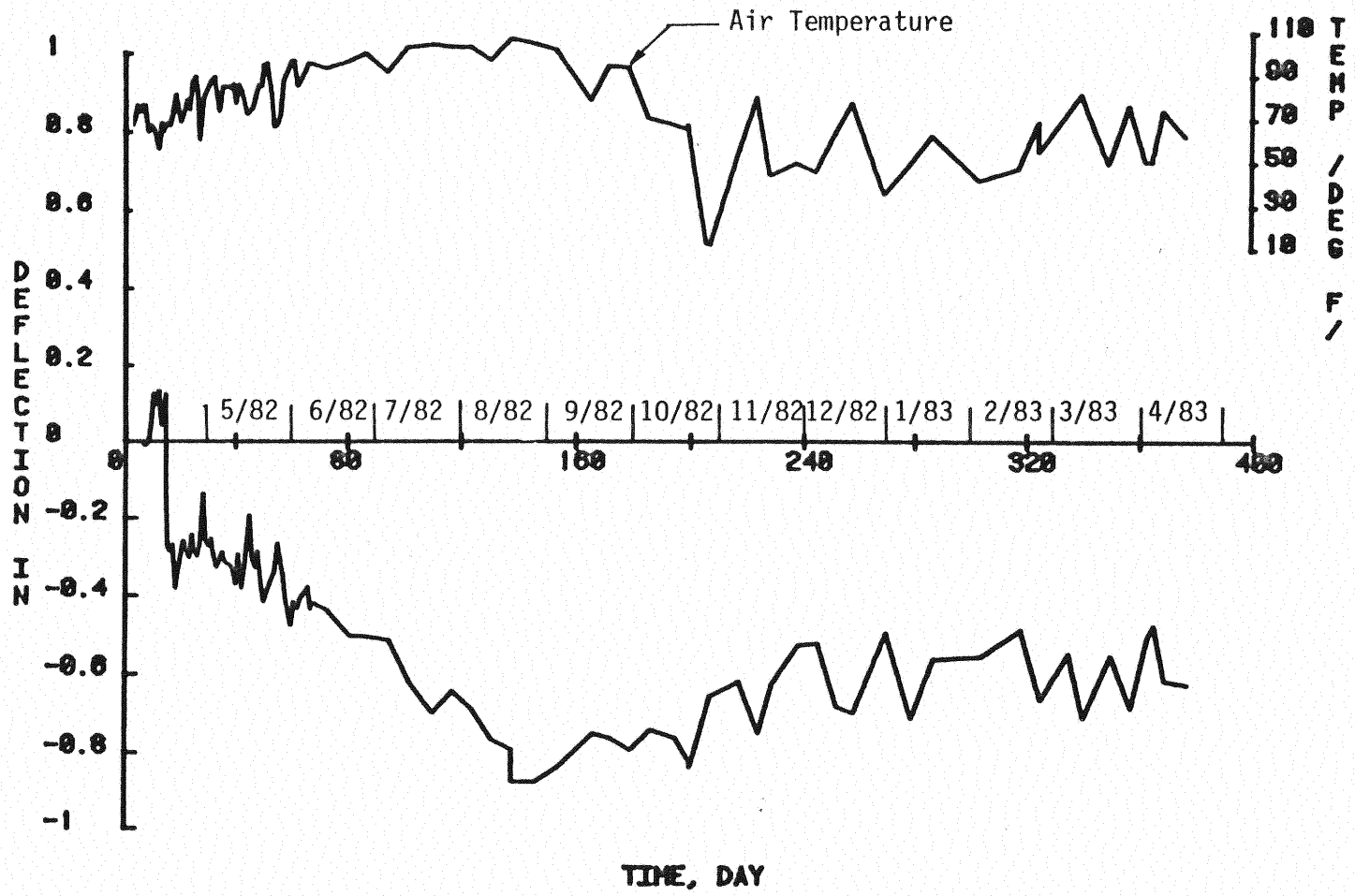
Figure D.1   Change vs. Time in Deflection, Phase I Sustained Loading

Table D.2

Beam Strains and Location of Neutral Axis, Phase I, Sustained Loading

| Days From Beginning of Observation | West Beam Strains $(10)^{-6}$ in/in | | | | Average Flange Strain | | Apparent Neutral Axis Location From Bottom of Beam (in.) |
| | Top of Top Flange | | Bottom of Bottom Flange | | | | |
	Ext.	Int.	Ext.	Int.	Top	Bottom	
0	-7	-5	626	670	-6	648	20.67
3	-37	-29	649	702	-33	765	19.89
7	-140	-140	728	788	-140	758	17.61
14	-146	-137	684	750	-141	717	17.43
14	-182	-175	716	769	-178	742	16.82
14	-174	-166	813	870	-170	841	17.36
15	-169	-162	810	873	-166	841	17.43
30	-184	-182	778	854	-183	816	17.04
60	-217	-219	816	908	-218	862	16.66
95	-300	-305	807	903	-302	855	15.42
121	-344	-350	813	915	-347	864	14.89
154	-326	-332	881	987	-329	934	15.43
179	-320	-326	873	977	-323	925	15.47
207	-277	-289	892	989	-283	940	16.04
238	-251	-258	890	981	-254	935	16.41
270	-224	-225	876	964	-224	920	16.77
304	-197	-191	889	973	-194	931	17.27
335	-268	-288	832	920	-278	876	15.84
363	-284	-221	801	865	-252	833	16.02
392	-334	-260	804	870	-297	837	15.4
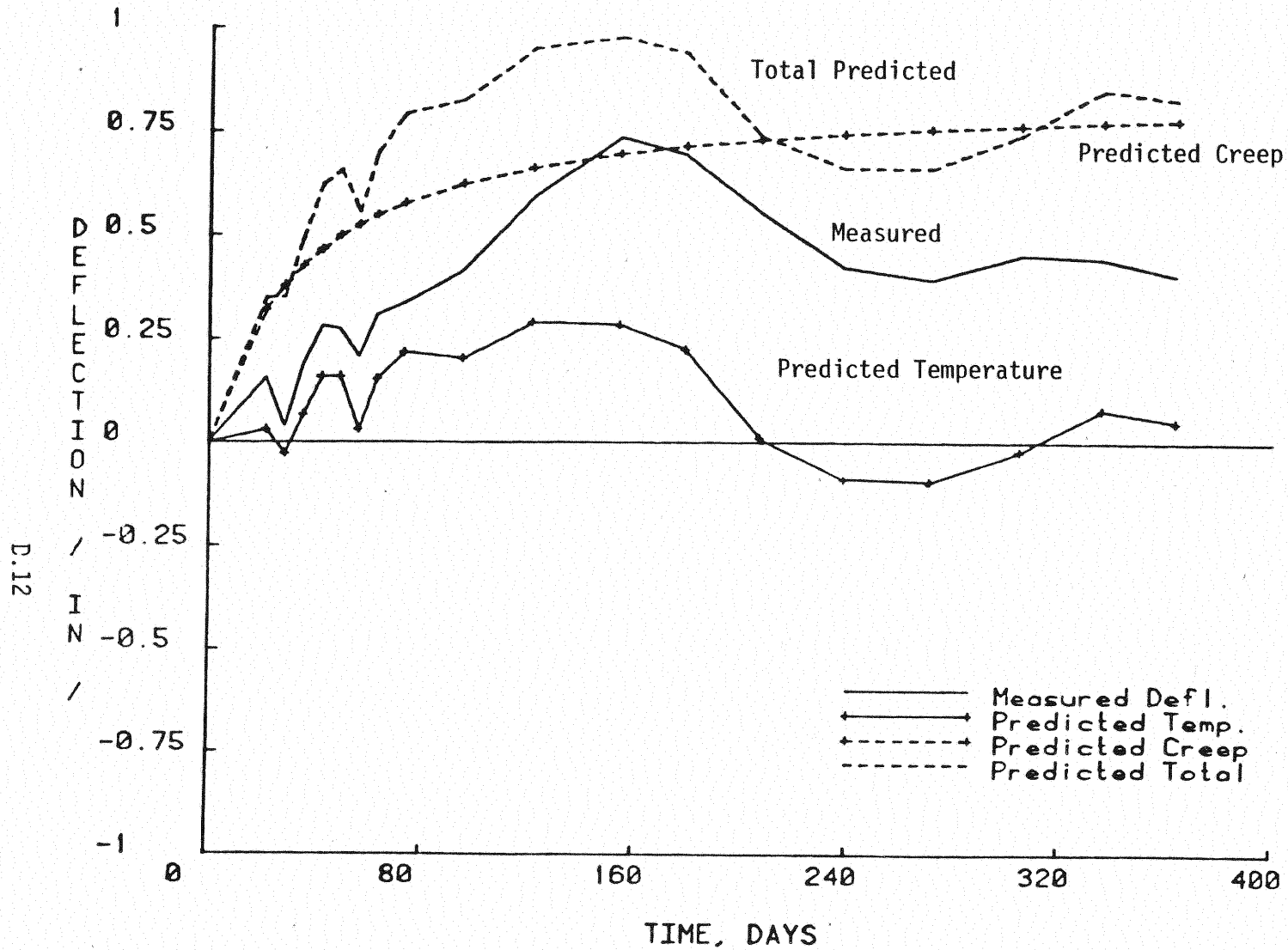
Figure D.2 Comparison of Measured Midspan Deflection Due to Shrinkage, Creep, and Temperature Effects with Predictions by Branson Method, Phase I Sustained Loading Test

D.12
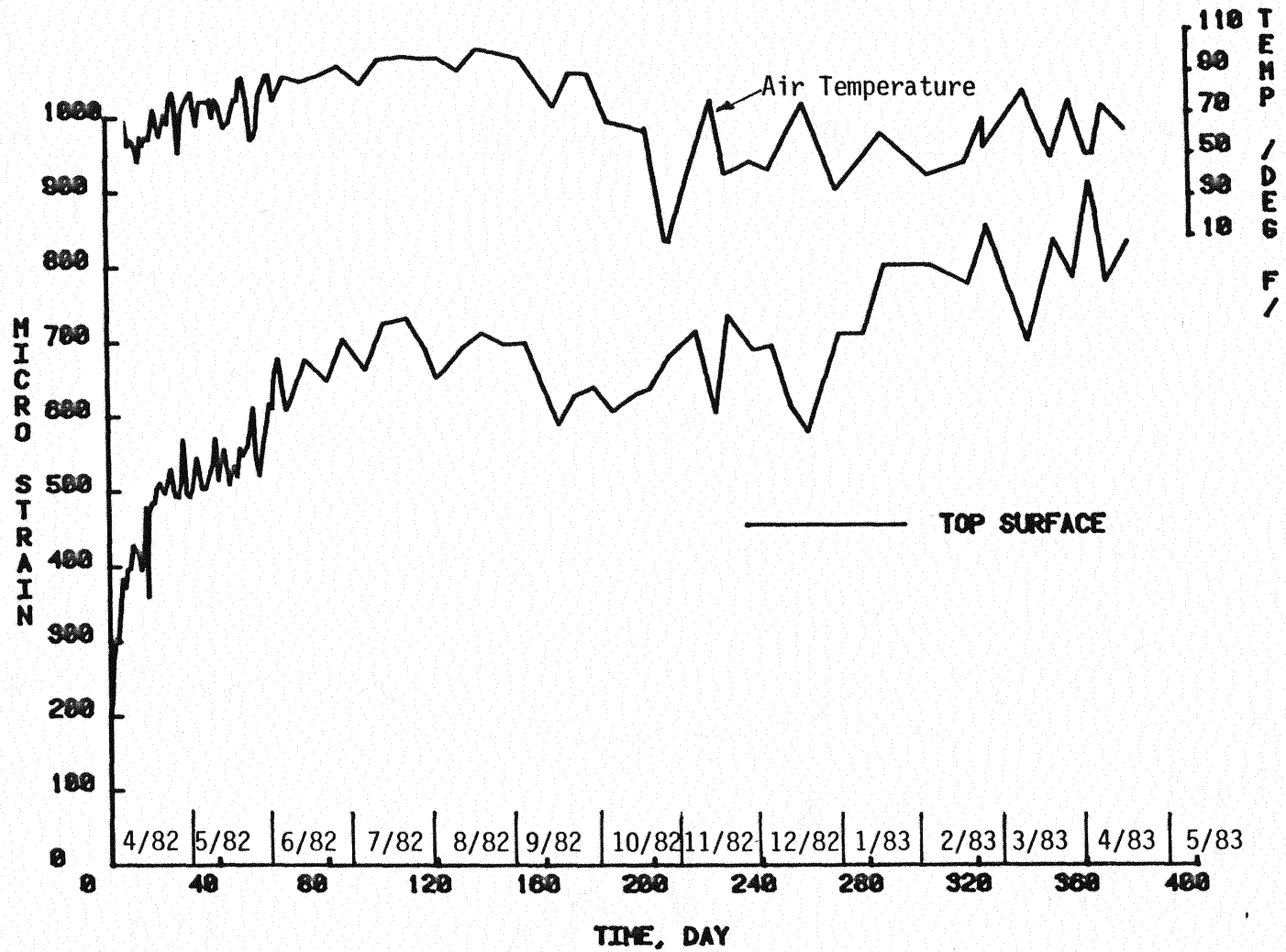
Figure D.3 Change in Strain of Concrete Surface vs. Time, Phase I Sustained Loading
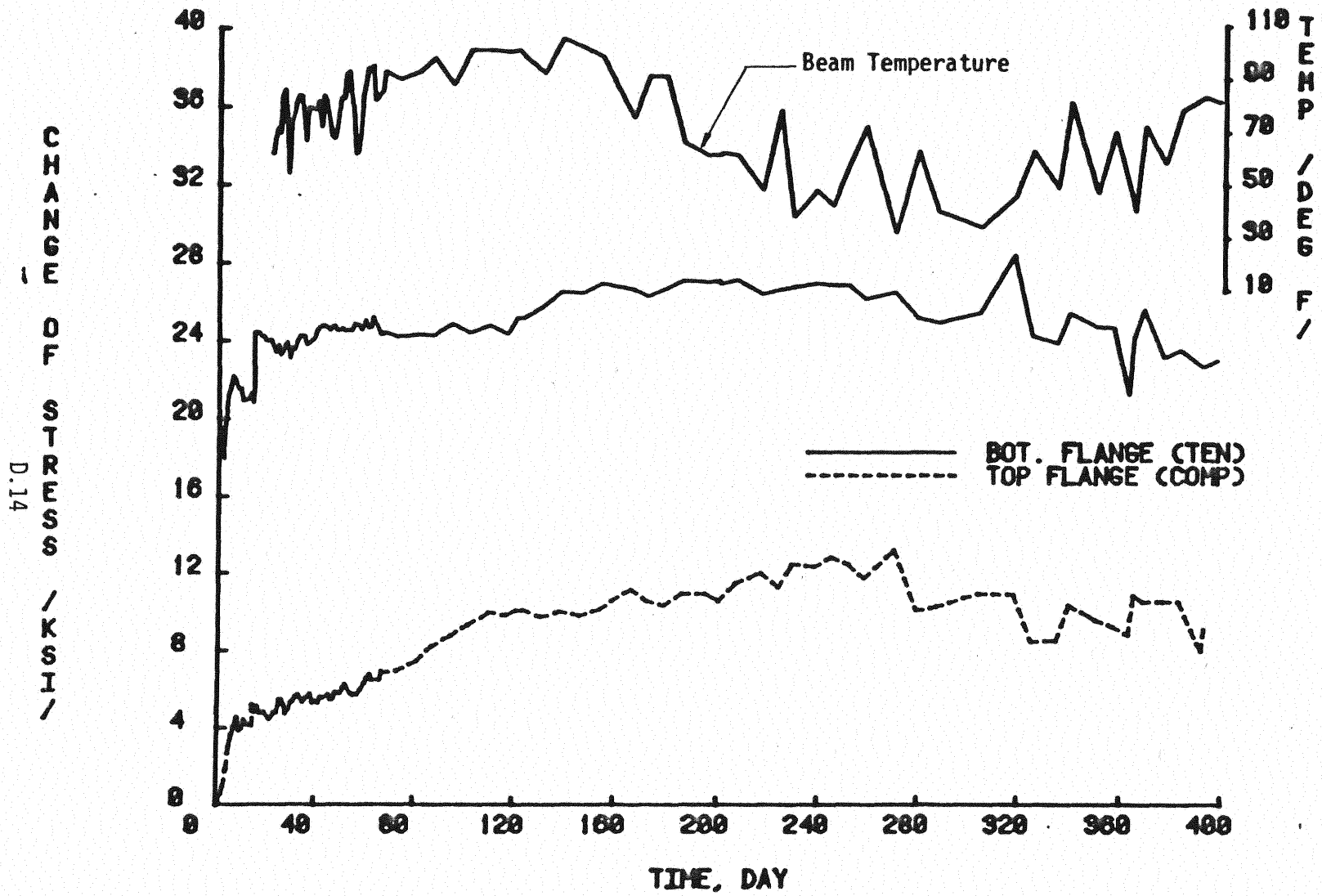
Figure D.4 Change in Stress in Beam Flanges vs. Time, Phase I Sustained Loading
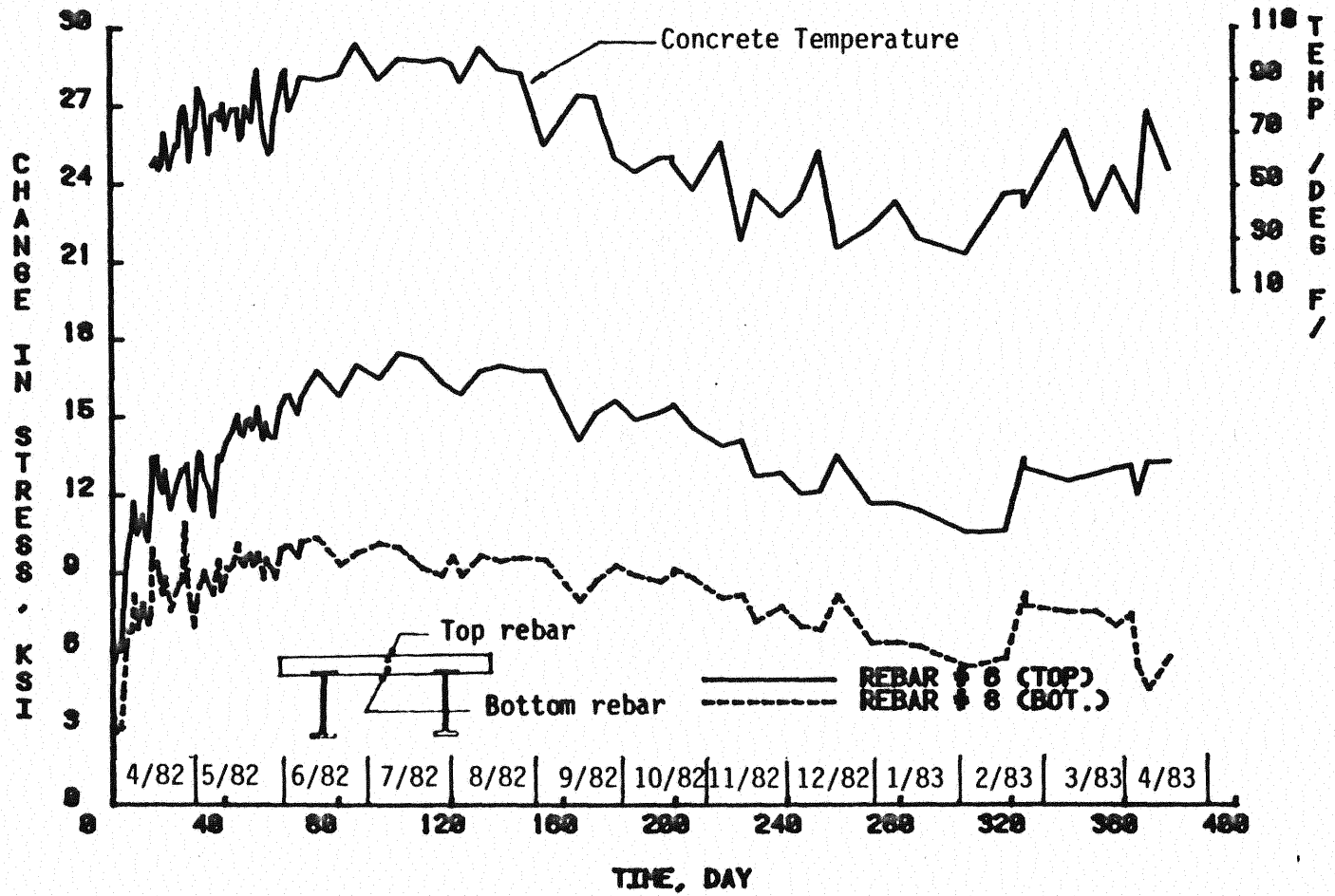
Figure D.5 Change in Stress of Rebars vs. Time, Phase I Sustained Loading
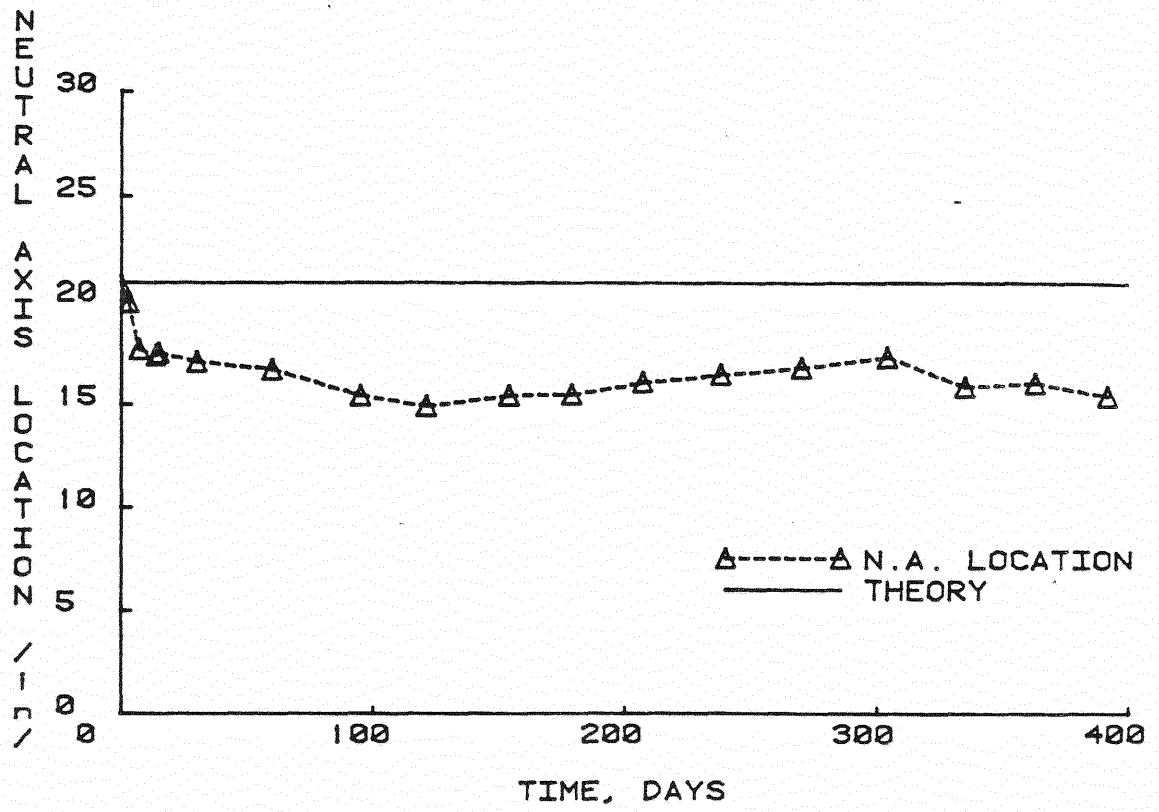
Figure D.6 Apparent Neutral Axis Location from Bottom of Beam,
Phase I Sustained Loading

TABLE D.3

Comparison of actual midspan deflection due to
Creep, Shrinkage, and Temperature effects with Prediction by
Branson's Method (Phase IV)

Day No.	Predicted Change in Deflection due to temperature change (in.)	Predicted Change in Deflection due to Creep plus Shrinkage (in.)	Predicted Change in Deflection due to Temperature + Creep + Shrinkage (in.)	Actual measured change in midspan Deflection (in.)
0	0.000	0.000	0.000	0.000
31	0.000	0.082	0.076	0.120
85	0.420	-0.057	0.363	0.290
123	0.196	-0.055	0.141	0.230
158	0.224	-0.046	0.178	0.210
195	0.147	0.084	0.231	0.235
223	0.098	0.013	0.111	0.210
256	-0.070	0.099	0.025	0.155
291	-0.119	0.089	-0.030	0.105
327	-0.070	0.090	0.020	0.090
369	-0.014	0.043	0.029	0.120
397	0.070	0.177	0.247	0.205
439	0.210	0.082	0.292	0.250
468	0.378	0.012	0.390	0.320
494	0.364	-0.034	0.330	0.200
521	0.224	-0.032	0.192	0.180
556	0.175	0.005	0.180	0.130
593	0.042	0.053	0.095	0.160
626	-0.091	0.090	-0.001	0.120
661	-0.070	0.115	0.045	0.085
689	-0.049	0.092	0.043	0.060
700	-0.098	0.069	-0.029	0.060
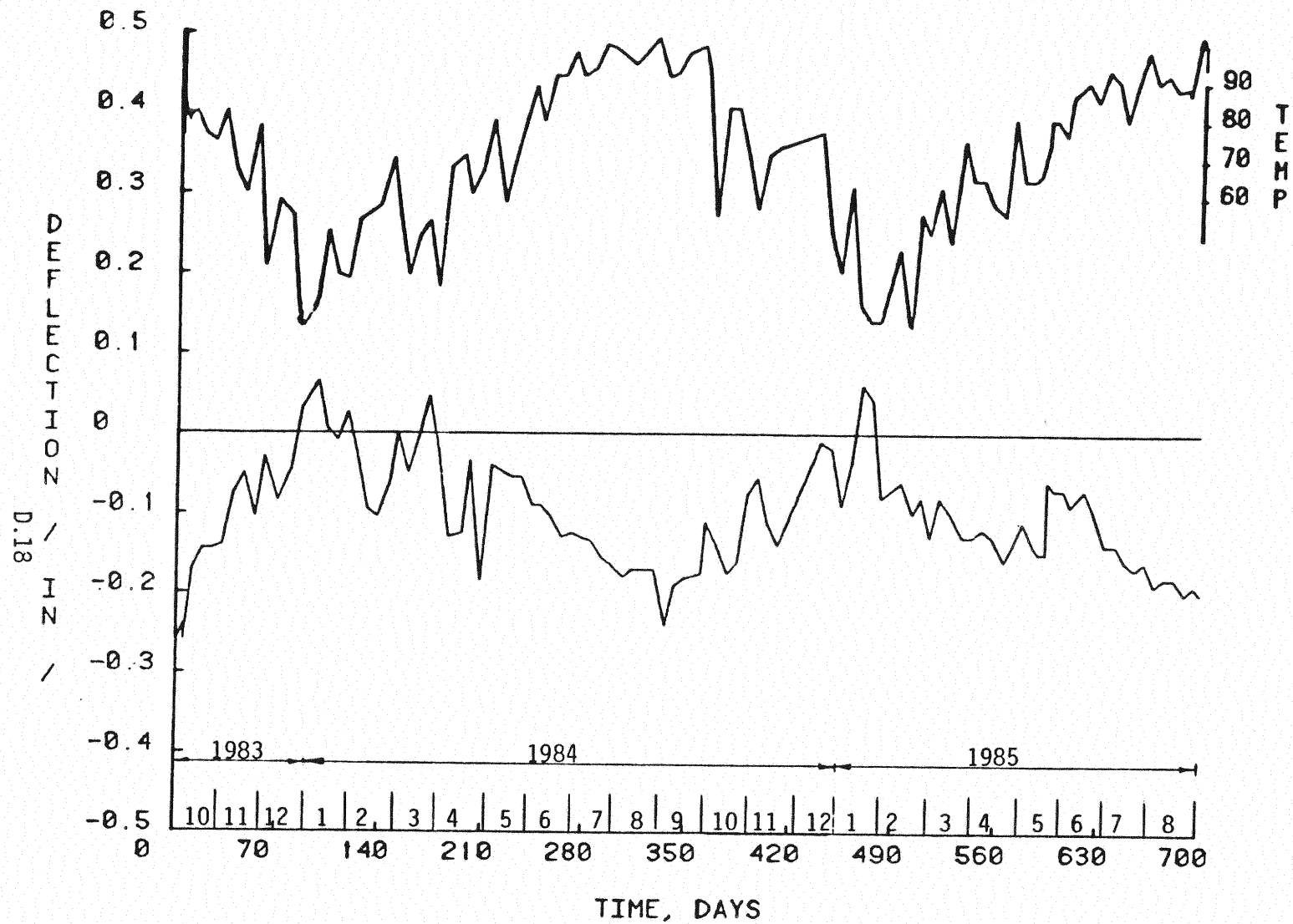
Figure D.7 Vertical Deflection vs. Time, Phase IV Sustained Loading Test
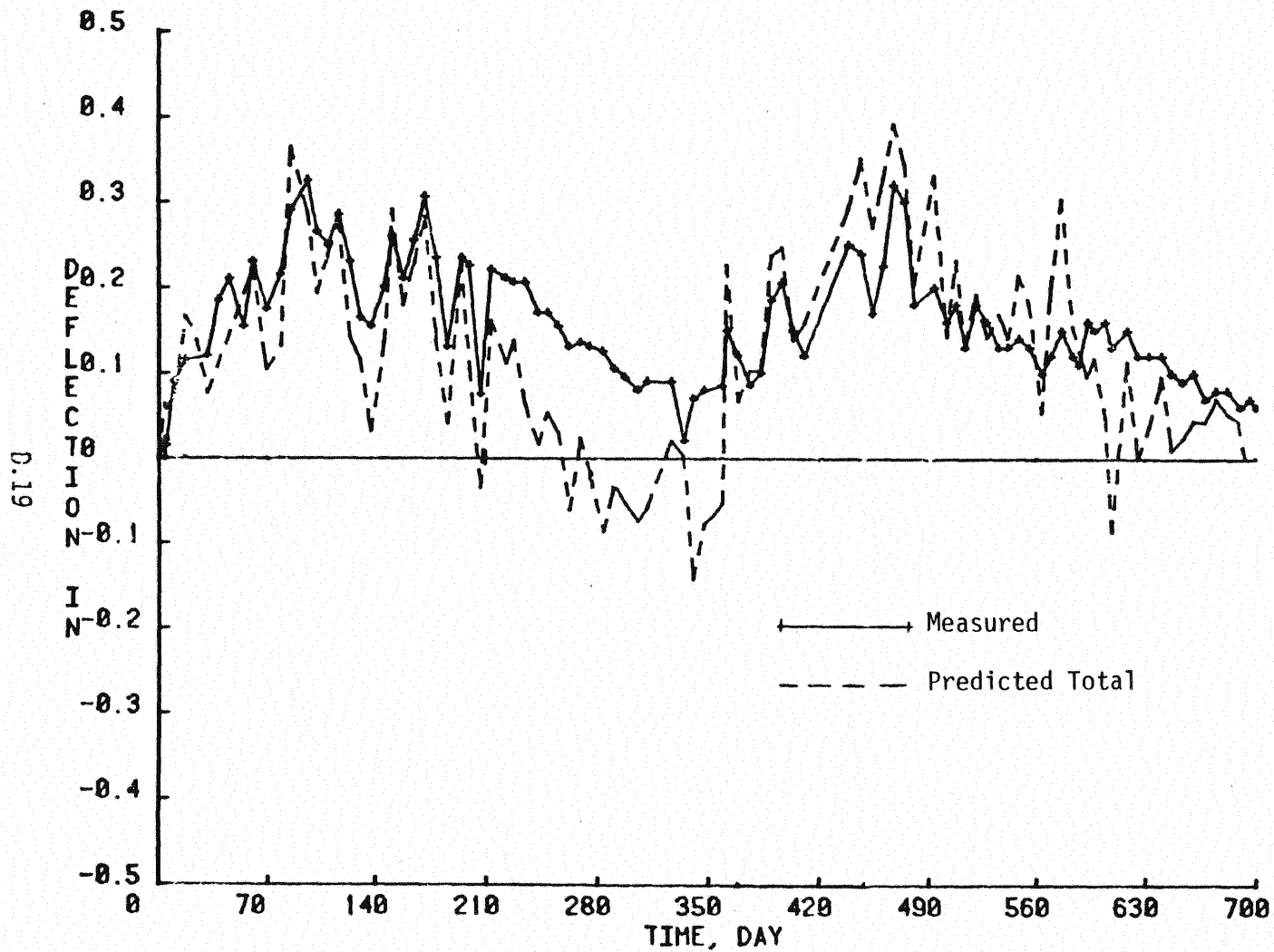
Figure D.8 Comparison of Measured Midspan Deflection with Branson's Predicted Deflection Due to Combined Effects of Creep and Shrinkage and Temperature, Phase IV Sustained Loading Test

D.19
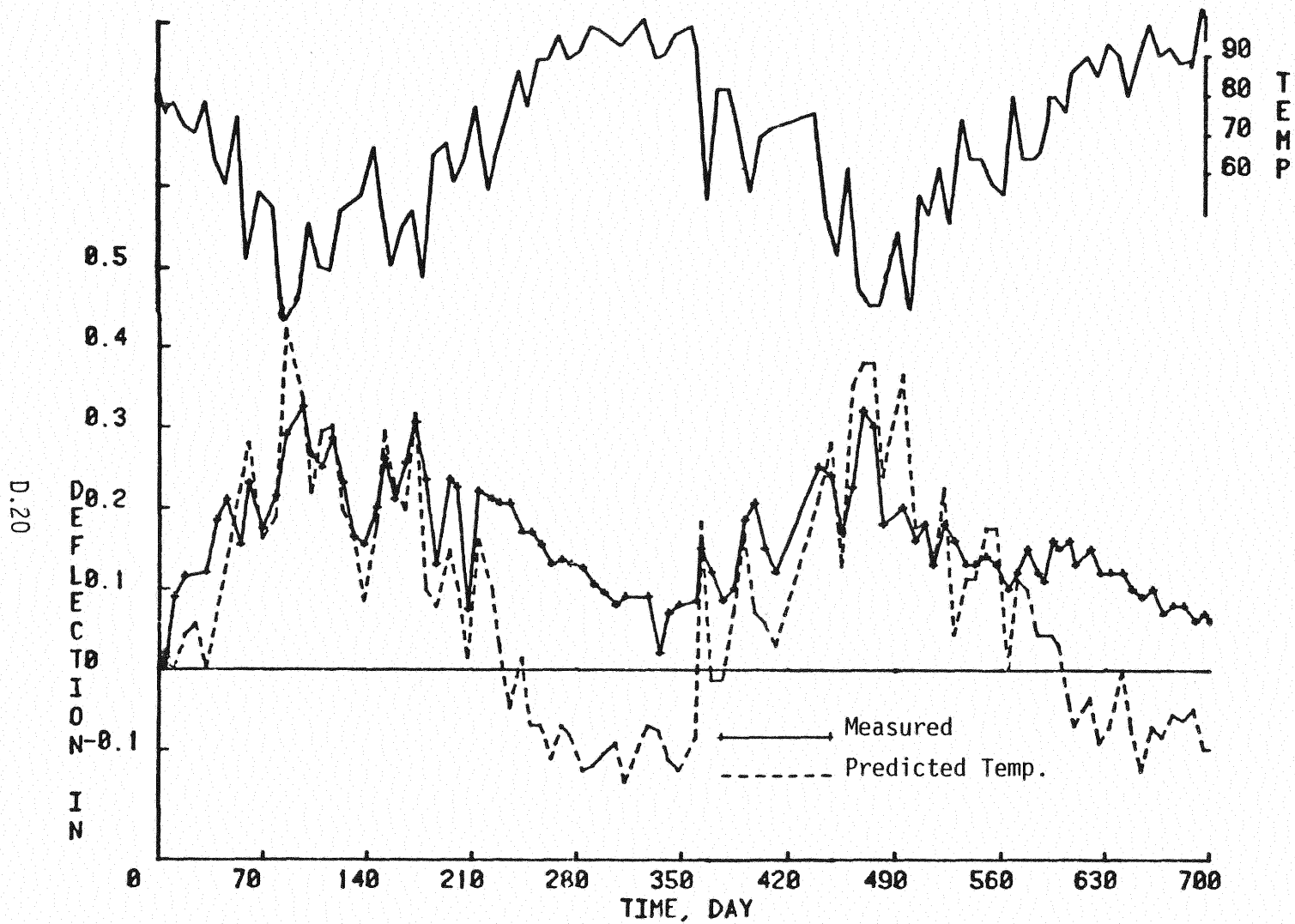
Figure D.9 Comparison of Measured Midspan Deflection with Branson's Predicted Deflection
Due to Temperature Effects, Phase IV Sustained Loading Test

D.20
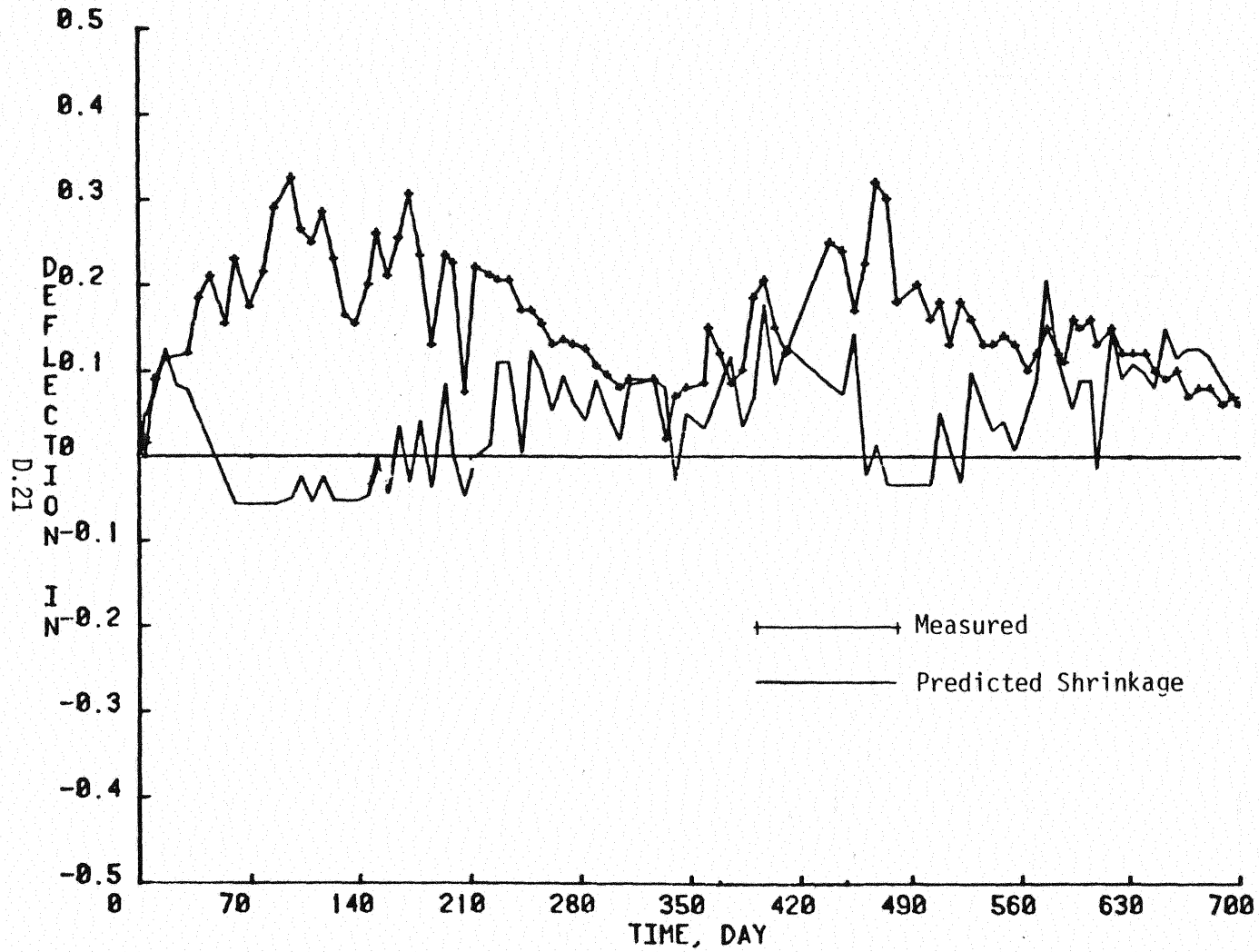
Figure D.10 Comparison of Measured Midspan Deflection with Branson's Predicted Deflection
Due to Shrinkage Plus Creep Effects, Phase IV Sustained Loading Test

D.21
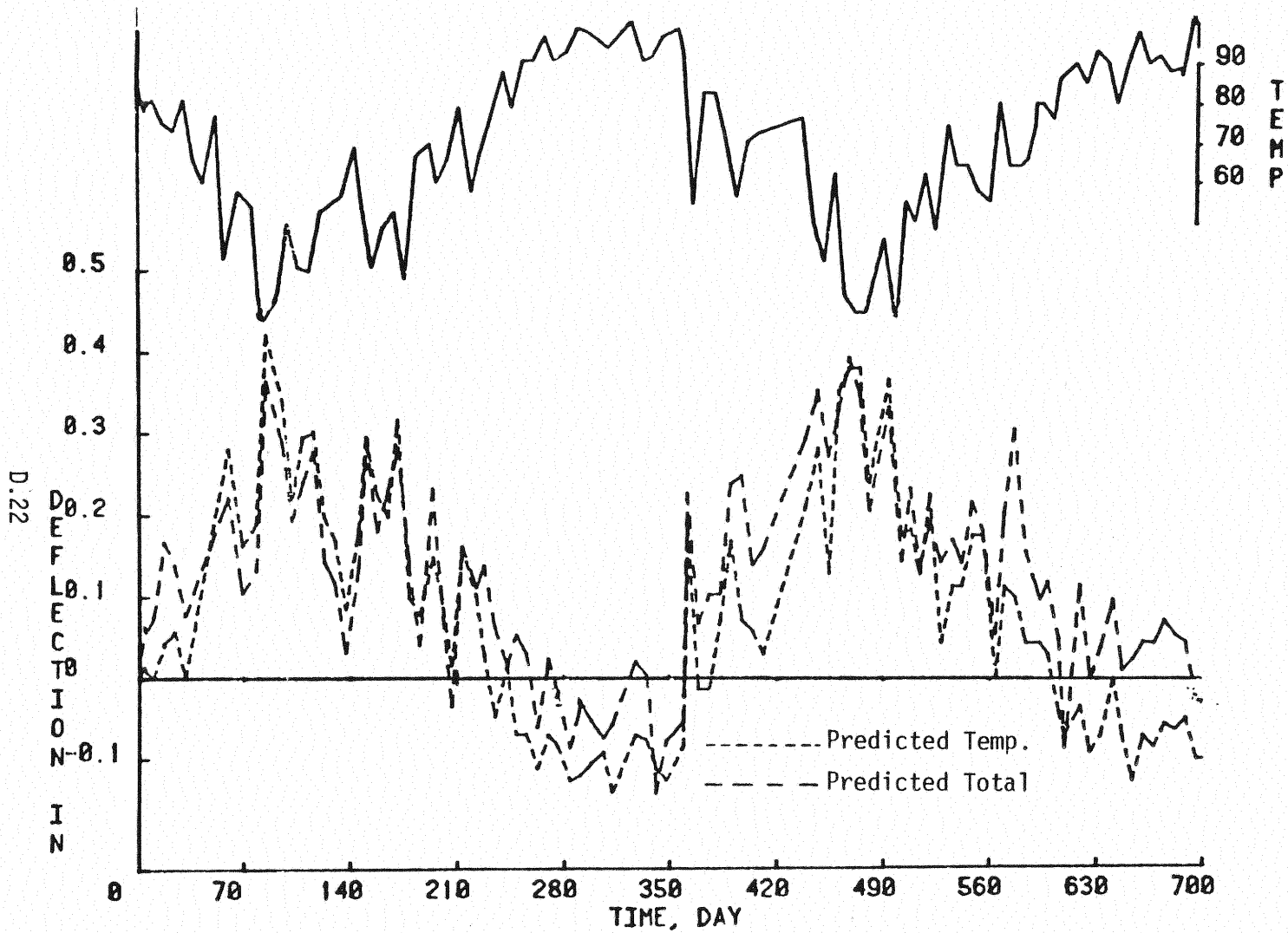
Figure D.11 Comparison of Branson's Predicted Deflection Due to Temperature Effects with Branson's Predicted Deflection Due to Combined Effects of Shrinkage and Creep and Temperature, Phase IV Sustained Loading Test
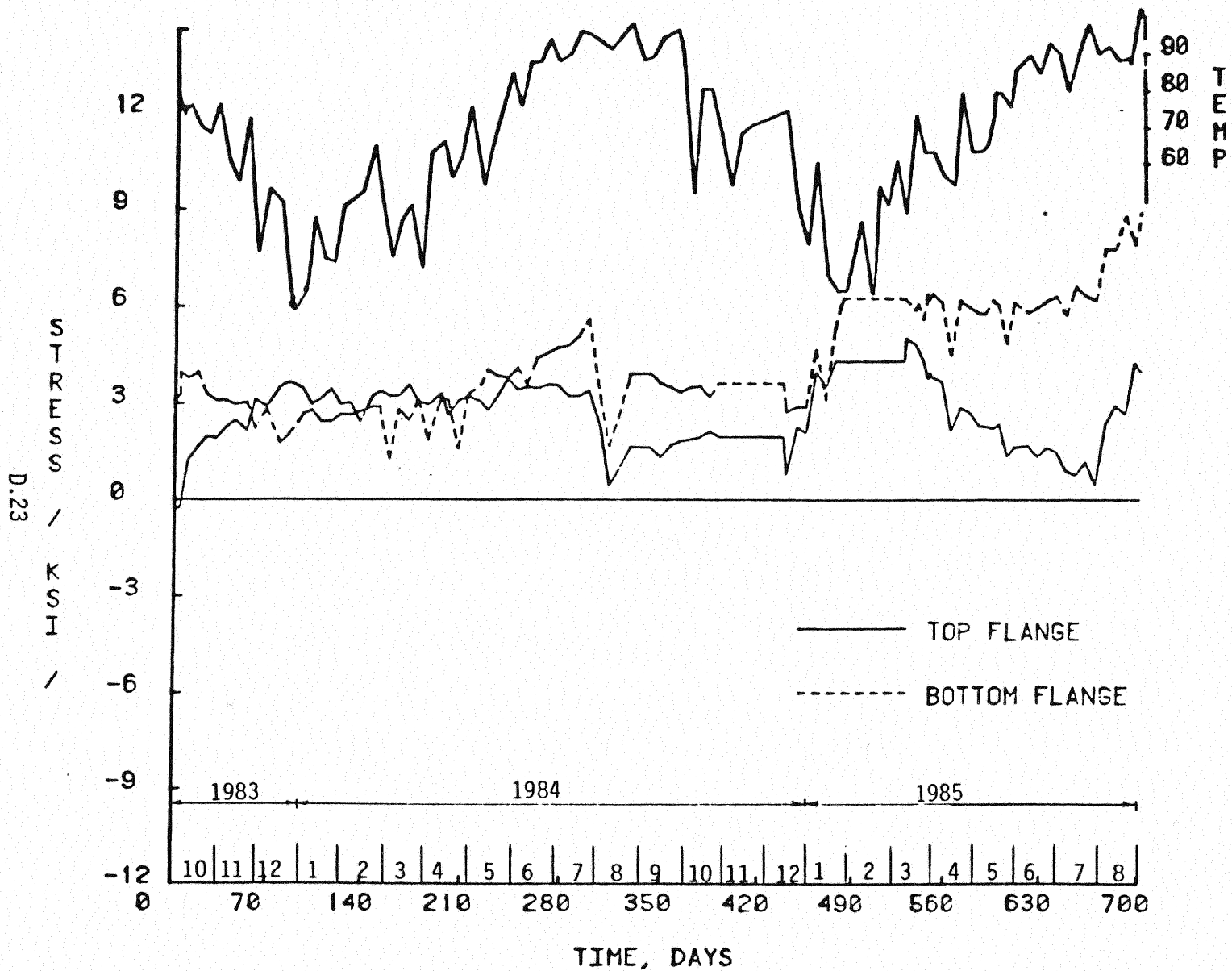
Figure D.12 Changes in Beam Flange Stresses vs. Time, Phase IV Sustained Loading Test

D.23
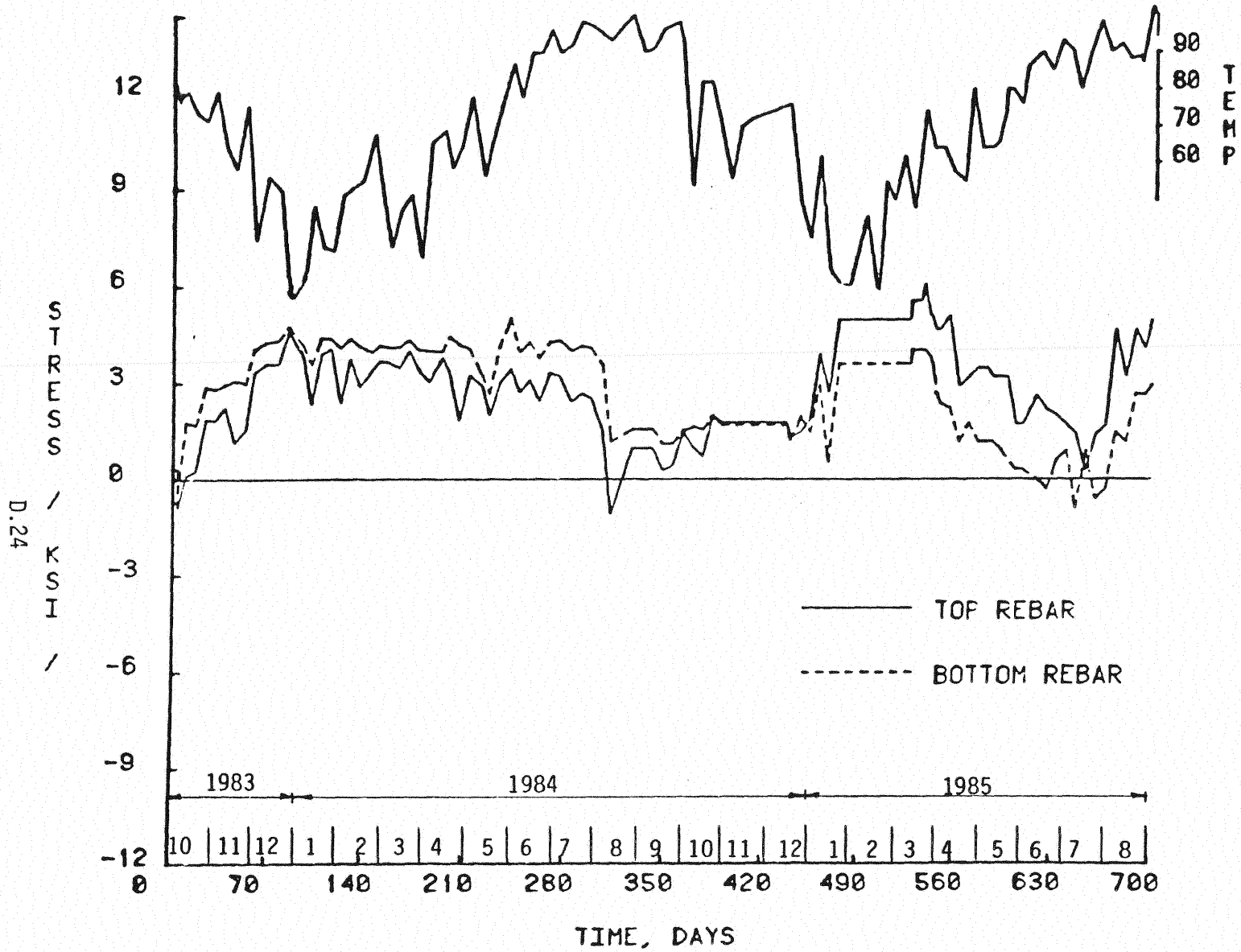
Figure D.13 Changes in Rebar Stresses vs. Time, Phase IV Sustained Loading Test

D.24

Table D.4   Notes on Plots for Phase XI, Sustained
             Loading Effects on Second Unit

MARK	NOTE
A	Unit set in Fears Laboratory
B	Spreader beams set in place
C	100,000 cycles HS-20 loading completed
D	200,000 cycles HS-20 loading completed
E	300,000 cycles HS-20 loading completed
F	400,000 cycles HS-20 loading completed
G	500,000 cycles HS-20 loading completed
H	First yield test performed
I	Spreader beams removed
J	Unit moved outside Fears Laboratory
K	Unit loaded with concrete blocks (40 psf)
L	End of observation of second unit

Table D.5

Beam Strains and Location of Apparent Neutral Axis, Phase XI Sustained Loading Effects on Second Unit

Days From Beginning of Observation	West Beam Strains (10^{-6}) in/in				Average Flange Strain		Apparent Neutral Axis Location from Bottom of Beam (In.)
	Top of Top Flange		Bottom of Bottom Flange				
	Ext.	Int.	Ext.	Int.	Top	Bottom	
1	− 12	− 6	571	563	− 9	567	20.50
2	− 11	− 6	592	583	− 9	588	20.52
3	− 12	− 22	601	591	− 17	596	20.25
4	− 18	− 27	607	598	− 23	603	20.06
5	− 16	− 25	601	600	− 21	601	20.13
6	− 28	− 41	612	608	− 35	610	19.70
13	− 57	− 96	647	642	− 77	645	18.61
19	− 70	−115	658	654	− 93	656	18.24
23	− 93	−135	659	654	−114	657	17.75
30	−103	−150	675	669	−127	672	17.52
36	−119	−161	692	686	−140	689	17.31
37	−127	−167	688	682	−147	685	17.15
38	−132	−170	686	681	−151	684	17.06
39	−134	−171	685	680	−153	683	17.02
40	−133	−169	690	685	−151	688	17.08
41	−134	−169	692	688	−152	690	17.07
42	−131	−166	699	695	−149	697	17.16
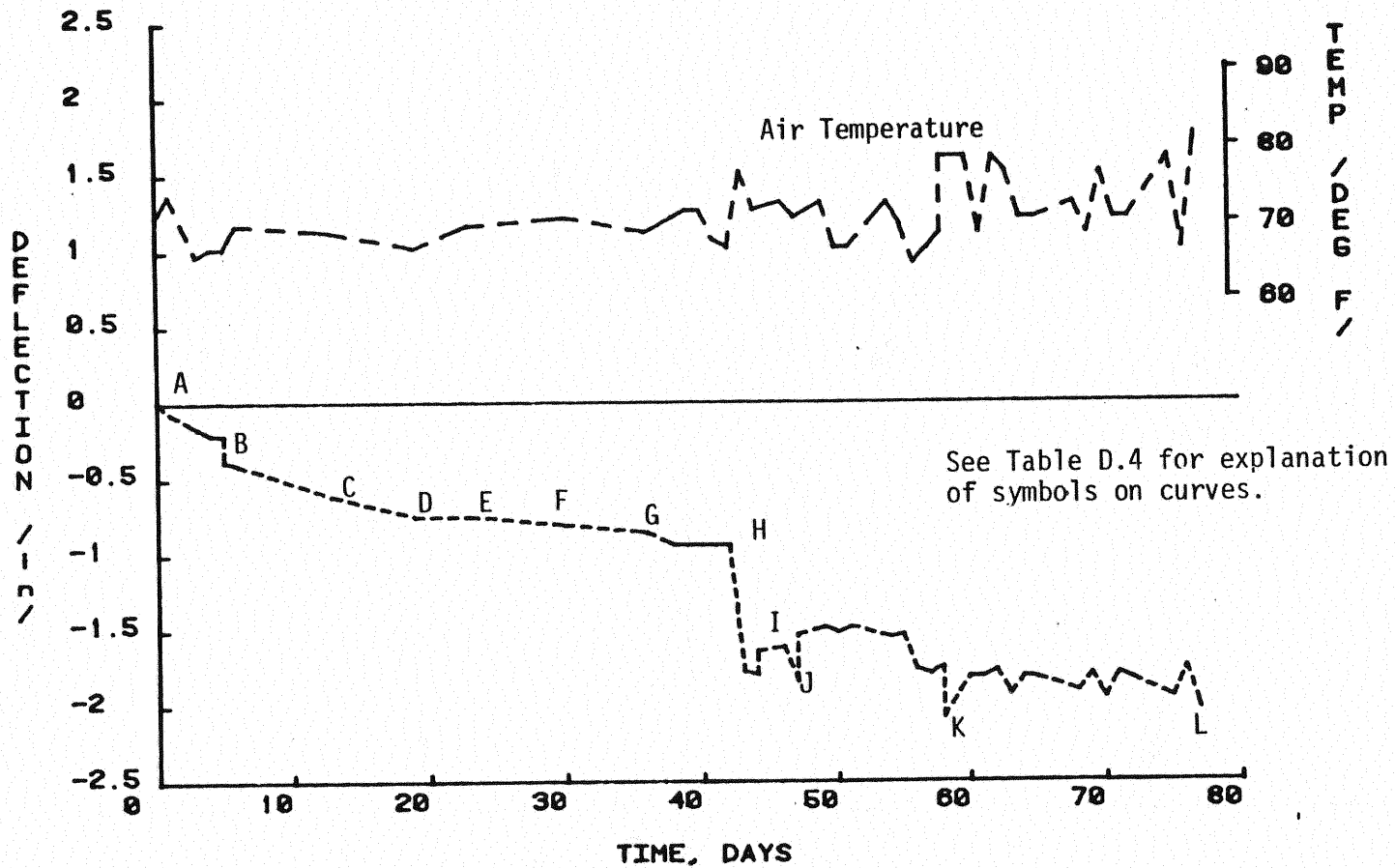
Figure D.14   Changes in Deflection vs. Time, Phase XI Sustained Loading Effects on Second Unit
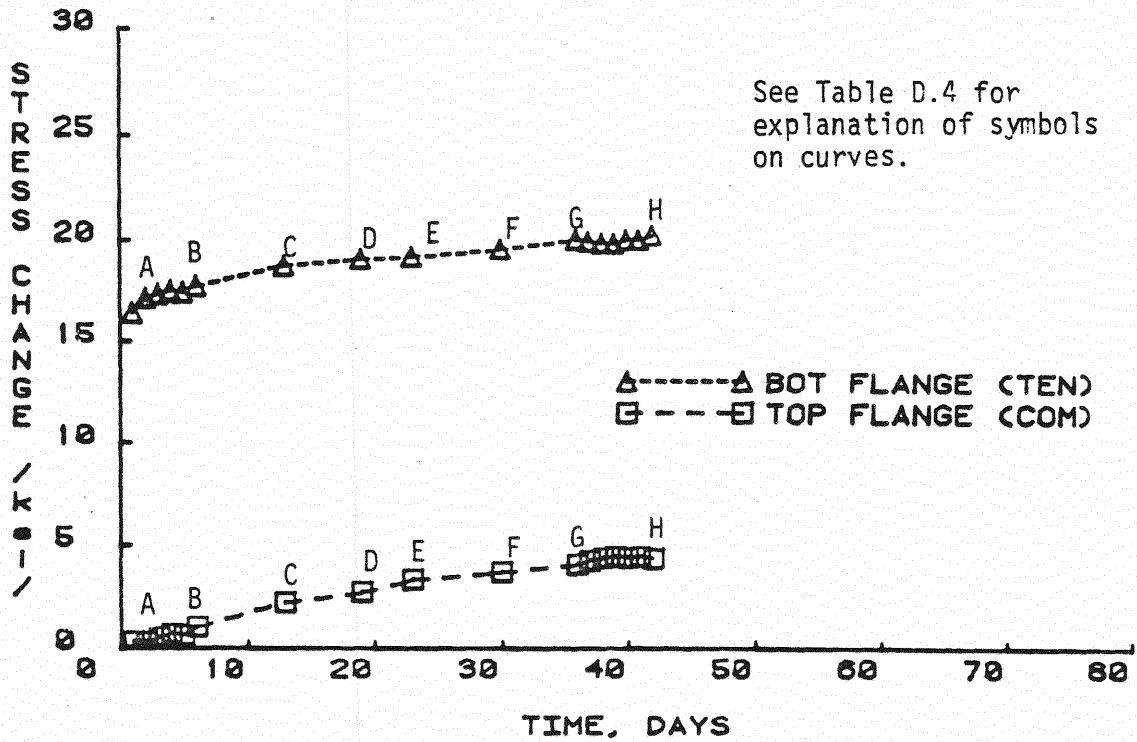
Figure D.15   Change in Stress in Beam Flanges vs. Time, Phase XI
Sustained Loading Effects on Second Unit
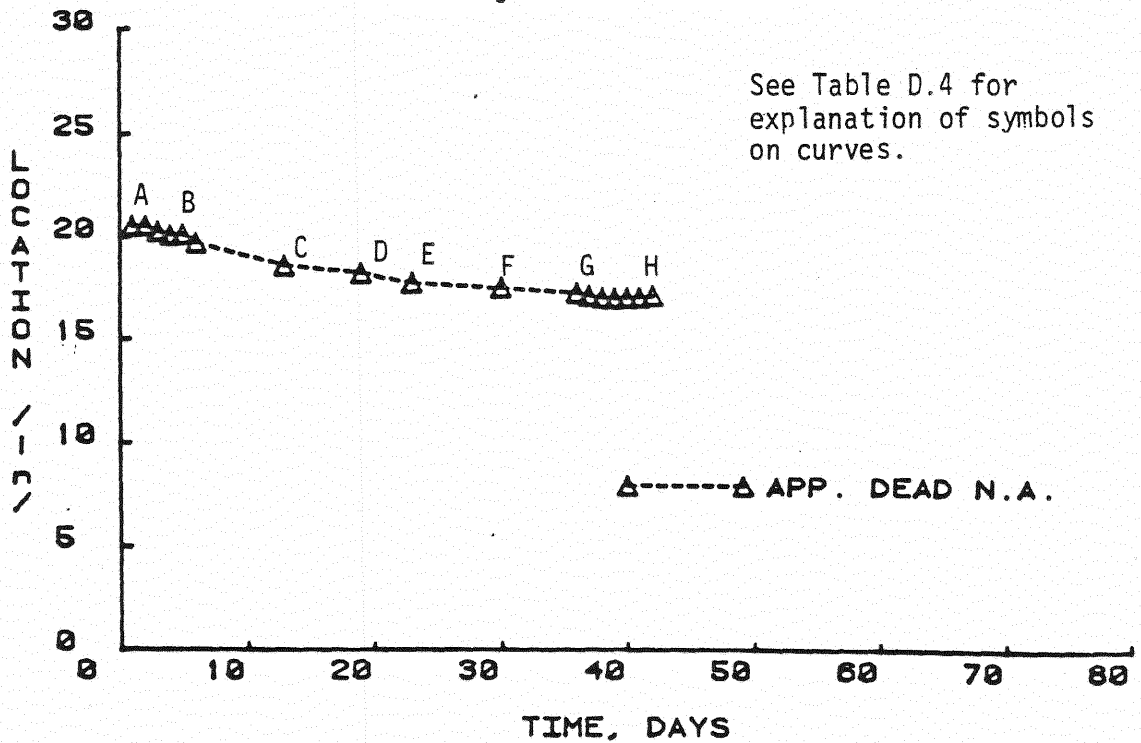
Figure D.16   Apparent Neutral Axis Location from Beam Bottom vs. Time,
Phase XI Sustained Loading Effects on Second Unit

D.28

Table D.6

Changes in Bottom Flange Stress and Camber, Phase XI
Sustain Loading Effects on Second Unit

Loading Step	Measured Bottom Flange Stress (ksi)	Stepwise Change in Measured Bottom Flange Stress (ksi)	Predicted Bottom Flange Stress (ksi)	Stepwise Change in Predicted Bottom Flange Stress (ksi)	Measured Camber (in)	Stepwise Change in Measured Camber (in)	Predicted Camber (in)	Stepwise Change in Predicted Camber (in)
1. Beams inverted and simply supported	- 2.6	- 2.6	- 2.4	- 2.4	0.14	-	0.34	-
2. Forms attached	- 7.7	- 5.1	- 7.5	- 5.1	0.91	0.77	1.08	0.74
3. Concrete poured	-19.4	-11.7	-21.3	-13.8	2.47	1.56	3.07	1.99
4. Extra weight added	-27.1	- 7.7	-28.8	- 7.5	3.34	0.87	3.93	0.86
5. Extra weight removed	-20.4	6.7	-24.4	4.4	2.95	-0.39	3.68	-0.25
6. Forms removed and unit turned 90°	- 8.2	12.2	-12.0	12.4	-	-	-	-
7. Unit turned additional 90° and set in Fears Laboratory	0.0	8.2	- 2.6	9.4	1.95	-1.00	2.14	-1.54
8. Spreader beams set in place	3.4	3.4	0.0	2.6	1.57	-0.38	1.97	-0.17
9. Prior to first yield test	6.2	2.8	3.0	3.0	1.02	-0.55	1.39	-0.58
Sum of Changes		6.20		3.0		0.88		1.05

APPENDIX E

REPEATED LOADING TEST RESULTS

SECTION E.1

PHASE II TEST RESULTS

500,000 CYCLES OF HS-20 LOADING
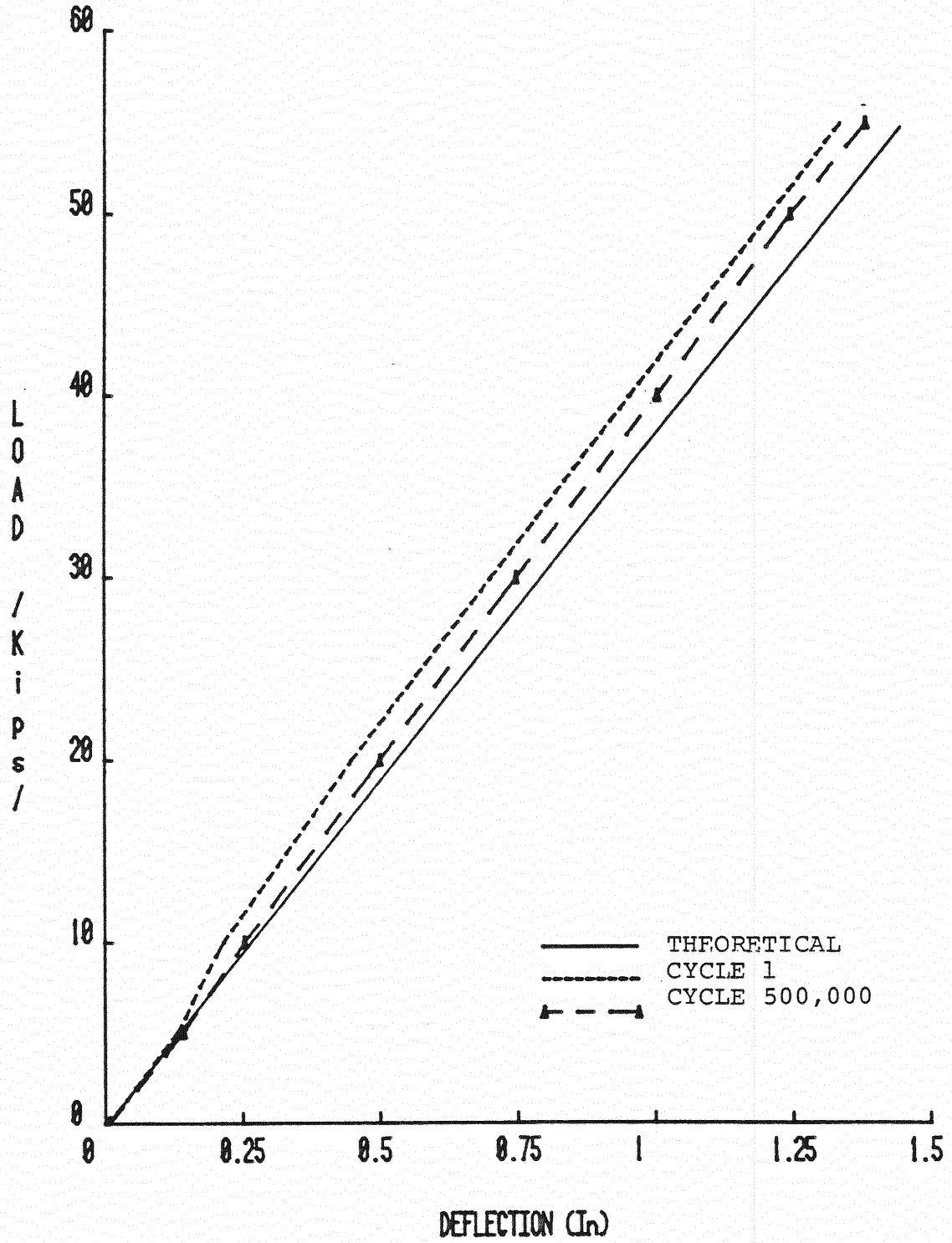
Figure E.1 Load vs. Deflection, Phase II Repeated Loading
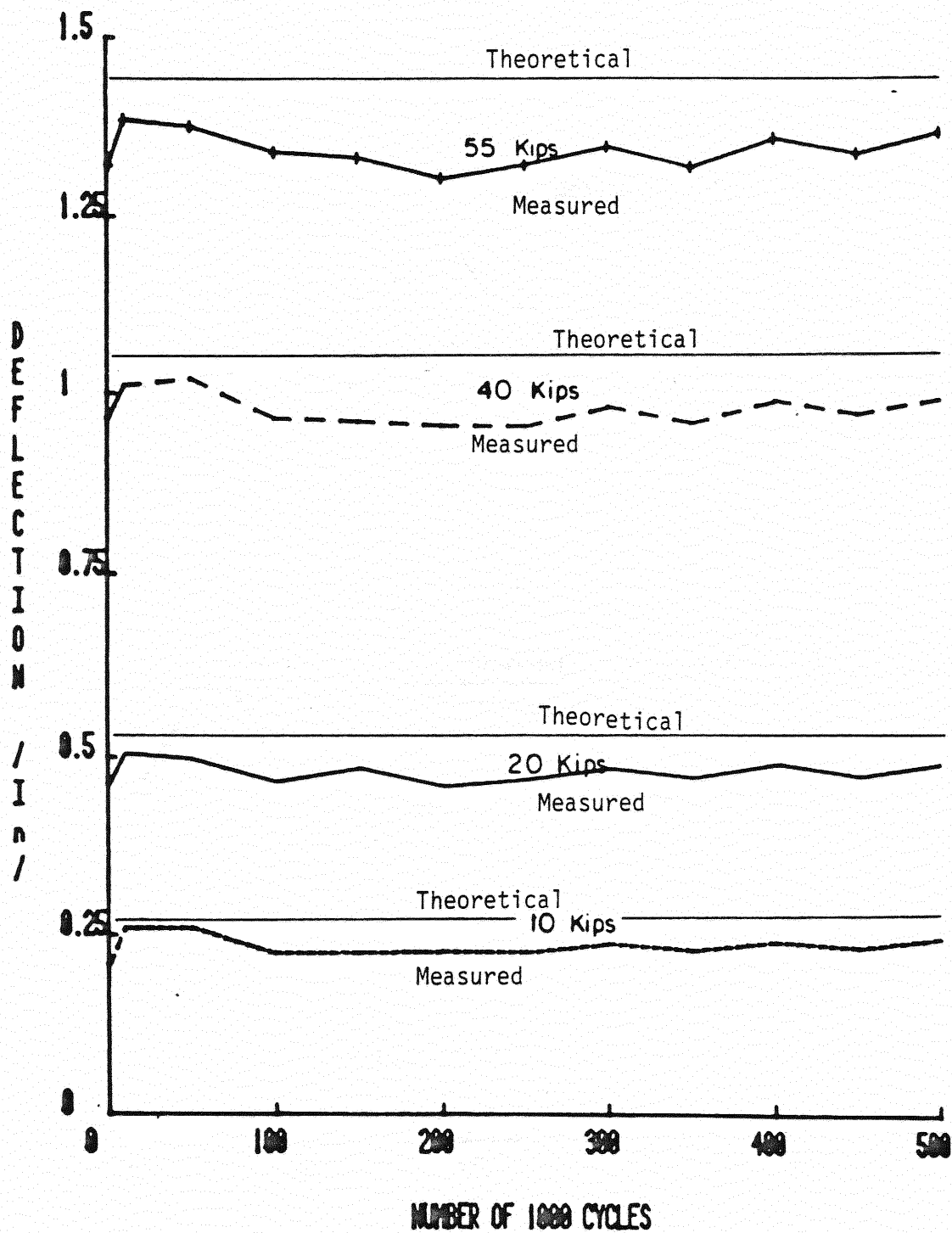
Figure E.2 Midspan Deflection vs. Number of Cycles, Phase II Repeated Loading
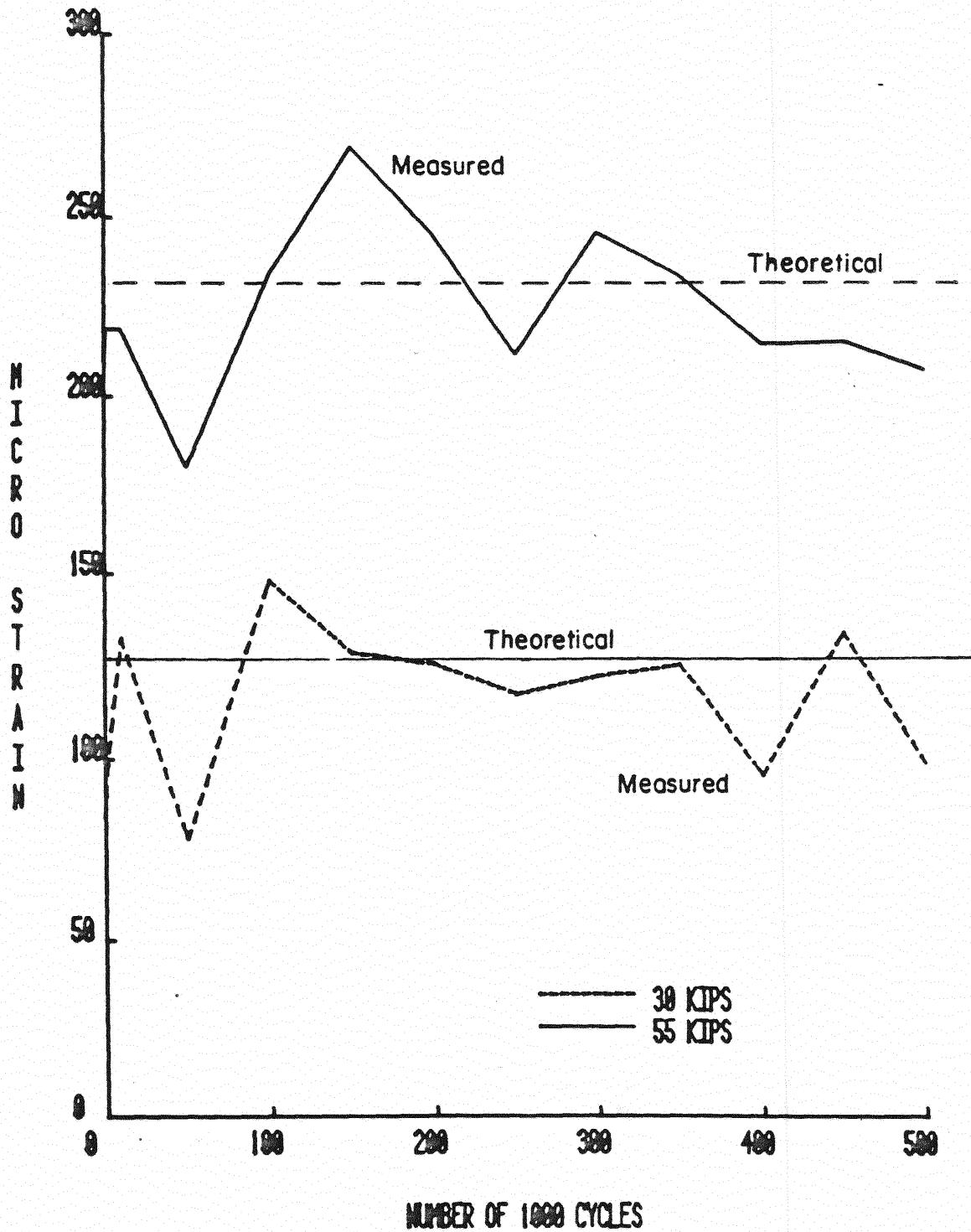
Figure E.3   Change in Strain of Top Concrete vs. Number of Cycles,
            Phase II Repeated Loading
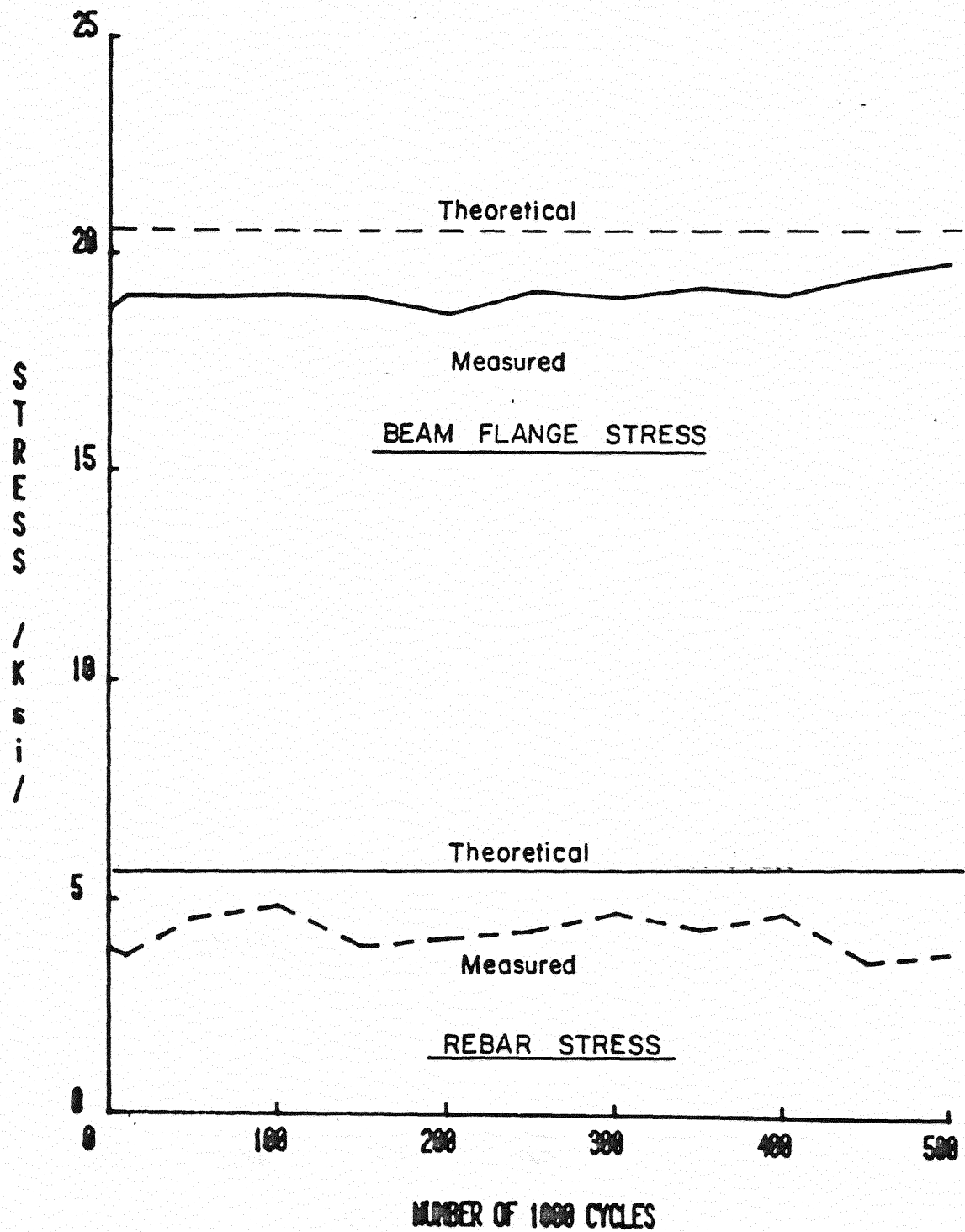
Figure E.4 Steel Stress vs. Number of Cycles, Phase II Repeated Loading
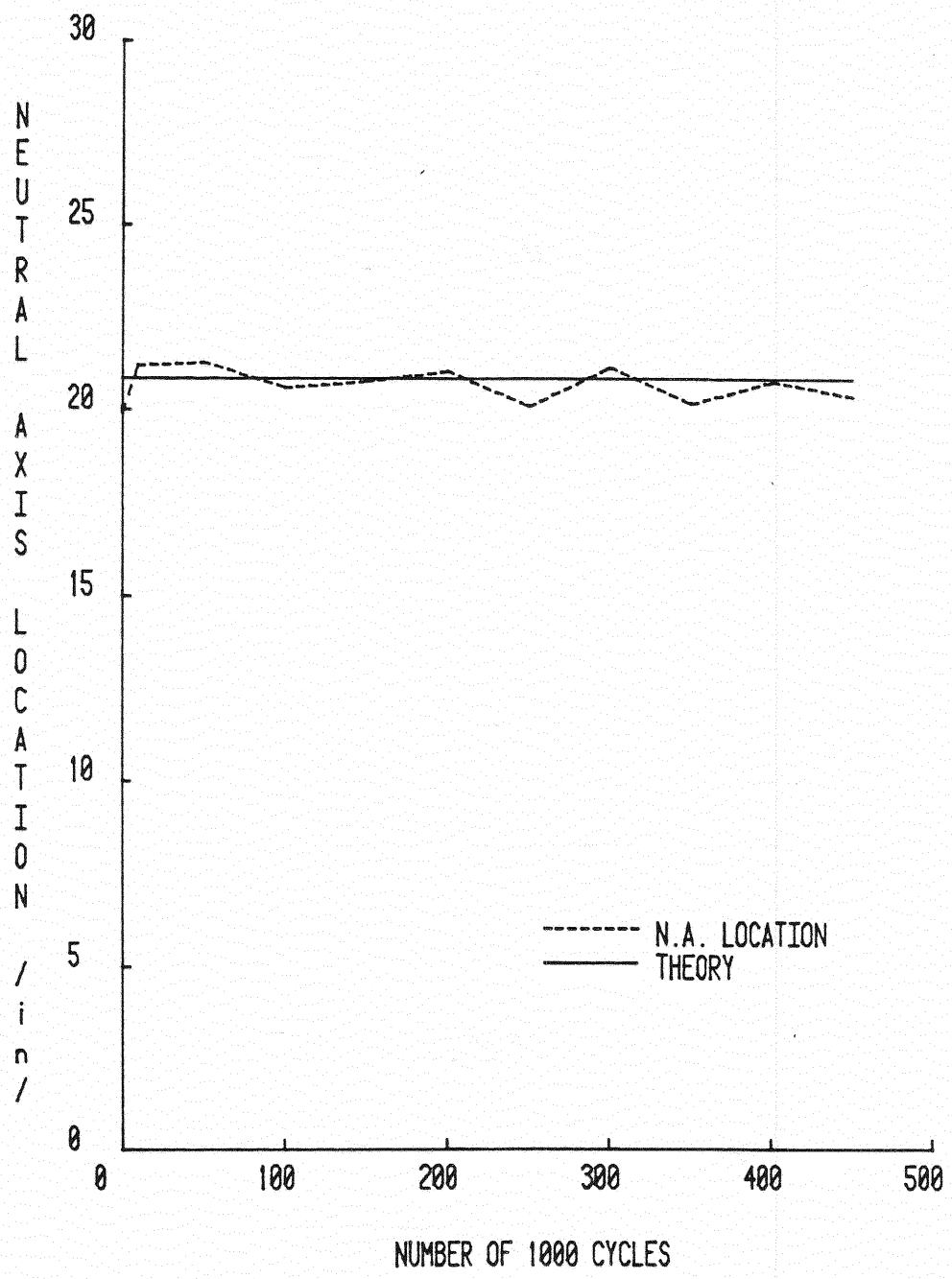
Figure E.5   Neutral Axis Location from Beam Bottom vs. Number of
             Cycles, Phase II Repeated Loading

SECTION E.2

PHASE V TEST RESULTS

1,500,000 CYCLES OF HS-20 LOADING
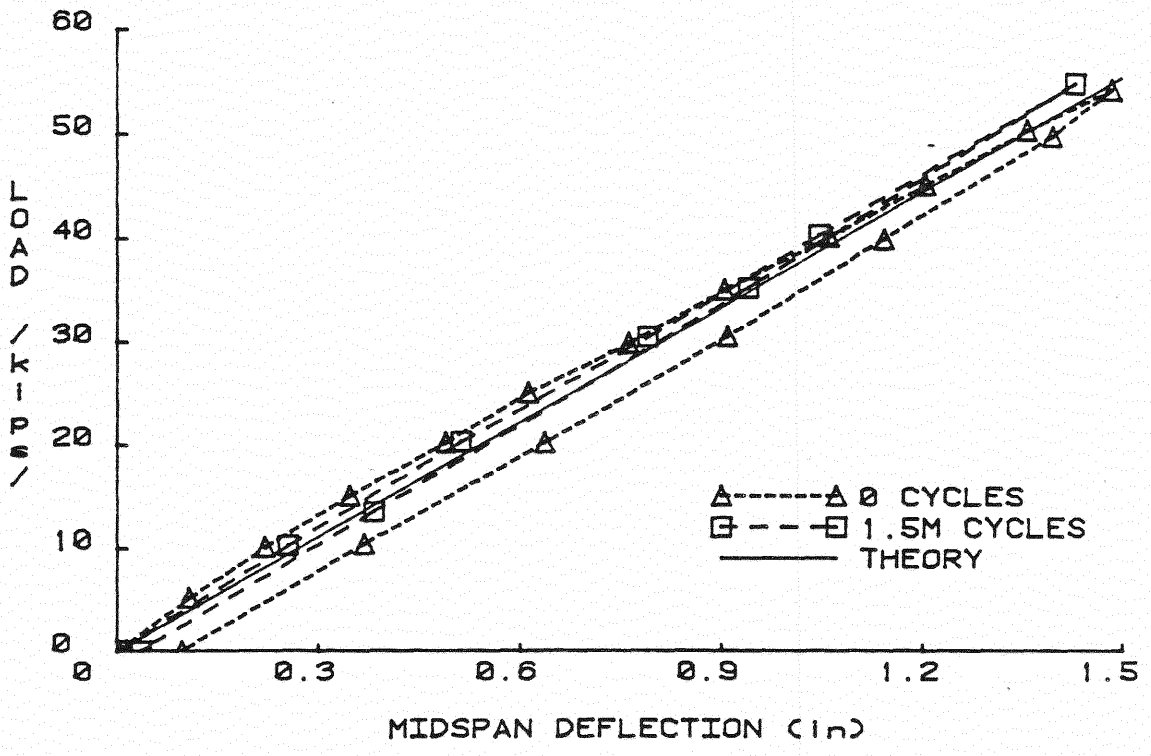
a. East Beam
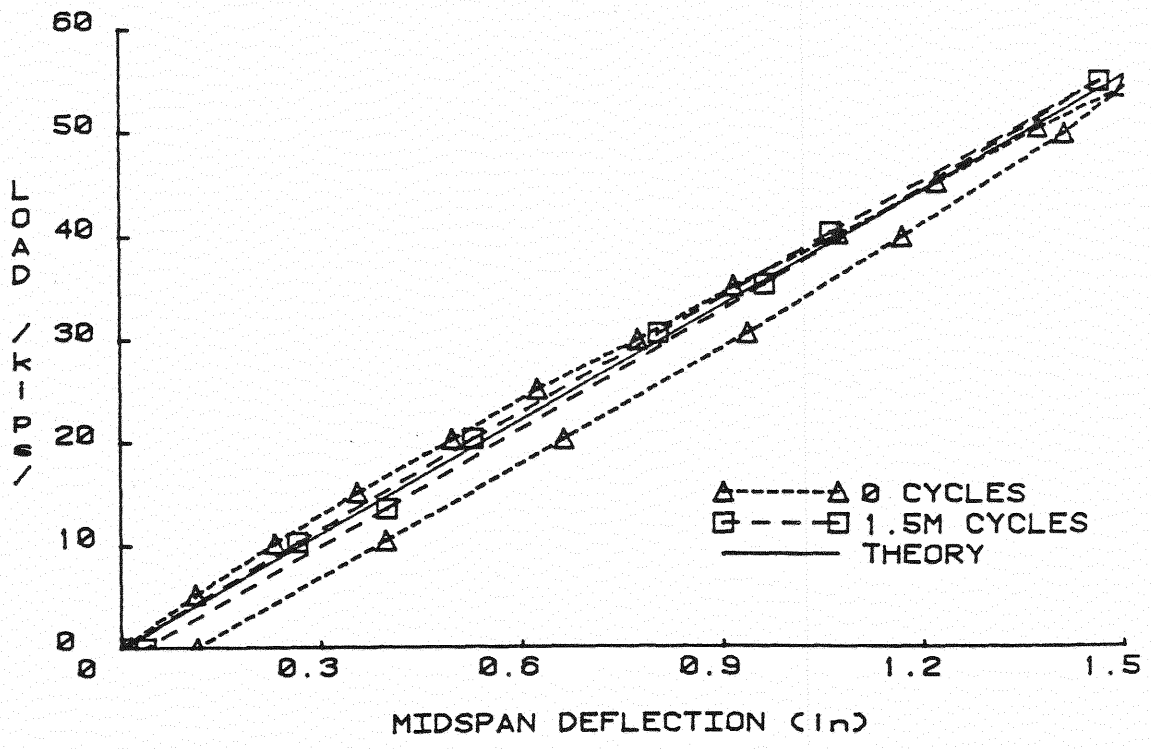
b. West Beam

Figure E.6 Load vs. Midspan Deflection, Phase V Repeated Loading

E.8
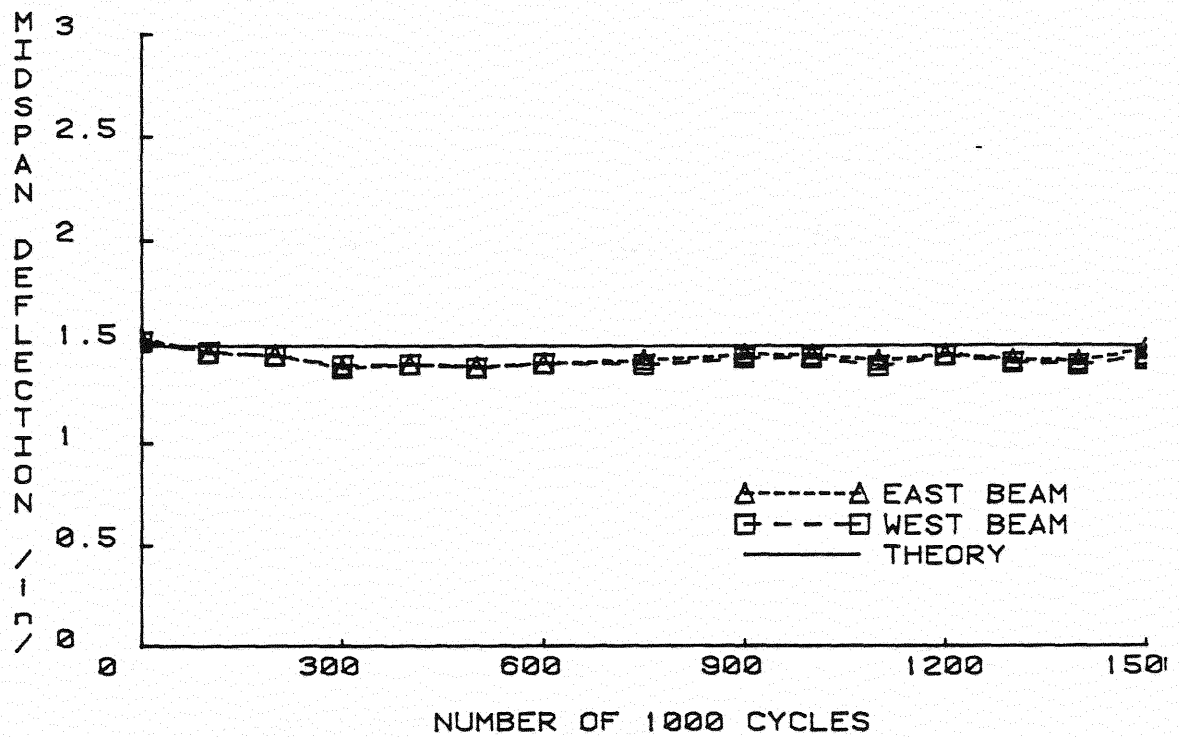
Figure E.7 Midspan Deflection vs. Number of Cycles, Phase V Repeated Loading
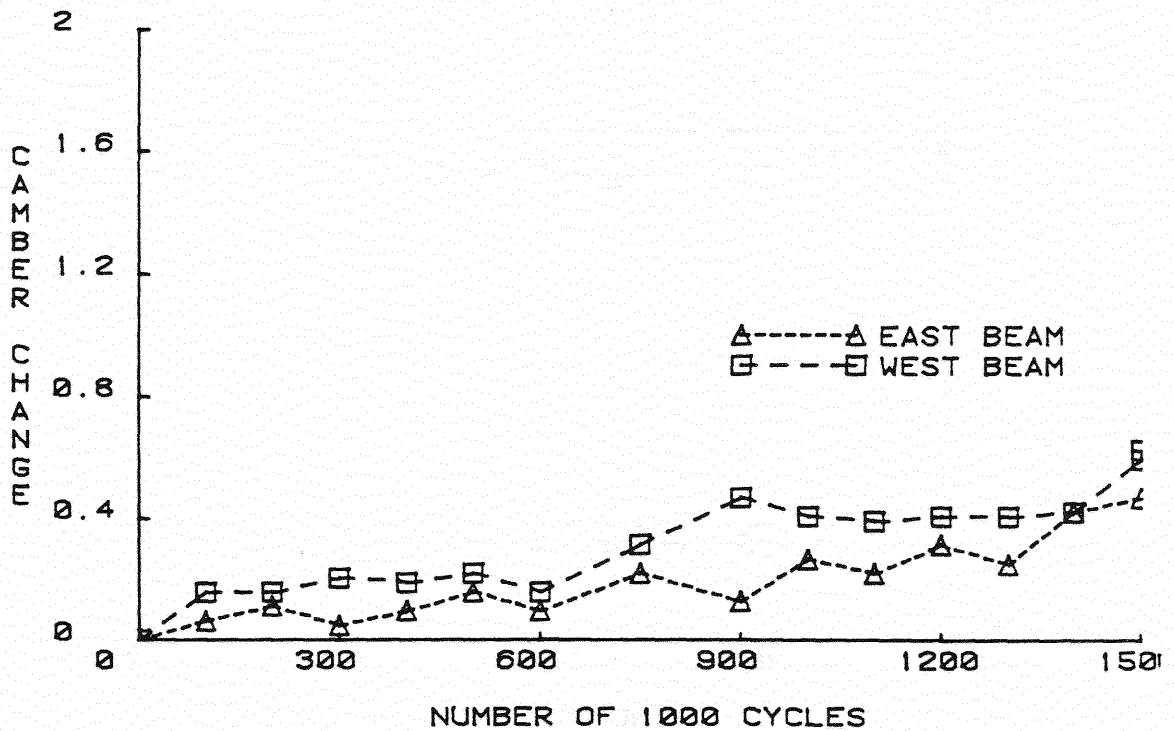
Figure E.8 Camber Change vs. Number of Cycles, Phase V Repeated Loading
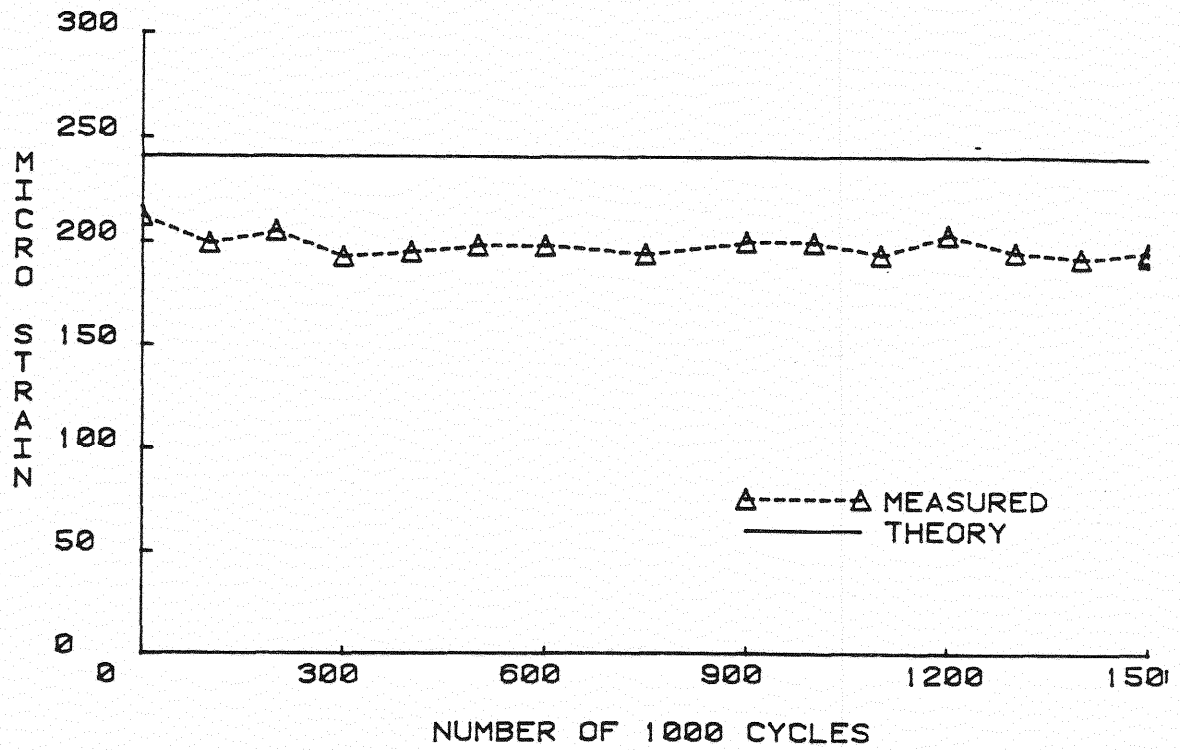
Figure E.9 Top of Concrete Strain vs. Number of Cycles, Phase V Repeated Loading
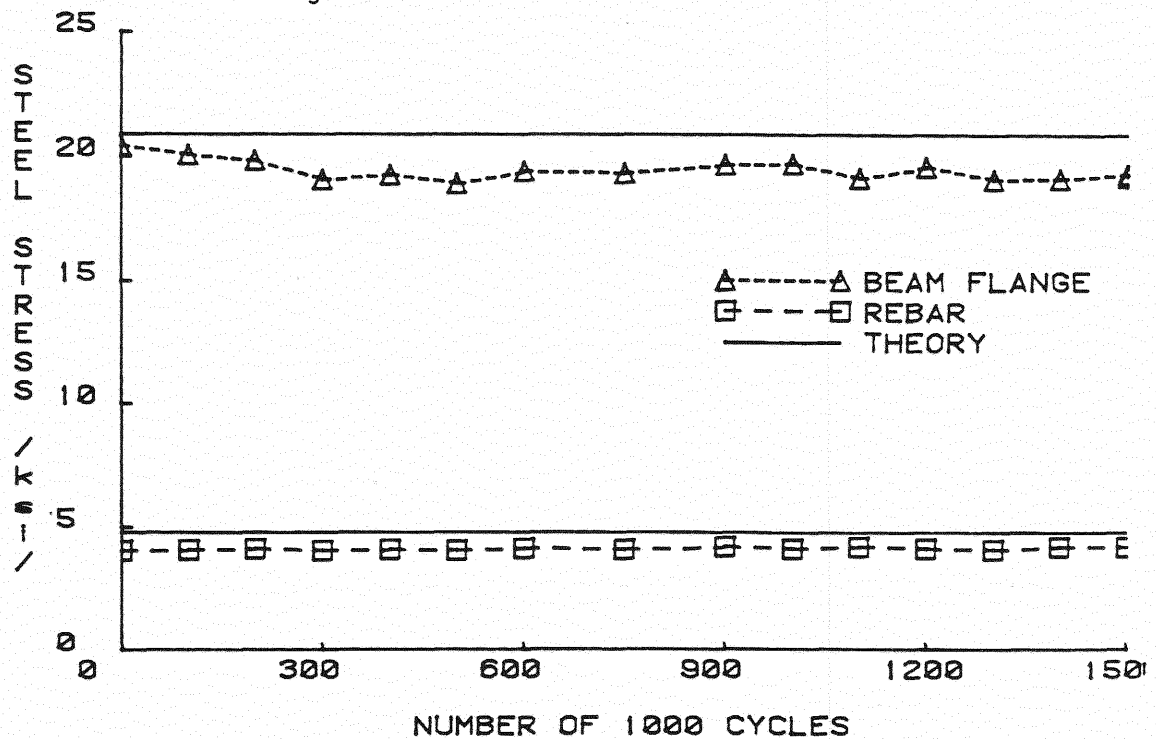
Figure E.10 Steel Stress vs. Number of Cycles, Phase V Repeated Loading

E.10
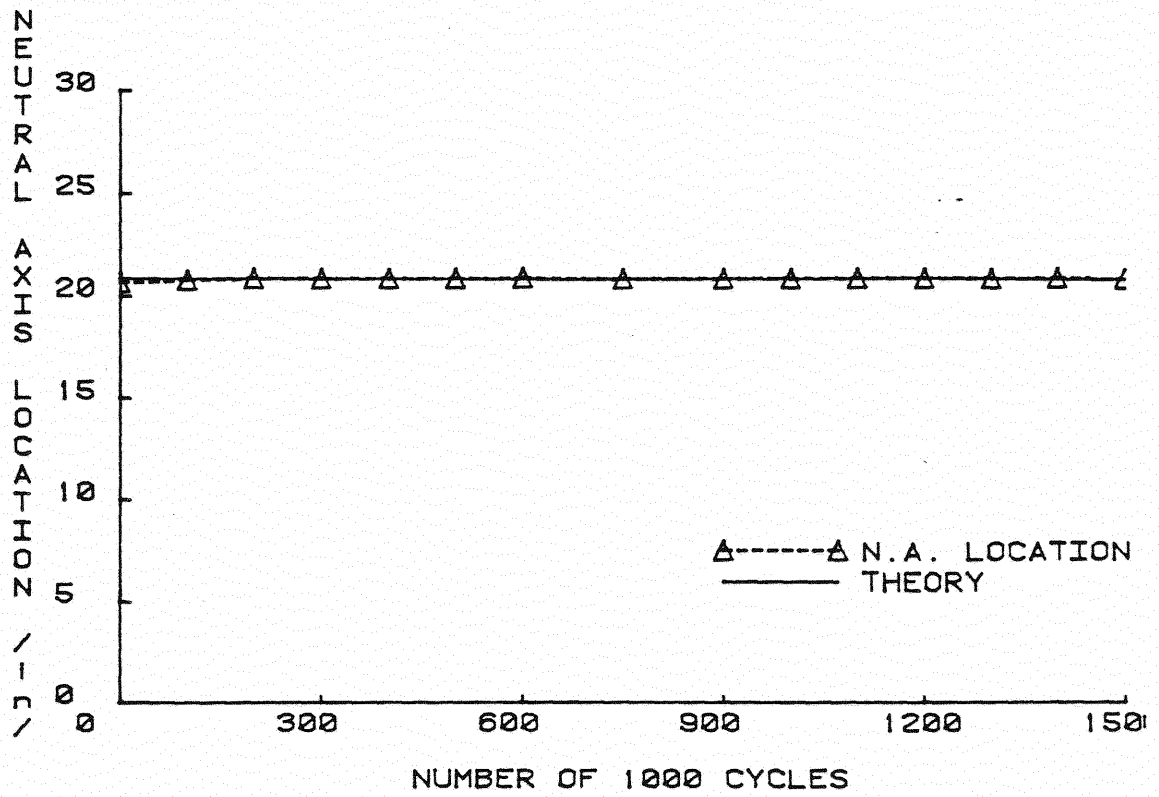
Figure E.11   Neutral Axis Location from Bottom of Beam vs. Number of
Cycles, Phase V Repeated Loading

SECTION E.3

PHASE VI TEST RESULTS

2000 CYCLES OF HS-30 LOADING
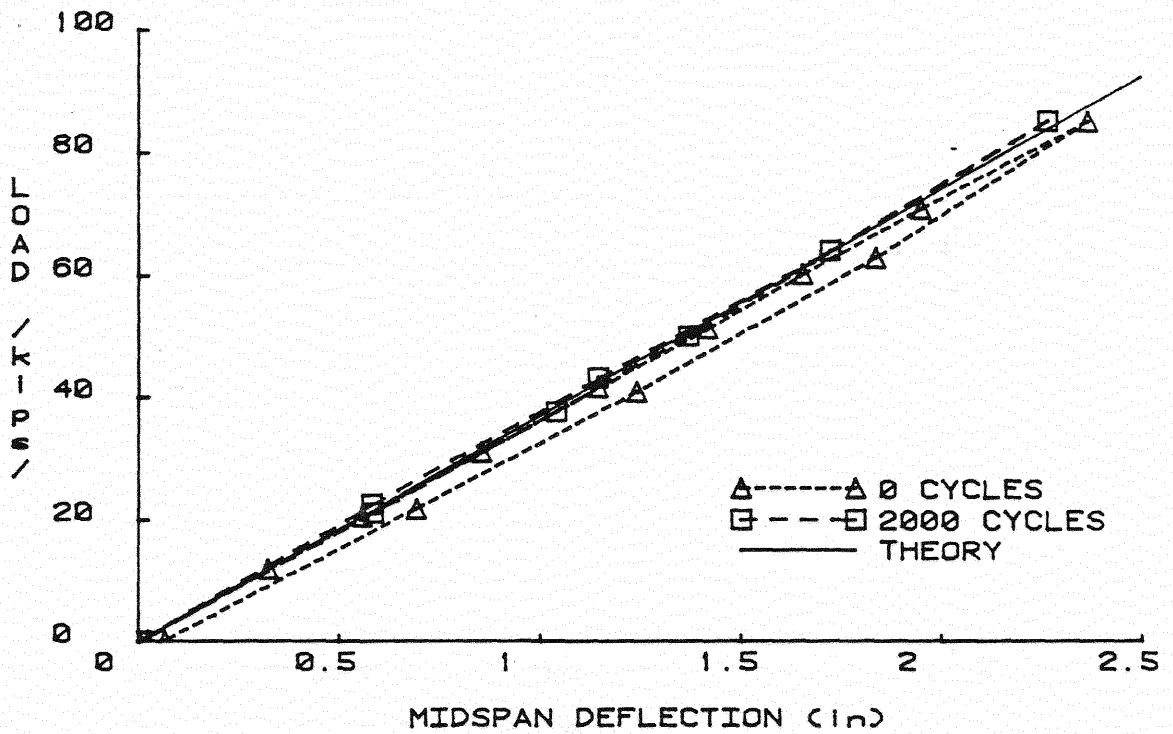
Figure E.12 Load vs. Midspan Deflection, Phase VI Repeated Loading
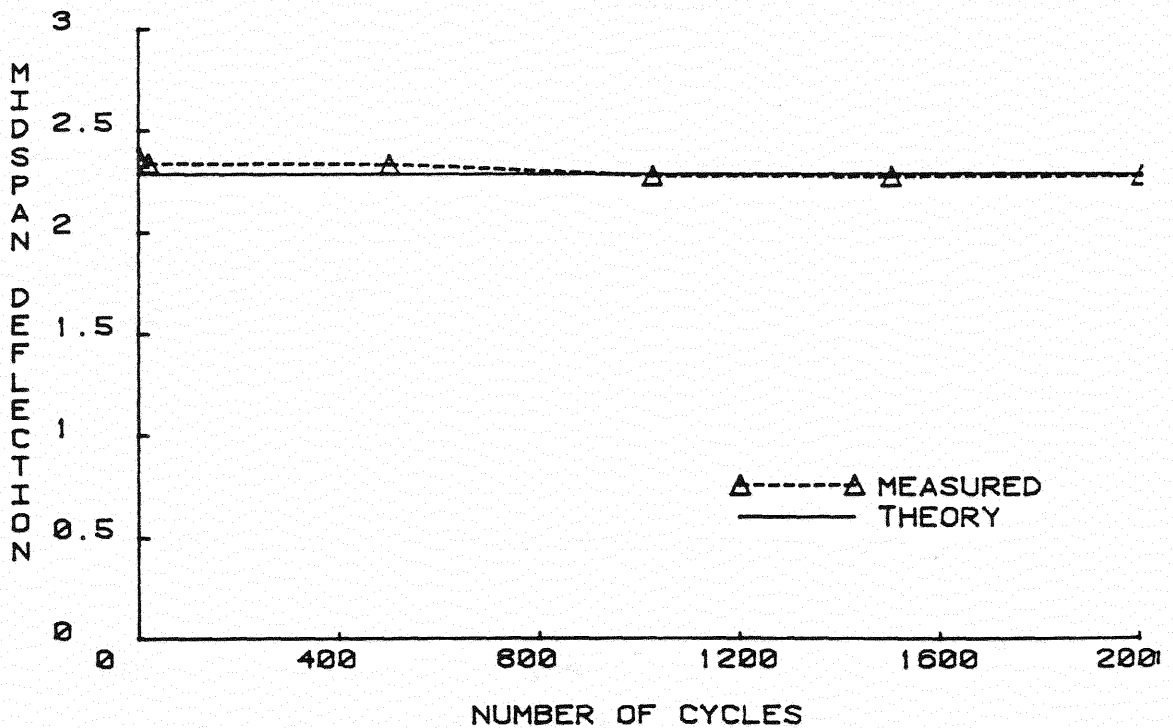
Figure E.13 Midspan Deflection vs. Number of Cycles, Phase VI Repeated
Loading

E.13
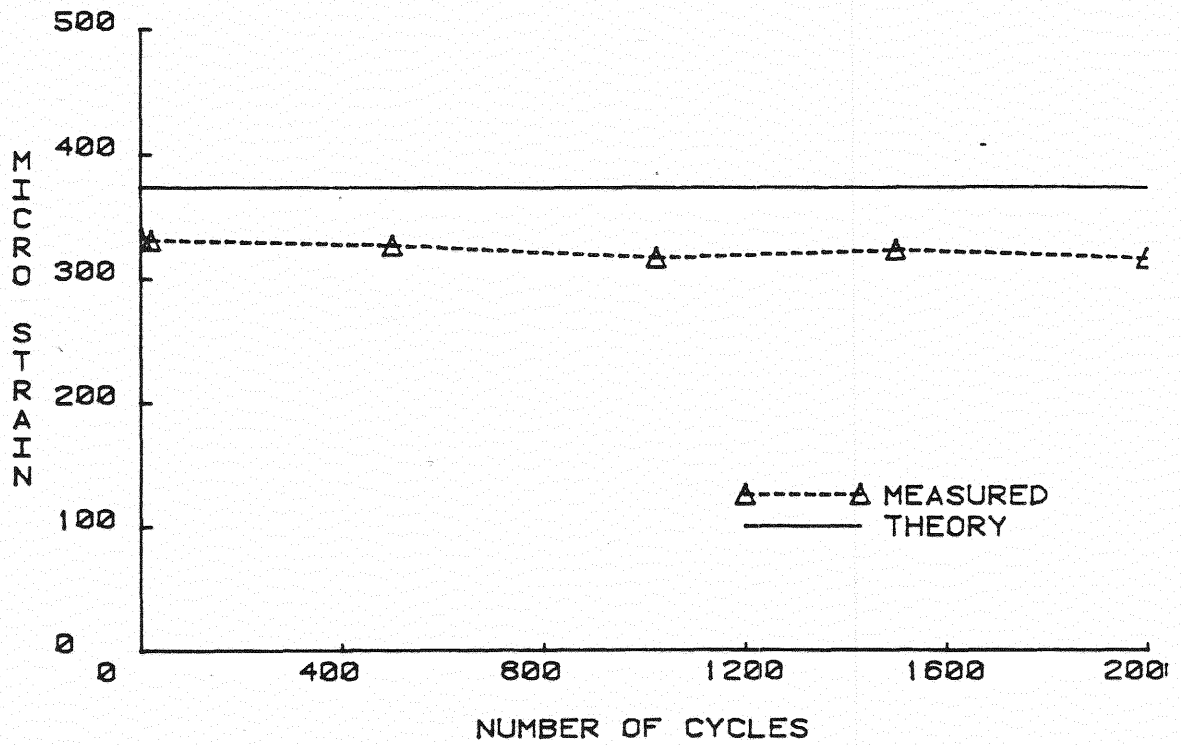
Figure E.14   Top of Concrete Strain vs. Number of Cycles, Phase VI
Repeated Loading
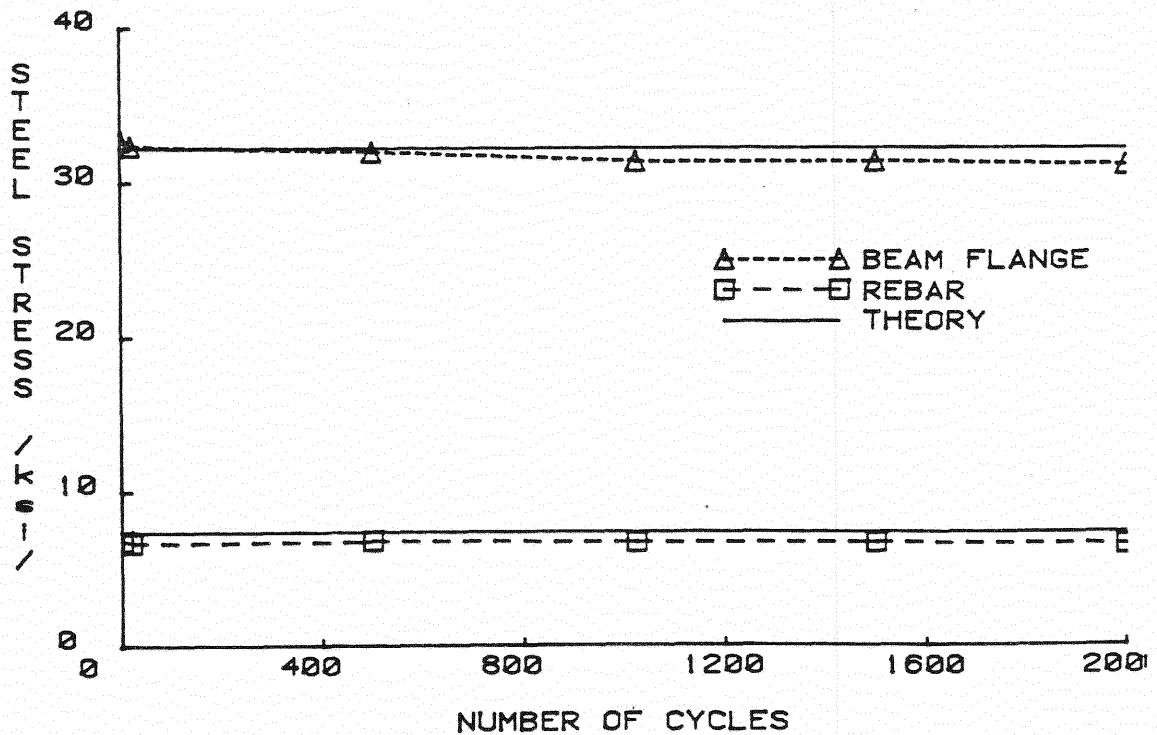
Figure E.15   Steel Stress vs. Number of Cycles, Phase VI Repeated Loading

E.14
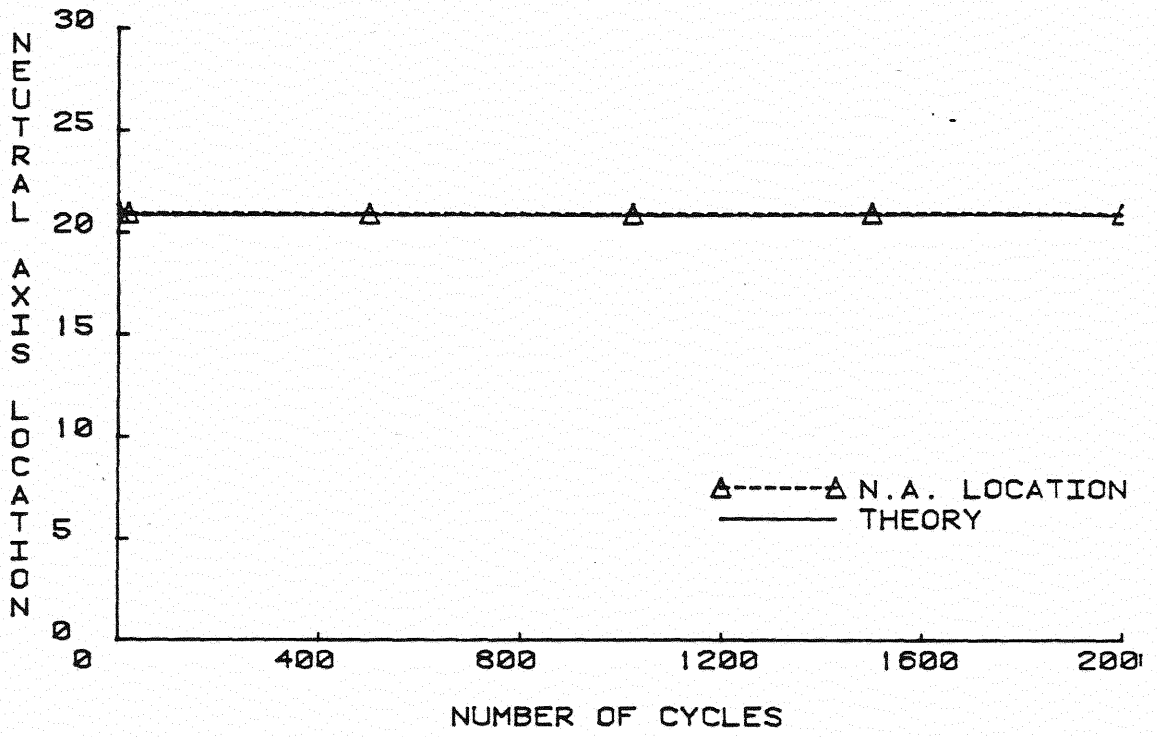
Figure E.16   Neutral Axis Location from Bottom of Beam, Phase VI
Repeated Loading

SECTION E.4

PHASE VII TEST RESULTS

100,000 CYCLES OF UNBALANCED HS-20 LOADING
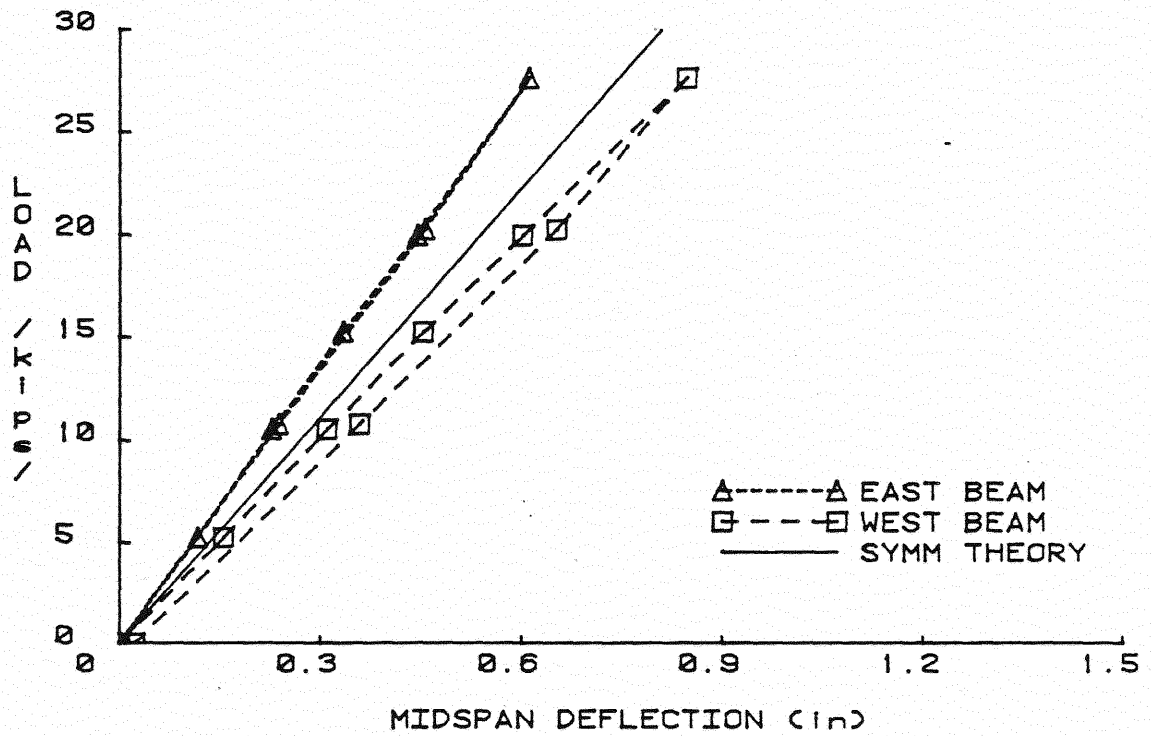
a. 0 Cycles
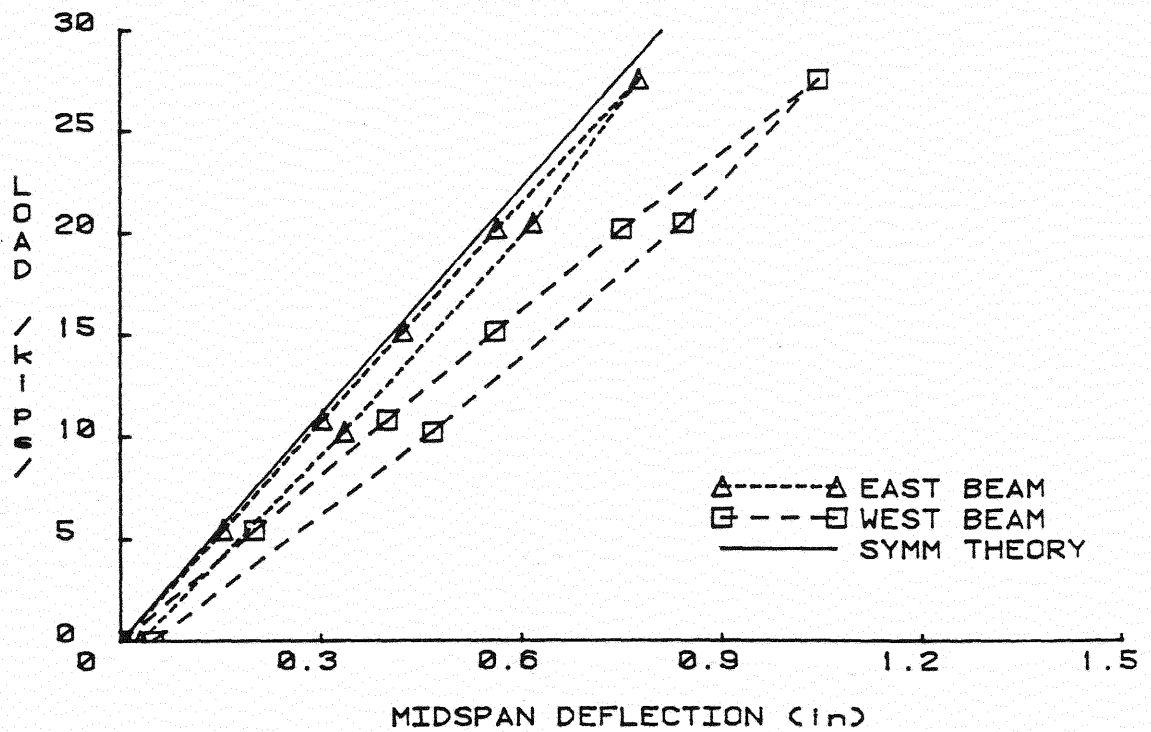
b. 100,000 Cycles

Figure E.17   Load vs. Midspan Deflection at 0 Cycles and 100,000 Cycles,
Phase VII Unbalanced Repeated Loading

E.17
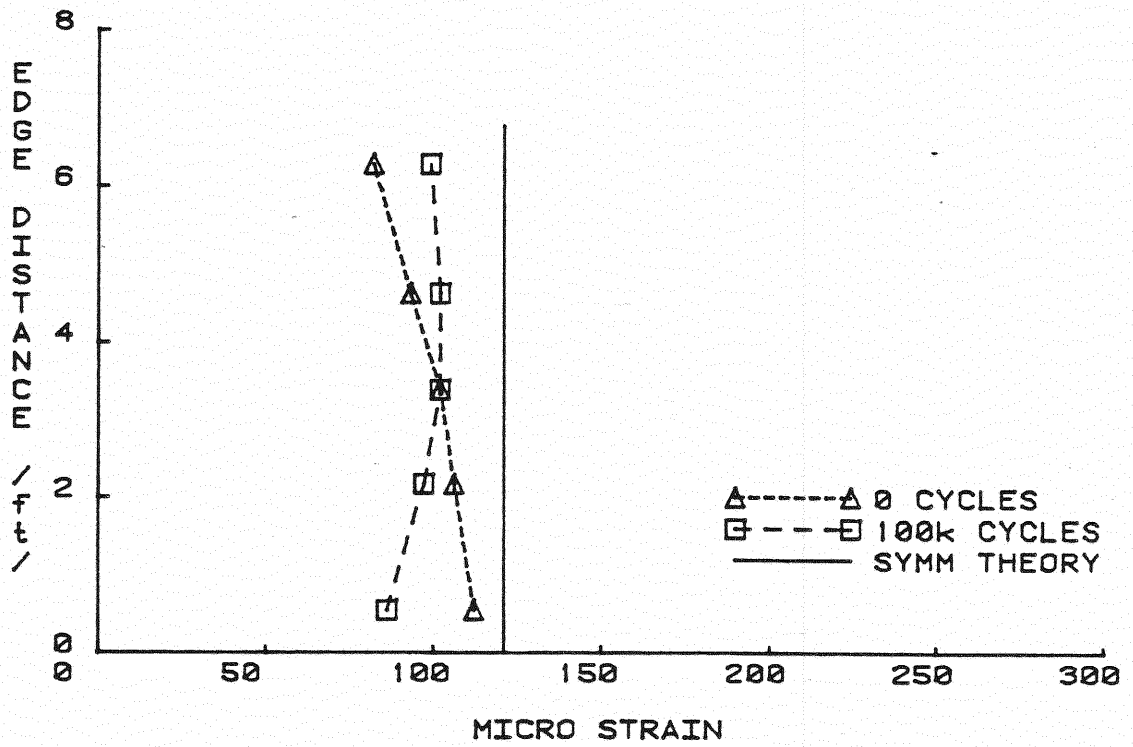
Figure E.18   Top Concrete Strain at Midspan Across the Slab Width,
Phase VII Unbalanced Repeated Loading
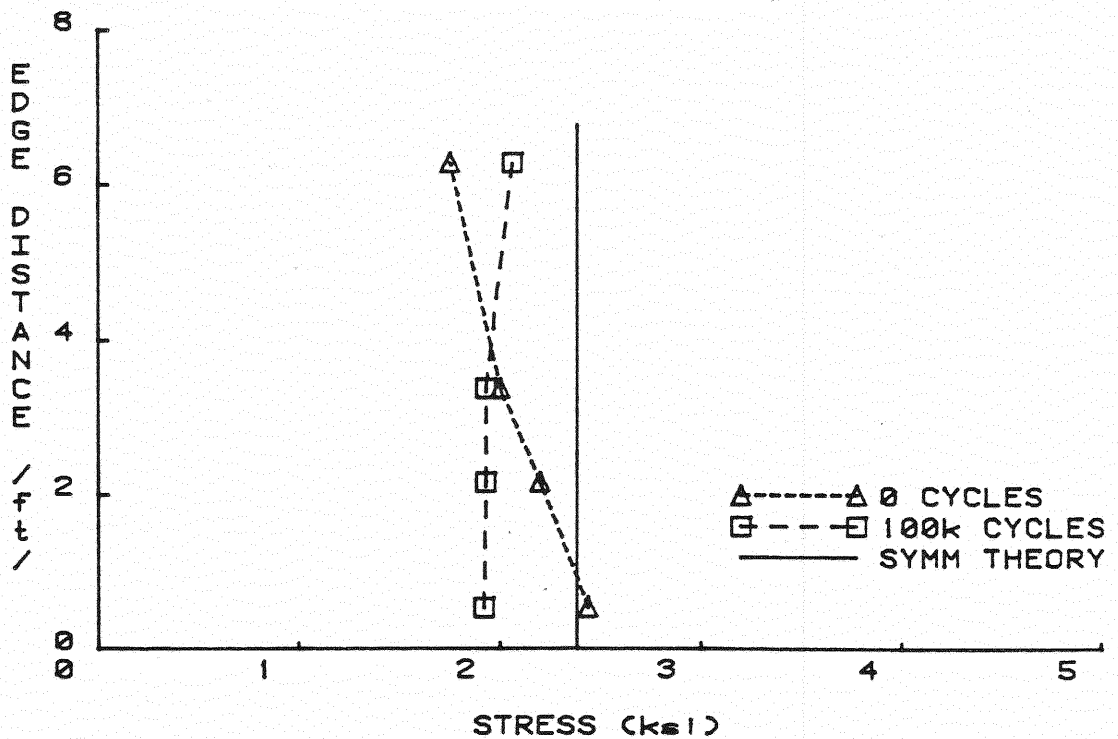
Figure E.19   Top Rebar Stress at Midspan Across the Slab Width,
Phase VII Unbalanced Repeated Loading

E.18
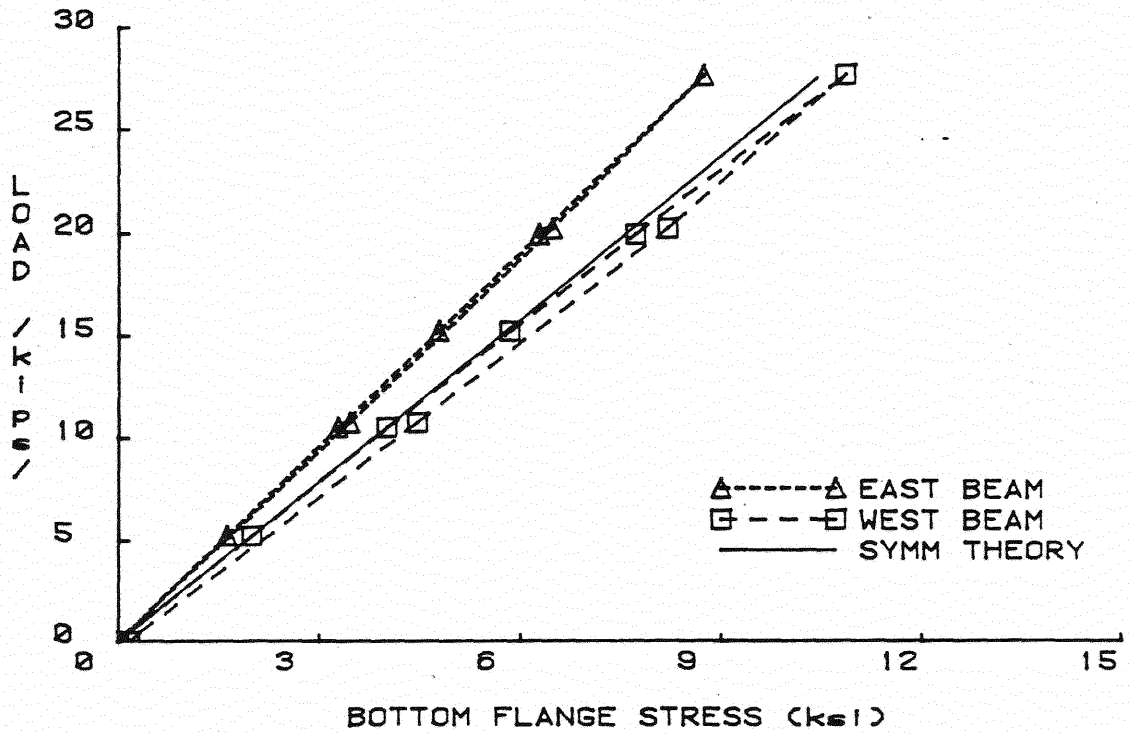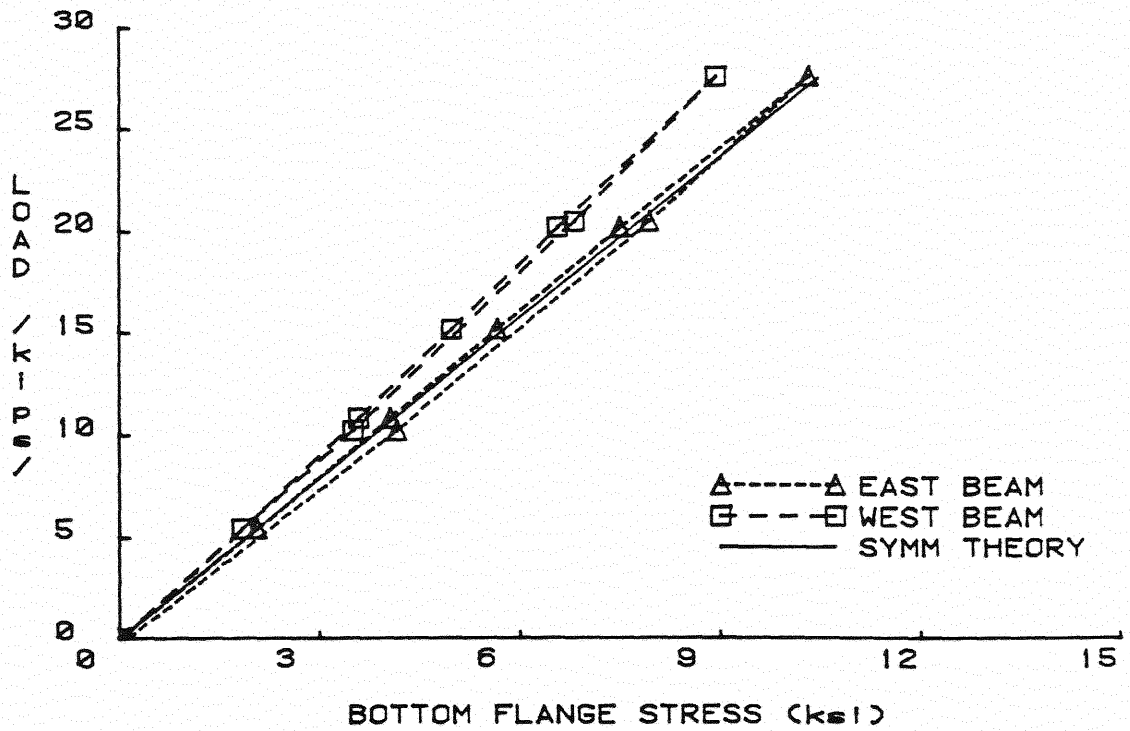
a. 0 Cycles

b. 100,000 Cycles

Figure E.20 Load vs. Beam Bottom Flange Stress at 0 Cycles and 100,000 Cycles, Phase VII Unbalanced Repeated Loading

E.19

SECTION E.5

PHASE IX TEST RESULTS

500,000 CYCLES OF HS-20 LOADING ON SECOND UNIT
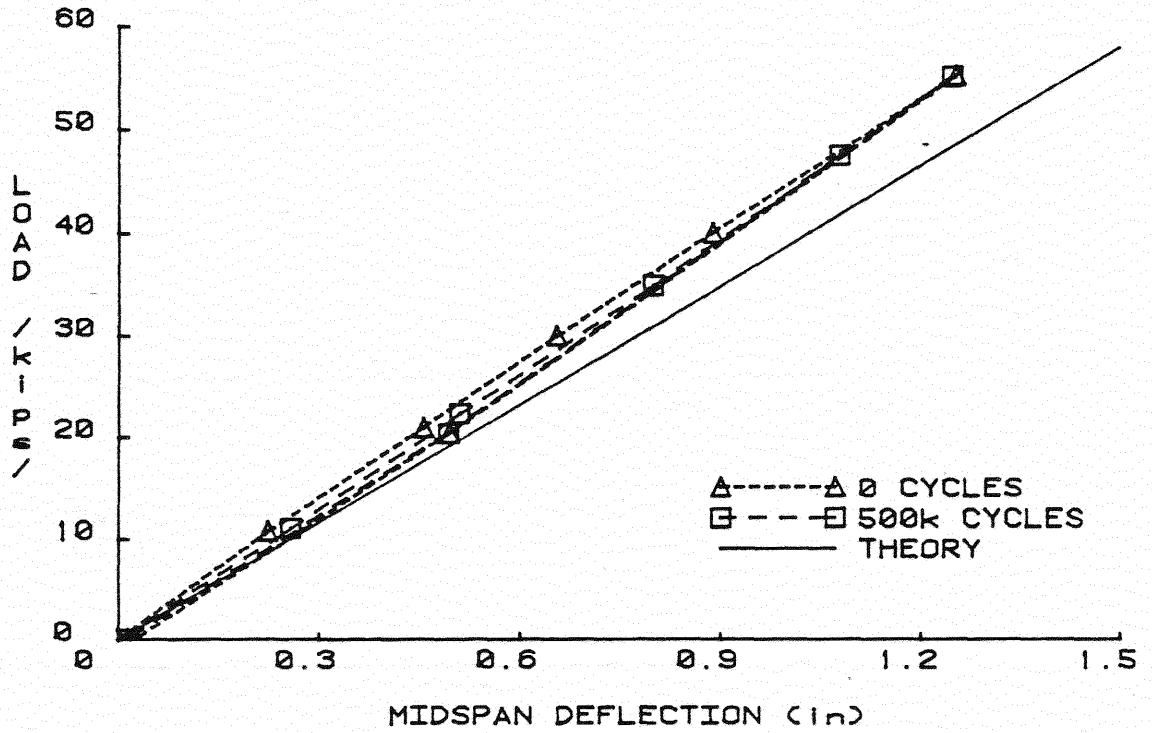
a. East Beam
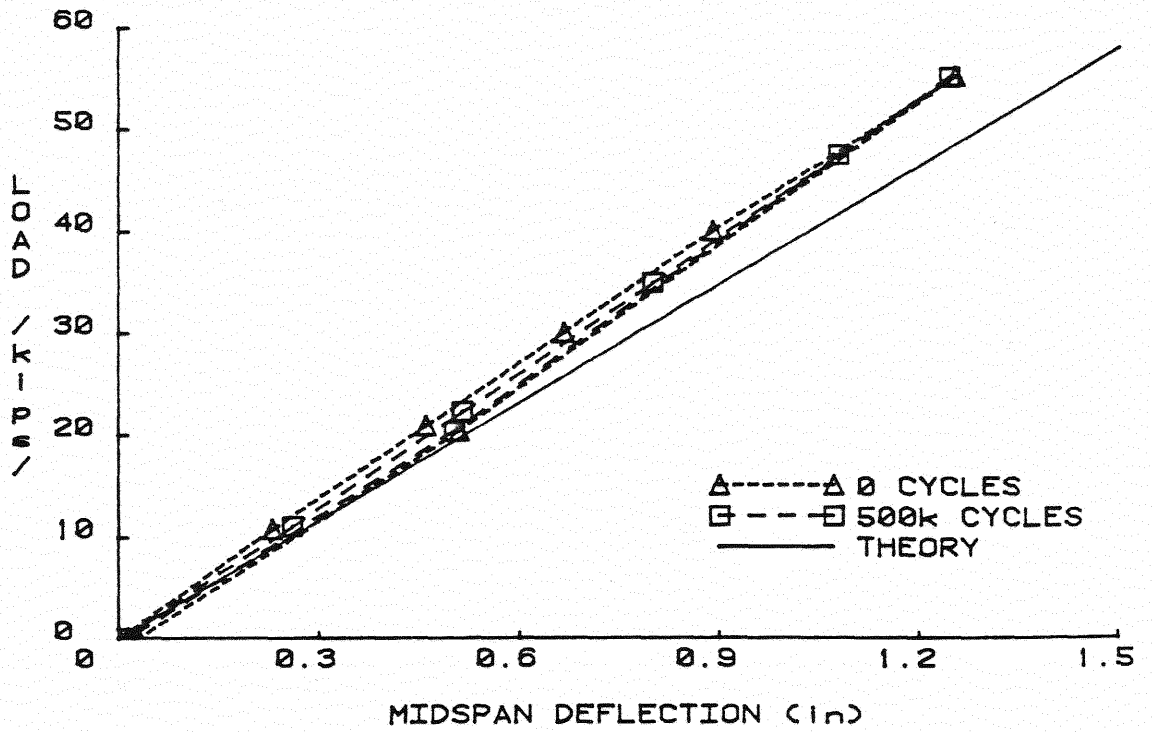
b. West Beam

Figure E.21 Load vs. Midspan Deflection, Phase IX Repeated Loading of
Second Unit

E.21
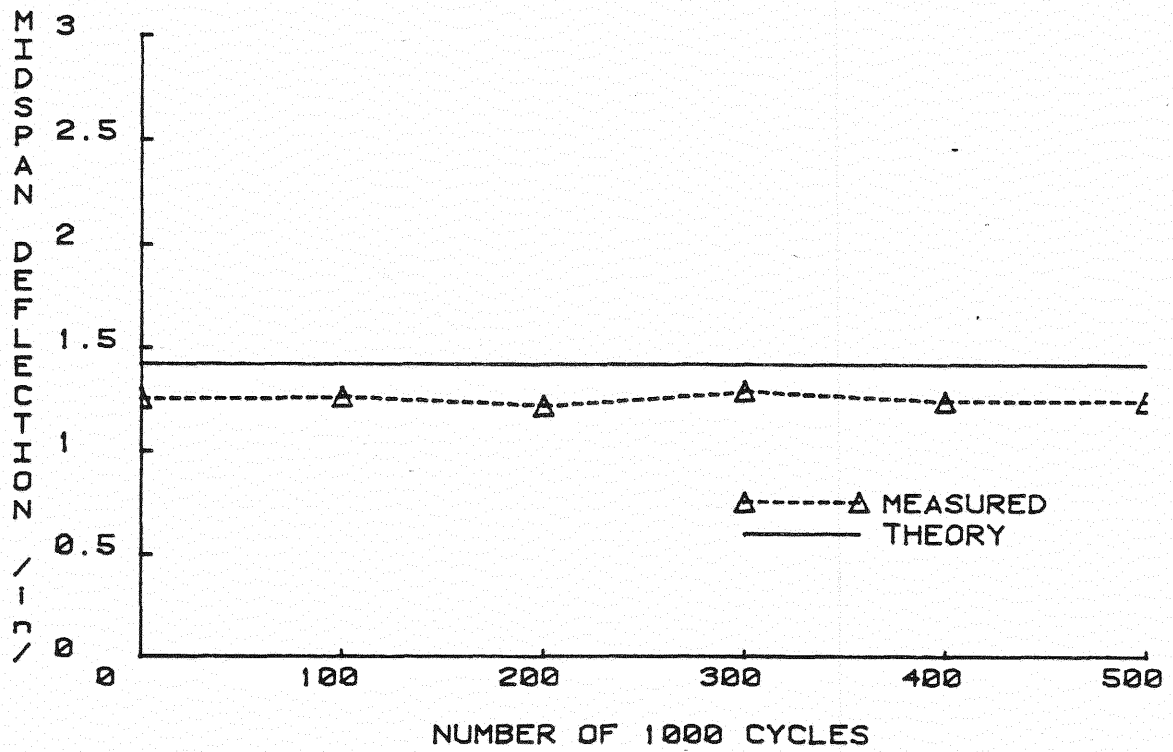
Figure E.22   Midspan Deflection vs. Number of Cycles, Phase IX Repeated
Loading of Second Unit
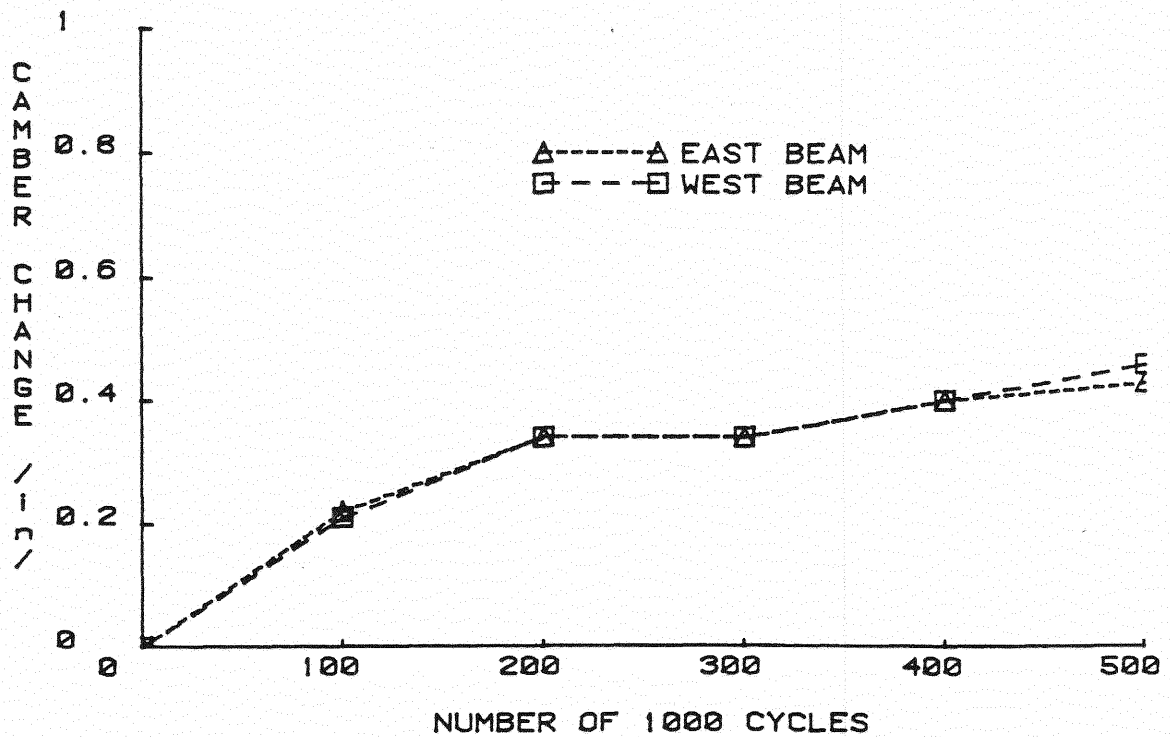
Figure E.23   Camber Change vs. Number of Cycles, Phase IX Repeated Loading
of Second Unit

E.22
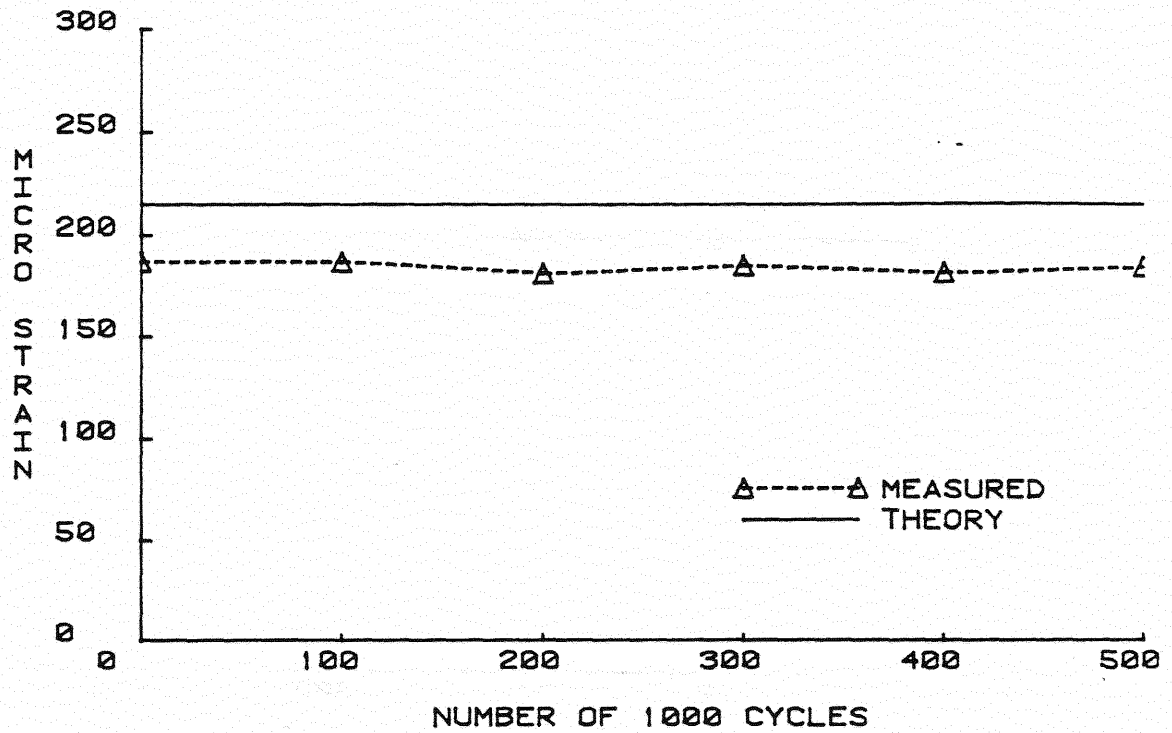
Figure E.24 Top of Concrete Strain vs. Number of Cycles, Phase IX
Repeated Loading of Second Unit
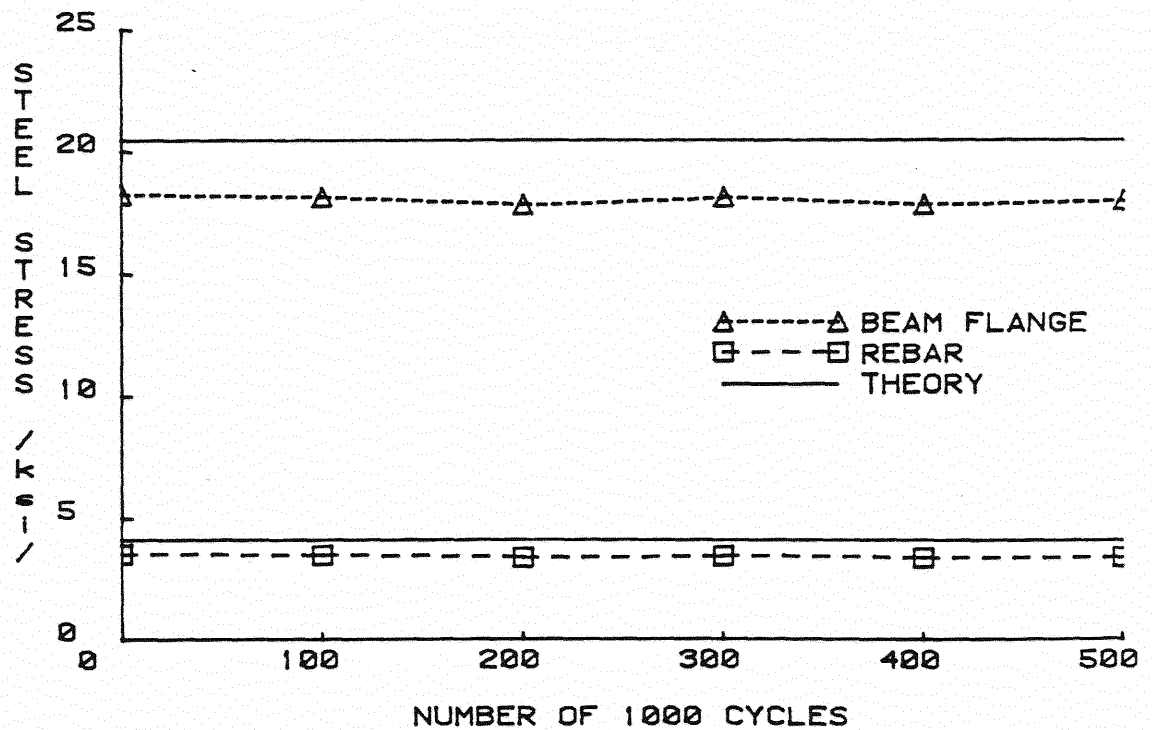
Figure E.25 Steel Stress vs. Number of Cycles, Phase IX Repeated Loading
of Second Unit

E.23
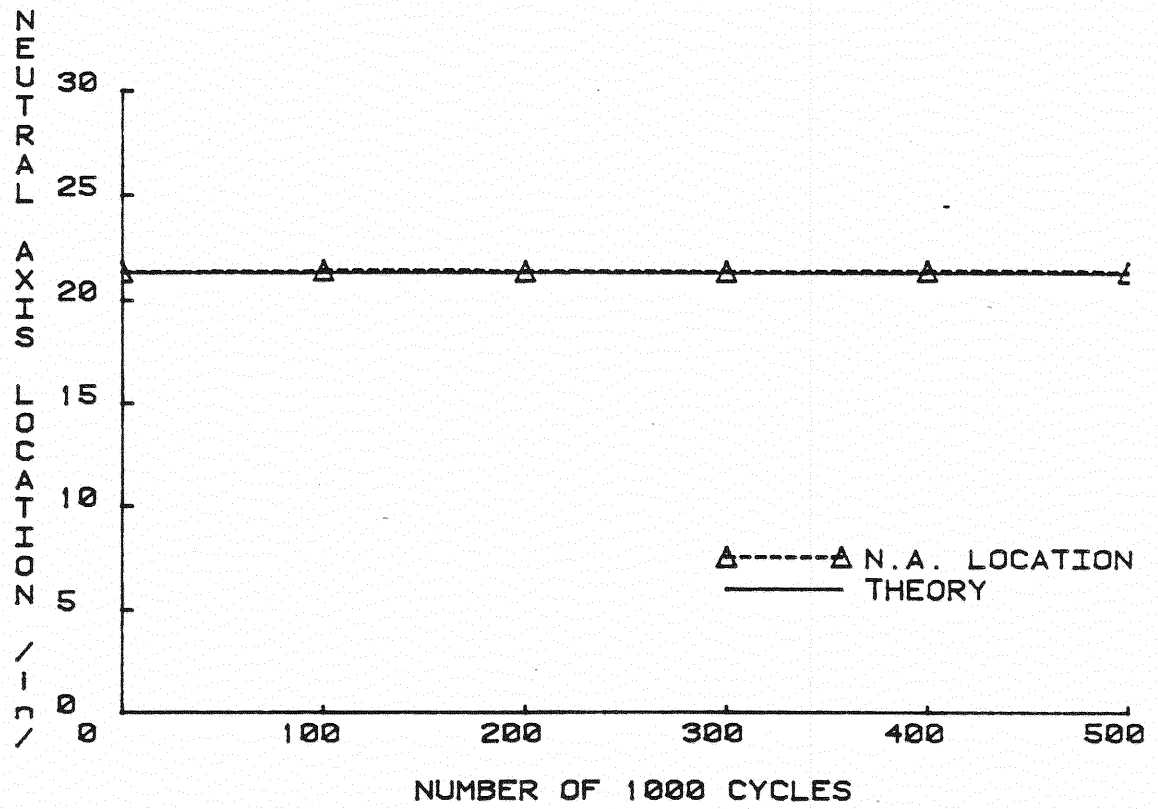
Figure E.26 Neutral Axis Location from Bottom of Beam, Phase IX
Repeated Loading of Second Unit

APPENDIX F

STATIC LOADING TEST RESULTS

SECTION F.1

PHASE III TEST RESULTS

OPERATING RATING LOADING TEST
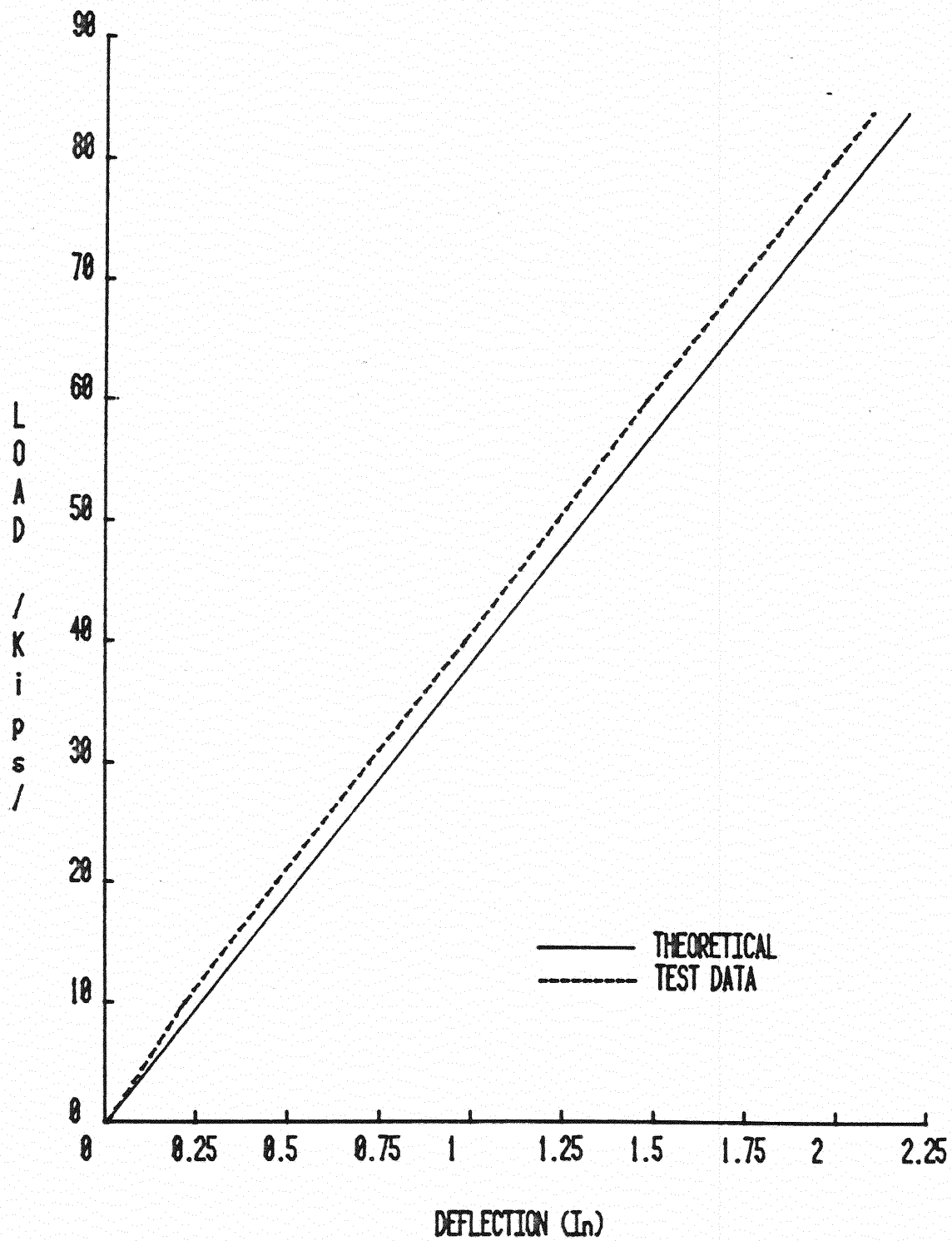
Figure F.1 Load vs. Midspan Deflection, Phase III Operating Rating Loading
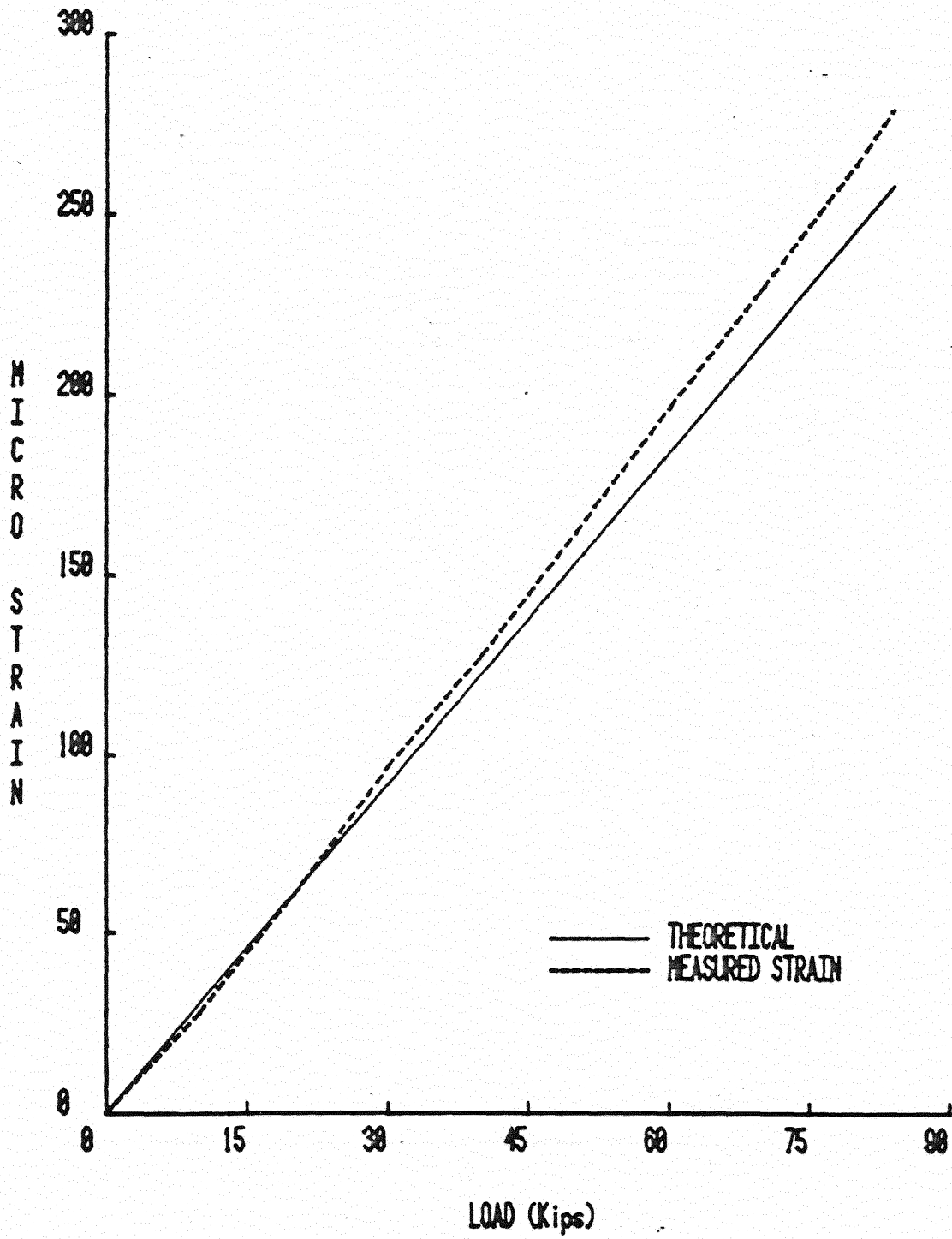
Figure F.2   Strain of Concrete Surface vs. Load, Phase III Operating
            Rating Loading
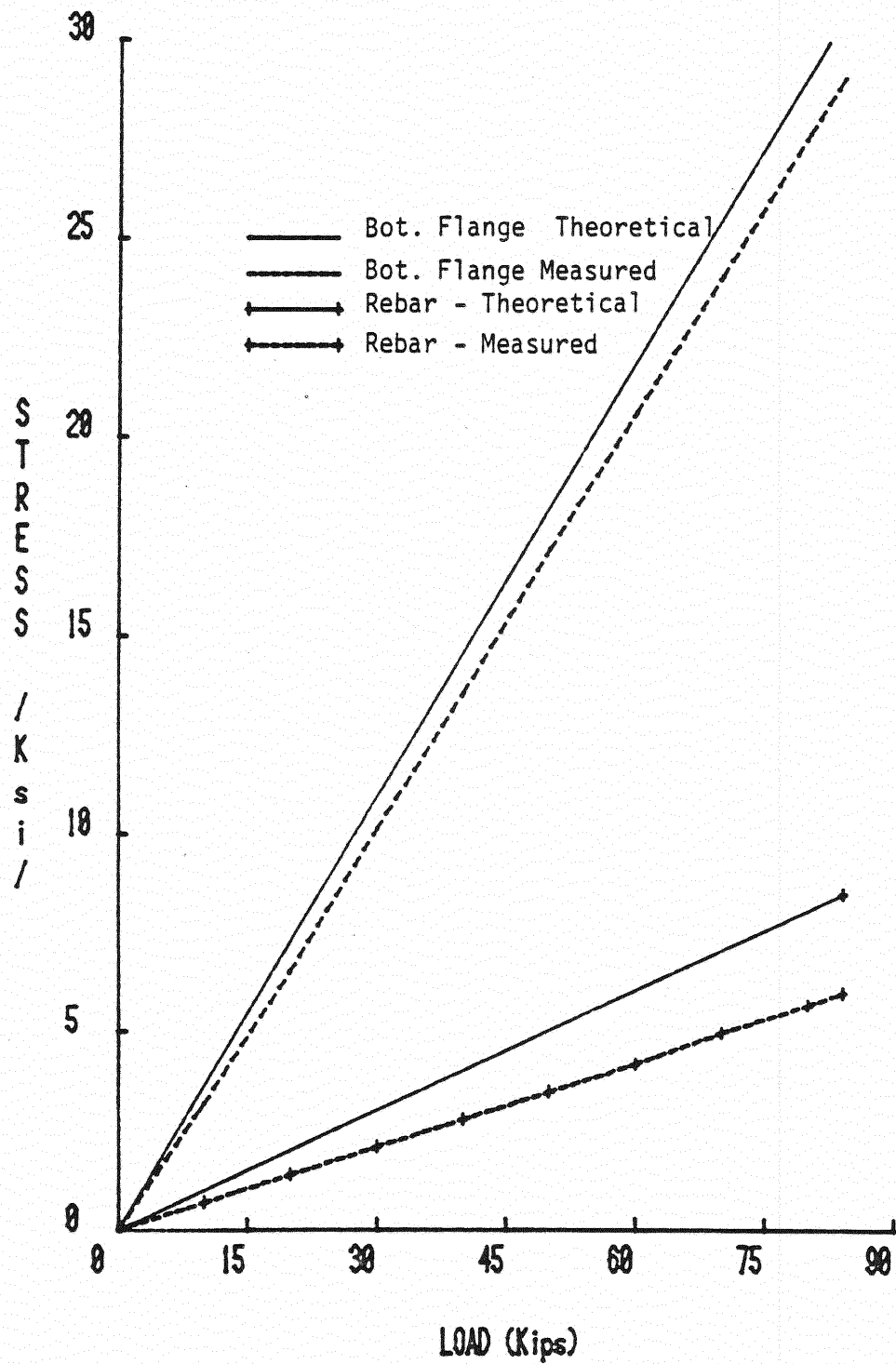
Figure F.3   Steel Stresses vs. Load, Phase III Operating
            Rating Loading

F.4

SECTION F.2

PHASE VIII TEST RESULTS

STATIC FLEXURAL TEST TO FAILURE OF FIRST UNIT
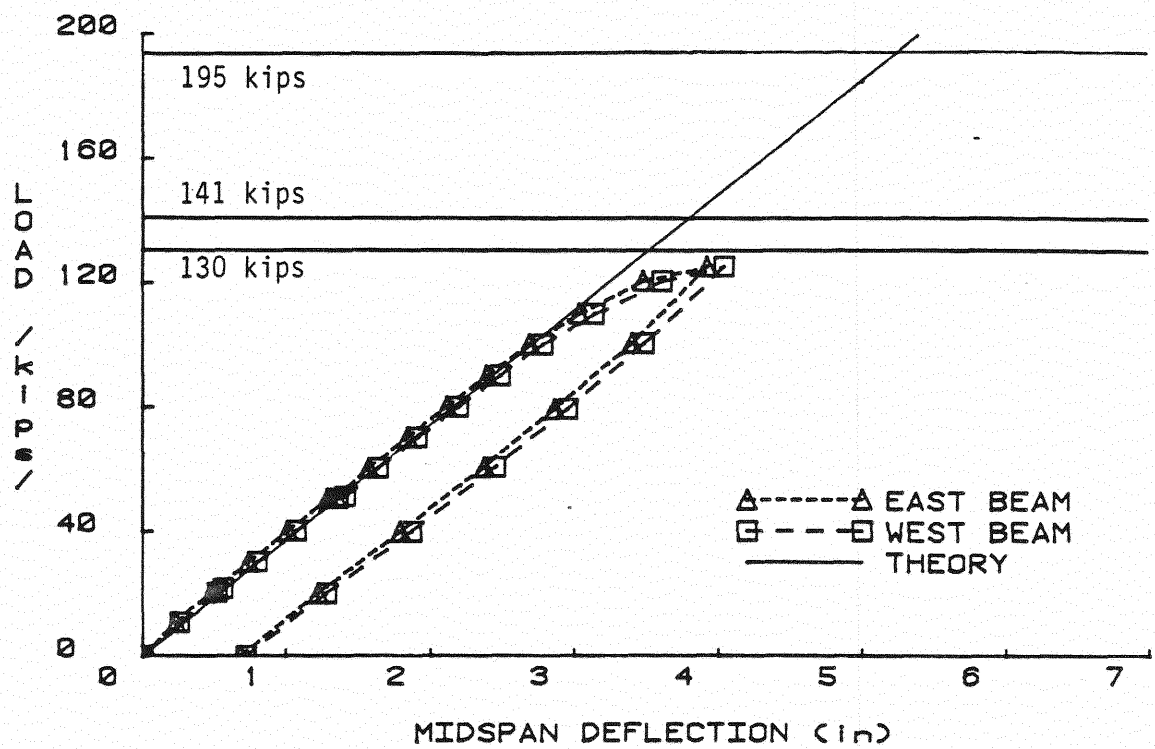
a. First Test
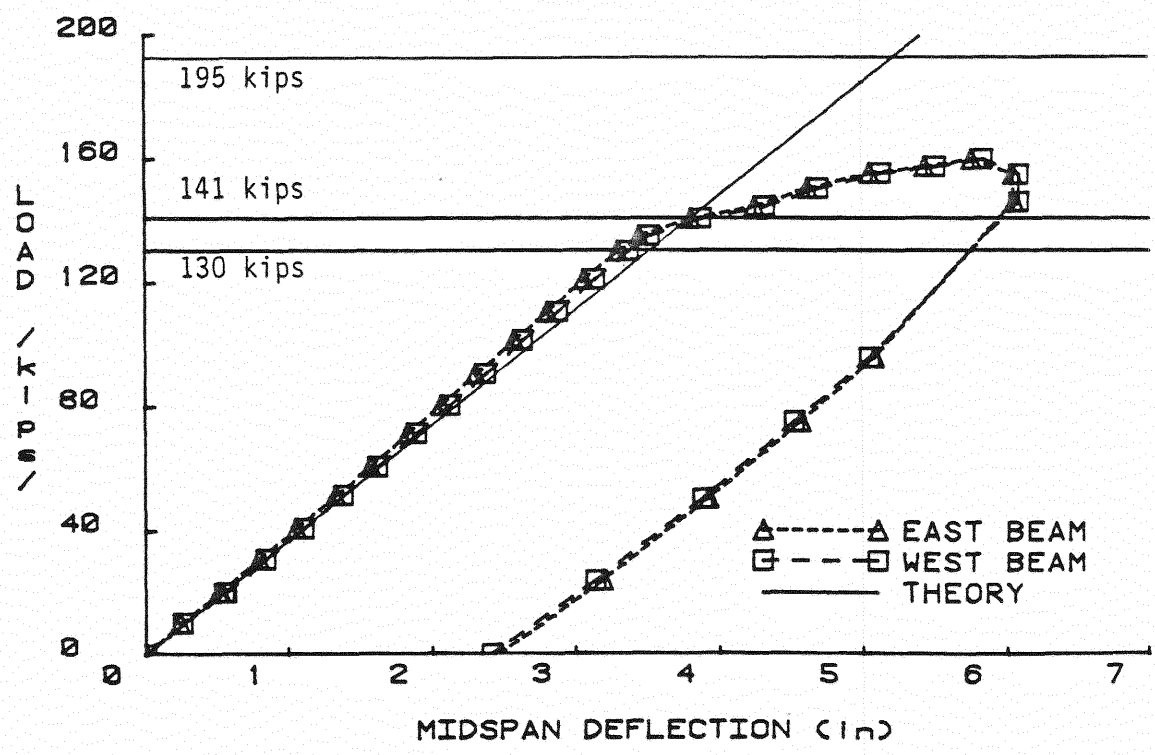
b. Second Test

Figure F.4 Load vs. Midspan Deflection, Phase VIII Flexural Failure Test

F.6
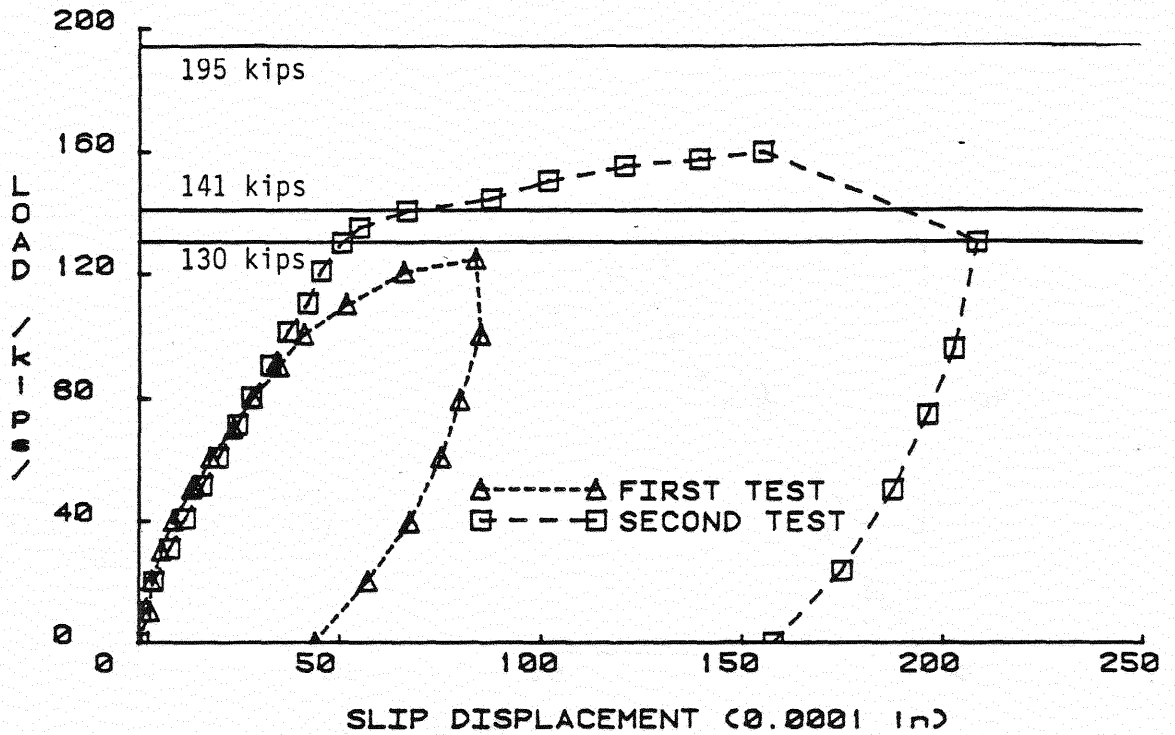
Figure F.5 Load vs. Slip Displacement, Phase VIII Flexural Failure Test
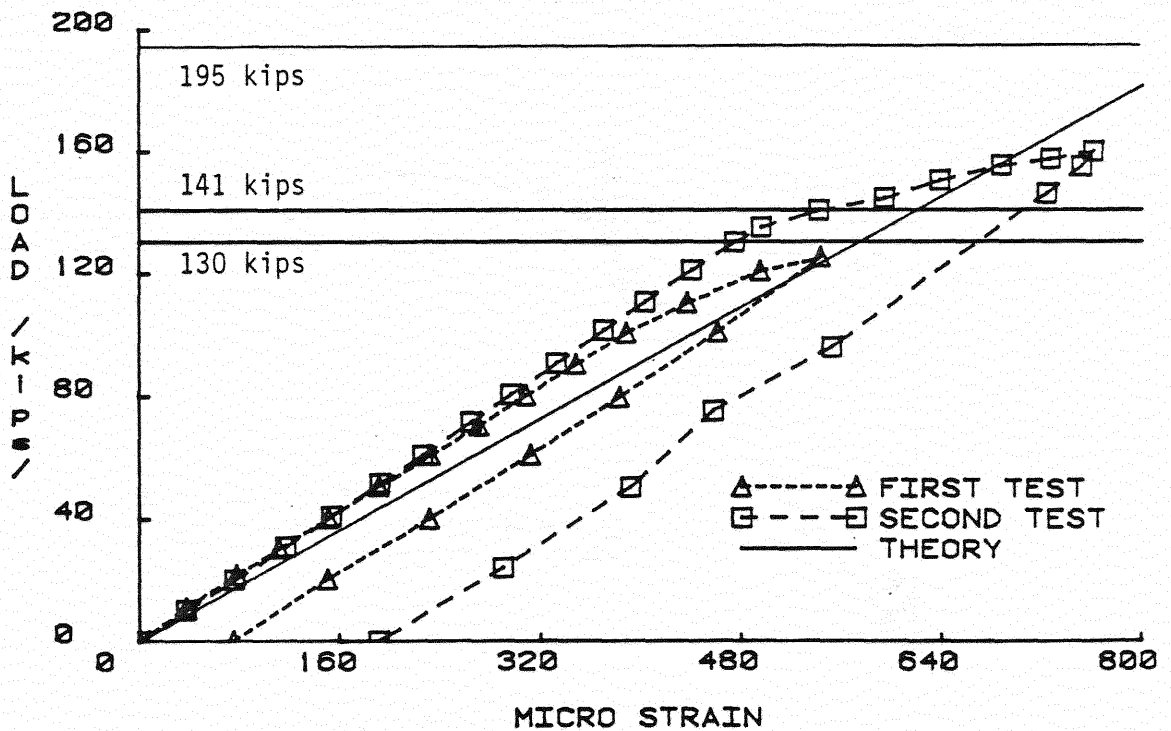
Figure F.6 Load vs. Strain of Concrete Surface, Phase VIII Flexural
            Failure Test   F.7
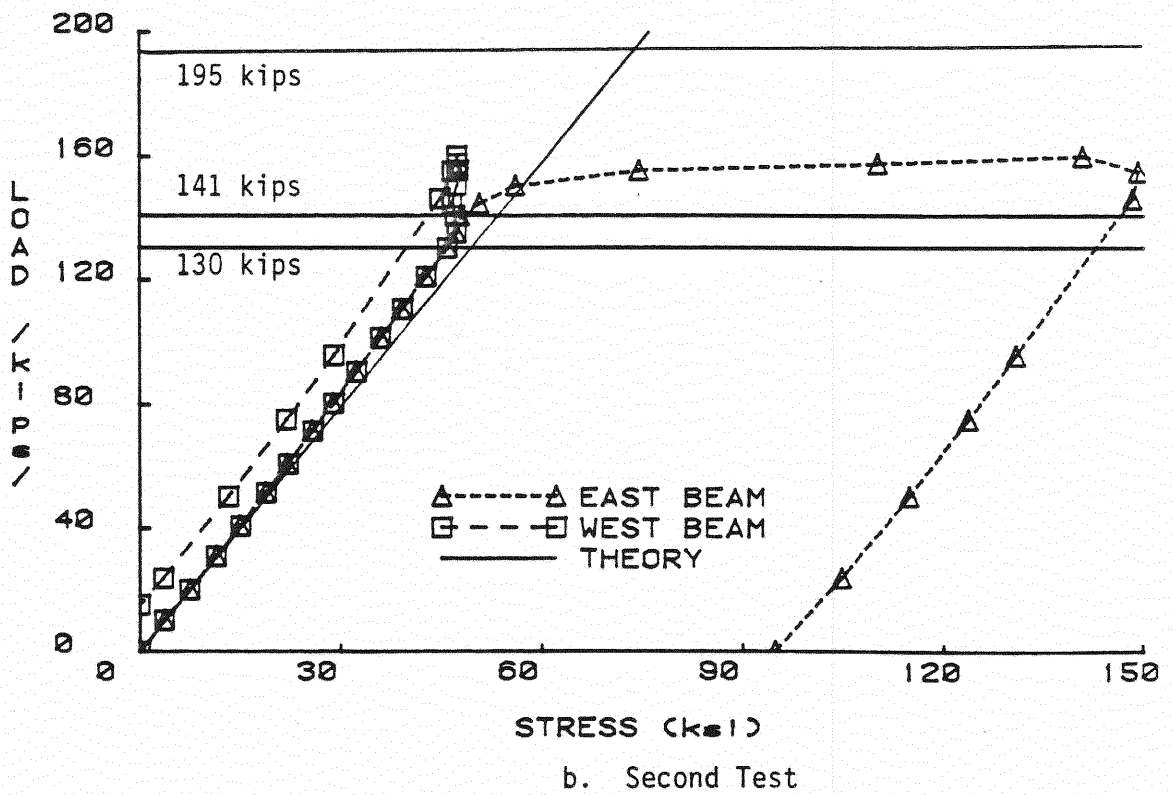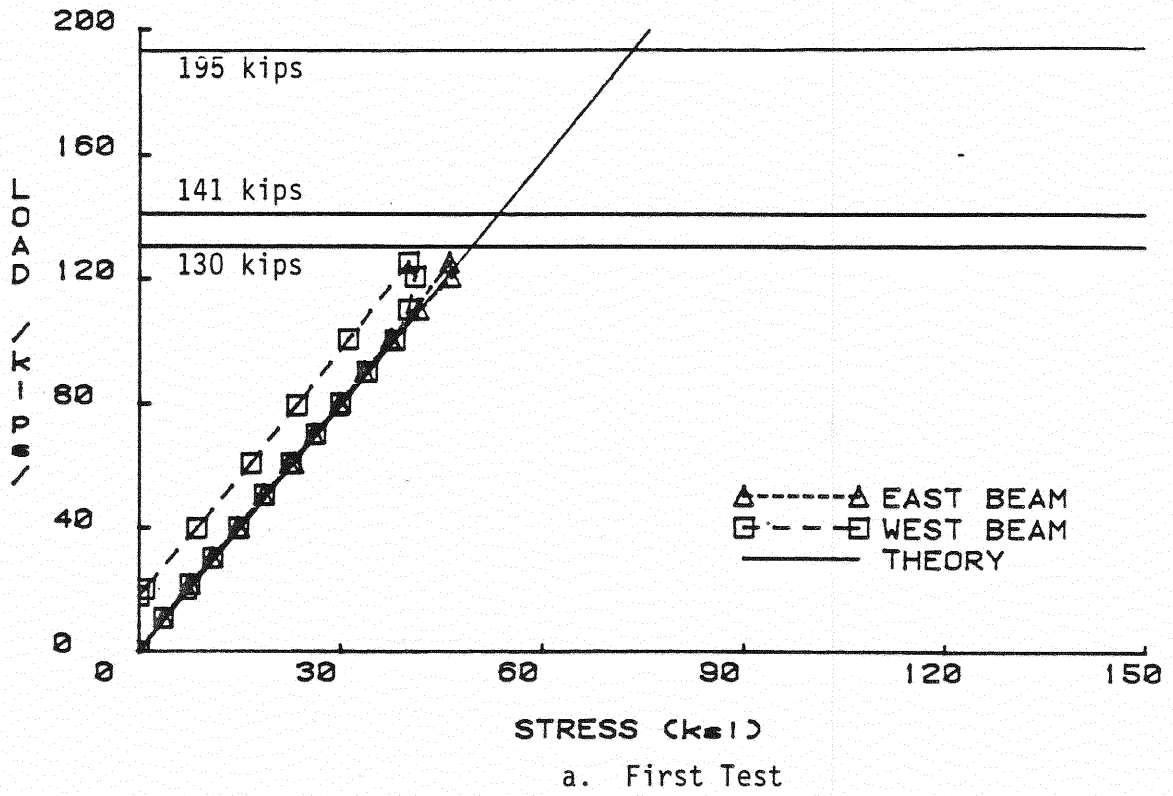
Figure F.7   Load vs. Beam Bottom Flange Stress, Phase VIII Flexural
Failure Test   F.8

Graph axes:

STRESS LOCATION (in)

STRESS (ksi)

Legend:
▲ ---- ▲ EXPERIMENT
——— THEORY
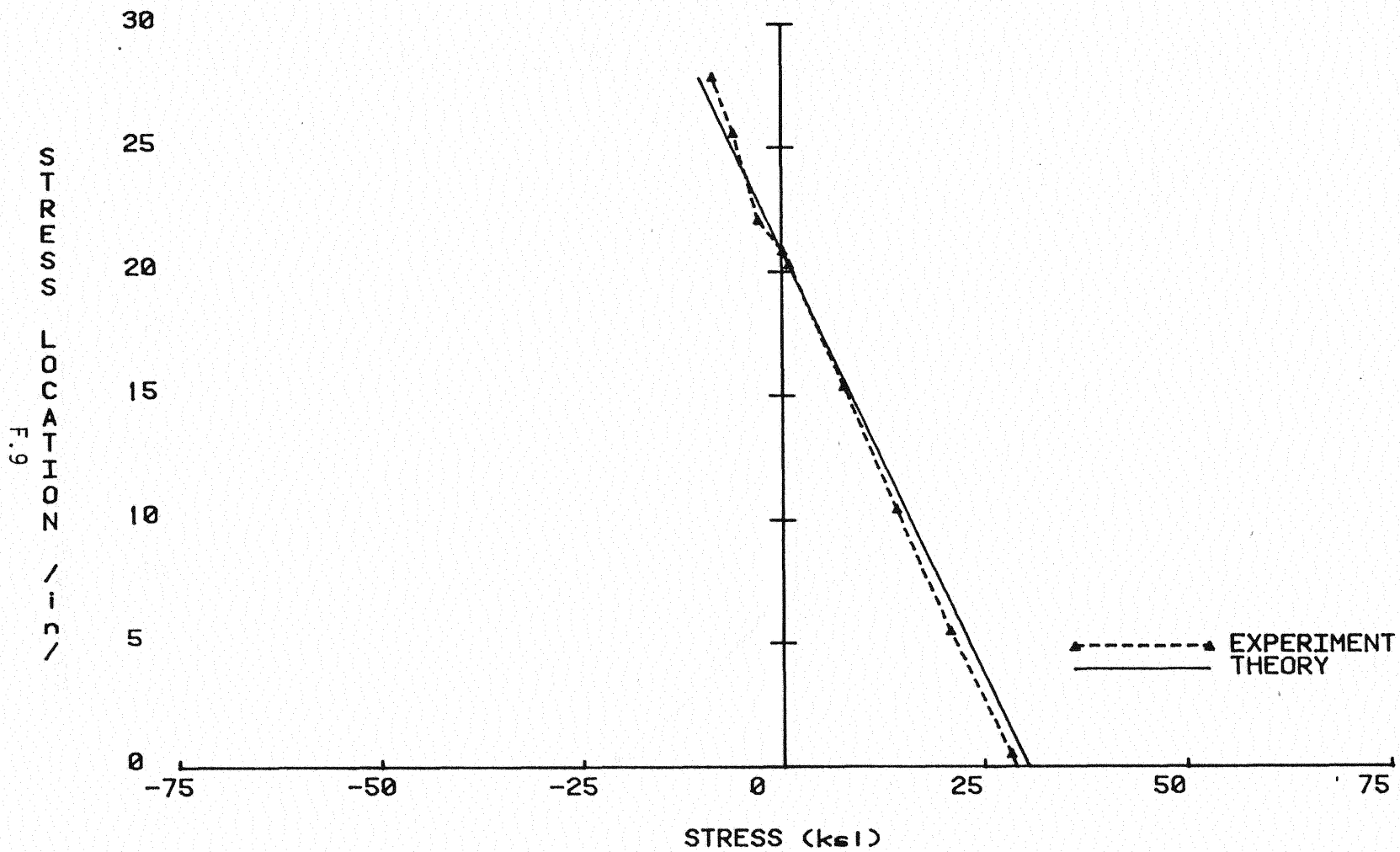
a. Stress Distribution at 80 kips Applied Load

Figure F.8 Stress Distribution Over Depth of Unit, Phase VIII Flexural Failure Test
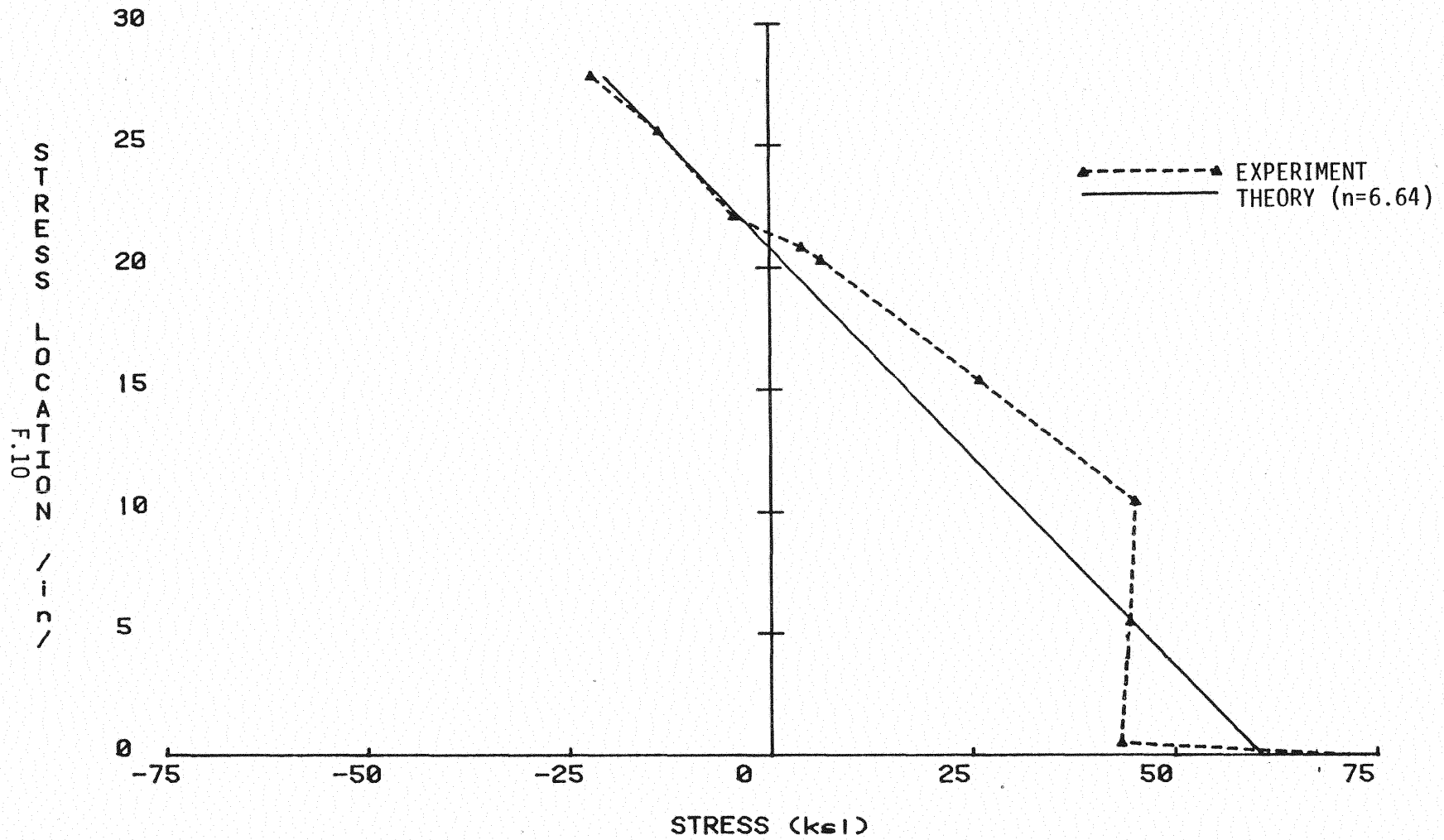
b. Stress Distribution at 160 kips Applied Load

Figure F.8 Stress Distribution Over Depth of Unit, Phase VIII Flexural Failure Test

SECTION F.3

PHASE X TEST RESULTS

STATIC FLEXURAL FIRST YIELD TEST OF SECOND UNIT
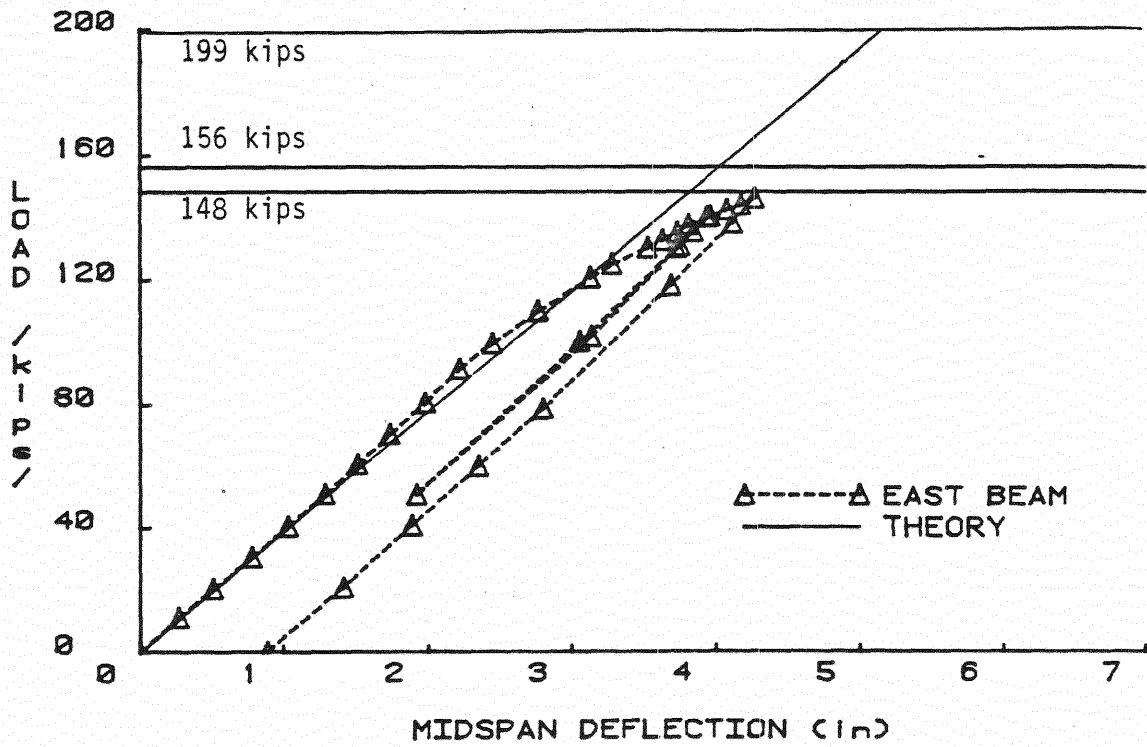
a. East Beam
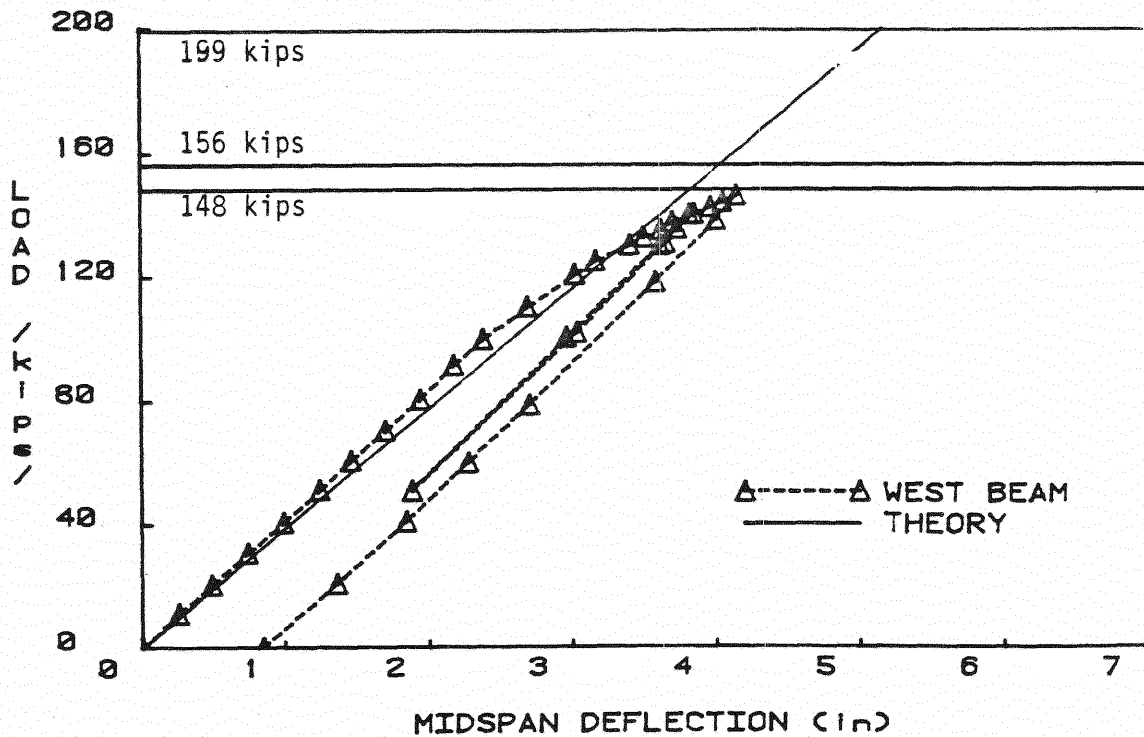
b. West Beam

Figure F.9 Load vs. Midspan Deflection, Phase X Flexural First Yield
Test of Second Unit

F.12
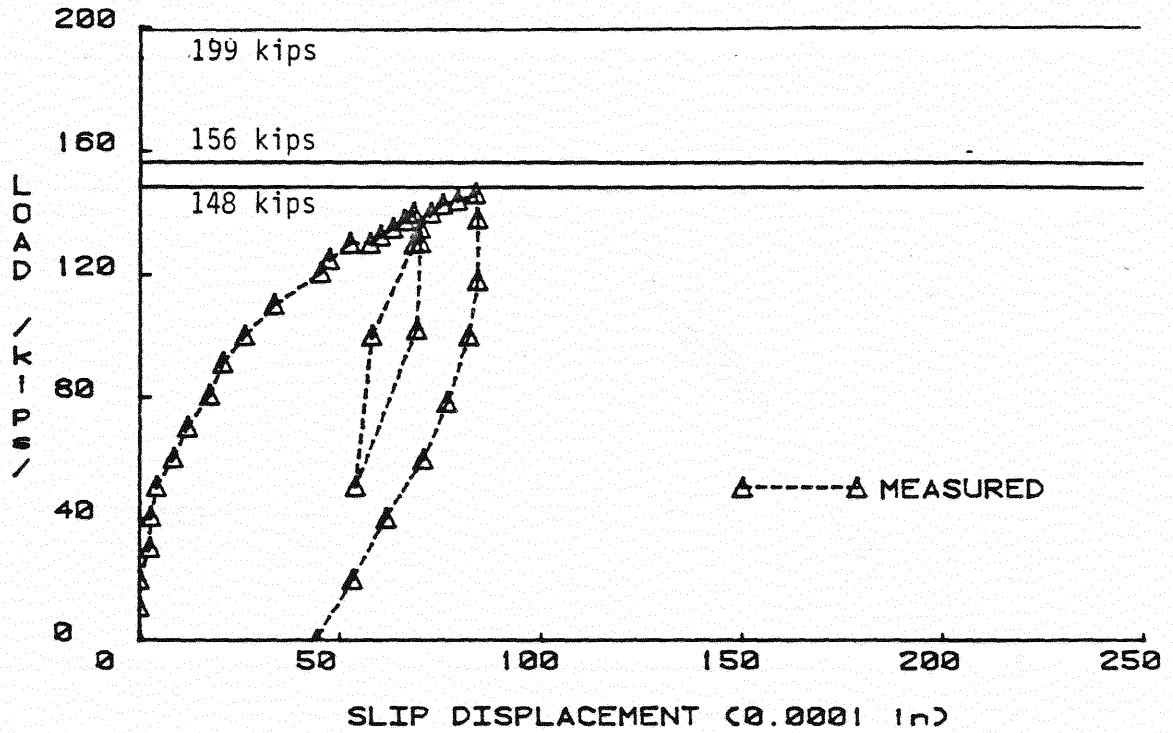
Figure F.10 Load vs. Slip Displacement, Phase X Flexural First Yield Test
of Second Unit
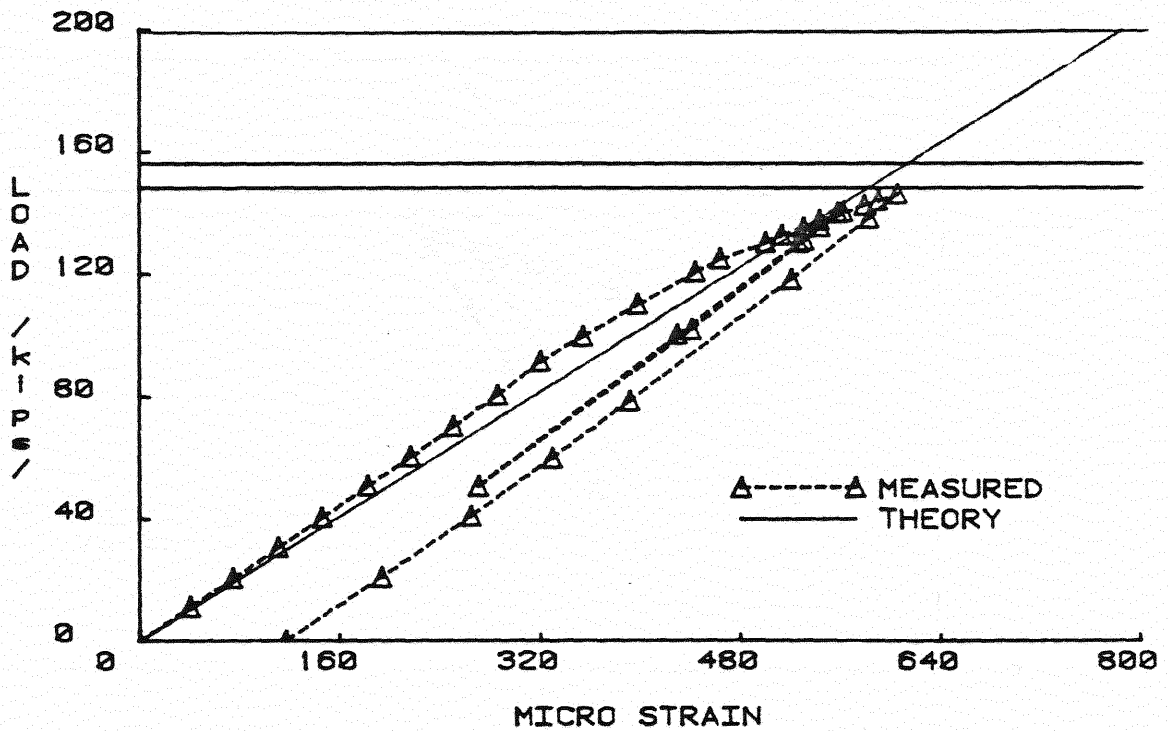
Figure F.11 Load vs. Strain of Concrete Surface, Phase X First Yield
Failure Test of Second Unit

F.13

a. East Beam

b. West Beam
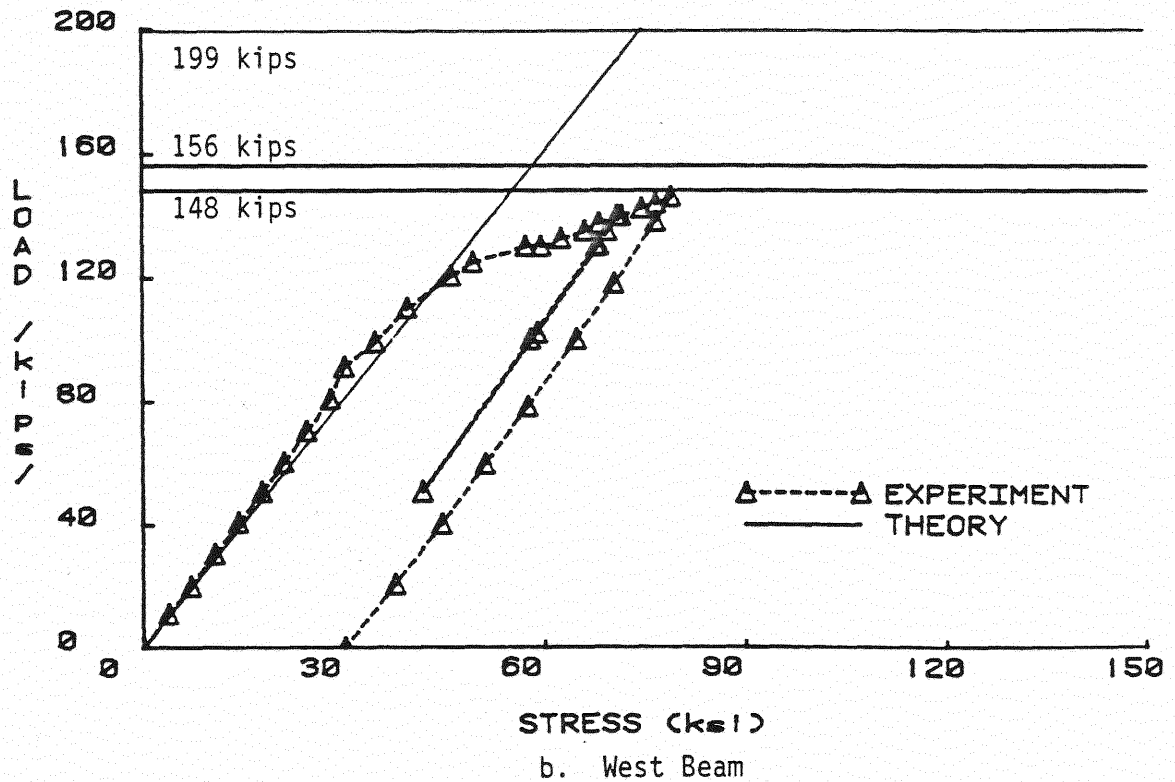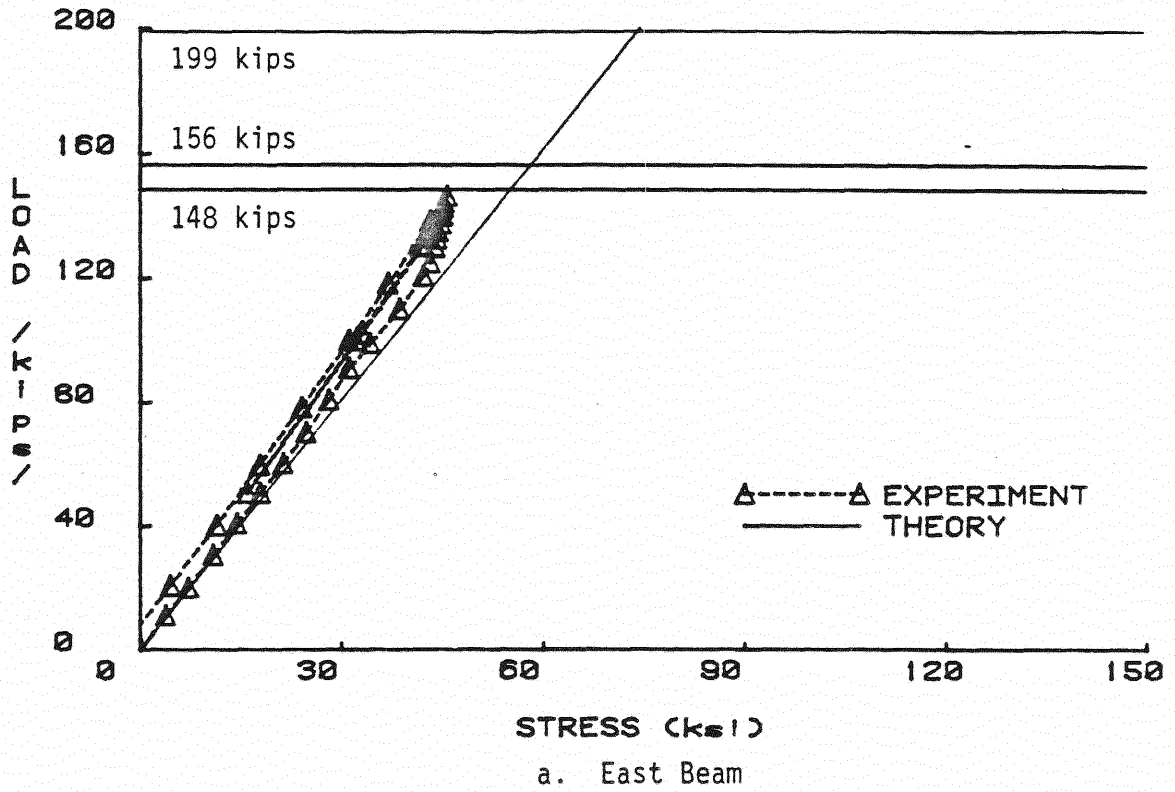
Figure F.12   Load vs. Beam Bottom Flange Stress, Phase X Flexural
First Yield Test of Second Unit

F.14
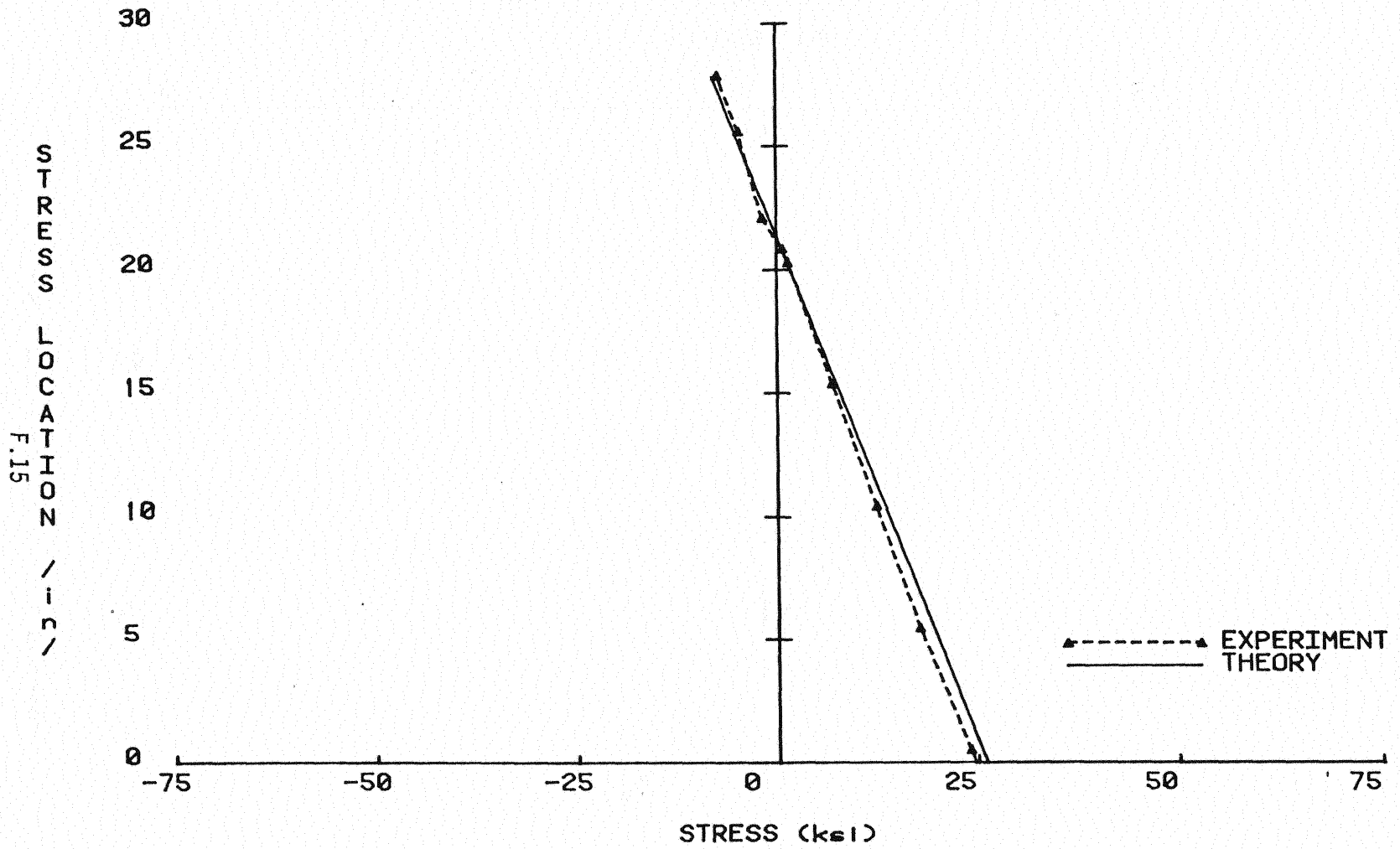
a.   Stress Distribution at 70 kips Applied Load

Figure F.13   Stress Distribution Over Depth of Unit, Phase X Flexural First Yield Test of
Second Unit
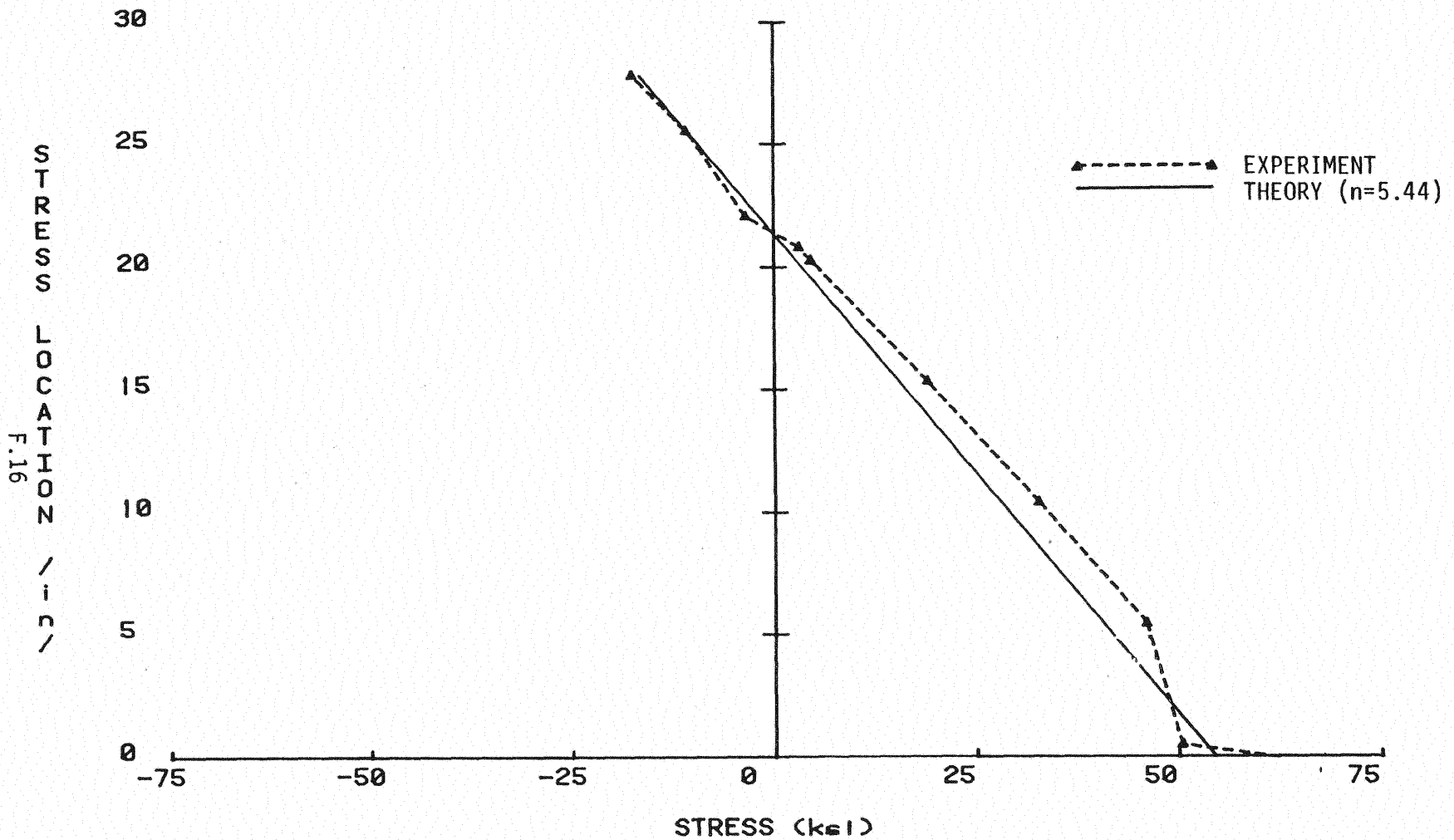
b.   Stress Distribution at 146.3 kips Applied Load

Figure F.13   Stress Distrubition Over Depth of Unit, Phase X Flexural First Yield Test of
Second Unit, Continued

APPENDIX G

SPECIMEN DETAILS FOR TRANSVERSE

SLAB STRENGTH TESTS
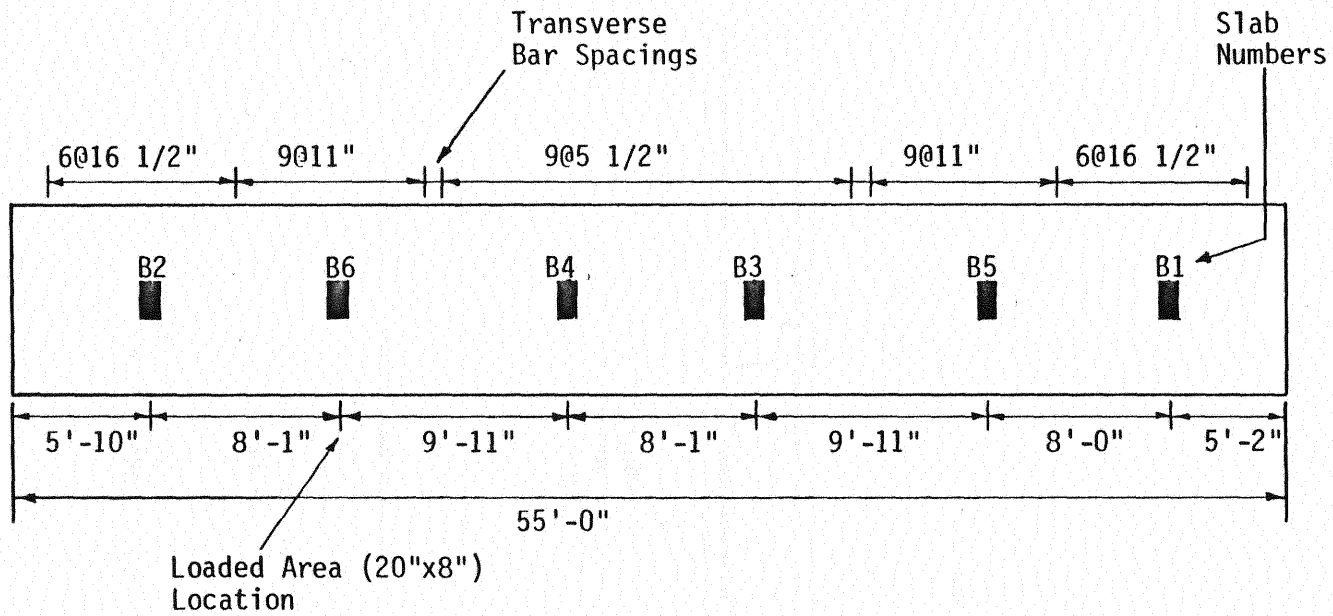
(a) Load Locations and Transverse Bar Spacings

Figure G.1 First Unit Details of Transverse Slab Strength Tests

9-#4 Longitudinal
Top Bars
@9" Spacings

#4 Transverse
Top and Bottom Bars

2 1/2"

3" 7 1/2"

2"

W21x50
Steel Beam

5-#4 Longitudinal
Bottom Bars
@18" Spacing

Concrete
Deck

1'-8"   3'-9 1/2"   1'-8"

6'-9 1/2"
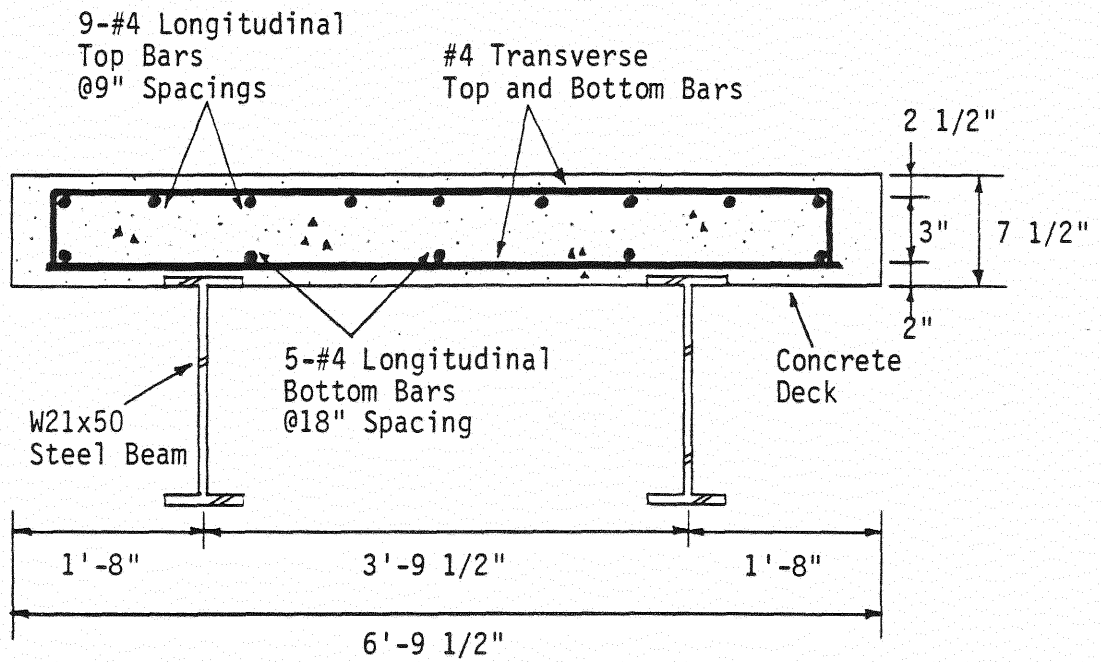
(b) Typical Section Showing Longitudinal
    and Transverse Bars

Figure G.1   First Unit Details for Transverse Slab
             Strength Tests, Continued
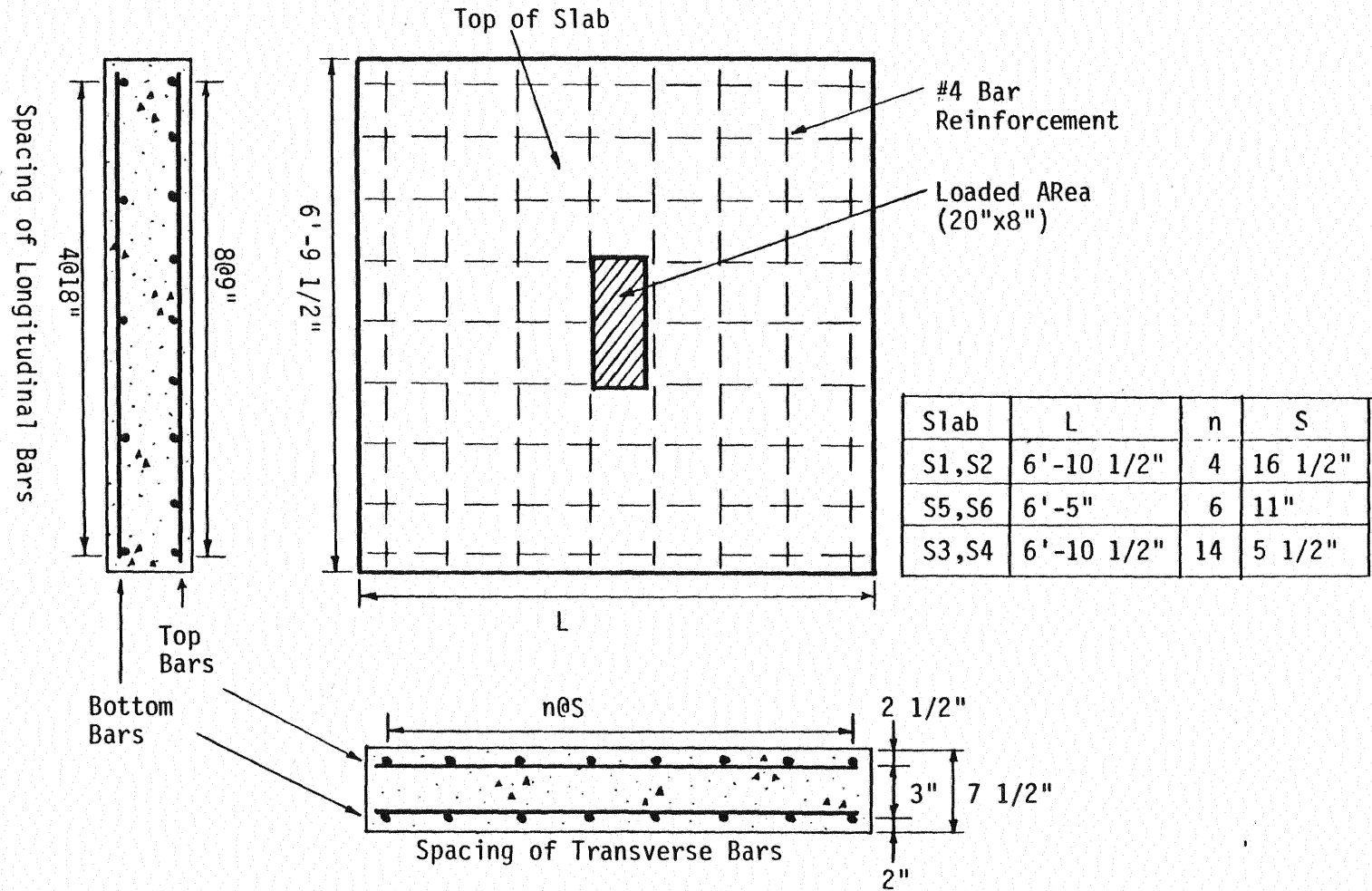
Figure G.2   Control Slab Specimen Details for Transverse
Slab Strength Tests

Top of Slab

#4 Bar
Reinforcement

Loaded ARea
(20"x8")

6'-9 1/2"

Spacing of Longitudinal Bars

4@18"

8@9"

Top
Bars

Bottom
Bars

n@S

2 1/2"

3"   7 1/2"

2"

Spacing of Transverse Bars

L

Slab	L	n	S
S1,S2	6'-10 1/2"	4	16 1/2"
S5,S6	6'-5"	6	11"
S3,S4	6'-10 1/2"	14	5 1/2"

G.3

APPENDIX H

SUPPLEMENTARY SHEAR CONNECTOR TEST SPECIMENS

APPENDIX H

SUPPLEMENTARY SHEAR CONNECTOR TEST SPECIMEN DETAILS

Construction of the specimens was as close as possible to that of the construction of the bridge unit. The same fabricator used for the bridge unit welded the shear connectors to the test specimens. However, it was observed after the failure tests that the stud connectors were welded around the base of the studs, rather than welded with a "gun", as is typical with stud connectors welded to girders, and presumably, the first bridge unit. This had no effect on the response of the specimens to sustained loading, but could have reduced the strength of the connectors.

As shown in the Figure H.1 each test specimen was constructed with a 27 in. long, W12x35, A36 steel wide flange section with two 7 in. thick, 24 in. wide, 30 in. long reinforced concrete slabs cast symmetrically on each flange of the steel section. Each slab was attached to the steel section by shear connectors. The same stud shear connectors, 4 in. long and 3/4 in. in diameter, as used in the bridge unit, were used in two rows, two studs per row. The rows were 12 in. apart. Hot rolled section, C3x4.1 and 4 in. long, were used as the channel shear connectors. They were welded to the steel sections along the toe and heel of the channel and were also spaced at 12 in. Details of each type of specimen are shown in Figure H.2.
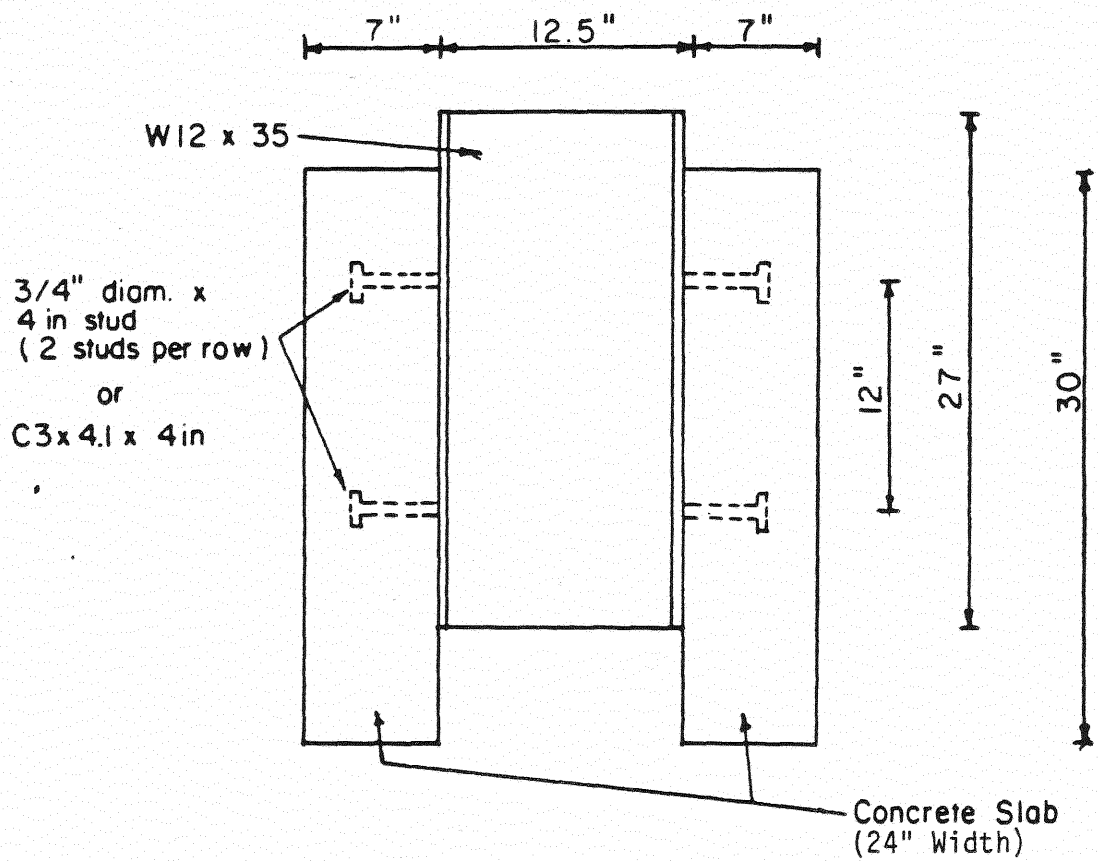
Figure H.1 Overall Dimensions of Shear
Connector Specimens
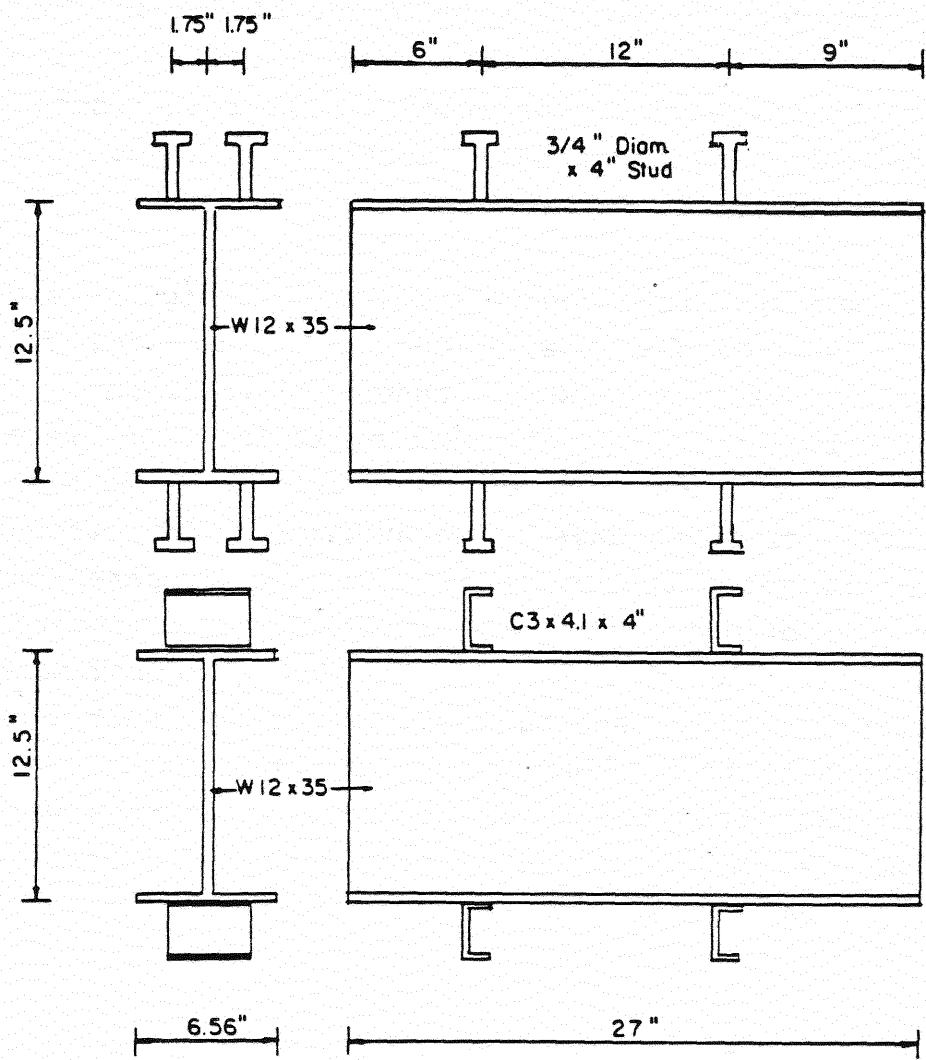
Figure H.2 Shear Connector Details of Shear Connector
         Specimens

The concrete slabs were reinforced with #4 bars of Grade 60 steel, both longitudinally and transversely. Spacing of the longitudinal bars was the same as that used in the bridge unit, i.e., 9 in. at the outside face and 18 in. at the beam flange face. Closer spacing at the outside face was intended to minimize the creep effect in the slab. However, unlike the bridge unit, the transverse bars were spaced at 11 in. with no variations. All reinforcement was pre-assembled using a specially constructed layout template and tied using standard practices.

The same specified concrete mix with design strength of 5000 psi as used for the bridge unit was used for the construction of the shear connector specimen. Twelve standard cylinders, 6 in. diameter by 12 in. high, were cast from the mixing truck. The concrete cylinders and slab were moist cured for seven days. The average 28 day strength of the concrete was found to be 5375 psi, as compared to 5300 psi for the bridge unit. The strength of cylinders cast from the first unit concrete and tested approximately 4 years after pouring, showed that the bridge unit concrete had increased from 5300 psi. to 7400 psi. Although cylinders made from the shear connector specimens were not tested before their failure (approximately 2.5 years after pouring), some increase in concrete compressive strength is believed to have occurred.

Prior to the shear connector failure test (Phase XII B), it was noticed that the beam flanges were partially embedded within the concrete slabs, rather than the flange surfaces being tangent with the slab surfaces, as shown in Figure H.1. The concrete in bearing contact with the flange ends was chipped away before the failure tests. But, the effects of the partial bearing of the flange ends during sustained loading observation are unknown.

APPENDIX I

PHASE XII TEST RESULTS

TRANSVERSE SLAB STRENGTH TESTS
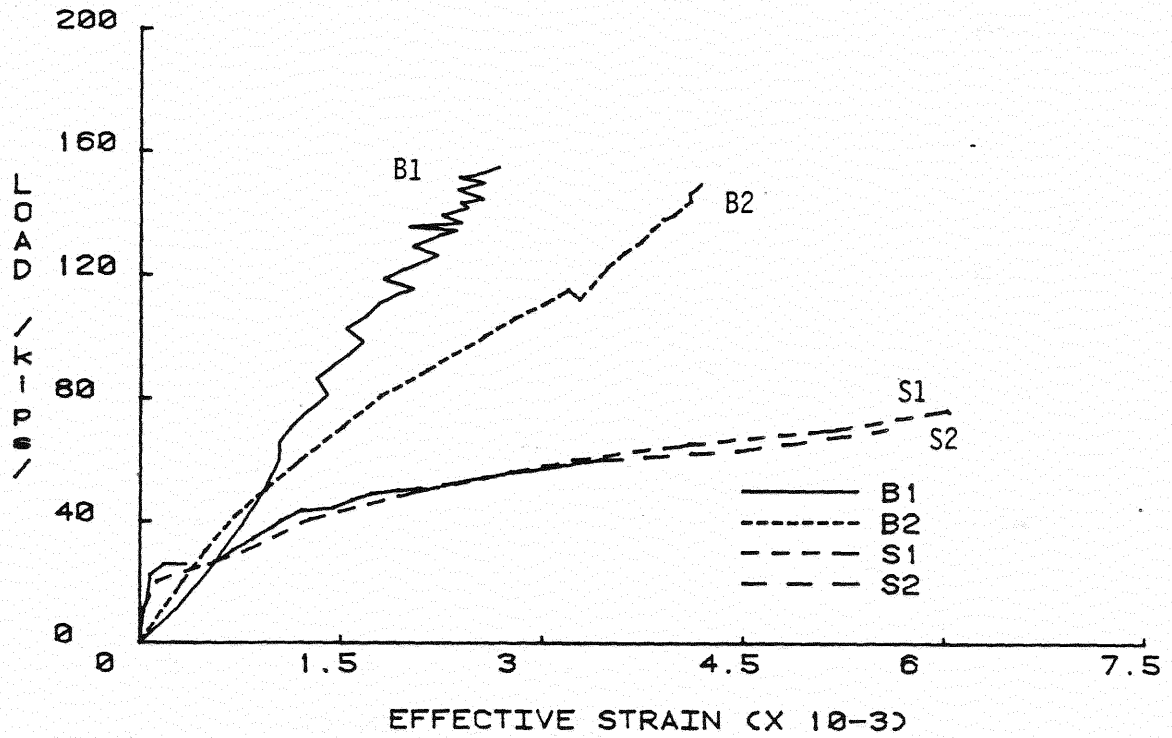
Figure I.1   Load vs. Effective Strain for Slabs with 0.19% Reinforcement
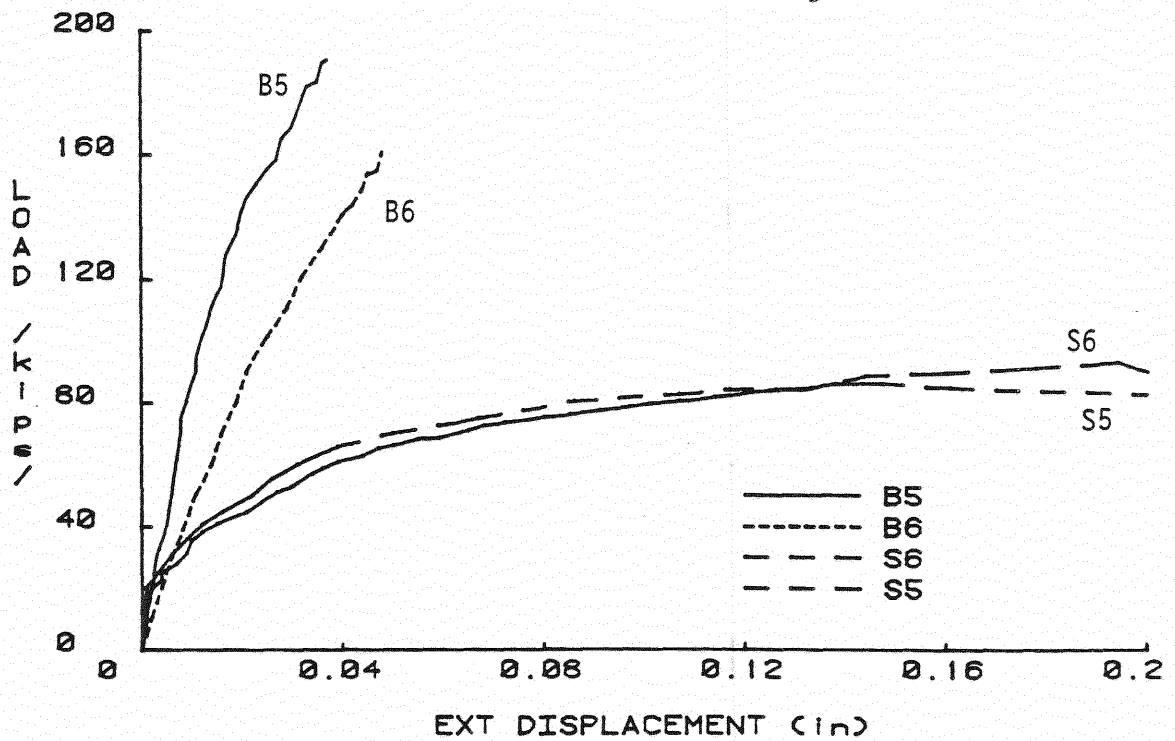Ratio, Phase XII Transverse Slab Strength Tests
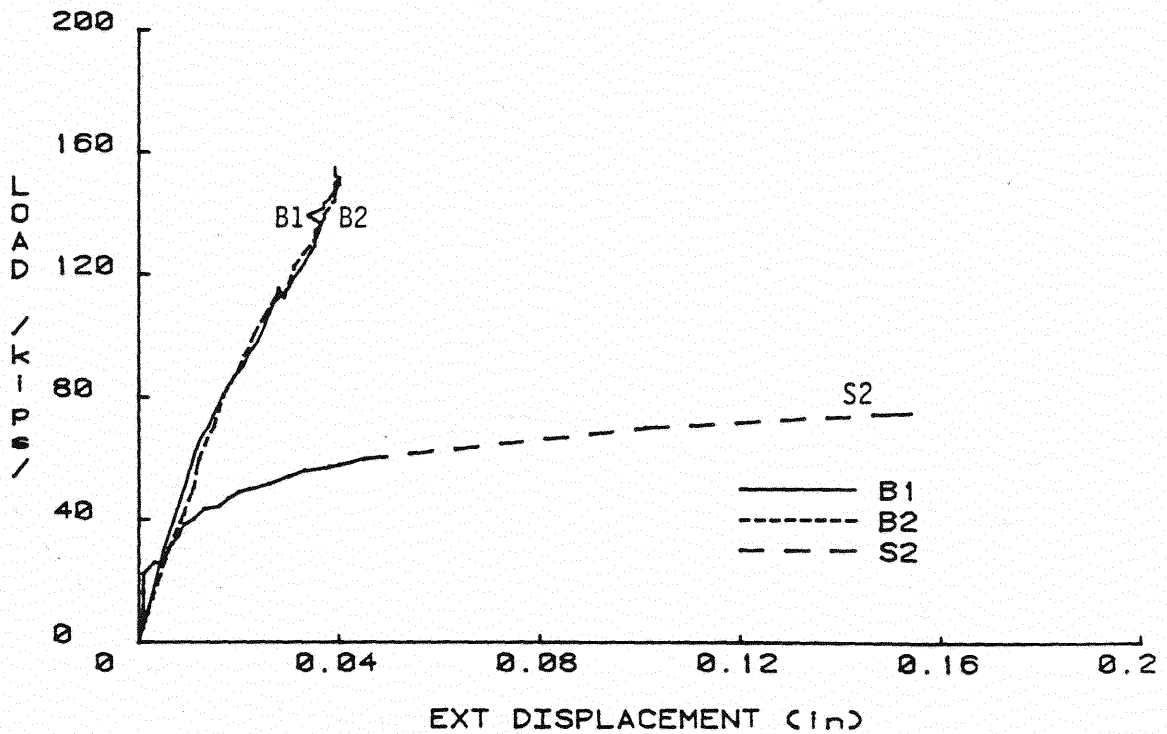
Figure I.2   Load vs. Restraint Displacement for Slabs with 0.19%
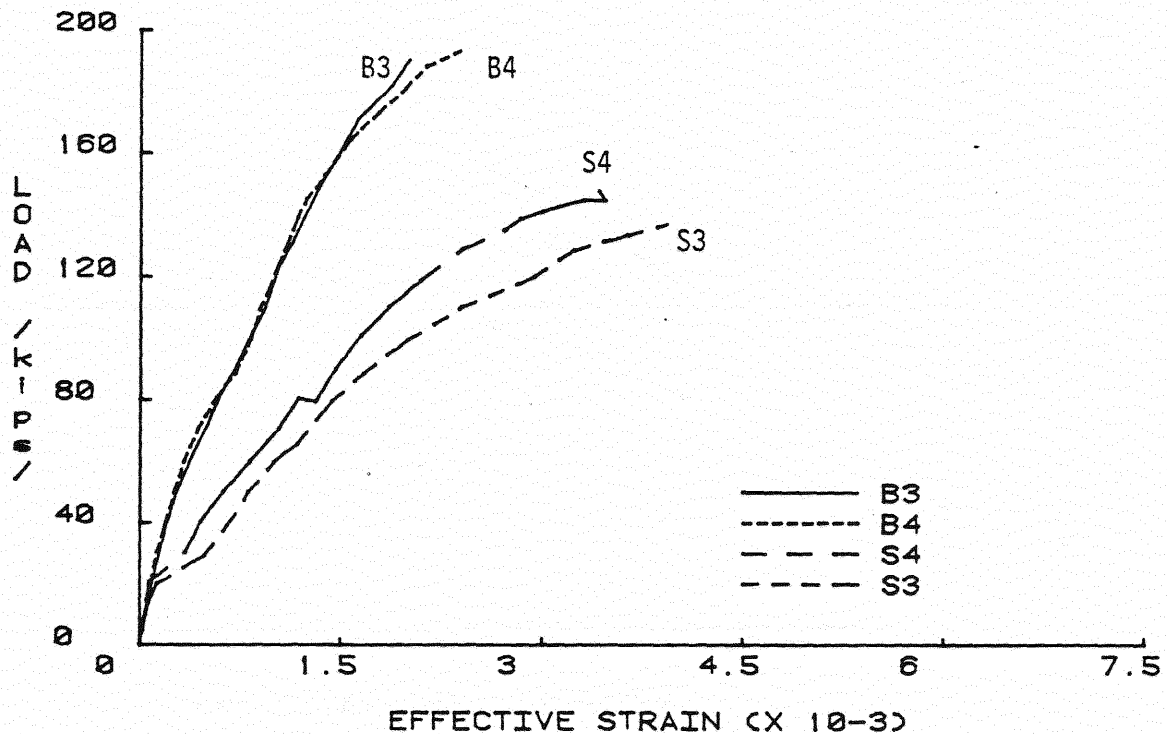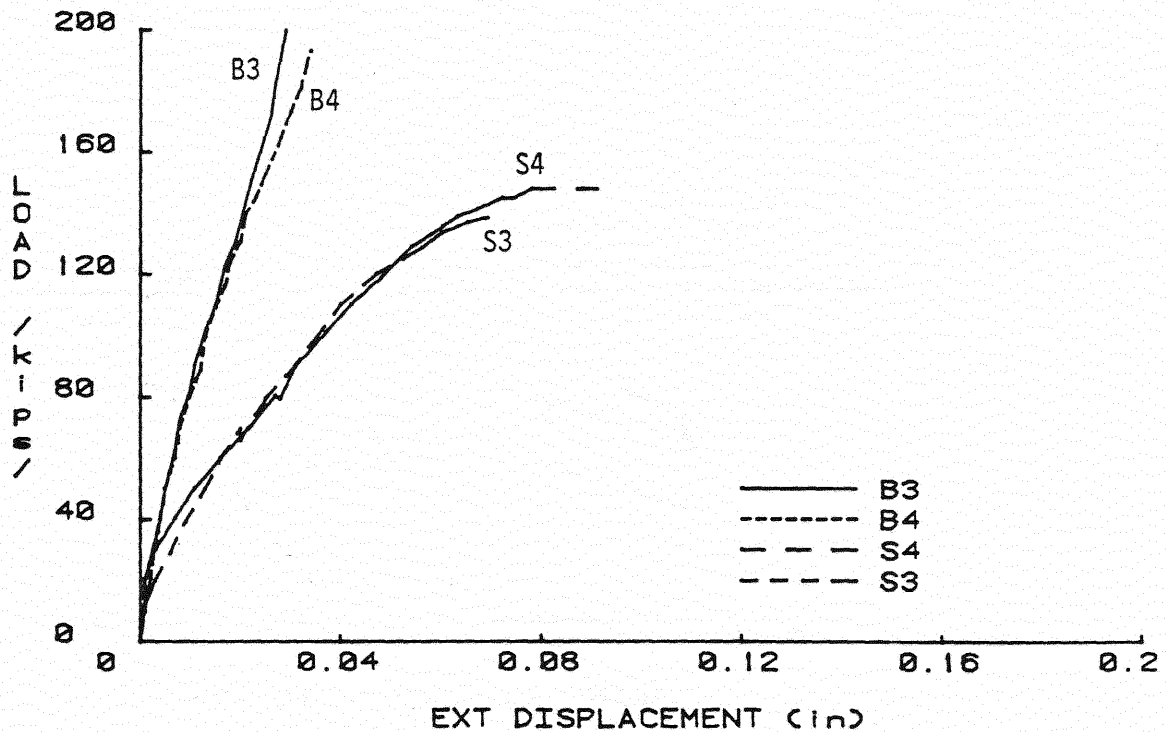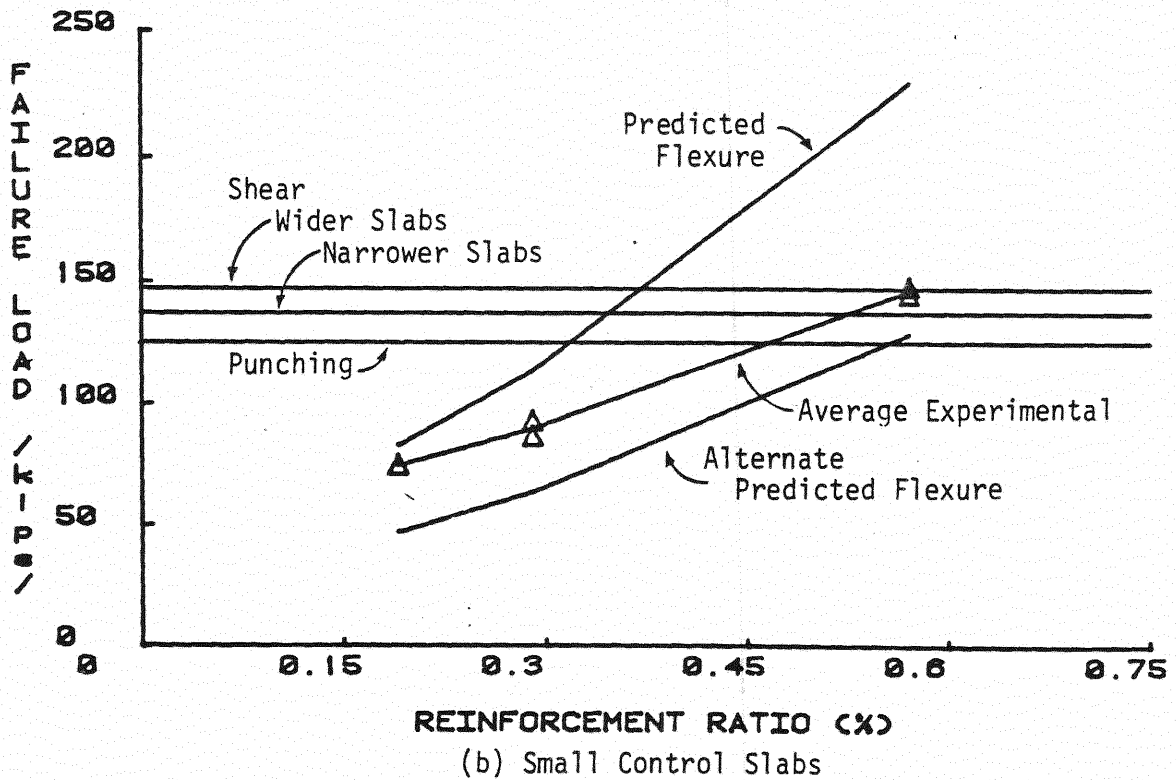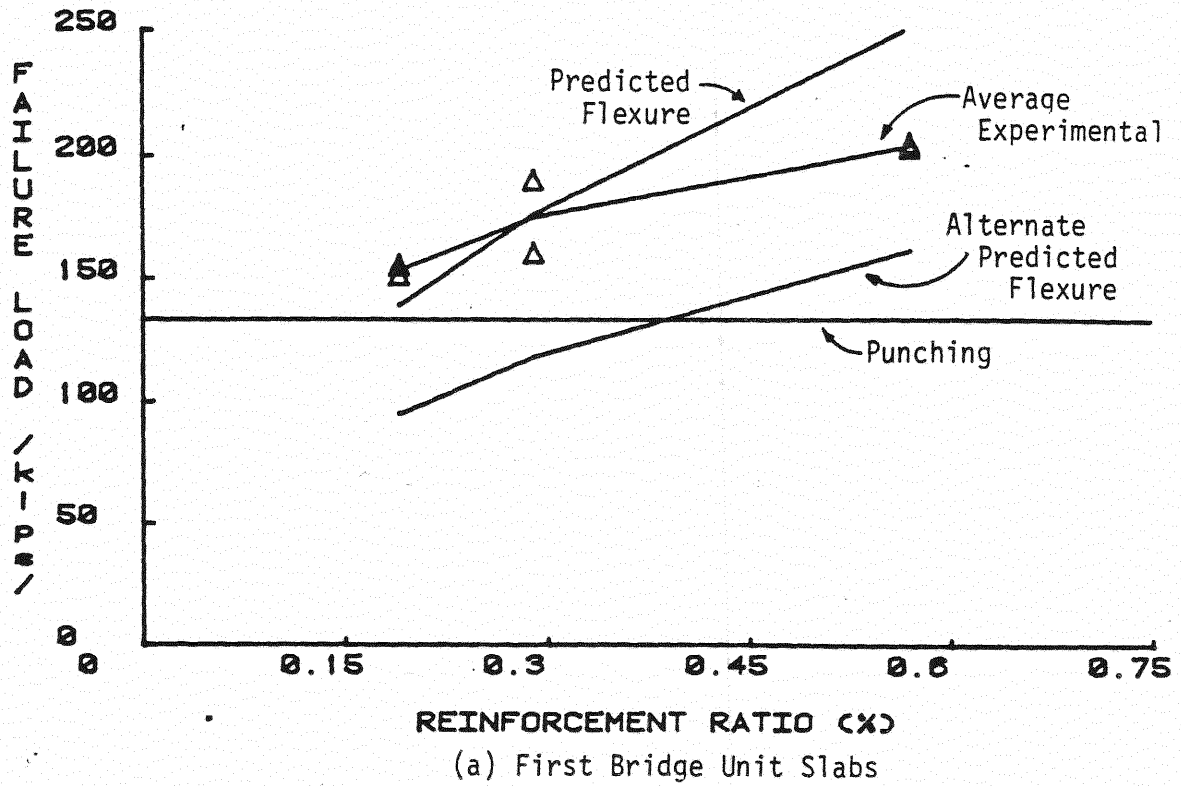Reinforcement Ratio, Phase XII Transverse Slab Strength
Tests

I.1
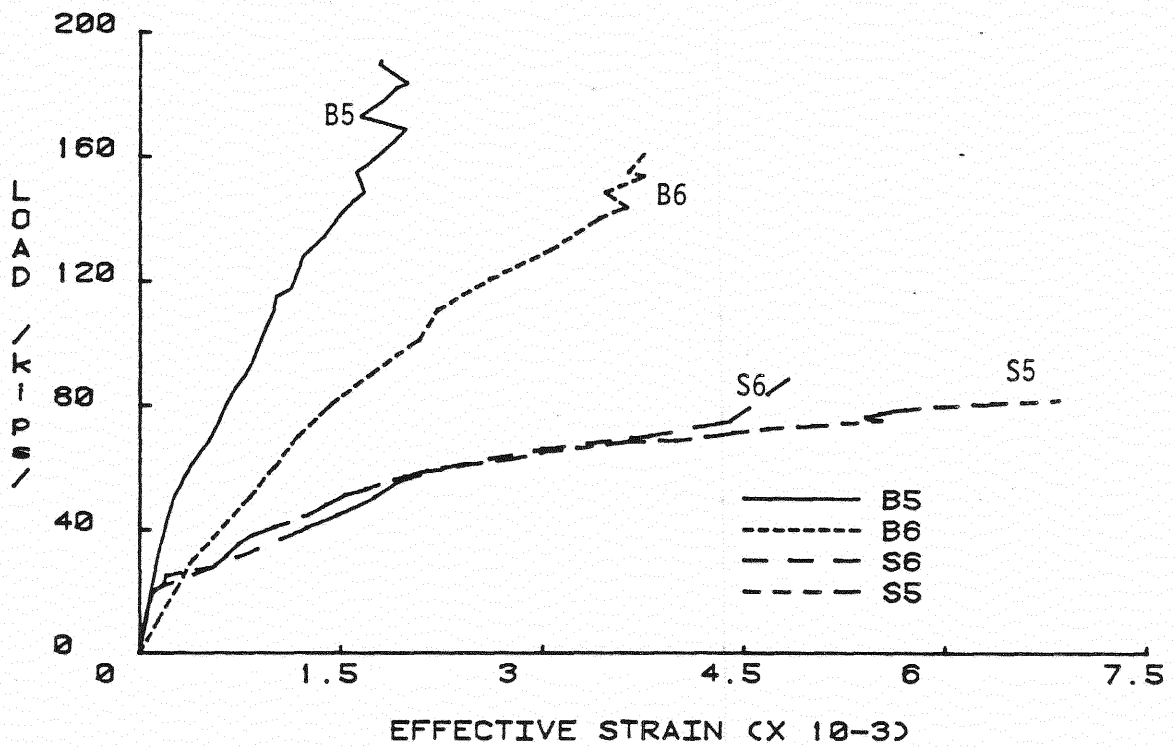
Figure I.3　Load vs. Effective Strain for Slabs with 0.29% Reinforcement Ratio, Phase XII Transverse Slab Strength Tests

Figure I.4　Load vs. Restraint Displacement for Slabs with 0.29% Reinforcement Ratio, Phase XII Transverse Slab Strength Tests

I.2

Figure I.5   Load vs. Effective Strain for Slabs with 0.57% Reinforcement
Ratio, Phase XII Transverse Slab Strength Tests

Figure I.6   Load vs. Restraint Displacement for Slabs with 0.57%
Reinforcement Ratio, Phase XII Transverse Slab Strength
Tests

I.3

Figure I.7 Failure Load vs. Slab Transverse Reinforcement Ratio,
Phase XII Transverse Slab Strength Tests

I.4

APPENDIX J

SHEAR CONNECTOR SPECIMEN TEST RESULTS

SECTION J.1

PHASE XIII A RESULTS

810 DAYS OF SUSTAINED LOADING
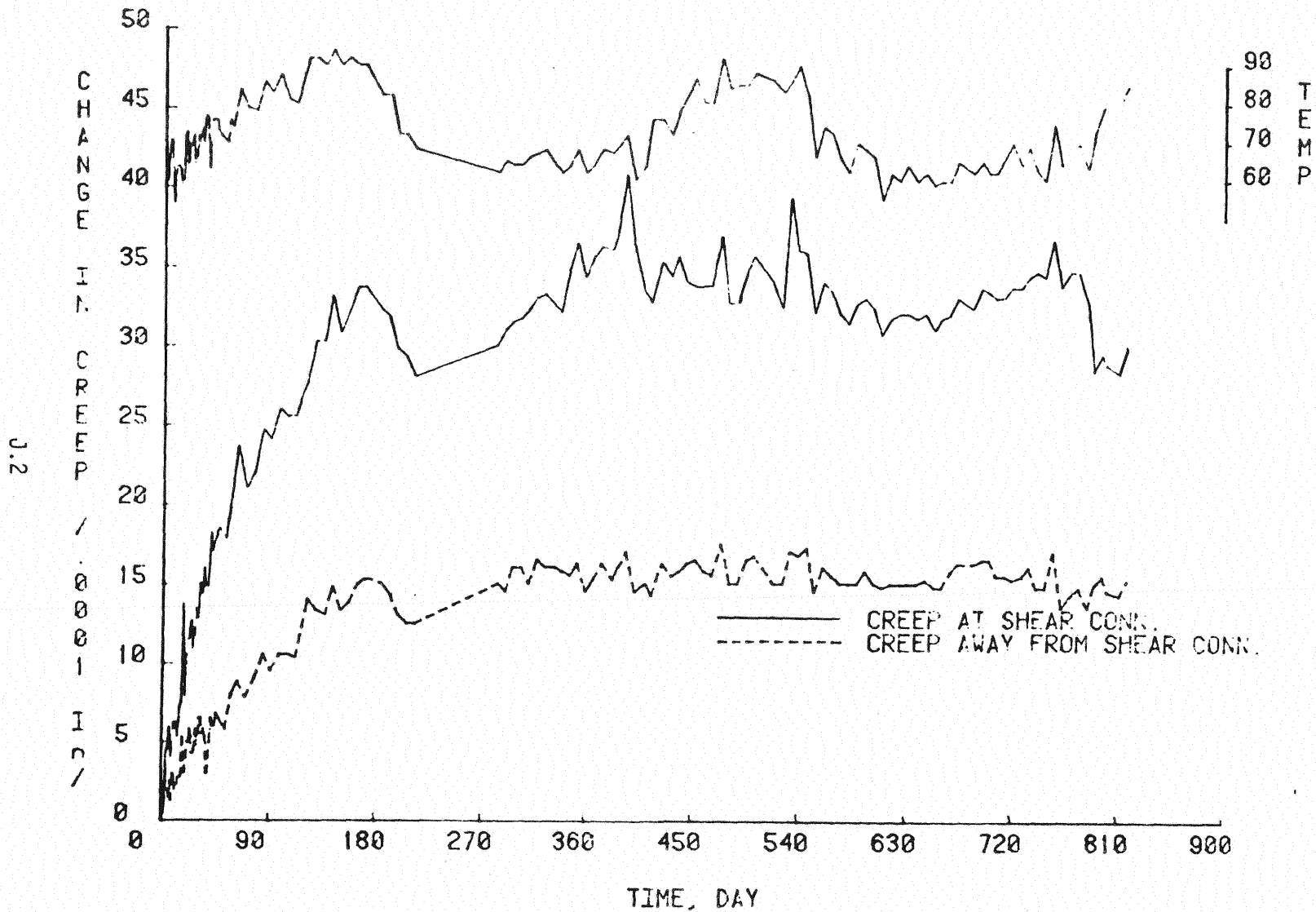
Figure J.1   Average Creep Displacement for Stud Type Connectors, Phase XIII A Sustained Loading of Shear Connector Specimens
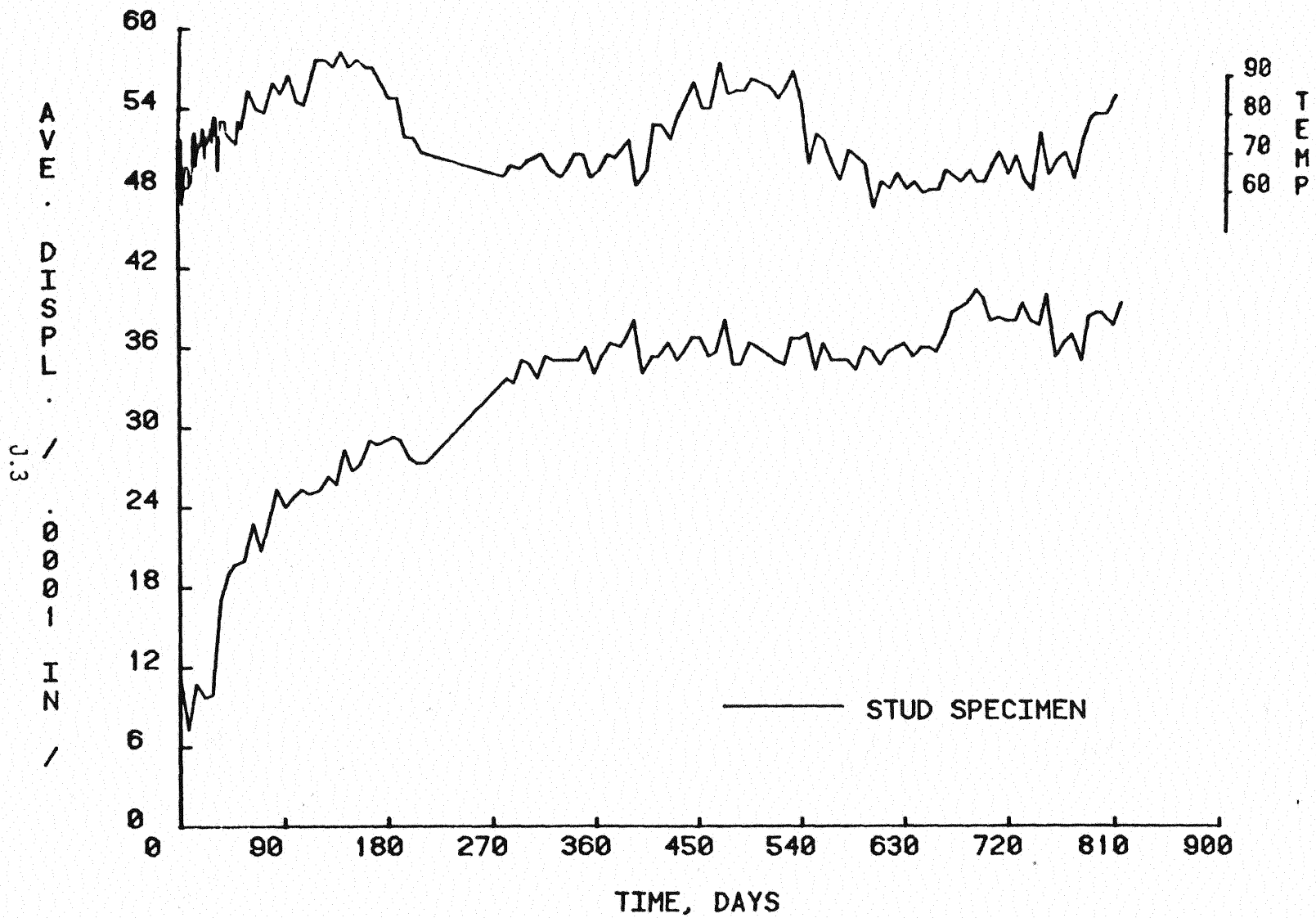
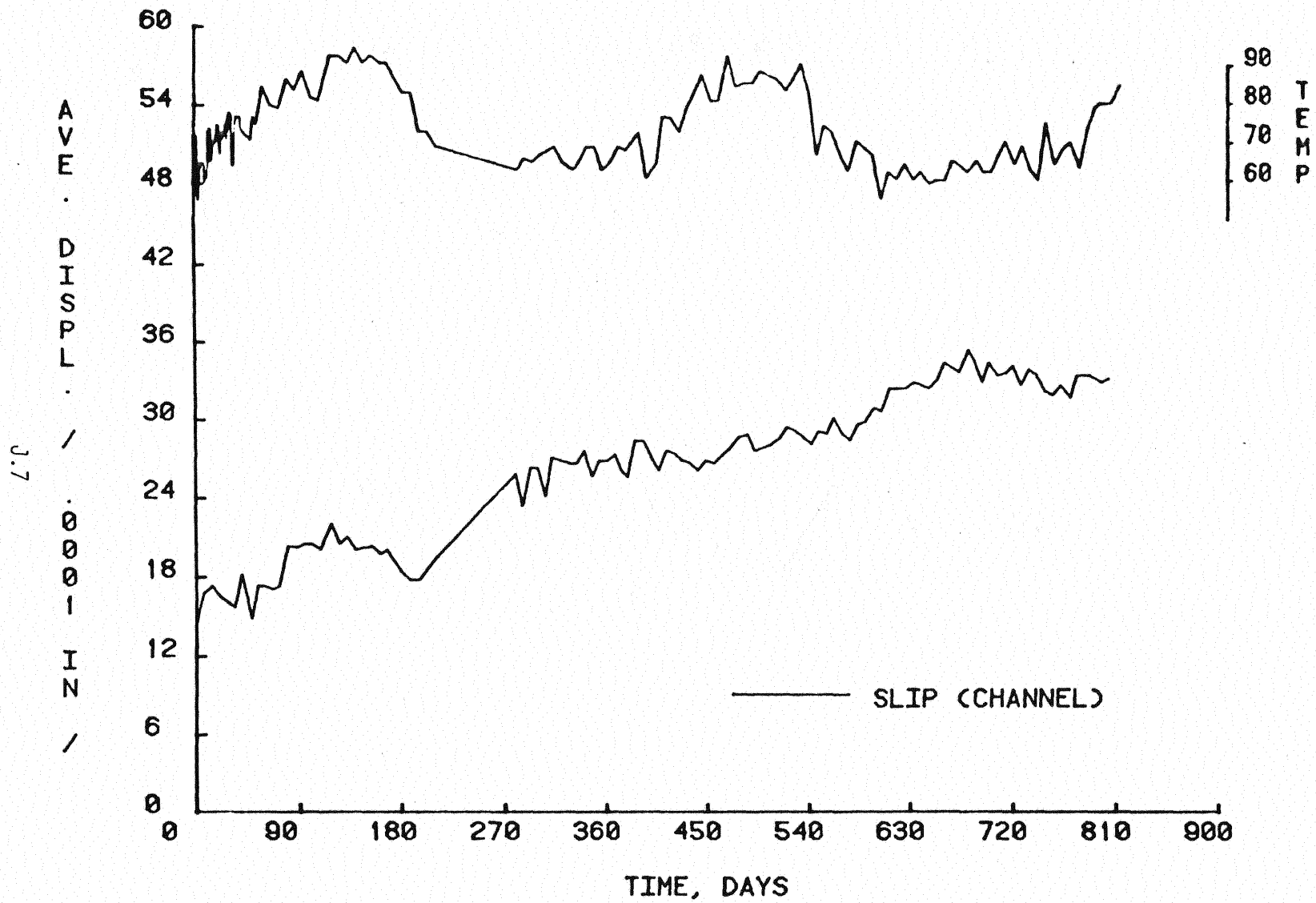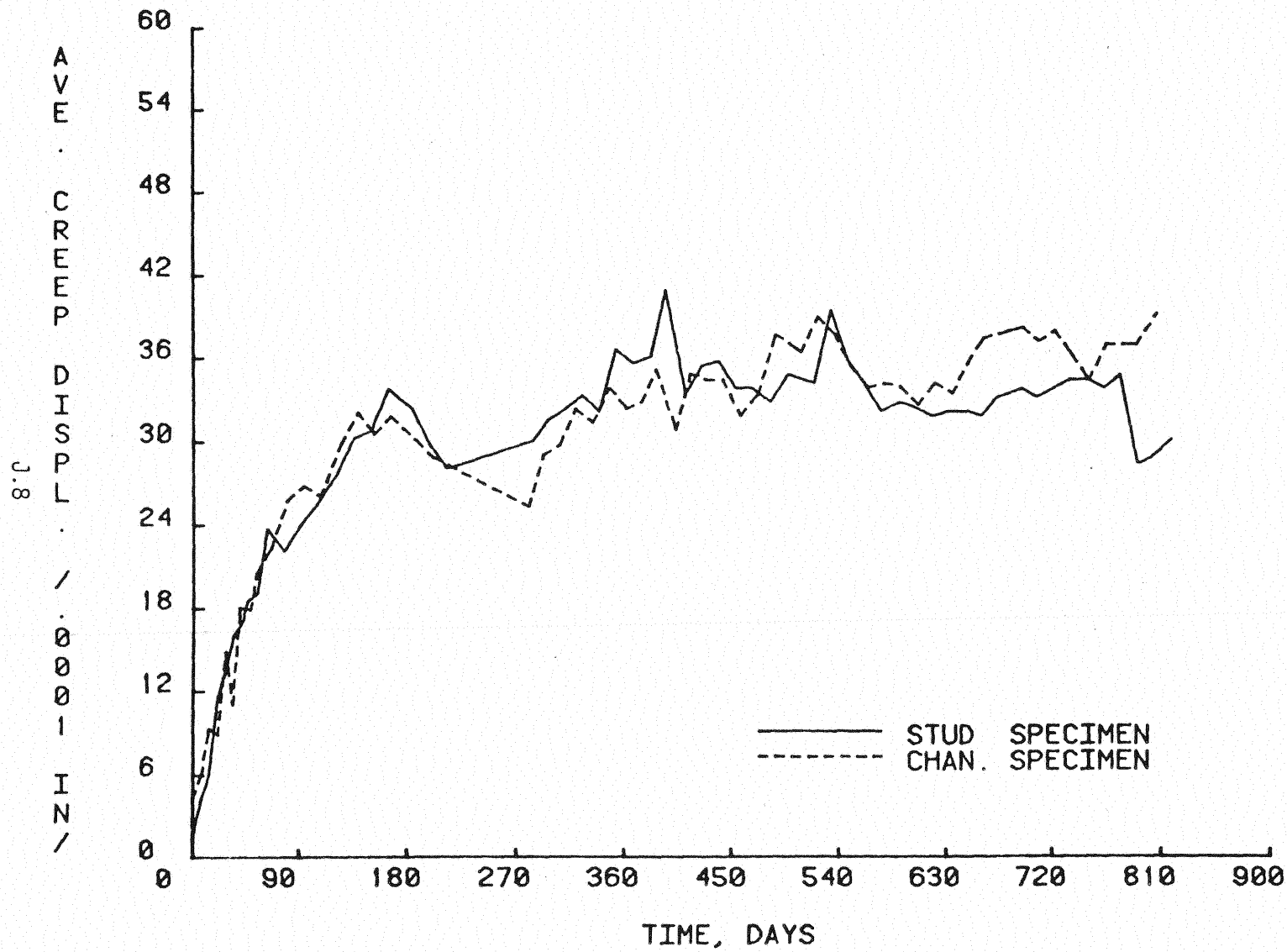Figure J.2   Average Slip Plus Creep Displacement for Stud Type Connectors, Phase XIII A of Shear Connector Specimens
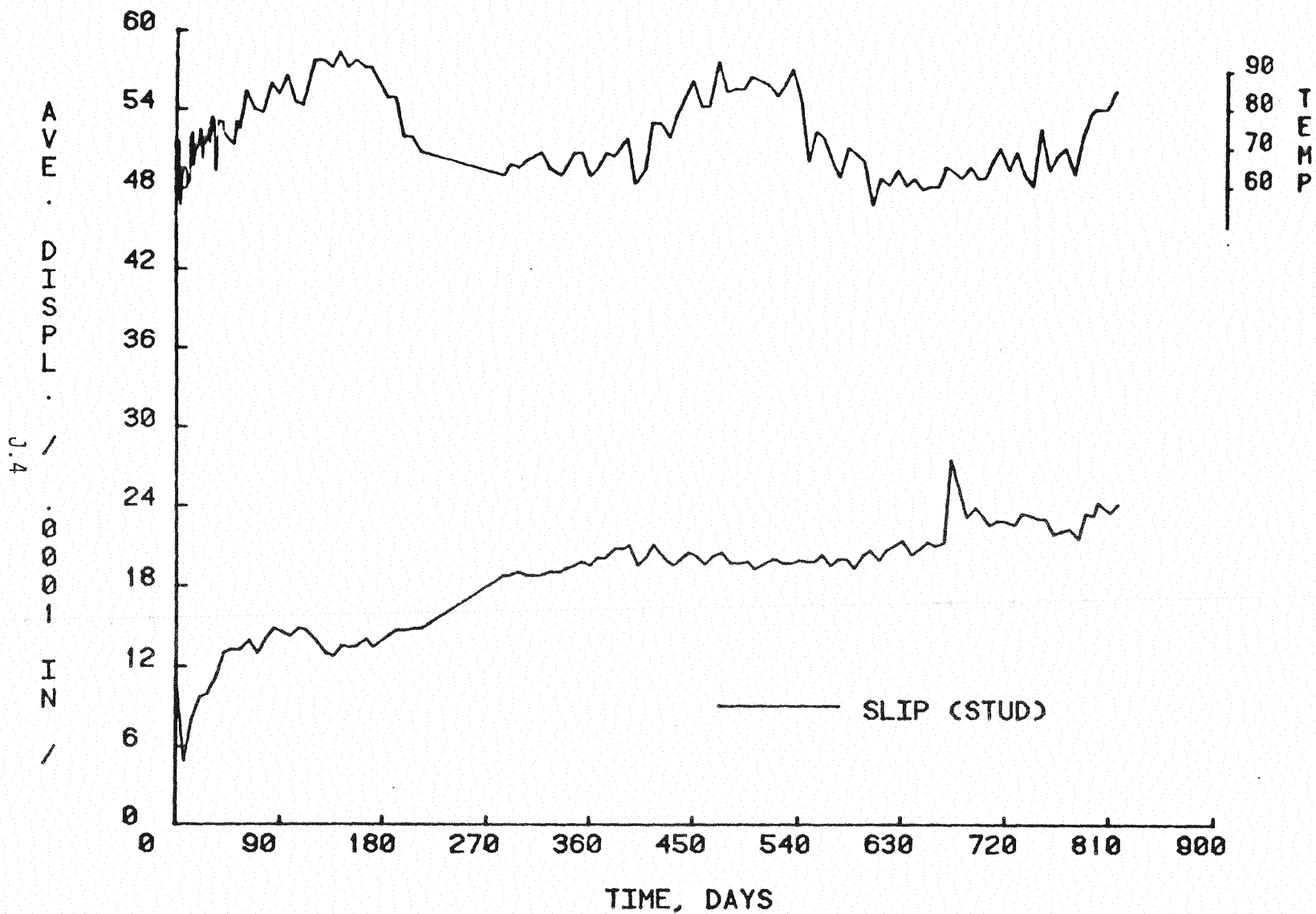
Figure J.3   Average Slip Displacement for Stud Type Connectors, Phase XIII A of Shear
Connector Specimens
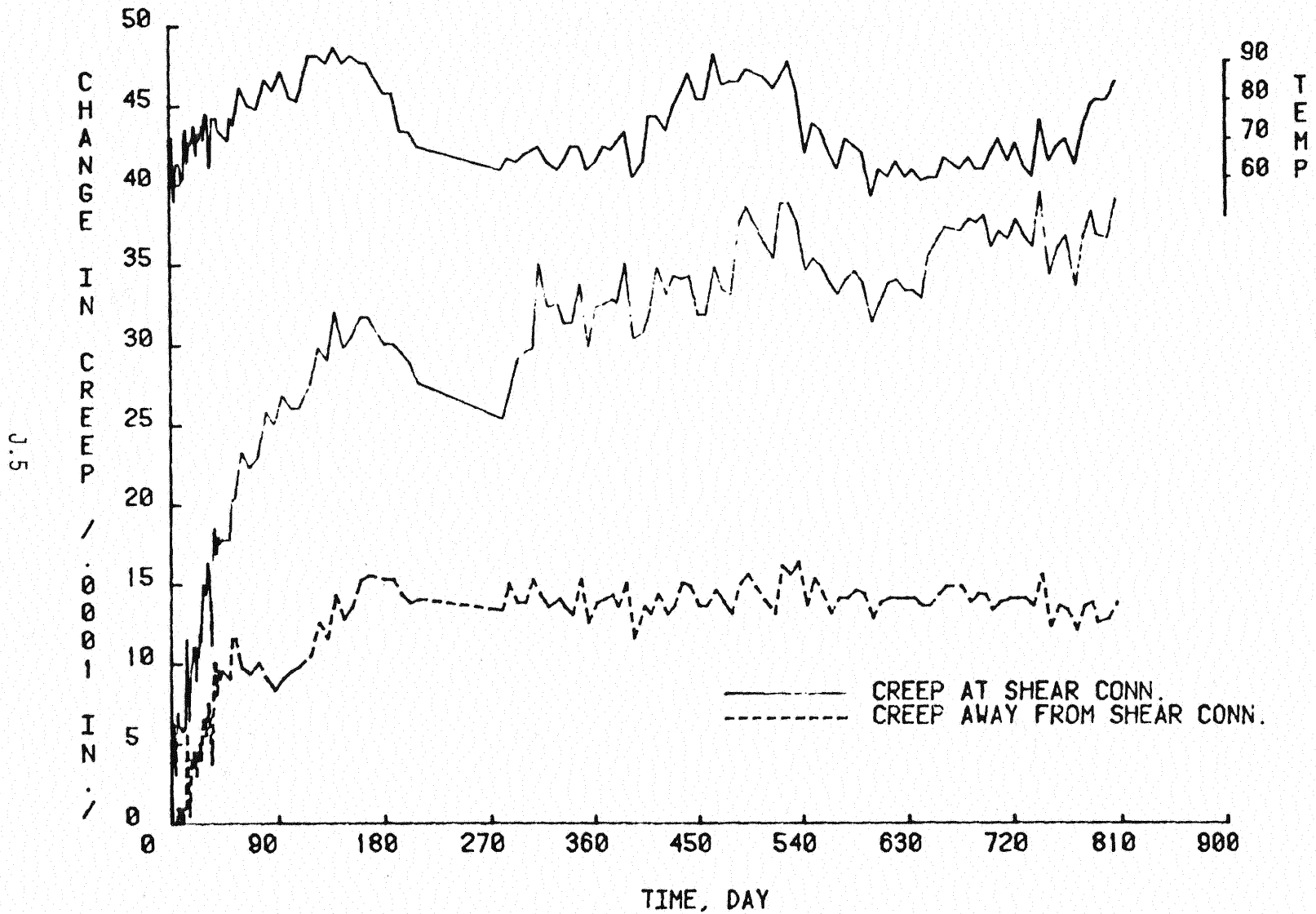
Figure J.4   Average Creep Displacement for Channel Type Connectors, Phase XIII A of Shear
             Connector Specimens

J.5
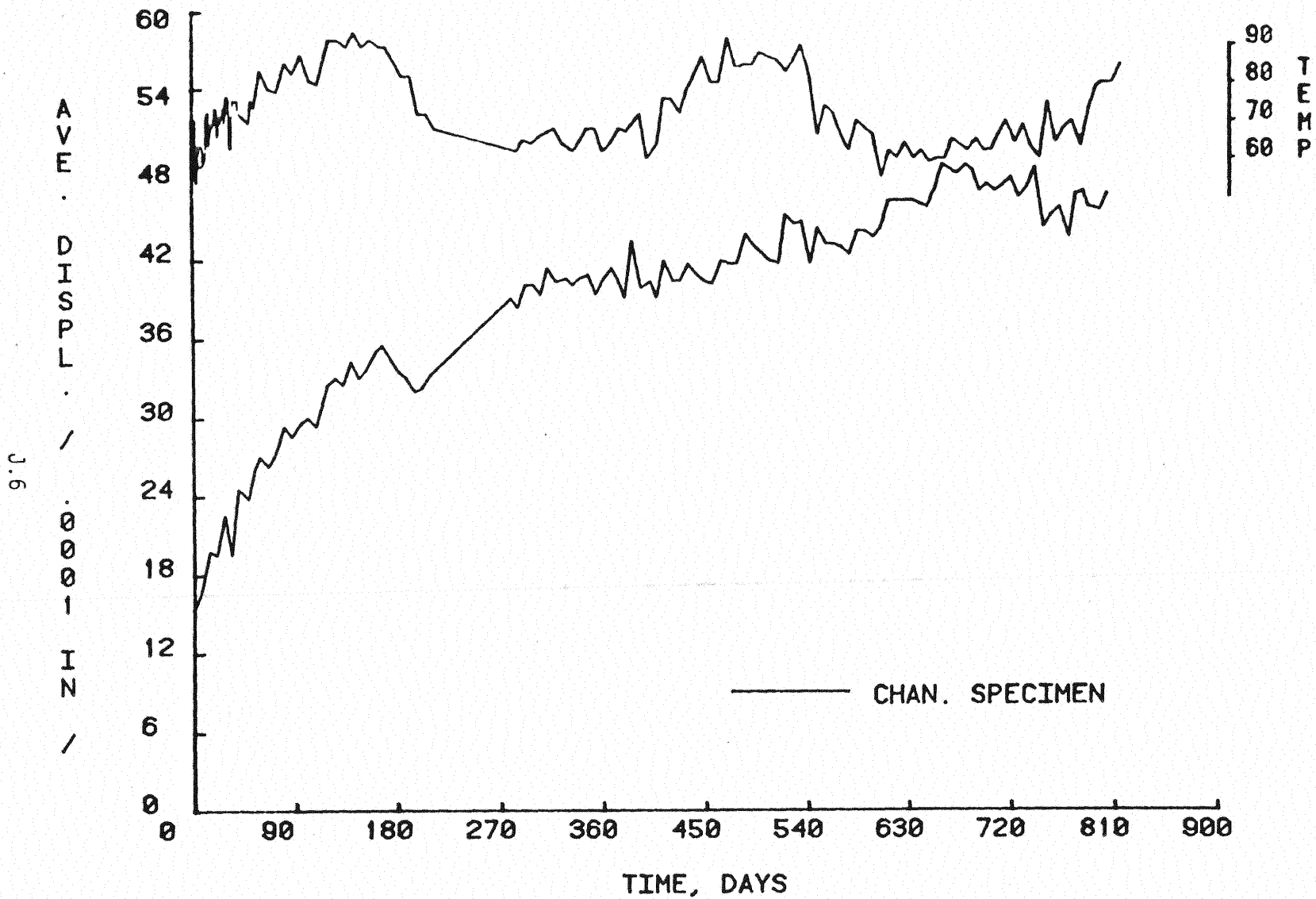
Figure J.5   Average Slip Plus Creep Displacement for Channel Type Connectors, Phase XIII A of Shear Connector Specimens

Figure J.6 Average Slip Displacement for Channel Type Shear Connectors, Phase XIII A of Shear Connector Specimens

J.7

Figure J.7 Comparison of Average Creep Values At Shear Connectors, Phase XIII A of
Shear Connector Specimens
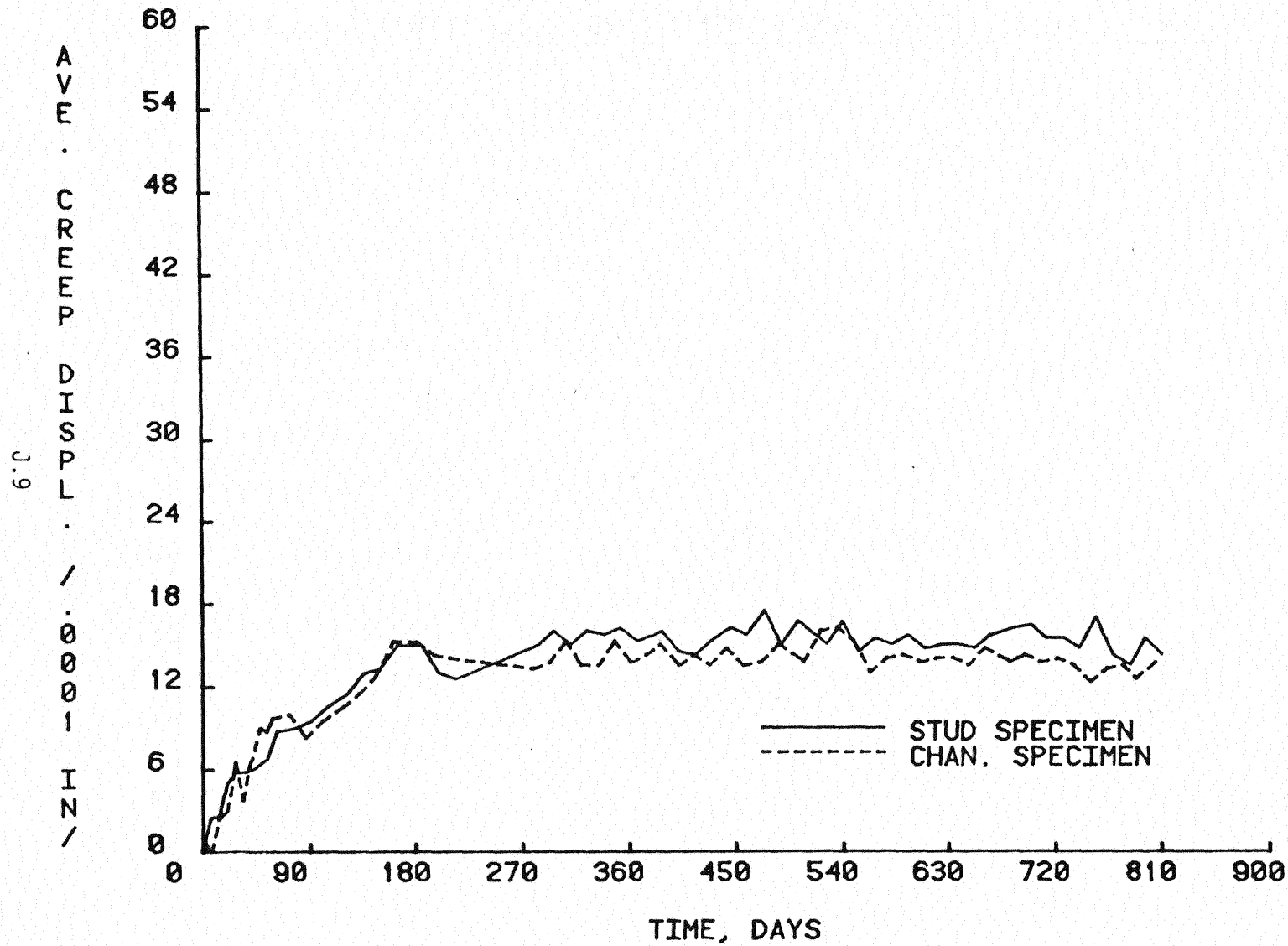
Figure J.8   Comparison of Average Creep Values Away from Shear Connectors, Phase XIII A
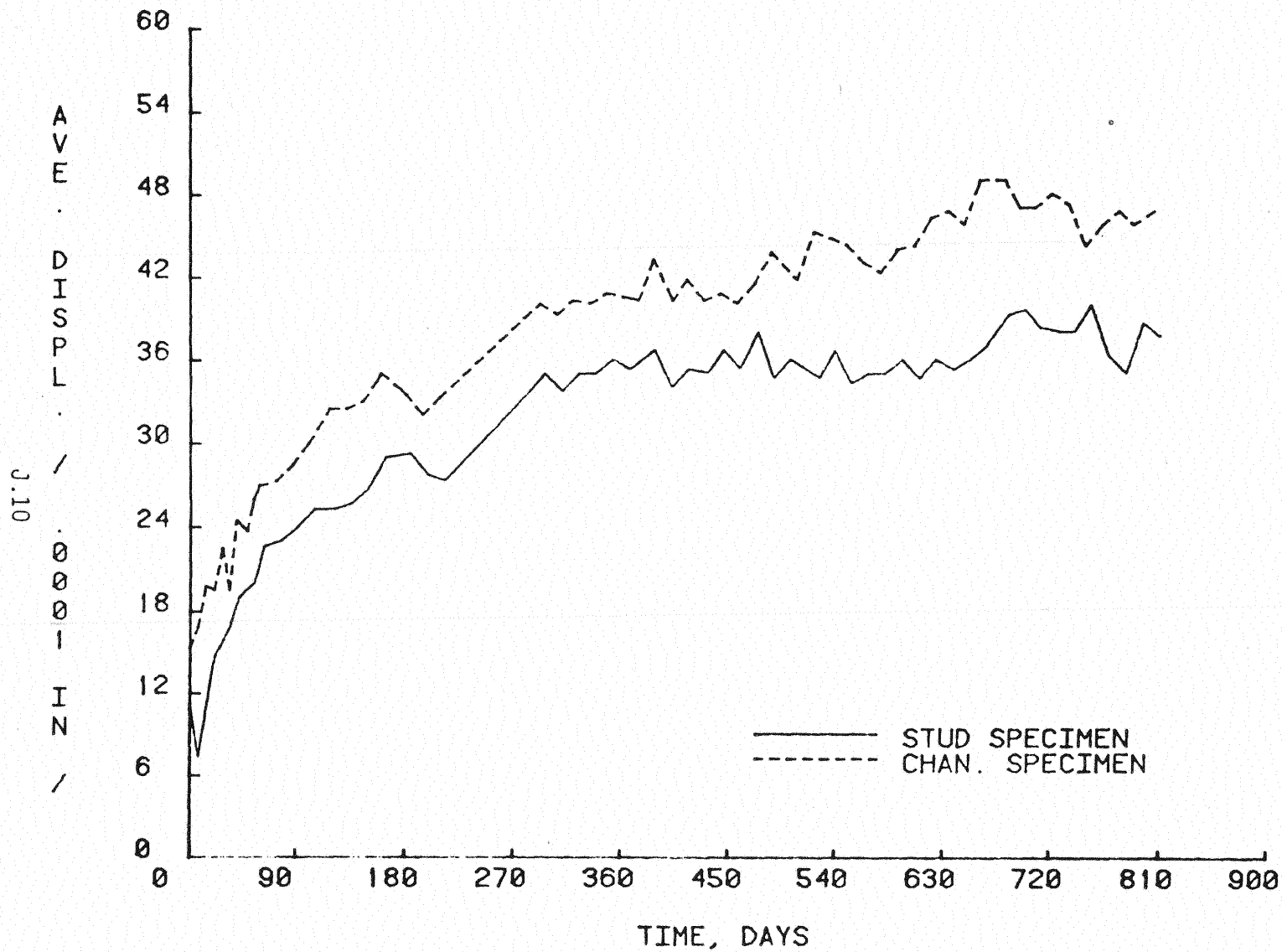of Shear Connector Specimens

Figure J.9 Comparison of Average Slip Plus Creep Values of Shear Connectors, Phase XIII
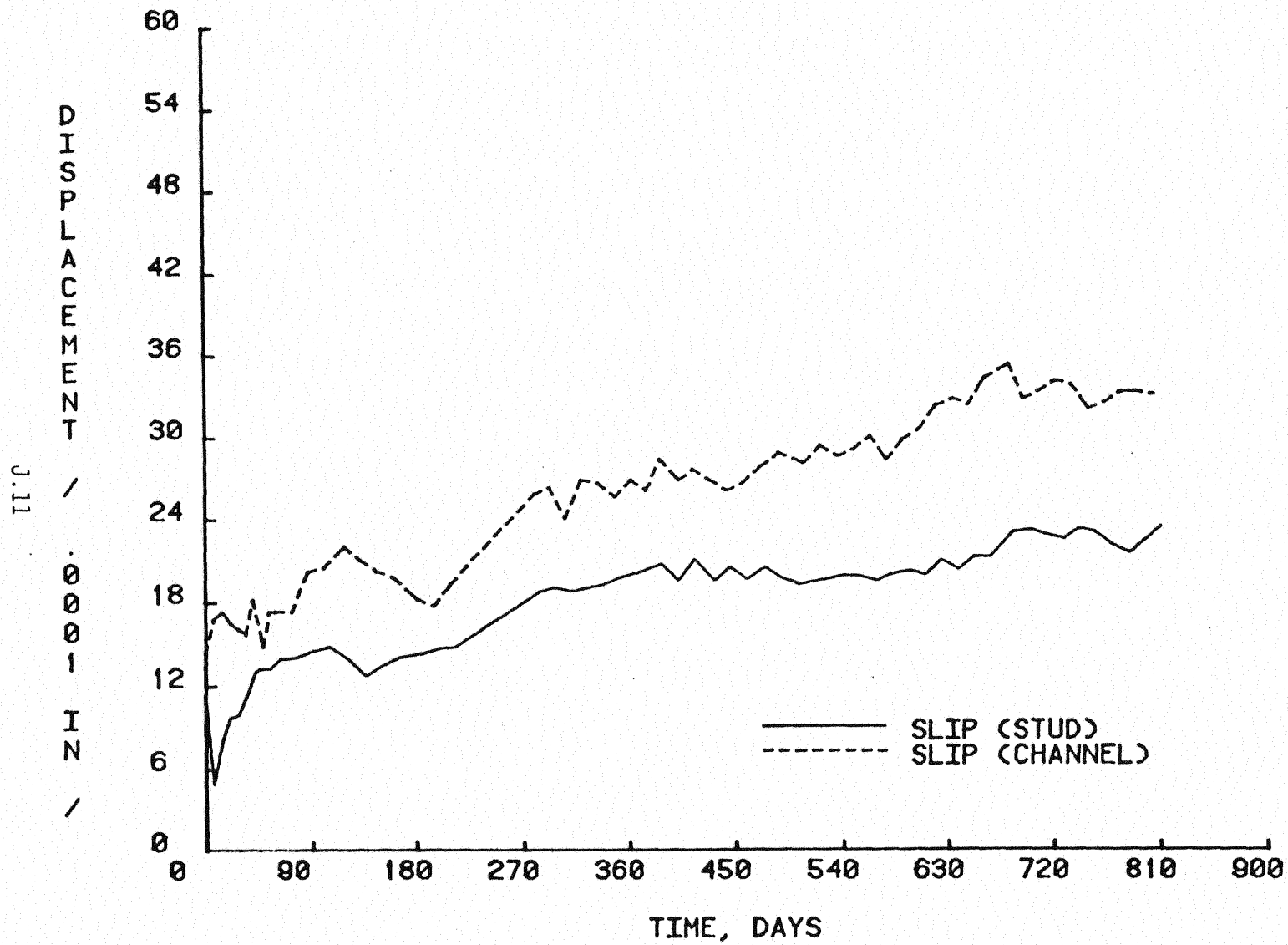A of Shear Connector Specimens

Figure J.10   Comparison of Average Slip Values of Shear Connectors, Phase XIII A
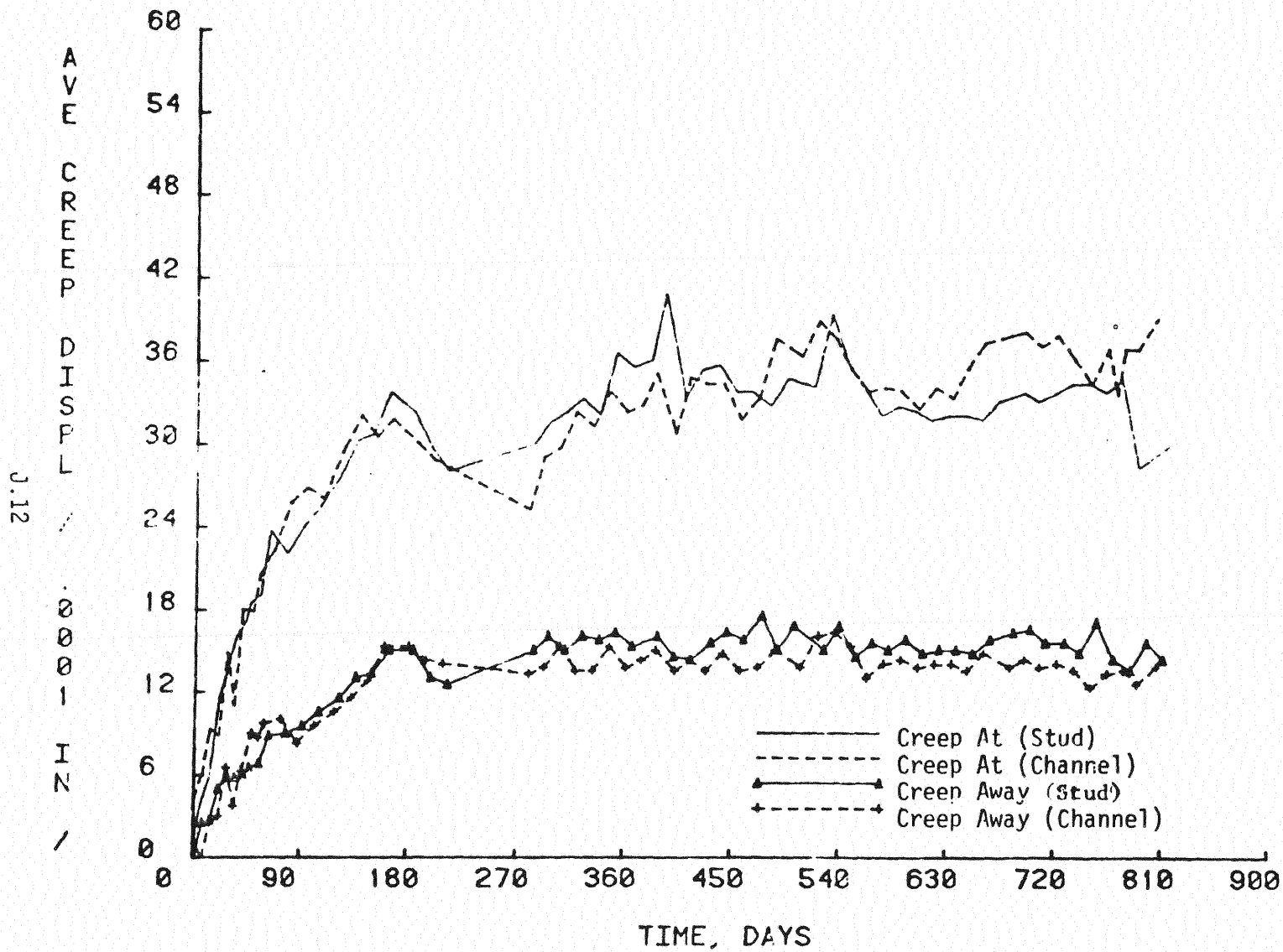of Shear Connector Specimens

J.11

Figure J.11   Comparison of Average Creep Values At and Away from Shear Connectors,
Phase XIII A of Shear Connector Specimens

SECTION J.2

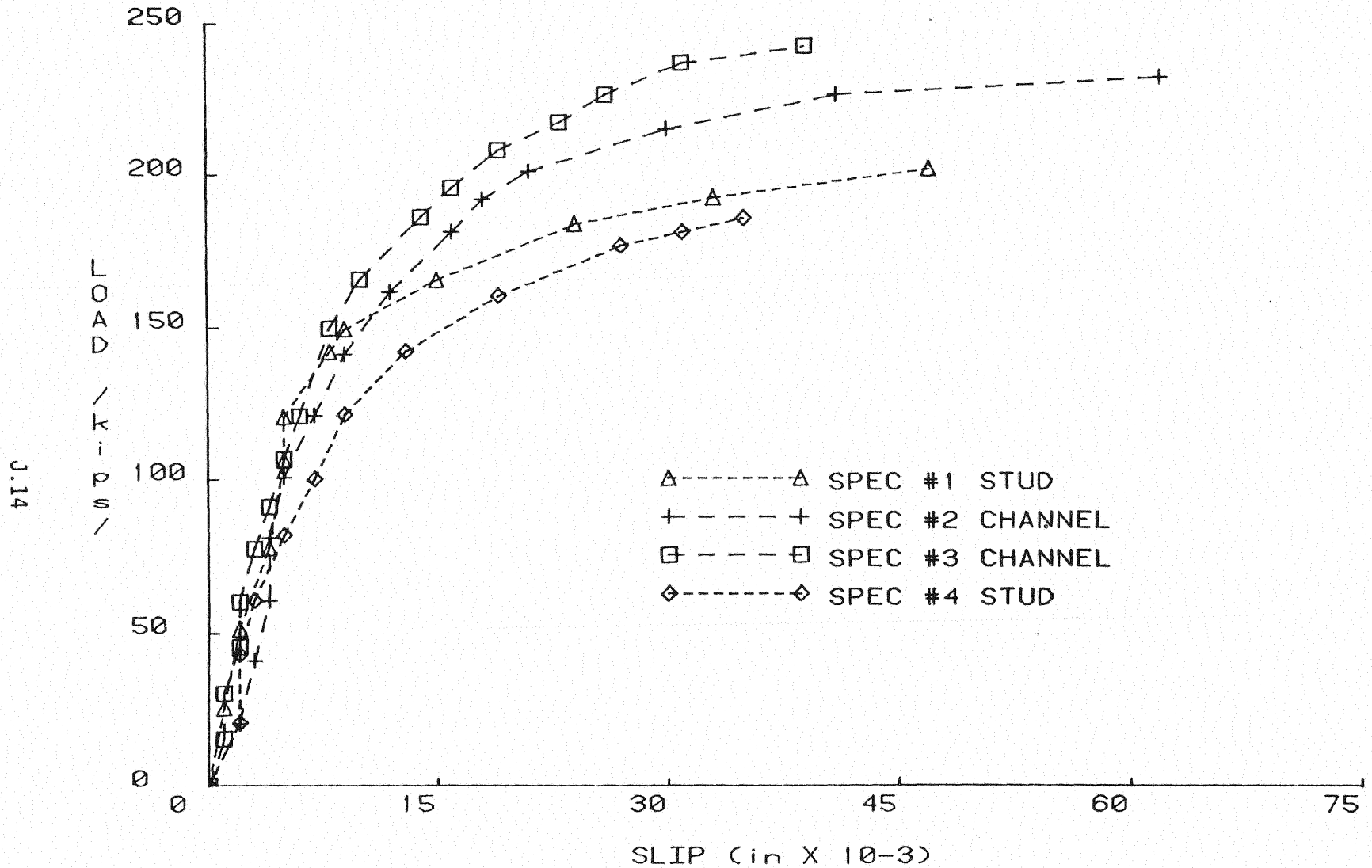PHASE XIII B RESULTS

SHEAR CONNECTOR SPECIMEN FAILURE TEST

Figure J.12   Load vs. Slip Displacement, Phase XIII B Shear Connector Specimen
Failure Test

J.14

Table J.1

Experimental and Predicted Ultimate Strengths
of Shear Connectors

(a) Stud Type Shear Connectors

Ultimate Load per Connector (kips)	
Experimental:	
Specimen #1	25.1
Specimen #4	25.9
Predicted:	
Equation 3.1	34.8
Equation 3.1*	27.9

*Results for f'_c = 4000 psi

(b) Channel Type Shear Connectors

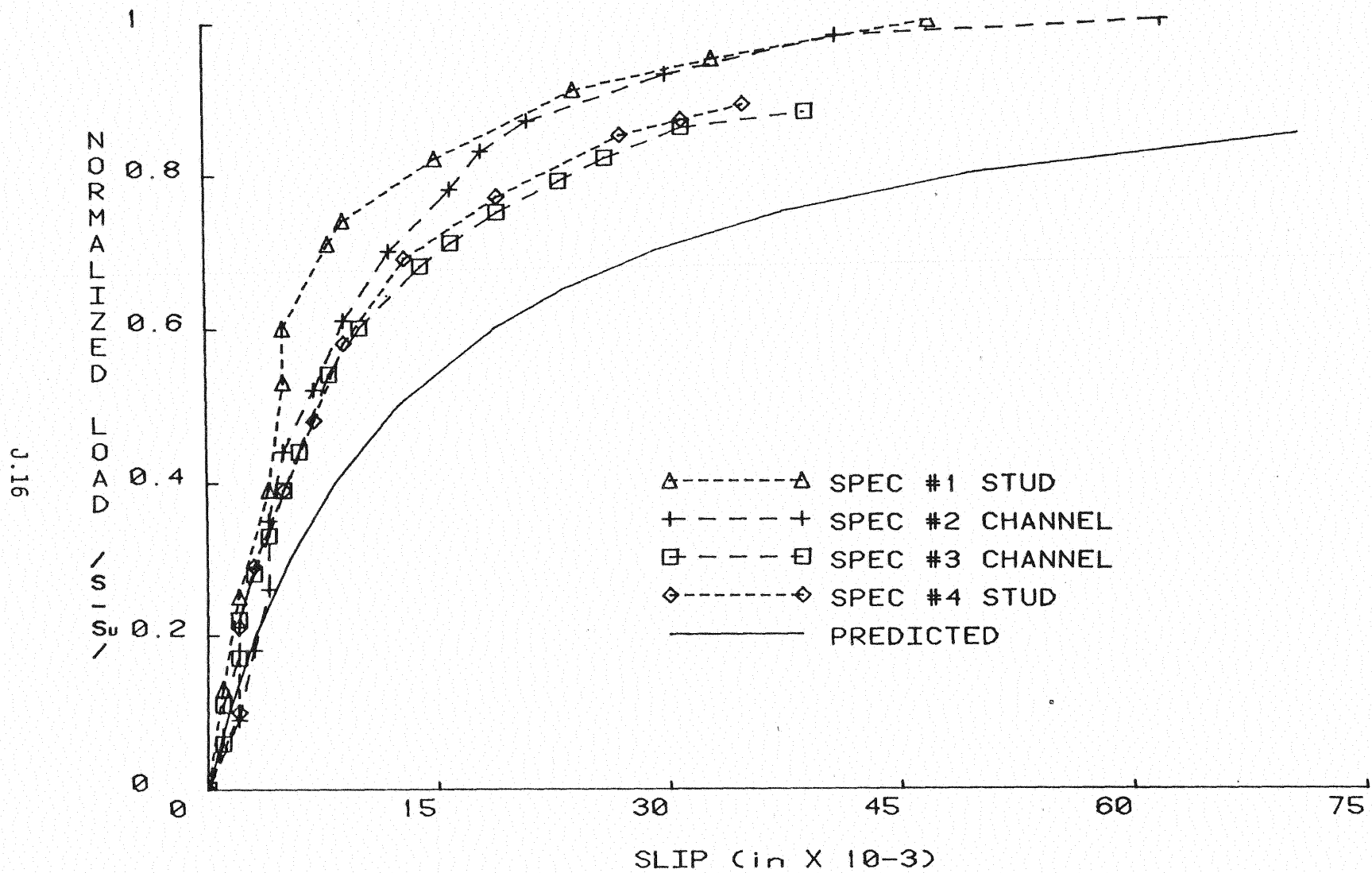| Ultimate Load per Connector (kips)	
Experimental:	
Specimen #2	57.8
Specimen #3	68.8
Predicted:	
Equation 3.2	57.7

Figure J.13   Normalized Load vs. Slip Displacement, Phase XIII B Shear Connector
Specimen Failure Test

APPENDIX K

CALCULATIONS FOR PRIMARY TESTS

APPENDIX K

In this appendix, the calculations used in the analysis of the test units are presented. Using simple flexure theory, response of the bridge units to construction prestress and test loading conditions was estimated to provide a comparison between observed and theoretical behavior. The section properties for Unit 1 may be found in Appendix A and the section properties used for Unit 2 may be found in Appendix B.

In this type of bridge unit construction, all gravity loads which are applied to the steel beams during construction (wet concrete weight, form weight, etc.) cause stresses in the steel beams which become locked in when the concrete deck cures. The section properties of the unit are thereby changed such that the reversal of loads which occurs in the unloading and righting of the unit are resisted by a much stiffer cross section. These locked in stresses result in the prestressing of the composite girders, which raises the load at which first yield occurs in the cross-section, over the first yield loads of shored or unshored composite construction. Even though the ultimate strength of the prestressed unit remains the same as an identical unshored unit, the service load range is increased in the prestressed composite unit since the allowable load is a fraction of the load which causes first yield in the cross-section. But, the first yield load of the prestressed unit is reduced by the effects of creep and shrinkage in the concrete which occur due to drying of the concrete and sustained loads

(which include prestress loads). Thus the reduction in strength of the unit due to sustained loading effects must be considered in the design of the unit.

The two most common ways of doing this are Branson's method and the effective concrete elastic modulus method. In Branson's method, actual stresses due to sustained loading which occur in the unit cross-section are determined using empirical estimates of concrete creep and shrinkage phenomena; the useable strength of the cross-section may then be reduced directly. Branson's method is discussed in greater detail in Section 2.2.1 of this report and in Reference 4.

The second method, the effective concrete modulus method, is prescribed in the AASHO Specification [1]. In this method, sustained load and live load stresses are, in effect, resisted by two different cross-sections of the same composite unit. Live load stresses are resisted by the cross-section obtained in standard transformed area analysis. The width of concrete is reduced (transformed) by the ratio of the steel elastic modulus to the concrete elastic modulus (the modular ratio, n) and section properties are determined for the transformed section. On the other hand, sustained load stresses are considered to be resisted by a transformed cross-section obtained with the modular ratio increased by a factor of 3.0. This results in the allowance for the increase in stress due to sustained load effects, since the sustained load stresses are considered to be resisted by a smaller cross-section.

It is interesting to note that for the composite sections tested, the analysis for sustained loading effects by this method results in the prediction that deflection of the unit is much more sensitive to sustained loading effects

than is the reduction in useable strength. Defining the
"modular ratio multiple" as the ratio of the concrete
elastic modulus used in sustained load analysis to the
concrete elastic modulus used in live load analysis (as
noted, the AASHO Specification prescribes a modular ratio
multiple of 3.0), the section properties of the second
bridge unit were determined for a modular ratio multiple
which varied from 1.0 to 10.0. Figure K.1 shows that the
moment of inertia (and therefore the stiffness) of the
bridge unit was sharply reduced as the modular ratio
multiple was increased from 1.0 to 5.0, and then remained
relatively stable--at a level of about twice the limiting
value of the moment of inertia of the naked steel beams.
Figure K.2 shows the change in section moduli for the top
concrete surface, top steel beam flange, and the bottom
steel beam flange as a function of the change in modular
ratio multiple. Since the highest bending stress in the
cross-section occurs where the section modulus is lowest,
the figure shows that the stress in the bottom flange will
always govern first yield occurrence. And as long as the
concrete has any resistance, the section modulus of the
composite unit will remain greater than the section modulus
of the steel beams alone.

     The controlling section modulus of the unit appears to
be much less affected by the increase in modular ratio
multiple when compared to the change in moment of inertia.
This is due to the shifting of the neutral axis in the
direction of the bottom flange as the modular ratio multiple
is increased, as shown in Figure K.3. Thus, as long as the
change in the neutral axis location as measured from the
bottom flange roughly parallels the change in moment of
inertia, their ratio (the section modulus of the beam bottom
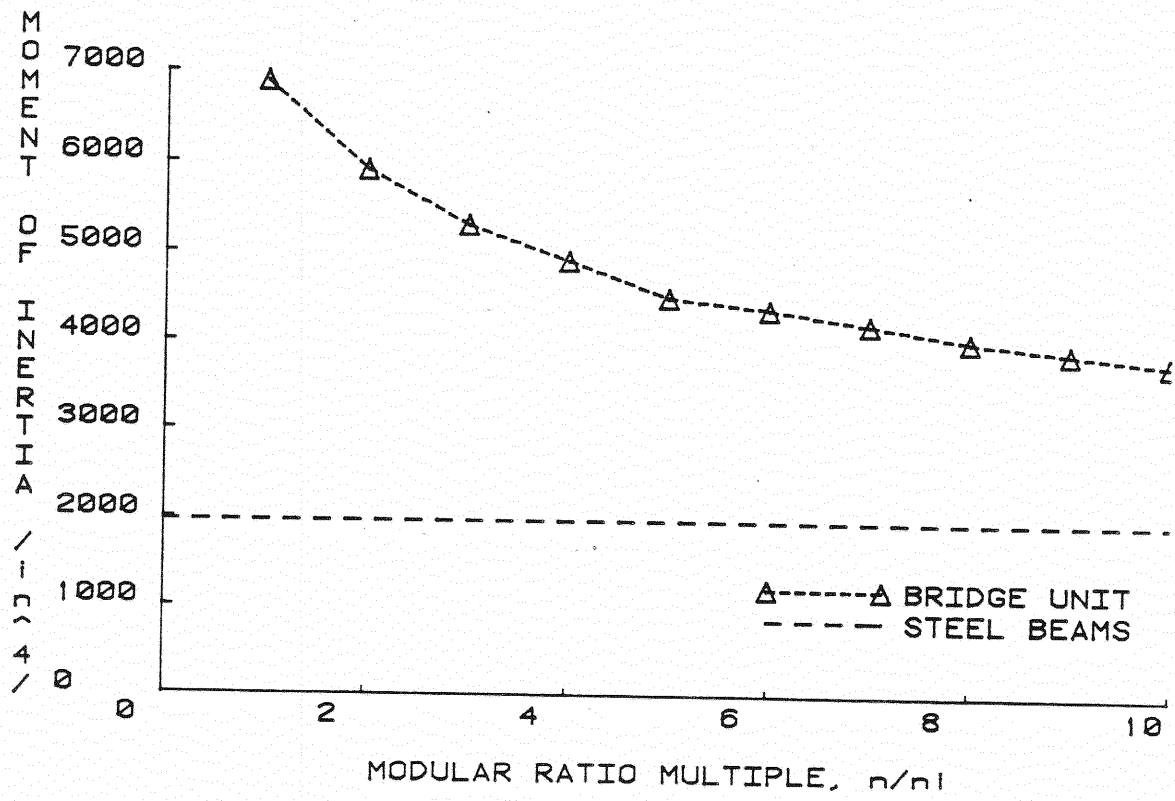flange) remains roughly stable.

Figure K.1 Moment of Inertia of Second Bridge Unit vs. Modular Ratio Multiple
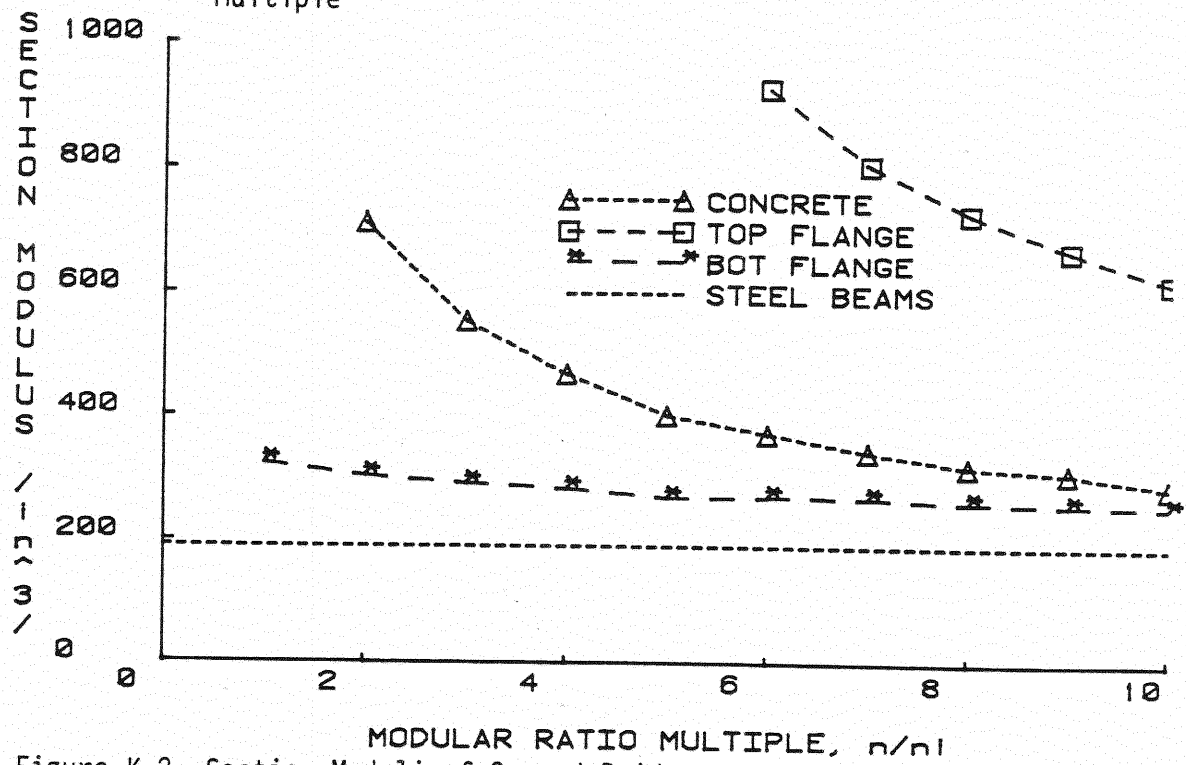

Figure K.2 Section Moduli of Second Bridge Unit vs. Modular Ratio Multiple

Figure K.4 is a plot of nondimensionalized moment of inertia (I), section modulus of the bottom beam flange (S), and neutral axis distance from the bottom of the beam (Y) as a function of the modular ratio multiple. The section properties are nondimensionalized with respect to their values when the modular ratio multiple is 1.0. The plot shows that for the design modular ratio multiple of 3.0, the moment of inertia of the section was reduced to 77% of its original value, whereas the section modulus was reduced much less in that it retained 90% of its original value. And for the extreme modular ratio multiple of 10.0, the moment of inertia of the section was reduced to 55% of its original value, but the section modulus was still 80% of its original value due to the change in the neutral axis location. This shows that the stiffness, or deflection, of the unit (which is inversely proportional to the moment of inertia of the section) is much more sensitive to sustained loading effects than the decrease in yield strength (which is proportional to the section modulus) of the unit due to loss of prestress in the critical bottom flange extreme fiber.

Since a major objective of this research project was concerned with determining the deviation between theoretical and actual yield strength of the unit, all loading conditions were necessarily considered in the theoretical analysis. During construction and testing, the unit was subjected to three different gravity loading types as shown in Table K.1, which includes the equations used in calculating midspan moments and deflections due to the particular loading types. Table K.2 gives a tabular summary of the order and magnitudes of the three loading types used in the construction and testing of the unit. The first column of Table K.2 denotes the end view of the unit in its inverted (⊥⊥) or upright (ͳͳ) position for the sequence of loadings. The "Resisting Section" of the unit is the steel
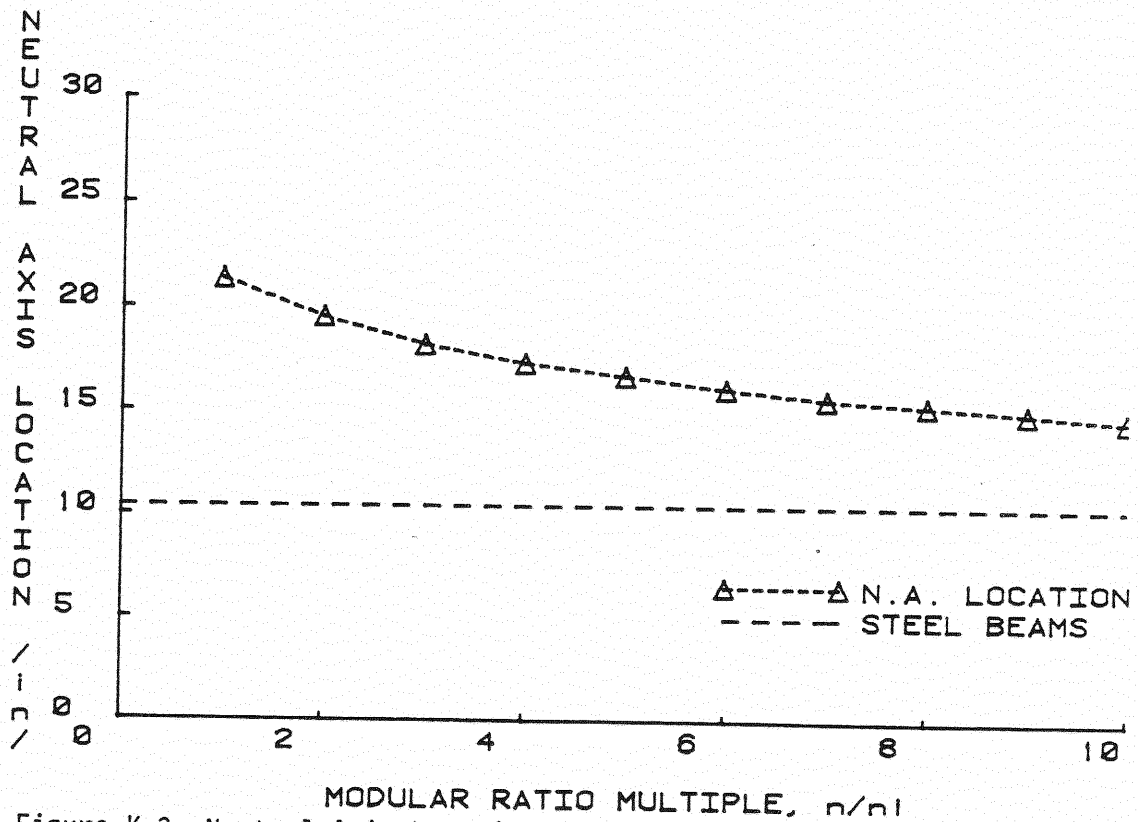
K.5

Figure K.3   Neutral Axis Location from Bottom of Beam vs. Modular
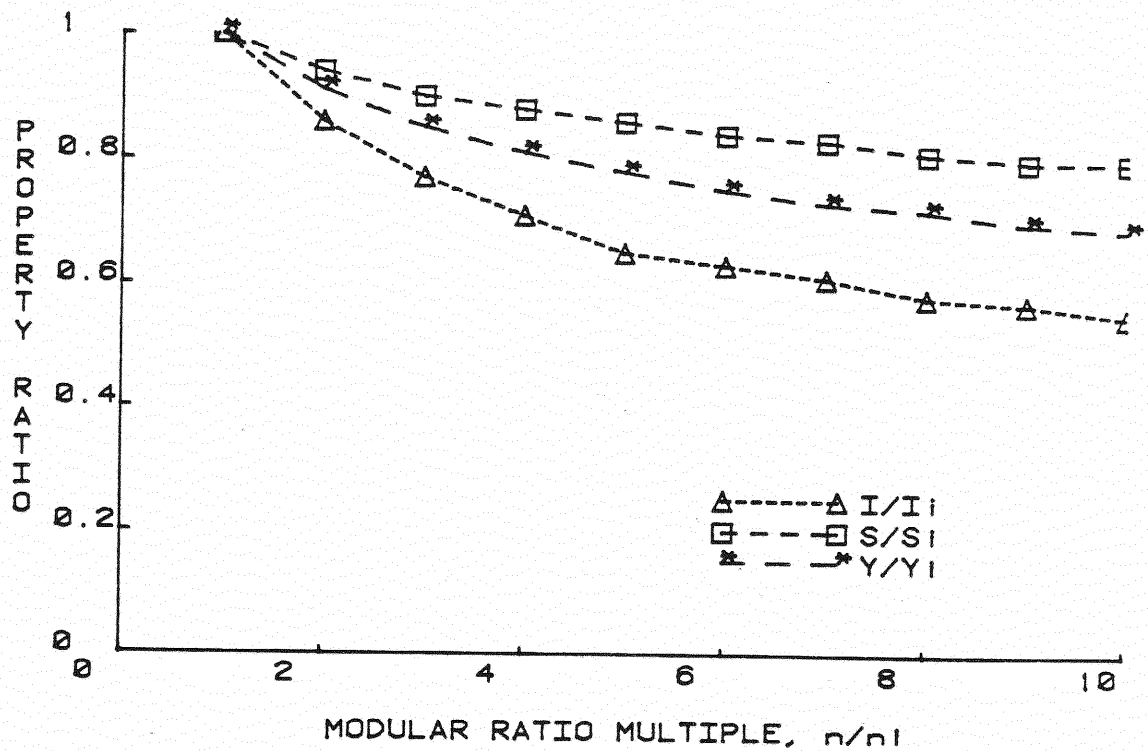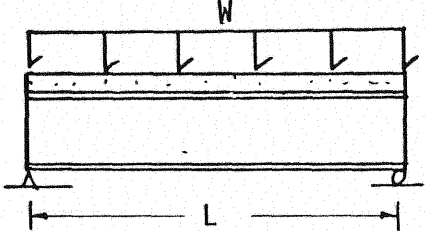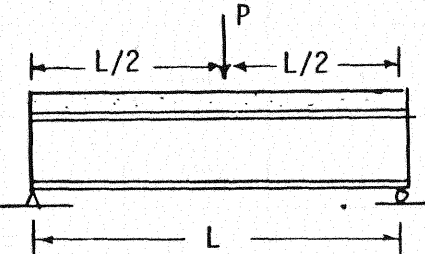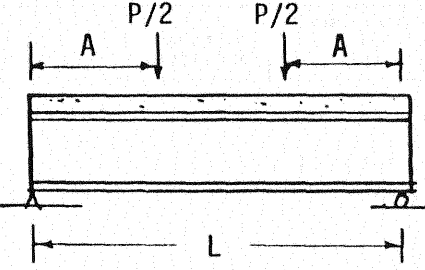Ratio Multiple

Figure K.4   Non-dimensionalized Section Properties vs. Modular Ratio
Multiple

Table K.1
Loading Configurations Used During Construction
and Testing of Bridge Units

LOADING TYPE	MIDSPAN MOMENT	MIDSPAN DEFLECTION
A:	$M = \dfrac{WL^2}{8}$	$D = \dfrac{5WL^4}{384\,EI}$
B:	$M = \dfrac{PL}{4}$	$D = \dfrac{PL^3}{48\,EI}$
C:	$M = \dfrac{P}{2a}$	$D = \dfrac{Pa}{48\,EI}(3L^2-4a^2)$ $a = 20'; \; L = 54'$

Table K.2

Summary of Loading Configurations Used During Construction and Testing of Bridge Units
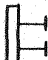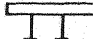
Configuration of Unit	Resisting Section	Loading Type (from Table K.1)	Load Magnitude Unit 1	Unit 2	Comment
	steel beams	A	$W = 0.10^{k/'}$	$0.10^{k/'}$	Steel beams set in inverse position
	steel beams	A	$W = 0.849^{k/'}$	$0.844^{k/'}$	Steel beams supporting forms and concrete
	steel beams	B	$P = 3.6^{k}$	8.7^{k}	extra load applied to obtain 3.5" total mid-span deflection
	composite unit	B	$P = 3.6^{k}$	8.7^{k}	extra load removed after concrete slab has cured
	composite unit	A	$W = 0.22^{k/'}$	$0.22^{k/'}$	forms removed
	composite unit	A	$W = 0.729^{k/'}$	$0.694^{k/'}$	unit turned 90°
	composite unit	A	$W = 0.729^{k/'}$	$0.694^{k/'}$	unit turned additional 90° to upright position
	composite unit	A	$W = \pm 0.272^{k/'}$	----	concrete blocks put on and then removed after sustained loading
	composite unit	C	$P = 7.0^{k}$ Spreader Beam Weight Plus Test Load		test load applied; see App. E for load magnitudes

K.8

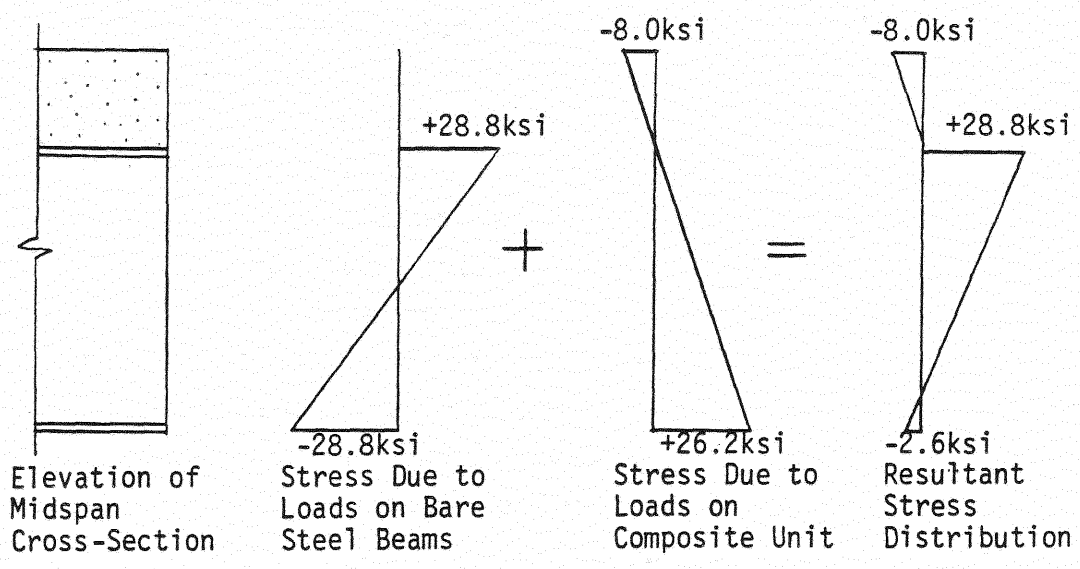beams before the concrete has cured and the composite unit after the concrete has cured. The "loading type" from Table K.1 and the corresponding load magnitude is also denoted, with the order of loading progression described in the "comment" column. The construction loading sequence essentially consisted of hanging concrete forms from the simply supported steel beams, pouring the concrete slab, and adding additional load to obtain the proper stress level in the steel beams (which may be inferred from measured deflection) prior to curing of the concrete. After the concrete has cured, the prestress load and forms are removed and the unit is turned upright, and the testing program begun.

Prestressing of the unit is the result of applying the construction loads to the steel beams before the concrete has cured, and then removing the same loads from the composite unit, with considerably more strength and stiffness, after the concrete has cured. The theoretical stress distributions for both the first and second units are shown in Figure K.5. The figure shows that as a result of prestressing the steel beams, the dead load stresses in the bottom flange of the composite section are very small. And as discussed previously, section modulus of the bottom flange of the composite section governs first yield in the cross-section; therefore, in the two units of this study, the unit may be stressed thru the full yield stress range of the bottom flange. However, the stress range will be reduced by sustained loading effects. The reduction in stress range due to sustained loading effects as determined using a modular ratio multiple of 3.0, is theoretically 4.3 ksi for the first unit, and 3.0 ksi for the second unit.

Although the effects of sustained loading tend to reduce the first yield strength of the unit, the ultimate

K.9

-8.4ksi   -8.4ksi

+25.2ksi   +25.2ksi

+

=

-25.2ksi   +25.2ksi   0ksi

| Elevation of Midspan Cross-Section | Stress Due to Loads on Bare Steel Beams | Stress Due to Loads on Composite Unit | Resultant Stress Distribution |
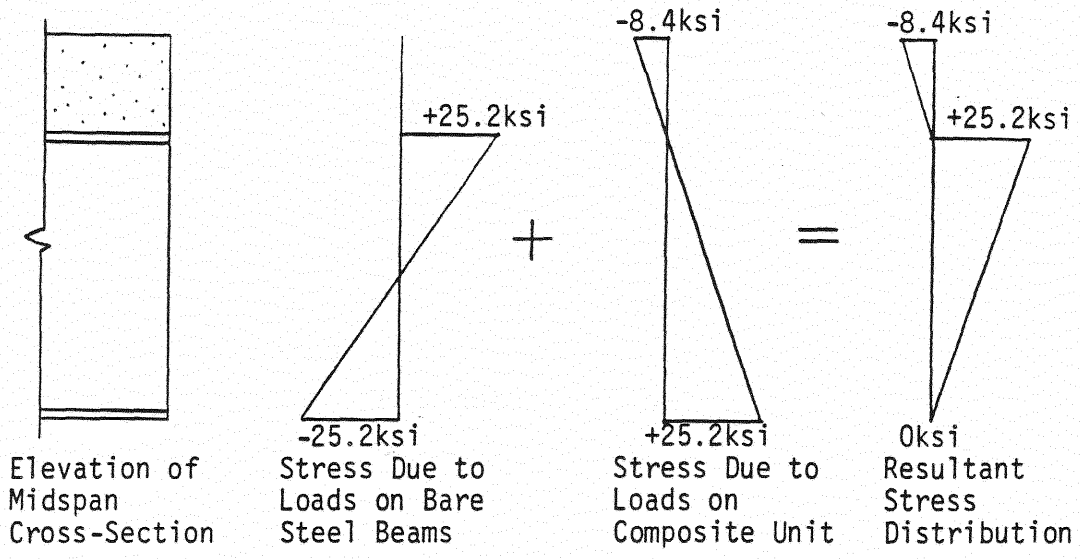
(a) Stresses on First Unit Midspan Transformed Cross-Section

-8.0ksi   -8.0ksi

+28.8ksi   +28.8ksi

+

=

-28.8ksi   +26.2ksi   -2.6ksi

| Elevation of Midspan Cross-Section | Stress Due to Loads on Bare Steel Beams | Stress Due to Loads on Composite Unit | Resultant Stress Distribution |

(b) Stresses on Second Unit Midspan Transformed Cross-Section

Figure K.5   Theoretical Stress Distribution Resultants on Transformed Sections of Upright Units Prior to Testing

K.10

strength is not affected. This is because the internal stresses due to prestressing of the unit balance themselves and require no external moment resistance; hence, the full ultimate moment capacity of the cross-section is available regardless of the internal stress state. The theoretical ultimate moment strengths of both units were calculated by standard ultimate strength methods.

The ultimate moment capacities were calculated to be 2273 ft-kips and 2310 ft-kips for the first and second units, respectively. The first yield strengths and ultimate strengths, as well as deflection and strain calculations made by the described methods, were used in comparing the experimental and theoretical behavior of the bridge units in Chapter II, Summary of Primary Test Results.

APPENDIX L

MATERIAL PROPERTIES

Table L.1

Material Properties

(a) Steel Beams (W21x50, A588 Grade 50 Steel)

Test Specimen	Tensile Strength (ksi)	Elastic Modulus (ksi)
First Unit	56.0	29000.0*
Second Unit	58.0	29000.0*

(b) Reinforcement (#4 Bar - Grade 60)

Test Specimen	Tensile Strength (ksi)	Elastic Modulus (ksi)
First Unit	67.2	29000.0*
Second Unit	-	29000.0*
Control Slabs	79.5	-
Shear Connector Specimens	-	-

(c) Concrete (5.0 ksi Design Strength)

Test Specimen	Age at Cylinder Test (days)	Compressive Strength (ksi)	Elastic Modulus (ksi)
First Unit	28	5.3	4394.0*
	1408	7.40	4365.0
Second Unit	51	6.45	5335.0
Control Slabs	120	6.54	-
Shear Connector Specimens	28	5.74	-

*   Assumed
-   Not Required